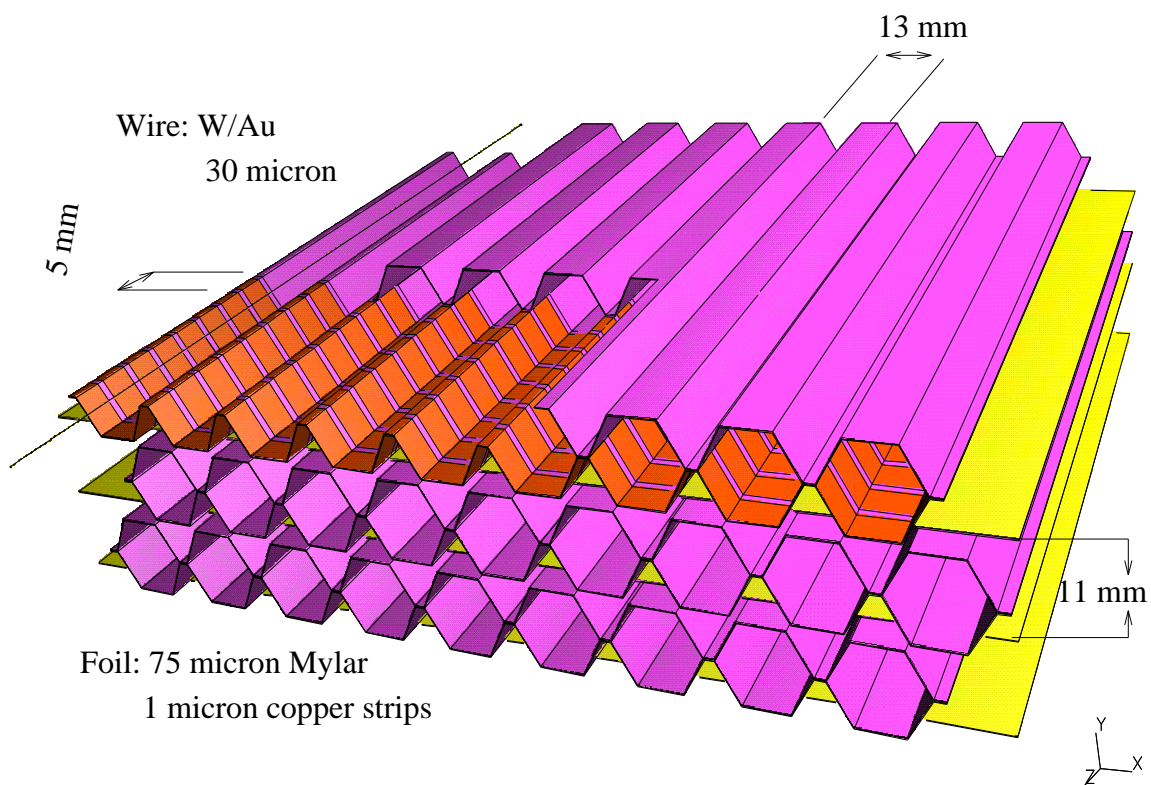


# THE HONEYCOMB STRIP CHAMBER:

## A TWO COORDINATE AND HIGH PRECISION MUON DETECTOR





# **THE HONEYCOMB STRIP CHAMBER:**

## **A TWO COORDINATE AND HIGH PRECISION MUON DETECTOR**

### **PROEFSCHRIFT**

ter verkrijging van  
de graad van doctor aan de Universiteit Twente,  
op gezag van de rector magnificus,  
prof. dr. Th. J. A. Popma,  
volgens besluit van het College voor Promoties  
in het openbaar te verdedigen  
op vrijdag 19 april 1996 te 13.15 uur.

door

**Hoite Pieter Theodoor Tolsma**  
geboren op 14 juli 1967  
te Rosmalen

Dit proefschrift is goedgekeurd door:

prof. dr. C. Daum (promotor) en  
dr. ir. H. van der Graaf (assistent-promotor)

# Contents

<b>Introduction</b>	<b>ix</b>
<b>1 Physics at the LHC in the muon channels</b>	<b>1</b>
1.1 Introduction . . . . .	1
1.2 The Large Hadron Collider . . . . .	1
1.2.1 Design parameters of the LHC . . . . .	2
1.2.2 Particle production rates . . . . .	2
1.3 Detection of the Higgs, top-quark and $Z'$ at LHC . . . . .	4
1.3.1 The Standard Model Higgs . . . . .	4
1.3.1.1 Higgs production and decay . . . . .	4
1.3.1.2 $H \rightarrow ZZ^* \rightarrow l^+l^-l^+l^-$ ( $m_H < 2m_Z$ ) . . . . .	7
1.3.1.3 $H \rightarrow ZZ \rightarrow l^+l^-l^+l^-$ ( $m_H > 2m_Z$ ) . . . . .	10
1.3.2 Top-quark physics . . . . .	11
1.3.2.1 Top-quark production and decay . . . . .	11
1.3.2.2 $t\bar{t} \rightarrow WWb\bar{b} \rightarrow lvq\bar{q}b\bar{b} \rightarrow lv + \text{jets}$ single-isolated-lepton channel . . . .	13
1.3.2.3 $t\bar{t} \rightarrow WWb\bar{b} \rightarrow l\nu l\nu b\bar{b}$ two-isolated-lepton channel . . . . .	13
1.3.3 New heavy vector bosons . . . . .	14
1.3.3.1 Production and decay of the $Z'$ . . . . .	14
<b>2 Requirements on muon detectors at LHC</b>	<b>17</b>
2.1 Introduction . . . . .	17
2.2 The invariant mass in the $\mu^+\mu^-$ system . . . . .	17
2.3 The ATLAS muon spectrometer . . . . .	18
2.3.1 The air core toroids . . . . .	21
2.3.2 Spectrometer performance . . . . .	22
2.4 The HSC as muon detector in the ATLAS barrel . . . . .	22
2.5 Alignment . . . . .	24
2.6 Muon backgrounds . . . . .	26
2.6.1 Decay muons and hadronic punchthrough . . . . .	27
2.6.2 Neutrons and gammas . . . . .	27
<b>3 The Honeycomb Strip Chamber</b>	<b>29</b>
3.1 Introduction . . . . .	29
3.1.1 The Proportional Counter . . . . .	30
3.1.2 The Multi Wire Proportional Chamber and the Drift Chamber . . . . .	30
3.1.3 The Honeycomb Strip Chamber . . . . .	30
3.2 The chamber principle . . . . .	30
3.3 Constructed prototypes . . . . .	32
3.3.1 The 'Prototype 1' (P1) chamber . . . . .	33
3.3.2 The TRACAL chambers . . . . .	35
3.3.3 The 'Prototype 2' (P2) chambers . . . . .	35
3.3.4 The 'Prototype 3' (P3) chamber . . . . .	38
3.3.5 The 'Prototype 3 Aluminium' (P3A) chamber . . . . .	39
3.4 Charged particle detection with the HSC . . . . .	40
3.4.1 Energy loss of relativistic particles in matter . . . . .	40
3.4.1.1 Primary ionisation . . . . .	40

3.4.1.2	Relativistic rise . . . . .	40
3.4.1.3	$dE/dx$ distribution for thin gas layers . . . . .	41
3.4.1.4	From $dE/dx$ to primary ionisation fluctuations . . . . .	42
3.4.1.5	Experimental cluster size distributions . . . . .	43
3.4.1.6	The range of $\delta$ -electrons . . . . .	44
3.4.2	The drift of electrons in gases . . . . .	46
3.4.2.1	The electric field . . . . .	46
3.4.2.2	The drift velocity . . . . .	46
3.4.2.3	The Lorentz angle $\alpha_L$ . . . . .	47
3.4.2.4	Longitudinal and transverse diffusion . . . . .	47
3.4.2.5	Attachment . . . . .	49
3.4.2.6	The Boltzmann transport equation . . . . .	50
3.4.3	The gas amplification process . . . . .	51
3.4.3.1	Photons in the gas amplification process . . . . .	51
3.4.3.2	The amplification factor: Gain . . . . .	51
3.4.3.3	Variations in the gain . . . . .	52
3.4.4	The signal development: Drift of ions . . . . .	54
3.4.5	Space charge effects . . . . .	55
3.4.5.1	Reduction of the gas gain . . . . .	55
3.4.5.2	The drift field . . . . .	56
3.4.5.3	Recombination . . . . .	58
3.4.6	Electrostatic force on the wire . . . . .	58
<b>4</b>	<b>Simulation methods of the HSC wire and strip readout</b>	<b>63</b>
4.1	Introduction . . . . .	63
4.2	The gas properties: MAGBOLTZ . . . . .	64
4.3	Detailed drift cell simulation: GARFIELD . . . . .	66
4.4	Front-end electronics simulation . . . . .	66
4.4.1	The input . . . . .	67
4.4.2	The wire . . . . .	67
4.4.3	Noise . . . . .	68
4.4.4	The amplifier . . . . .	68
4.4.5	The shaper . . . . .	69
4.4.6	The discriminator . . . . .	69
4.4.7	The TDC . . . . .	69
4.4.8	Some results . . . . .	69
4.5	Simulation of the strip response of the HSC . . . . .	71
4.5.1	Determination of the second coordinate $x$ from $Q_L/Q_M$ and $Q_R/Q_M$ . . . . .	73
<b>5</b>	<b>Autocalibration of the relation between drift distance and drift time</b>	<b>75</b>
5.1	Introduction . . . . .	75
5.2	Determination of the initial $r(t)$ . . . . .	76
5.3	The autocalibration algorithm . . . . .	78
5.3.1	The track fit . . . . .	78
5.3.2	Correcting the $r(t)$ relation . . . . .	80
5.3.2.1	Definition of the $r(t)$ relation . . . . .	80
5.3.2.2	Correction of the $r(t)$ relation . . . . .	80
5.3.2.3	Definition and minimisation of the error function . . . . .	80
5.3.2.4	Linearisation of the error function . . . . .	81
5.3.2.5	Writing $N_p$ equations in matrix notation . . . . .	83

5.3.3	An example: autocalibration of simulated data with a large and small angular distribution . . . . .	83
5.3.3.1	The setup . . . . .	84
5.3.3.2	The analysis . . . . .	84
5.3.3.3	Data with a Gaussian angular distribution of 200 mrad (rms) . . . . .	84
5.3.3.4	Data with an angular distribution of 2, 20 and 100 mrad (rms) . . . . .	87
5.4	The MSGC/P1 experiment . . . . .	89
5.4.1	Introduction . . . . .	89
5.4.2	The experimental setup . . . . .	89
5.4.2.1	The P1 HSC . . . . .	91
5.4.2.2	The Micro Strip Gas Counter . . . . .	92
5.4.3	The analysis . . . . .	92
5.4.3.1	Reference chamber analysis . . . . .	92
5.4.4	Results . . . . .	93
5.4.4.1	Reference chamber . . . . .	94
5.4.4.2	$r(t)$ determination . . . . .	94
5.4.4.3	Autocalibration . . . . .	95
5.4.4.4	Comparison and conclusion . . . . .	96
<b>6</b>	<b>Detector performance</b>	<b>99</b>
6.1	Introduction . . . . .	99
6.2	Experimental setup . . . . .	99
6.2.1	Cosmic muon setup . . . . .	100
6.2.2	The RD5 test facility . . . . .	101
6.3	Results from chamber tests . . . . .	104
6.3.1	Drift gas mixture . . . . .	104
6.3.2	High voltage and threshold settings . . . . .	111
6.3.3	The angle of incidence $\theta$ . . . . .	113
6.3.4	Primary ionisation density . . . . .	115
6.3.5	The segmentation of the cathode in strips . . . . .	118
6.3.6	The coordinate along the wire . . . . .	119
6.3.7	$B$ -field study . . . . .	121
6.3.8	P3 versus P3A . . . . .	127
6.4	Conclusions and outlook . . . . .	128
	<b>Appendices</b>	<b>131</b>
<b>A</b>	<b>The classical theory of drift of electrons in gases</b>	<b>133</b>
A.1	Equation of motion for a free electron with $E \perp B$ . . . . .	133
A.2	The macroscopic drift velocity . . . . .	134
A.3	The Lorentz angle $\alpha_L$ . . . . .	135
A.4	Diffusion in the microscopic picture . . . . .	136
A.5	Determination of $v_0$ by energy conservation . . . . .	136
A.6	Druyvesteyn versus Maxwell model . . . . .	138
A.6.1	Electron-velocity distribution . . . . .	138
A.6.2	Electron-position distribution . . . . .	139
A.6.3	Determination of $D_L^2$ and $D_T^2$ . . . . .	140

<b>B</b>	<b>Alignment with the CCD/RASNIK</b>	<b>141</b>
B.1	Principle . . . . .	141
B.2	Practical realisation . . . . .	141
B.3	Prototype Results . . . . .	142
<b>C</b>	<b>The HGANA analysis programme</b>	<b>145</b>
C.1	Introduction . . . . .	145
C.2	Layout of the programme . . . . .	146
C.3	The wire data analysis . . . . .	146
C.4	The strip data analysis . . . . .	147
C.5	The datacards . . . . .	148
	<b>Glossary and abbreviations</b>	<b>151</b>
	<b>Bibliography</b>	<b>153</b>
	<b>Summary</b>	<b>157</b>
	<b>Samenvatting</b>	<b>159</b>
	<b>Acknowledgements</b>	<b>161</b>
	<b>Curriculum vitae</b>	<b>163</b>



# Introduction

When Charpak built the first proportional counter in 1966 at CERN, he gave an important impulse to the field of physics that studies the tiniest building blocks of matter. With his detector, charged particles were detected electronically (instead of optically), resulting in an enormous reduction in the recording time of an event, making more rare events accessible for detailed studies. The precision of the particle position measurement with the proportional counter was given by the wire pitch and therefore very poor with respect to the precision achieved before by photographs of bubble chambers.

The proportional counter evolved into the drift chamber. By measuring the time difference between the passage of the charged particle through the detector and the registration of the signal on the anode wire the time of drift of the electrons was measured. The drift time was converted into a drift distance using the known drift velocity of the electrons. Those detectors had a separate drift volume with a constant electric field and an amplification region close to the wire, with a  $1/r$  dependence of the electric field. The drift path of the electrons in this type of detectors is in the range from 5 cm to more than a metre. The spatial resolution is then dominated by the diffusion in the drift region of the detector. This type of detectors is used in the muon and inner tracker systems of e.g. the LEP experiments.

It was observed that on wires in the neighbourhood of the anode wire which carries the signal an opposite signal was induced, which amplitude was a function of the distance of the wire to the anode wire. This induced charge was also observed on the cathode planes of conventional wire chambers. By segmenting the cathode planes in strips perpendicular to the direction of the wires and measuring the centre of gravity of the charge on several adjacent strips a precision in the position of the avalanche along the wire of less than 100  $\mu\text{m}$  has been achieved.

The Large Hadron Collider (LHC) will produce enormous amounts of charged particles in a short bunch spacing (25 ns), high density (up to 400 Hz/cm<sup>2</sup>) and large range of momenta (for muons up to 1 TeV/c). For the small area detectors close to the interaction vertex, silicon strip and pixel detectors will be the adequate detectors to handle the particle density. For the inner tracker in front of the calorimeters, silicon detectors can be used, but a scaled down version of the Multi Wire Proportional Chamber (MWPC), the Micro Strip Gas Counter (MSGC), is also well applicable.

The muon systems of the future LHC experiments will have to cover an enormous surface of thousands of square metres. Neither silicon detectors, nor MSGCs can be considered because of prohibitive costs and some sort of drift chamber has to be optimised for the particle densities and required spatial precision of the tracks. In this thesis the Honeycomb Strip Chamber (HSC) will be introduced, described and studied as a muon detector for the largest LHC detector ATLAS. The bending coordinate will be measured by a drift time measurement in a hexagonal cell with inner radius of only 10 mm. For these small drift cells, the spatial precision of the device is no longer dominated by diffusion of the drifting electrons, but a complicated interference between primary ionisation statistics, diffusion and electronic response occurs. In addition, the detectors will be put in inhomogeneous magnetic fields. This results in a deviation of the drift path from the electric field lines during the drift of the electrons towards the anode. All these topics will be discussed in this thesis.

Chapter 1 will focus on a few processes at the LHC for which the muon system will play a dominant role in their study. As benchmark process for the 'stand alone' optimisation of the

muon spectrometer the production of the Higgs and decay to  $ZZ^{(*)} \rightarrow \mu^+ \mu^- \mu^+ \mu^-$  will be discussed. Also the production and (semi-)leptonic decay of the top-quark and the decay of the  $Z'$  and its signature in the muon system will be described.

In chapter 2 the requirements in terms of occupancy and momentum resolution will be set for the ATLAS muon spectrometer. The resulting layout of the ATLAS muon spectrometer will be described and particle rates from backgrounds will be estimated.

Chapter 3 will describe the construction of the multilayer HSCs and the physics processes affecting the performance of the drift tube.

In chapter 4 the detector simulation package will be introduced. This package of programs is used to compare the measured performance in chapter 5 with the theory of the drift tube as described in chapter 3.

Chapter 5 is devoted to the internal calibration (autocalibration) of the relation between the drift distance  $r$  and the drift time  $t$  from the redundancy in the data. An algorithm will be described that offers the possibility to verify the uniqueness of the obtained result.

Chapter 6 summarises the performance of the various prototypes for a large number of conditions.

*Aan mijn Ouders*

*Ceux qui ne comprendront pas sont priés par moi  
d'observer une attitude toute de soumission, toute  
d'infériorité.*

Erik Satie (1866–1925)

The small hon-  
of the odd pages  
wards the anode wire in  
The solid line represents  
extracted from a simula-  
Ar/CO<sub>2</sub>/ethane 70/25/5  
was 2475 V. The  
wire makes the

eycomb cell in  
shows the drift of  
a strong magnetic field  
the muon track, ionising  
tion of the P3 Honeycomb  
and the applied high  
3 T magnetic field  
electrons spiral

the right corners  
the electrons to-  
in time steps of 15 ns.  
the gas. The frames are  
detector. The drift gas was  
voltage on the wire  
parallel to the  
around the wire.



# Chapter 1

## Physics at the LHC in the muon channels

### Contents

---

<b>1.1</b>	<b>Introduction . . . . .</b>	<b>1</b>
<b>1.2</b>	<b>The Large Hadron Collider . . . . .</b>	<b>1</b>
1.2.1	Design parameters of the LHC . . . . .	2
1.2.2	Particle production rates . . . . .	2
<b>1.3</b>	<b>Detection of the Higgs, top-quark and Z' at LHC . . . . .</b>	<b>4</b>
1.3.1	The Standard Model Higgs . . . . .	4
1.3.2	Top-quark physics . . . . .	11
1.3.3	New heavy vector bosons . . . . .	14

---

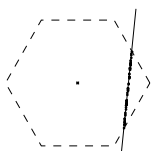
### 1.1 Introduction

**T**his chapter will introduce the LHC and the physics potential of the collider. Since this thesis is devoted to the development of a muon detection technology, I will focus on the channels where the leptons are an important signature of the process. Amongst those physics processes, I will treat the detection of the Higgs, top-quark and new heavy vector bosons.

### 1.2 The Large Hadron Collider

Already in the beginning of the 1980's, people at CERN started to think about testing the standard model beyond LEP energies. The LEP machine ( $e^+e^-$ ) has worked around the Z-resonance ( $m_Z = 91 \text{ GeV}/c^2$ ) and is momentarily upgraded to LEP200 with a maximum centre of mass energy  $\sqrt{s}$  of 200 GeV. This  $\sqrt{s}$  value is the practical maximum achievable with a circular electron accelerator in the 27 km circumference LEP tunnel due to the rapid increase of synchrotron radiation loss with energy. The large mass of hadrons with respect to electrons has the advantage that less energy is lost due to this effect. The main disadvantage of a hadron collider is the compositeness of the hadron. This means that the available energy of the hadron is distributed over the individual constituents (quarks and gluons). Since the cross sections have in general a  $1/s$  dependence, a centre of mass energy in the TeV domain means the highest possible event rate.

Considering the above arguments and given that a new collider at CERN has to match the existing LEP tunnel, the Large Hadron Collider (LHC) was designed.



### 1.2.1 Design parameters of the LHC

The LHC will be able to accelerate and store protons as well as heavy ions. Although one can use the LHC with Pb-Pb at a centre of mass energy in the PeV range, the energy will be distributed over many partons and the theoretical description of the collisions will be dramatically complicated.

At the Aachen workshop on the LHC in 1990 [1], the machine was presented as a p-p collider with a centre of mass energy  $\sqrt{s}$  of  $2 \times 7.7 = 15.4$  TeV. The maximum luminosity with three interaction points should be  $1.7 \cdot 10^{34} \text{ cm}^{-2}\text{s}^{-1}$  and the bunch spacing 15 ns [2]. The machine was planned to be built on top of the LEP collider with a vertical spacing of approximately 1 metre. The idea was to keep LEP intact and to construct in a later phase of the LHC project an e-p collider [3].

Detailed studies on the machine have changed the project. The LEP machine will be removed from the tunnel and stored for later reuse. So the LHC will replace LEP in the tunnel. The bunch spacing has been increased to 25 ns. This means that several events from successive bunch crossings will be present simultaneously in the LHC detectors, which is very different with respect to the LEP machine with a bunch spacing of several  $\mu\text{s}$ . Due to the longer bunch spacing, the maximum luminosity has decreased to  $10^{34} \text{ cm}^{-2}\text{s}^{-1}$ . Furthermore the centre of mass energy has been decreased from 15.4 to 14.0 TeV due to a slight decrease of the magnetic field in the bending magnets [4].

Notwithstanding the large circumference of LHC of nearly 27 km, all available space along the beamline will be occupied with superconducting NbTi bending magnets, beam optics and accelerating cavities. Those magnets will house two separated beam lines with opposite magnetic fields of 8.4 T strength. The dipole magnets will be 14.2 m long and 1232 magnets are foreseen along the beam line [5].

At the interaction points, the bunches will have a transverse radius of 15  $\mu\text{m}$  and the length of the bunch will be 30 cm. This means that the position of the vertex in the detector will have a rather large spread along the beam direction. The effective spread of the distribution of the vertex position is expected to be 5.5 cm (rms) along the beam direction.

### 1.2.2 Particle production rates

In figure 1.1 some important production cross sections and interaction rates are shown as function of the centre of mass energy  $\sqrt{s}$  of the LHC. The total interaction rate of soft proton-proton scattering is 1 interaction per ns at full luminosity ( $10^{34} \text{ cm}^{-2}\text{s}^{-1}$ ). This means that on average 25 interactions will be present in the centre of the detectors per bunch crossing. With an average number of 30 charged particle tracks per interaction this results in approximately 750 charged tracks in the detectors every bunch crossing.

The total cross section at LHC is subject to large uncertainties. The total cross section can only be extrapolated from UA4, UA5 and E710 (Tevatron) measurements at a  $\sqrt{s}$  of respectively 546, 900 and 1800 GeV, while the theoretical uncertainties of the behaviour of  $\sigma_{\text{tot}}(s)$  are large [6]. Depending on the model, the total cross section is estimated to be between 90 and 130 mb.

In case of small angle elastic and inelastic proton-proton scattering it is not possible to compute the scattering properties directly from the QCD Lagrangian. The transverse momenta of the produced particles will be small (less than a few GeV/c) and a large fraction of those particles will disappear undetected in the beampipe. Notwithstanding the very forward-backward topol-

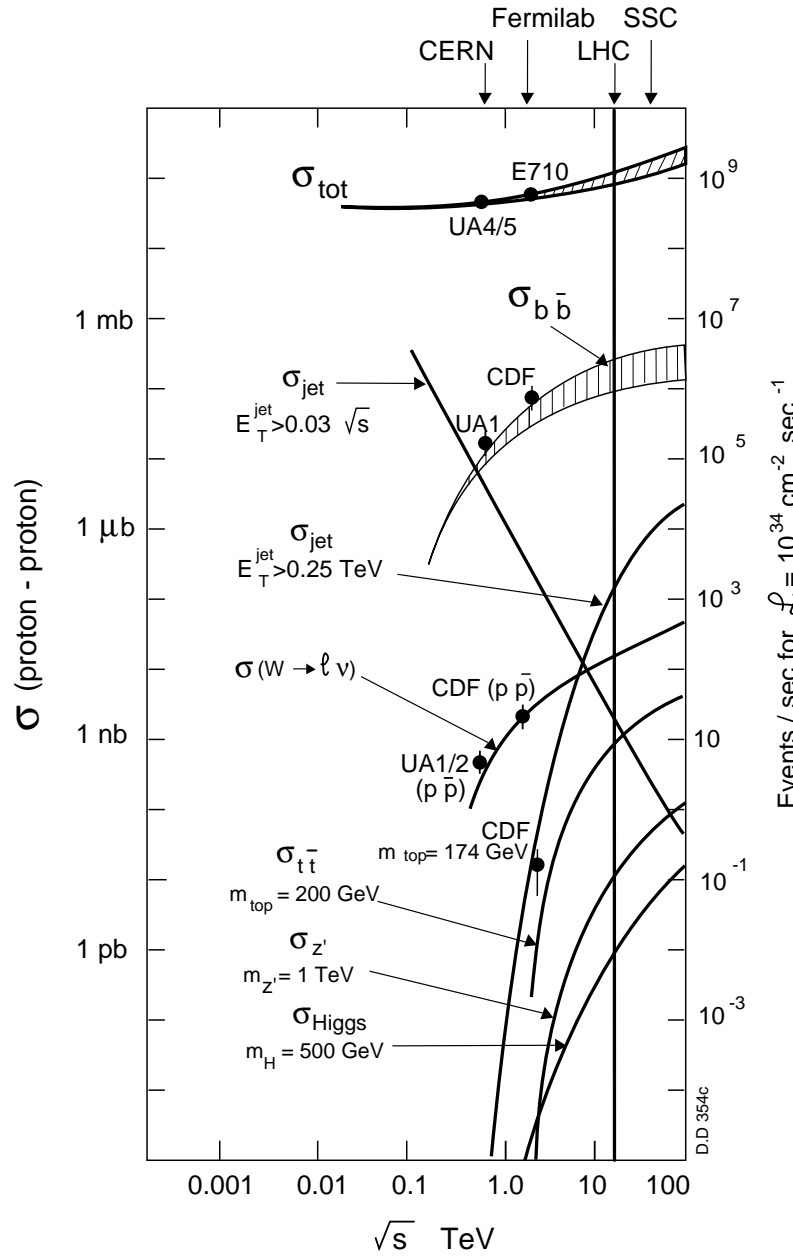
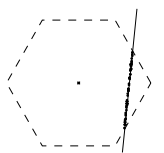


**Figure 1.1:** The cross-section of some characteristic processes. The centre of mass energy of LHC is indicated at the top. At  $\sqrt{s} = 14 \text{ TeV}$  the production of the Higgs is eleven orders of magnitude less frequent than small angle  $p$ - $p$  scattering [6].

ogy of the soft proton-proton interactions, it is important to know the main characteristics of this type of events. Since those interactions will be numerous, they will dominate the 25 underlying events per bunch crossing and can cause pile up problems in the detectors. A detector trigger which is sensitive for this type of events is called a 'minimum bias' trigger. In case of LHC detectors with the LHC machine at full luminosity this trigger is essentially equal to a random bunch cross trigger.



## 1.3 Detection of the Higgs, top-quark and Z' at LHC

One of the main goals of LHC is to study the actual mechanism for symmetry breaking in the electro-weak sector of the standard model. This phenomenon is associated with the nature of the Higgs mechanism, the existence of the Higgs particle and the behaviour of the cross sections involving the gauge bosons,  $W^\pm$  and  $Z$ . At the moment, the lower mass limit of the Higgs is  $60 \text{ GeV}/c^2$  from Higgs searches at LEP1. In case the Higgs is not discovered at LEP200 the lower limit will be  $\approx 80 \text{ GeV}/c^2$  at the startup of the LHC [7].

Experiments at the LHC will be able to search for the Higgs up to  $1 \text{ TeV}/c^2$ . In section 1.3.1 the various decay channels will be discussed which give the optimal signal-to-background ratio for various Higgs masses.

At the LHC, heavy fermions (bottom and top-quarks) will be produced in large quantities. The main issue of B physics is the observation of CP violation in the B-system, and the goal is to measure the three interior angles of the unitarity triangle corresponding to the Cabibbo-Kobayashi-Maskawa (CKM) matrix [8]. Since the topology of  $b\bar{b}$  events are very forward or backward oriented with the two B's in the same direction, a dedicated B-physics experiment has been proposed at the LHC: LHC-B [9].

In 1994, the CDF experiment has presented evidence for the existence of the top-quark and this evidence was confirmed by the D0 collaboration and more statistics in the 1995 run. At this moment the mass of the top-quark is  $180 \pm 12 \text{ GeV}/c^2$  [10, 11]. At this mass,  $t\bar{t}$  production will dominate top-quark production. The LHC machine will produce approximately  $10^6$   $t\bar{t}$  events per year already at a luminosity of  $10^{32} \text{ cm}^{-2}\text{s}^{-1}$ . This will make the LHC a real 'top factory' and allows to study its production and decay in detail. We will see in section 1.3.1 that top-quark decays will be a serious background in the Higgs signal.

### 1.3.1 The Standard Model Higgs

At the bottom of figure 1.1 the production cross section of the rather heavy Higgs of  $500 \text{ GeV}/c^2$  is shown. The Higgs with this mass will be produced every 2 minutes at LHC, resulting in  $10^5$  produced Higgs bosons per year. The problem in detection of the Higgs decay rises from the small branching ratio ( $\approx 3 \times 10^{-4}$ ) of the cleanest signal:  $H \rightarrow ZZ \rightarrow l^+l^-l^+l^-$ . Here, the lepton  $l$  can be an electron or muon [6]. The Higgs  $\rightarrow \mu^+\mu^-\mu^+\mu^-$  will be one quarter of the above described channel. This very small branching ratio of the Higgs to 4 muons will result in a total production of 10 events of this kind per year. We will see in section 1.3.1 that the Higgs production rate for a less massive Higgs will be significant larger, but the scale of the problem is set.

Within the Standard Model, the Higgs production cross section and decay branching ratios can be well computed. Only relatively small uncertainties are introduced by the gluon structure functions of the proton.

#### 1.3.1.1 Higgs production and decay

Because the Higgs is heavy and its coupling being proportional to mass, it essentially does not couple to light particles. This means that heavy real or virtual states must be excited to produce the Higgs and the Higgs will decay to heavy fermions or intermediate vector bosons ( $b\bar{b}$ ,  $t\bar{t}$ ,  $WW$ ,  $ZZ$ ).



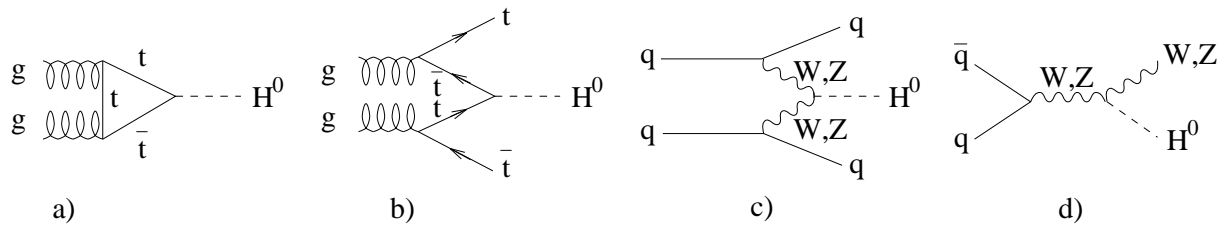


**Figure 1.2:** The production of a Higgs boson through four channels: a) gluon-gluon fusion; b)  $t\bar{t}$  fusion; c) WW and ZZ fusion; d) W and Z bremsstrahlung.

The basic Higgs production mechanisms are shown in figure 1.2. The dominant processes are the gluon-gluon fusion and WW(ZZ) fusion.

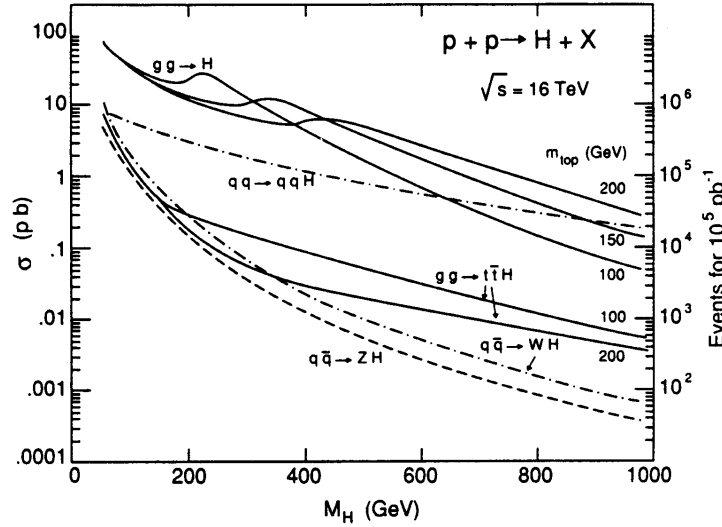
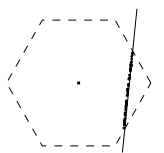


**Figure 1.3:** Total cross-section for Higgs production at LHC as a function of the Higgs mass  $m_H$ , as given by the four production mechanisms illustrated in figure 1.2 [12].

In figure 1.3 the production cross sections are shown. In this figure WW(ZZ) fusion is labelled by  $qq \rightarrow qqH$ . The expected Higgs production rates range from  $10^6$  to  $10^4$  events per year at full luminosity for  $m_H$  varying from  $100 \text{ GeV}/c^2$  to  $1 \text{ TeV}/c^2$ . The production cross section of the Higgs increases rapidly for a low mass Higgs. If the Higgs mass is below the ZZ or WW threshold, the heaviest accessible pair of quarks ( $b\bar{b}$ ) is overlayed with a huge QCD background and therefore not an appropriate channel to detect the Higgs.

In case the Higgs is heavy ( $m_H > 200 \text{ GeV}/c^2$ ), not only the production cross section goes down, but also its width increases rapidly. This is shown in figure 1.4. The experimental mass resolution is only important for a low mass Higgs ( $m_H < 200 \text{ GeV}/c^2$ ) where the width is smaller than  $2 \text{ GeV}/c^2$ . For large Higgs masses, ( $m_H \gg m_W$ ) the width varies as  $\Gamma_H \approx 0.5 \text{ TeV}/c^2 (m_H / 1 \text{ TeV}/c^2)^3$ , and the Higgs signal dissolves in the background.

In figure 1.5 the branching ratios are shown for Higgs masses between  $50$  and  $600 \text{ GeV}/c^2$ . Especially in the region between  $80 \text{ GeV}/c^2 < m_H < 100 \text{ GeV}/c^2$  it is hard to find a suitable process to fill the gap between LEP200 ( $m_H < 80 \text{ GeV}/c^2$ ) and the region where  $ZZ^*$  production provides a reasonably clean lepton signal. The two candidate processes are  $H \rightarrow \gamma\gamma$  (figure 1.2a) and associated WH(ZH) production (figure 1.2d)  $WH \rightarrow l\nu\gamma\gamma$  [15]. The  $H \rightarrow \gamma\gamma$  process suffers an enormous background from  $q\bar{q} \rightarrow \gamma\gamma$  and jet-jet production, where both jets fake a  $\gamma$ . Although the associated WH production is very rare (only 30 of those events are expected per  $10^5 \text{ pb}^{-1}$ ) a



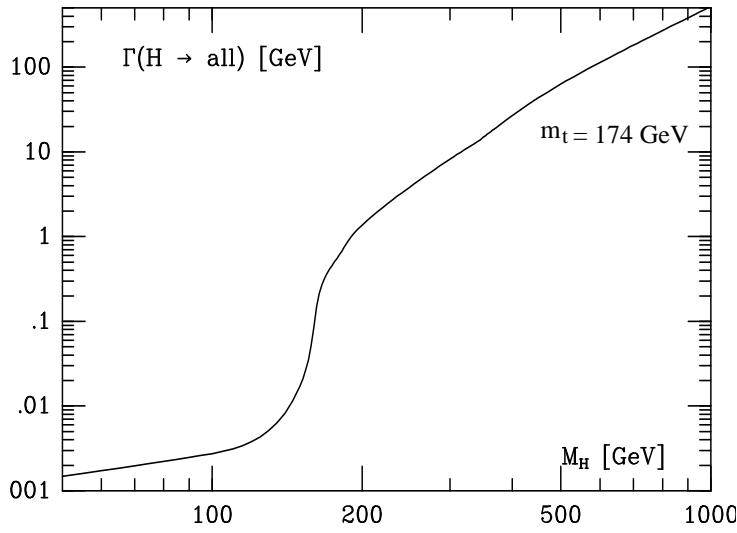


**Figure 1.4:** Total Higgs width as a function of  $m_H$  [13].

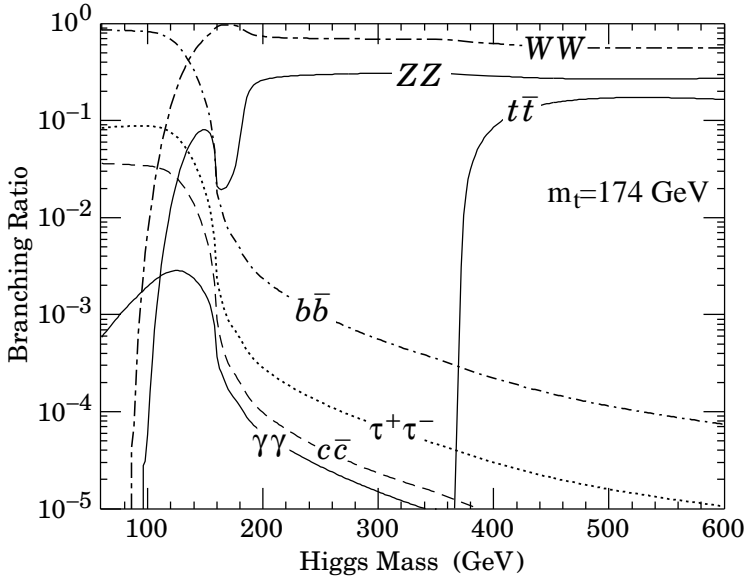


**Figure 1.5:** Branching ratios of the Higgs in the mass range  $60 < m_H < 600 \text{ GeV}/c^2$  [14].

better background rejection is possible than in the two photon channel. Therefore this channel is preferred for the Higgs searches at the LHC for Higgs masses down to the LEP200 upper limit.

For Higgs masses between 130 and  $800 \text{ GeV}/c^2$  the decays  $H \rightarrow ZZ^*$  ( $m_H < 2m_Z$ ) and  $H \rightarrow ZZ$  ( $m_H > 2m_Z$ ) deliver the most convenient topology. Each Z boson will decay into two leptons ( $e^+e^-$  or  $\mu^+\mu^-$ ) and will thus deliver a clear signature over a large mass range. The only drawback of the  $H \rightarrow ZZ \rightarrow l^+l^-l^+l^-$  channel is the small branching ratio of  $\approx 10^{-3}$ . At  $m_H \approx 120$  to  $130 \text{ GeV}/c^2$ , about 100  $H \rightarrow l^+l^-l^+l^-$  events are produced per  $10^5 \text{ pb}^{-1}$ , and the acceptance is low [6]. About 1500 of those events are expected for  $m_H = 200 \text{ GeV}/c^2$ , 200 events for  $m_H = 500 \text{ GeV}/c^2$  and 10 events for  $m_H = 1 \text{ TeV}/c^2$ , where the width of the Higgs becomes too large to be resolved from the background. The  $H \rightarrow ZZ \rightarrow \mu^+\mu^-\mu^+\mu^-$  channel is used as a benchmark process to optimise the performance of the muon systems of the LHC experiments.

In case the Higgs mass is between  $800 \text{ GeV}/c^2$  and  $1 \text{ TeV}/c^2$ , one can profit from the relatively large branching ratio of 0.8 % of the  $H \rightarrow ZZ \rightarrow l^+l^- \nu \nu$  channel. The event signature is a Jacobian

peak in the  $p_T^Z$  ( $Z \rightarrow l^+l^-$ ) distribution from the two-body  $H \rightarrow ZZ$  decay. The broad peak will appear above the irreducible  $q\bar{q}, gg \rightarrow ZZ$  electroweak continuum background. Assuming that the large reducible QCD background can be suppressed by an effective  $E_T^{\text{miss}}$  cut, a signal of 190 events for  $m_H = 0.8 \text{ TeV}/c^2$  with an integrated luminosity of  $10^5 \text{ pb}^{-1}$  can be expected [6].

If the Higgs mass exceeds  $1 \text{ TeV}/c^2$ , the  $H \rightarrow WW(ZZ) \rightarrow l^+l^- \text{jet-jet}$  channel will be favoured compared to the leptonic channels [6]. This is due to the large branching ratio (70%) of  $W(Z) \rightarrow q\bar{q} \rightarrow \text{jet-jet}$ . The dominant backgrounds are  $t\bar{t} \rightarrow W^+W^-bb$  and  $W$ +jets production. The background will also contain the continuum  $WW(ZZ)$  mass distribution, as compared with the broad width of the Higgs.

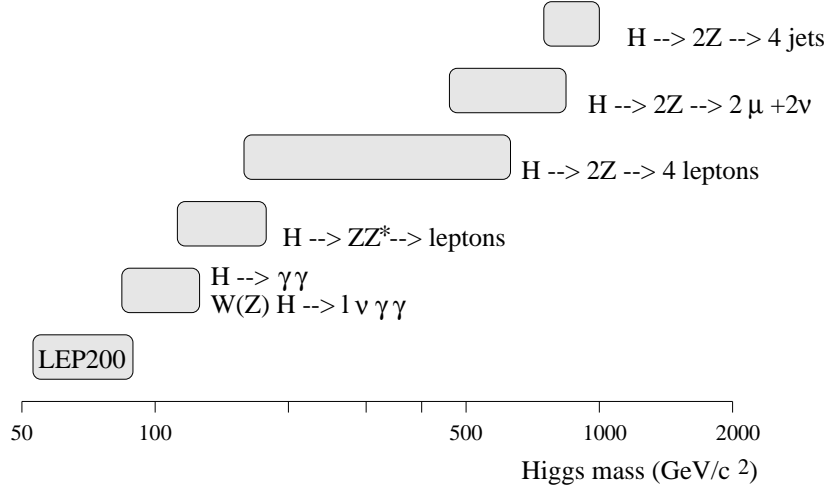


**Figure 1.6:** Higgs discovery potential in various channels. See the text for a discussion on the various channels.

The above discussion is summarised in figure 1.6, where the Higgs discovery potential of the various channels is indicated as function of the Higgs mass. It is important that the whole Higgs mass region from LEP200 search potential up to  $1.5 \text{ TeV}/c^2$  is covered.

### 1.3.1.2 $H \rightarrow ZZ^* \rightarrow l^+l^-l^+l^-$ ( $m_H < 2m_Z$ )

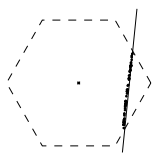
The Higgs decay channel to four leptons via two Zs has been studied extensively in the past. I will summarise the characteristics of this channel in case the Higgs is less massive than  $2m_Z$  ( $120 \text{ GeV}/c^2 < m_H < 180 \text{ GeV}/c^2$ ), and thus one Z is off-shell.

In the 4-lepton channel the rapidity coverage and single lepton efficiency of the detector are important. The (pseudo)rapidity  $\eta$  is defined as:

$$\eta \equiv -\ln \tan \left( \frac{\Theta}{2} \right), \quad (1.1)$$

where  $\Theta$  is the polar angle with respect to the beamline. In figure 1.7 the lepton rapidity distribution is plotted for the lepton with the highest rapidity in the Higgs decay. The rapidity cut-off of the CMS muon system at  $\eta = 2.4$  is indicated. Here it appears immediately that a significant fraction of the Higgs decays to 4 leptons is lost due to the limited rapidity coverage of the detector.

In order to separate the low momenta background leptons from leptons produced in  $H \rightarrow ZZ^{(*)} \rightarrow l^+l^-l^+l^-$ , one has to apply a  $p_T$  cut on the lepton momentum. This cut will reduce the background, but will also affect the Higgs detection efficiency. Figure 1.8 shows the expected



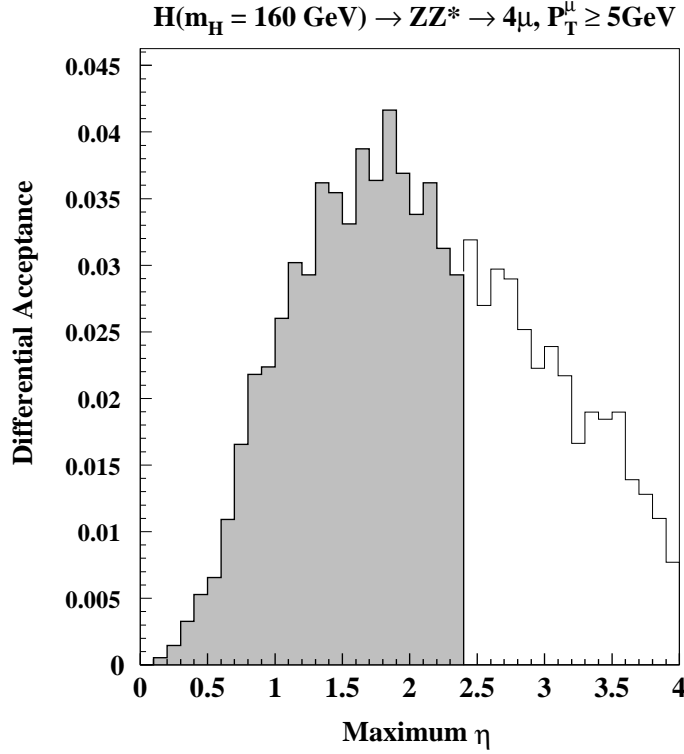


**Figure 1.7:** Derivative of the acceptance for the muon with the highest pseudorapidity in Higgs decay ( $m_H = 160 \text{ GeV}/c^2$ ) to four leptons. The shaded area covers the detector acceptance of the CMS muon system. The importance of a large rapidity acceptance for the decay of a low mass Higgs is obvious [16].

rates for detected  $H \rightarrow Z^{(*)}Z^{(*)} \rightarrow \mu^+\mu^-\mu^+\mu^-$  (or  $e^+e^-e^+e^-$ ) decays for an integrated luminosity of  $10^5 \text{ pb}^{-1}$  at LHC, as a function of lepton detector rapidity coverage ( $\eta_1$ ) and lepton  $p_T$ -threshold ( $p_T^{\min}$ ). It can be seen that for a low Higgs mass the rapidity coverage and  $p_T$ -threshold has a large impact on the Higgs detection efficiency.

In addition to the  $p_T$ -cut on single leptons, one can constrain the invariant mass of one of the lepton pairs to be equal to the Z mass. A typical cut-off criterion is  $|m_{12} - m_Z| < 10 \text{ GeV}/c^2$  (dominated by the momentum resolution of the detector), while  $m_{34} > 12 \text{ GeV}/c^2$ .

$m_H [\text{GeV}/c^2]$	120	130	140	150	160	170	180
$\sigma_{\text{tot}} \times \text{BR}(H \rightarrow ZZ^*) \text{ (pb)}$	0.231	0.600	1.012	1.218	0.687	0.350	0.934
Events per $10^5 \text{ pb}^{-1}$	14.4	41.7	75.4	92.4	54.0	27.5	76.2
Acceptance:	$ \eta_1  < 2.5, p_T^1 > 10 \text{ GeV}/c, p_T^{1,2} > 20 \text{ GeV}/c,$ $ m_Z - m_{1,2}  < 6 \text{ GeV}/c^2, m_{3,4} > 12 \text{ GeV}/c^2$						
Observed signal ( $m_H \pm 2\sigma_H$ )	1.3	8.4	19.5	29.8	19.0	10.3	31.0

**Table 1.1:** Summary of study by Hawkings [18] (see text).

The results of a study by Hawkings in the ATLAS detector is summarised in table 1.1 [18]. For this study the inner tracker was used to measure the  $p_T$  of muons below  $30 \text{ GeV}/c$ . For muons with  $p_T > 30 \text{ GeV}/c$  the ATLAS air core toroid magnet with high precision muon detectors was used (see chapter 2). This table shows that for  $m_H = 120 \text{ GeV}/c^2$  the detection rate of the Higgs

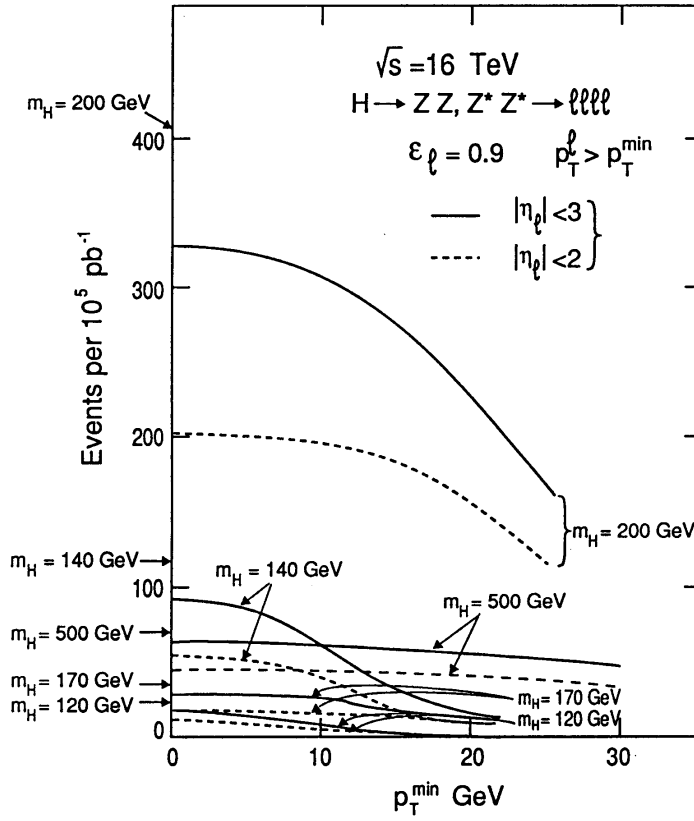


**Figure 1.8:** Number of detected Higgs events versus lepton  $p_T$  threshold and geometrical acceptance cuts. On the vertical scale the total production rate is indicated without any cuts or detector acceptance applied. From this figure it becomes clear that the low mass Higgs acceptance ( $m_H < 180 \text{ GeV}/c^2$ ) is much more sensitive for the applied  $p_T$  and  $\eta$  cuts than the rather heavy Higgs of  $500 \text{ GeV}/c^2$  [17].

in this channel is very low.

There are three main sources of background in the  $H \rightarrow ZZ^* \rightarrow l^+l^-l^+l^-$  channel, these will be discussed in decreasing order of importance [19]:

a) **non-resonant reducible background from  $t\bar{t} \rightarrow l^+l^-l^+l^- + X$**

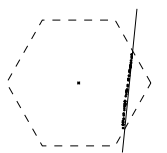
In case the same cuts are applied on the produced leptons from  $t\bar{t}$  decay as discussed above, the total number of background events is reduced from  $10^5$  to 2200 for  $10^5 \text{ pb}^{-1}$  [19]. Since the inclusive dilepton mass distribution is approximately flat around  $m_Z$ , it is clear that the  $t\bar{t}$  background is directly proportional to the window allowed around  $m_Z$ , and therefore sensitive to the detector resolution.

b) **semi-resonant reducible background from  $Zb\bar{b} \rightarrow l^+l^-l^+l^- + X$**

This background arises mainly from  $gg \rightarrow Zb\bar{b}$  and is potentially dangerous since it contains a Z boson in the final state. The production of this type of events is simulated with the PYTHIA [20] event generator. Also on this background source one can apply the cuts as described above and one finds for  $10^5 \text{ pb}^{-1}$  a total of  $2.5 \times 10^4$   $Zb\bar{b} \rightarrow l^+l^-l^+l^-$  from which 1240 survive the applied cuts [19, 21].

c) **irreducible background from  $Z^*Z^*$  and  $\gamma^*Z^* \rightarrow l^+l^-l^+l^-$**

This background turns out to be small, but can not be neglected since it is the only one which cannot be reduced by lepton isolation cuts. About 60 events (from 260) survive the acceptance criteria for  $10^5 \text{ pb}^{-1}$  [19].



Since most of the background events contain at least two non-isolated leptons from b-decay, demanding isolated leptons is a powerful background suppression tool. For this cut one has to use the position sensitivity of the calorimeter and combine this information with the position of the lepton in the tracking detector. A good understanding of the shower production in the calorimeter is, therefore, required.

$m_H$ [GeV/ $c^2$ ]	130	150	170
Signal	8.4	29.8	10.3
Backgrounds			
from $t\bar{t}$	12.3	20.0	23.0
from $Zb\bar{b}$	7.4	14.4	19.6
from $Z^*Z^*, \gamma^*Z^*$	1.9	2.8	3.0
Total	21.6	37.2	45.6
After lepton isolation			
Signal	6.7	23.8	8.3
Background	2.9	4.6	5.4

**Table 1.2:** Signal/Background for low mass Higgs before and after lepton isolation [18].

In table 1.2 a summary is given of signal and background rates for a Higgs mass from 120 to 180 GeV/ $c^2$ . I have only quoted the numbers for the muon channel. Comparative numbers are available for the electron channel. In figure 1.9 the Higgs signal is computed on top of the background for different Higgs masses. The measured invariant four muon mass is given without and with lepton isolation cut and is computed for a total integrated luminosity of  $10^5$  pb $^{-1}$ .

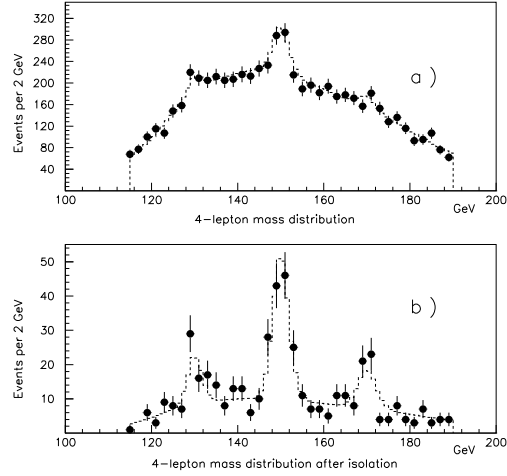


**Figure 1.9:** Higgs mass for 130, 150 and 180 GeV/ $c^2$  with and without lepton isolation [22].

### 1.3.1.3 $H \rightarrow ZZ \rightarrow l^+l^-l^+l^-$ ( $m_H > 2m_Z$ )

In case the Higgs mass is larger than twice the mass of the Z, both final state Z bosons are on shell and the Z-mass constraint (e.g.  $|m_{l^+l^-} - m_Z| < 10$  GeV/ $c^2$ ) can be applied on both pairs of produced leptons. On the other hand, the natural width of the Higgs increases rapidly in this mass regime, resulting in a smearing of the signal over the background.

Concerning the backgrounds the same (semi-)resonant and non-resonant sources exist as for the low mass Higgs. The non-resonant and semi-resonant background can be efficiently reduced by requiring that the invariant mass of both  $l^+l^-$  pairs has to be equal to the Z mass within a tight window. The momentum resolution of the muon (electron) measurement has to be small compared with the natural width of the Z (2.5 GeV/ $c^2$ ).

The resonant background is irreducible and all other backgrounds should be compared to it. The momentum resolution of the calorimeter and lepton spectrometers has to be good enough to bring the non-resonant background reasonably below the Z pair level. For large Higgs masses, the Higgs width is the dominant effect on the four-lepton mass reconstruction and the single lepton momentum resolution is of less importance.

In figure 1.10 the differential cross-sections are given for the discussed backgrounds and for Higgs production at  $m_H = 200, 400$  and 700 GeV/ $c^2$  [23]. The solid curves represent the expected signal. In figure 1.10a) no detector resolution is included and no mass constraint on the  $\mu^+\mu^-$  pairs is applied. As can be seen, the signal drowns in the background. In figure 1.10b) a detector

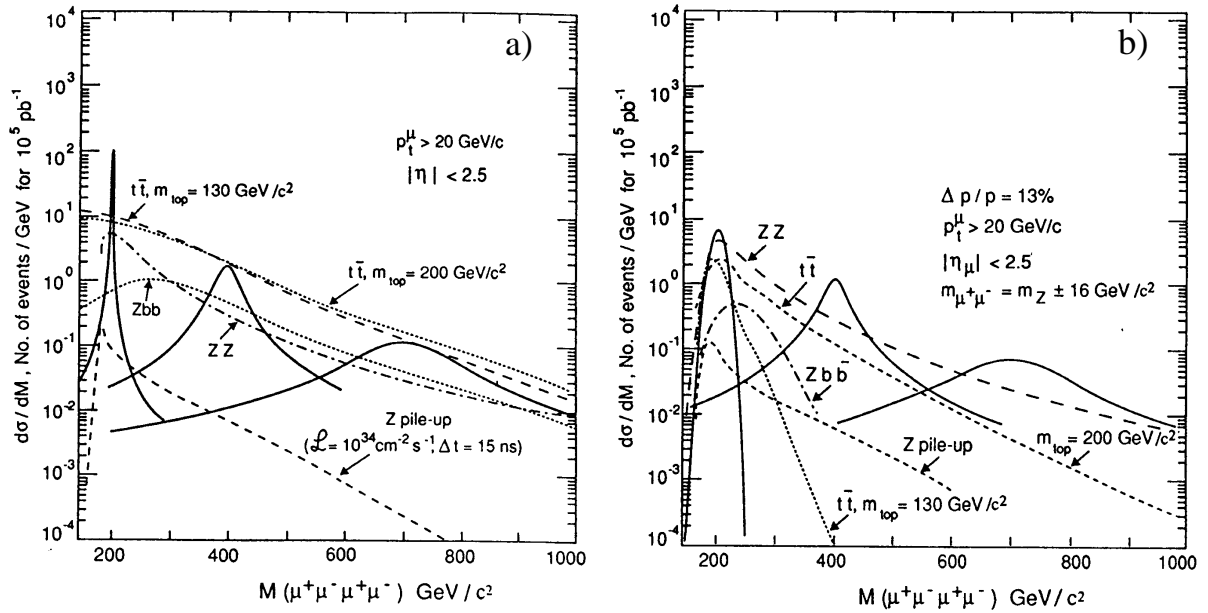


**Figure 1.10:** a)  $\mu^+\mu^-\mu^+\mu^-$  differential cross-section for several processes; muons have  $p_T > 20 \text{ GeV}/c$  and  $|\eta| < 2.5$ . b)  $\mu^+\mu^-\mu^+\mu^-$  differential cross-section after detector simulation; muons are required to have  $p_T > 20 \text{ GeV}/c$  and  $|\eta| < 2.5$ . The  $\mu^+\mu^-$  invariant mass is equal to the  $Z$  mass within  $\pm 16 \text{ GeV}/c^2$  for both muon pairs [23].

smearing of  $\Delta p/p = 13\%$  has been applied on the signal, affecting only the signal of the low mass ( $m_H = 200 \text{ GeV}/c^2$ ) Higgs. Also the mass of the two muon pairs was constrained to the mass of the  $Z \pm 16 \text{ GeV}/c^2$ . Now the signal appears on top of the background where the significance is only marginal for the Higgs with mass of  $200 \text{ GeV}/c^2$ . The signal to background ratio can be improved by increasing the momentum resolution of the muon spectrometer. In case of the ATLAS muon spectrometer the single muon momentum resolution is certainly better than  $13\%$ . For this spectrometer it is foreseen to have a momentum resolution  $\Delta p/p$  below  $2.5\%$  between  $p = 20$  and  $250 \text{ GeV}/c$  (at  $\eta = 0$ ).

## 1.3.2 Top-quark physics

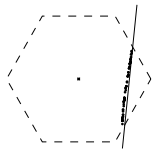
The production and decay of the top-quark can be studied in detail at the LHC. Not only can its mass be measured in different channels, but also the decay branching ratios and searches for rare top-quark decays such as  $t \rightarrow bH^+$  or  $t \rightarrow Zc$  can be performed [4].

### 1.3.2.1 Top-quark production and decay

At  $m_t = 180 \text{ GeV}/c^2$ , the  $t\bar{t}$  production dominates top production. I noted already that the  $t\bar{t}$  production is a serious background for the Higgs search and the LHC is considered to be a genuine top-factory. Even at low luminosity of  $10^{32} \text{ cm}^{-2} \text{ s}^{-1}$  approximately 6000  $t\bar{t}$  pairs should be produced per day.

The diagrams of the most dominant production processes are shown in figure 1.11, where the single top production via process c) is more rare than the  $t\bar{t}$  production processes.

Within the framework of the Minimal Standard Model (MSM) the top-quark decays exclusively into a  $W$  boson and a quark. Since the value of  $|V_{tb}|$  in the CKM matrix is close to unity we will only consider the decay of the top to a  $W$  boson and a  $b$ -quark. If one extends the MSM



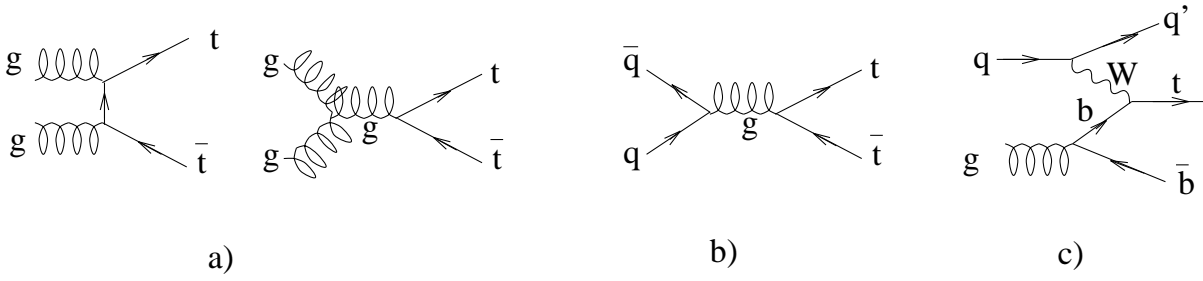


**Figure 1.11:** Top-quark production diagrams (see text).

to include a charged Higgs,  $H^\pm$ , there is a possibility for a competitive  $t$ -decay mechanism of  $t \rightarrow H^\pm (m_{H^\pm} < m_t - m_b)$ . I will only consider the MSM with  $\text{BR}(t \rightarrow W b) = 1$ .

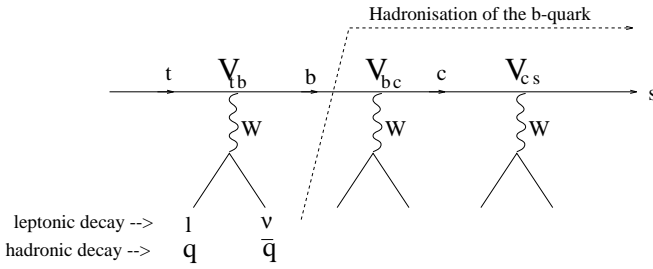


**Figure 1.12:** Cascade decay of the top-quark.

Decay mode	Branching ratio
$t\bar{t} \rightarrow (q\bar{q}'b)(q\bar{q}'\bar{b})$	36/81
$t\bar{t} \rightarrow (q\bar{q}'b)(e\nu\bar{b})$	12/81
$t\bar{t} \rightarrow (q\bar{q}'b)(\mu\nu\bar{b})$	12/81
$t\bar{t} \rightarrow (q\bar{q}'b)(\tau\nu\bar{b})$	12/81
$t\bar{t} \rightarrow (e\nu b)(\mu\nu\bar{b})$	2/81
$t\bar{t} \rightarrow (e\nu b)(\tau\nu\bar{b})$	2/81
$t\bar{t} \rightarrow (\mu\nu b)(\tau\nu\bar{b})$	2/81
$t\bar{t} \rightarrow (e\nu b)(e\nu\bar{b})$	1/81
$t\bar{t} \rightarrow (\mu\nu b)(\mu\nu\bar{b})$	1/81
$t\bar{t} \rightarrow (\tau\nu b)(\tau\nu\bar{b})$	1/81

**Table 1.3:**  $t\bar{t}$  branching ratio in the approximation that  $\text{Br}(t \rightarrow Wb) = 1$ .

As shown in figure 1.12 the two  $W$  bosons subsequently decay either to a lepton and a neutrino, or a quark and an antiquark, while the  $b$ -quarks hadronise to jets.

The approximate branching fractions for the different decay modes are listed in table 1.3. The  $t\bar{t}$  decays can be categorised by the decay mode of the final state  $W^+W^-$  pair. Most often both  $W$  bosons will decay to a quark-antiquark pair, leading to a fully hadronic final state, but a huge background from all other QCD multi-jet production processes makes detection of the  $t\bar{t}$  signal extremely difficult [11].

If one requires that at least one of the  $W$  bosons decays leptonically to an electron or muon, the background is substantially reduced. Because of the difficulties associated with identifying the hadronic decays of  $\tau$  leptons, the background to these decays can not be substantially reduced. Thus, in practise, only muons and electrons will be used to tag the isolated lepton from  $t$  decay.

According to whether one or both  $W$ 's decay to a  $(l, \nu)$  pair we have 'single' or 'di'-lepton decay channels. For the hard and isolated leptons from  $W$  decays, both electrons and muons can be considered. The  $b$ -decay and  $c$ -decay leptons are usually softer and embedded in the  $b$ -jet; thus only muons will be used for  $b$ -tagging.

Multilepton ( $\geq 3$ ) final states will clearly have lower backgrounds at the expense of lower statistics. Therefore, it is important to consider the single-lepton signature. This channel can also be used to determine directly  $m_t$  in a  $t \rightarrow 3$  jets decay without missing energy.



### 1.3.2.2 $t\bar{t} \rightarrow WWb\bar{b} \rightarrow lvq\bar{q} b\bar{b} \rightarrow lv + \text{jets}$ single-isolated-lepton channel

This channel allows direct reconstruction of  $m_t$  through the invariant mass of the 3-jet system. The trigger is based on a high  $p_T$  lepton from the other top-quark decay. The main backgrounds for this channel are [24]:

a)  $b\bar{b} \rightarrow lv + \text{jets}$

This background can be reduced below the unavoidable  $W + \text{jets}$  background by a cut on the lepton  $p_T$  threshold, on lepton isolation, on the  $W$  mass ( $m_{\text{jet-jet}} = m_W \pm \delta m_W$ ), on the missing transverse energy, and with a lepton-jet non-back-to-back azimuthal correlation cut.

b)  $W + \text{jets} \rightarrow lv + \text{jets}$

This background source can be reduced through kinematic cuts on the transverse energy and on the rapidity of jets and leptons, since  $t\bar{t}$  production with two massive top-quarks is more central than the production of  $W + \text{jets}$ .

The signal-to-background ratio becomes larger than one by requiring that three jets with  $p_T > 40 \text{ GeV}/c$  and  $|\eta| < 2$  be reconstructed in the hemisphere opposite to the trigger lepton, that one of them be tagged as a b-jet and that the remaining pair has an invariant mass consistent with  $m_W$ . With this selection procedure one can achieve about 100 events of this type ( $t\bar{t} \rightarrow (lvb)(q\bar{q} b\bar{b})$ ) per day at a luminosity of  $10^{32} \text{ cm}^{-2}\text{s}^{-1}$ .

### 1.3.2.3 $t\bar{t} \rightarrow WWb\bar{b} \rightarrow l\nu l\nu b\bar{b}$ two-isolated-lepton channel

The experimental signature in this channel is the presence of two isolated high  $p_T$  leptons (electrons and muons) coming from the  $t\bar{t}$  decay:  $t\bar{t} \rightarrow W^+W^- b\bar{b} \rightarrow l\nu l'\nu + \geq 2 \text{ jets}$ . The dominant backgrounds are discussed with the remark that processes c) and d) below only have to be considered for the  $e^+e^-$  or  $\mu^+\mu^-$  final states, but can obviously be avoided just asking for a mixed  $e-\mu$  lepton pair.

a)  $b\bar{b} (c\bar{c}) \rightarrow l\nu l'\nu + \text{jets}$

In addition to the cuts suggested in the single-lepton channel, a cut can be applied on the angle between the two leptons ( $\Delta\Phi$ ) in the transverse plane. The  $\Delta\Phi$  distribution is peaked at  $\Delta\Phi = \pi$  while the  $b\bar{b}$  decay produces a  $\Delta\Phi$  distribution which is peaked in  $\Delta\Phi = 0$  and  $\Delta\Phi = \pi$  due to the  $b\bar{b}$  production mechanism. Lepton isolation is, however, the most powerful rejection criterion. Both leptons from  $t\bar{t}$  are isolated, while the leptons from the  $b\bar{b}$  background are not.

b)  $W^+W^- \rightarrow l\nu l'\nu$

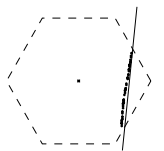
This background is much smaller than the above discussed process. Applying the same kinematical cuts as for the  $b\bar{b}$  reduction, i.e. a  $p_T^l \geq 50 \text{ GeV}/c$  on both leptons in the central rapidity region  $|\eta| \leq 1.5$ , the signal to background ratio becomes larger than 20.

c)  $Z + \text{jets} \rightarrow l\nu l'\nu + \text{jets}$

A cut on  $m_{l+l'}$  around the  $Z$  mass gives the most efficient reduction of this background. A good lepton momentum resolution will allow to reject a narrow band around the  $Z$  mass, resulting in minimal loss of the  $t\bar{t}$  signal, while  $Z$  reconstruction efficiency remains high.

d) **Drell-Yan + jets  $\rightarrow l\nu l'\nu + \text{jets}$**

The di-lepton Drell-Yan production [25] is concentrated at low invariant mass of the two



leptons. A signal to background ratio close to one can be obtained just by requiring a  $p_T^l \geq 30 \text{ GeV}/c$  cut on both leptons, and  $m_{l+l-} > 30 \text{ GeV}/c^2$ .

An efficient way to suppress both the Z+jets and Drell-Yan+jets background would be to apply a missing transverse energy cut, but a more practical way to reduce backgrounds in both the single and di-lepton channels, and in particular for  $e^+e^-$  and  $\mu^+\mu^-$  final states, is to use b-tagging with muons, which will be discussed in the next section. In the two-isolated-lepton channel one expects to reconstruct about 10 clean isolated  $e\mu$  events per day at a luminosity of  $10^{32} \text{ cm}^{-2}\text{s}^{-1}$  [4].

### 1.3.3 New heavy vector bosons

The existence of new neutral and charged vector bosons ( $Z', W^{\pm'}$ ) at the TeV energy scale is predicted by several theoretical models that can be divided in two groups [26, 27]:

- Minimal extensions of the standard model attempting to unify interactions, and are characterised by elementary Higgses: E6 models, left-right models, extended gauge models, etc.
- More drastic models involving a different mechanism for the electroweak symmetry breaking like Bess models, models with composite W and Z bosons and technicolour models.

Since it is not my intention to have an elaborate discussion about the various models to describe the characteristics of possible heavy bosons, I will limit myself to the Extended Gauge Model (EGM) where the coupling to fermions is as in the Standard Model (SM) and the  $Z'$  coupling to ordinary W and Z are suppressed by a factor  $\approx m_Z^2/m_{Z'}^2$  [28]. This leads to a linear increase of the total  $Z'$  width with mass. The total  $Z'$  width in the EGM is about 3 % of the  $Z'$  mass.

In the following I will concentrate on the production, decay and detection limits at LHC of the  $Z'$ . Comparable studies have been addressed to the  $W'$  and for further reading see e.g. [29, 30, 4].

#### 1.3.3.1 Production and decay of the $Z'$

If one considers the  $Z'$  to have the same branching ratios as the Z, the following decay modes can be considered:  $Z' \rightarrow e^+e^-$ ,  $Z' \rightarrow \mu^+\mu^-$  and  $Z' \rightarrow q\bar{q}$  ( $g \rightarrow \text{jet-jet}$ ), where the branching ratios are equal to the Z branching ratios. Most of the simulations studies of the  $Z'$  have concentrated on the leptonic decay modes, since these are the cleanest channels to detect the signal. As can be seen in figure 1.13 the background levels from Drell-Yan and  $t\bar{t}$  production are negligible. The figure shows the invariant  $e^+e^-$  mass production cross section and its backgrounds. All electron pairs in a range of  $\pm \Gamma_{\text{tot}(Z')}$  around the  $Z'$  mass peak have been included in the rapidity region  $|\eta| < 2.0$  and  $p_T > 15 \text{ GeV}/c$ . Those last two cuts are of minor importance since the  $\eta$  distribution of the produced leptons is centred around  $\eta = 0$ . The number of produced  $Z' \rightarrow e^+e^-$  and  $Z' \rightarrow \mu^+\mu^-$  in the acceptance of a typical detector with  $|\eta| < 2.0$  is only 20 for an integrated luminosity of  $10^5 \text{ pb}^{-1}$  and  $m_{Z'} = 4 \text{ TeV}/c^2$ . But the background for this type of signals is low both in the electron as well as in the muon channel, thus no problems are expected for this  $Z'$  mass.

Due to the small width of the  $Z'$  in the EGM ( $\Gamma_{Z'} = 0.03 m_{Z'}$ ), and the high lepton momenta (several  $\text{TeV}/c$ ), the high energy (momentum) response of the electro-magnetic calorimeter and muon system becomes dominant for the  $Z'$  discovery potential. Although a good resolution of the muon spectrometer helps to detect the  $Z'$  in the muon channel, the electro-magnetic calorimeter will show a better performance for this typical signal. This performance of the calorimeter and muon systems of ATLAS is demonstrated in figure 1.14.

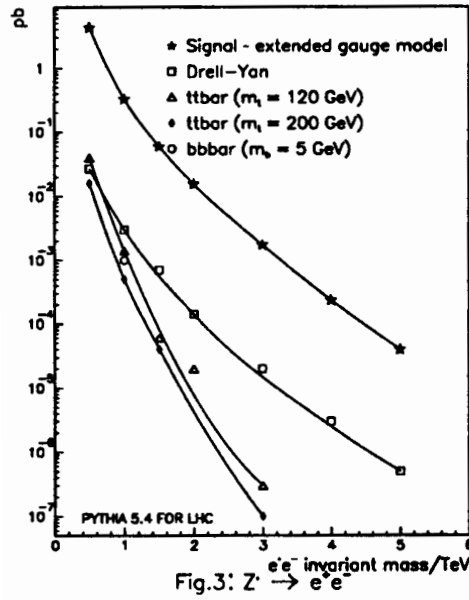


**Figure 1.13:** Production cross section of  $Z'$  as function of its mass [31].

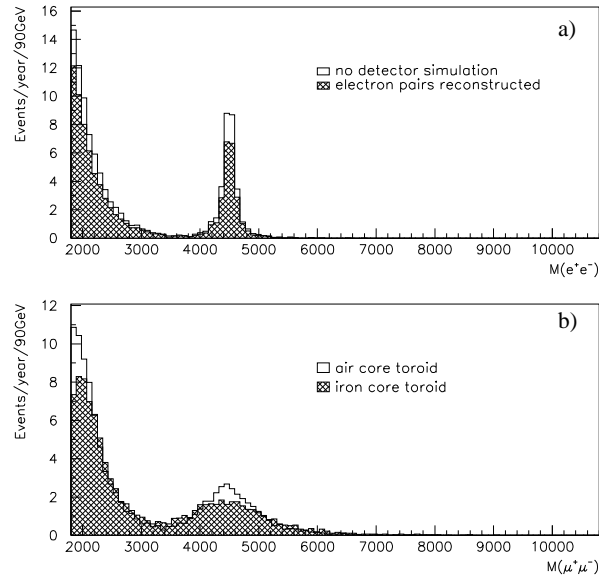
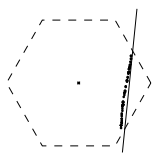


**Figure 1.14:** Reconstructed dilepton mass in ATLAS for  $Z' \rightarrow e^+e^-$  and  $\mu^+\mu^-$ , with  $m_{Z'} = 4.5 \text{ TeV}/c^2$ .  
a)  $e^+e^-$  measurement with the calorimeter. b)  $\mu^+\mu^-$  measurement with the muon spectrometer for an air core and an iron core toroid [22].

In order to distinguish between the different models, however, it is important to measure the forward-backward lepton asymmetries. For this purpose, a muon system with excellent muon momentum resolution for high momentum muons and a large  $\eta$  coverage performs better in the dimuon channel than the inner tracker plus calorimeter in the  $e^+e^-$  channel.



## References

- [1] Proceedings of the Large Hadron Collider Workshop, Aachen, 4–9 October 1990, Vol I,II,III, CERN 90-10.
- [2] G. Brianti, The Large Hadron Collider in the LEP tunnel, LHC Working group, published in [1].
- [3] J. Feltesse, Experimentation at LEP/LHC, published in [1].
- [4] The ATLAS collaboration, ATLAS Technical Proposal, CERN/LHCC/94-43, LHCC/P2, 15 December 1994.
- [5] The LHC study group, The Large Hadron Collider, Conceptual design, CERN/AC/95-05 (LHC), 20 October 1995.
- [6] D. Denegri, Standard Model physics at the LHC (pp collisions), 27 November 1990, published in [1].
- [7] A. Sopczak, Status of Higgs Hunting at the Z Resonance and its Prospects at LEP2, CERN-PPE/94-73, 9 May 1994.
- [8] I.I. Bigi, V.A. Khoze, N.G. Uraltsev, and A.I. Sanda, The question of CP noninvariance as seen through the eyes of neutral Beauty, published in “CP Violation, Advanced series on directions in High Energy Physics-Vol 3, ed. C. Jarlskog, World Scientific, 1989”.
- [9] The LHC-B collaboration, LHC-B, A dedicated LHC Collider Beauty Experiment, for Precision Measurements of CP-Violation, Letter of intent, CERN/LHCC 95-5, LHCC/I 8, 25 August, 1995.
- [10] L. Montanet *et al.*, Physical Review **D50**, 1173 (1994) and 1995 off-year partial update for the 1996 edition, available on the PDG WWW pages (URL: <http://www-pdg.lbl.gov/>).
- [11] The CDF collaboration, Evidence for Top Quark Production in  $\bar{p}p$  Collisions at  $\sqrt{s} = 1.8$  TeV, FERMILAB-PUB-94/097-E, CDF/PUB/TOP/PUBLIC/2561.
- [12] Z. Kunszt, The Standard Model Higgs at LHC: Branching Ratios and Cross-Sections, published in [1].
- [13] S. Spira, A. Djouadi, D. Graudenz and P.M. Zerwas, Higgs boson production at the LHC, DESY 94-123, GPP-UdeM-TH-95-16, CERN-TH/95-30, hep-ph/9504378, February 1995.
- [14] I. Hinchliffe, The Higgs Boson, LBNL publication, published in [10].
- [15] C. Seez and T. Virdee, L. DiLella, R. Kleis, Z. Kunszt and W.J. Stirling, Photon decay modes of the intermediate mass Higgs, published in [1].
- [16] The CMS collaboration, CMS Technical Proposal, CERN/LHCC/94-38, LHCC/P1, 15 December 1994.
- [17] D. Froidevaux, Experimental review of the search for the Higgs boson, published in [1].
- [18] R. Hawkings, Intermediate mass  $H \rightarrow 4l$ : A particle level and isolation study, ATLAS Internal note, PHYS-NO-062, 5 January 1995.
- [19] M. Della Negra, D. Froidevaux, K. Jakobs, R. Kinnunen, R. Kleiss, A. Nisati and T. Sjöstrand, Search for  $H \rightarrow Z^*H^*$  leptons at LHC, published in [1].
- [20] T. Sjöstrand (CERN), High-energy physics event generation with PYTHIA 5.7 and JETSET 7.4., CERN-TH-7111-93, December 1993. Published in Comput. Phys. Commun. **82** (1994), 74–90.
- [21] B. van Eijk and R. Kleiss, On the calculation of the exact  $gg \rightarrow Zb\bar{b}$  cross section including Z decay and b quark mass effects, published in [1].
- [22] The ATLAS collaboration, Letter of Intent for a General-Purpose p-p Experiment at the Large Hadron Collider at CERN, CERN/LHCC/92-4, LHCC/I 2, 1 October 1992.
- [23] A. Nisati, Search for  $p-p \rightarrow H \rightarrow ZZ \rightarrow \mu^+\mu^-\mu^+\mu^-$  at the LHC, published in [1].
- [24] F. Cavanna, D. Denegri and T. Rodrigo, Top search at the LHC: Signal versus Background, published in [1].
- [25] S. Drell and T.M. Yan, Phys. Rev. Lett. **25** (1970) 316. G. Moreno *et al.*, Phys. Rev. **D43** (1991) 2815. P.L. McGaughy *et al.*, Phys. Rev. **D50** (1994) 3038. <http://www.rarf.riken.go.jp/~rarf/rhic/phys/DY/DY.html>.
- [26] A. Henriques and L. Poggioli, Detection of the  $Z'$  vector boson in the jet decay mode ( $Z' \rightarrow q\bar{q}$ )( $g \rightarrow jj$ ): Resolution and pile-up studies, ATLAS Internal note, PHYS-NO-010, 1 October 1992.
- [27] F. Del Aguila *et al.*, New vector bosons at LHC, published in [1].
- [28] G. Altarelli, B. Mele and M. Ruiz-Altaba, Searching for new heavy vector bosons in  $p\bar{p}$  colliders, Z. Phys. C **45**, (1989), 109–121.
- [29] M.C. Cousinou and C.P.P.M. Marseille, Search for a  $W'$  in the  $lv$  channel, ATLAS Internal note, PHYS-NO-059, 19 December 1994.
- [30] F. Pauss, Beyond the Standard Model in pp collisions, published in [1].
- [31] P. Camarri, V. Cavasinni and C. Wulz,  $Z'$  into leptons, published in [1].

# Chapter 2

## Requirements on muon detectors at LHC

### Contents

---

<b>2.1</b>	<b>Introduction</b>	<b>17</b>
<b>2.2</b>	<b>The invariant mass in the <math>\mu^+\mu^-</math> system</b>	<b>17</b>
<b>2.3</b>	<b>The ATLAS muon spectrometer</b>	<b>18</b>
2.3.1	The air core toroids	21
2.3.2	Spectrometer performance	22
<b>2.4</b>	<b>The HSC as muon detector in the ATLAS barrel</b>	<b>22</b>
<b>2.5</b>	<b>Alignment</b>	<b>24</b>
<b>2.6</b>	<b>Muon backgrounds</b>	<b>26</b>
2.6.1	Decay muons and hadronic punchthrough	27
2.6.2	Neutrons and gammas	27

---

### 2.1 Introduction

**T**he physics goals as described in chapter 1 will be translated into requirements on muon detectors of LHC experiments. Good momentum (and angular) resolution is essential for the detection of decays such as  $H \rightarrow ZZ^* \rightarrow l^+l^-l^+l^-$  or  $Z' \rightarrow \mu^+\mu^-$ . We will see how the ATLAS experiment is optimised for the detection of this type of decays.

Furthermore, the problem of alignment will be introduced and the strategy of projective alignment will be discussed. This chapter will conclude with an overview of the expected background rates in the ATLAS muon spectrometer.

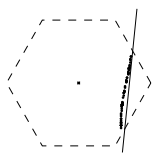
### 2.2 The invariant mass in the $\mu^+\mu^-$ system

For two particles with 3-momenta vectors  $\vec{p}_1$  and  $\vec{p}_2$  and energies  $E_1$  and  $E_2$  the invariant mass is (in units  $c = 1$ ):

$$m^2 = (E_1 + E_2)^2 - (\vec{p}_1 + \vec{p}_2)^2. \quad (2.1)$$

In case we compute the  $\mu^+\mu^-$  mass in the process  $Z' \rightarrow \mu^+\mu^-$  or  $H \rightarrow ZZ^* \rightarrow \mu^+\mu^- l^+l^-$  the invariant mass  $m$  will be much larger than the muon mass of  $0.1 \text{ GeV}/c^2$  and the muon mass can thus be ignored. The expression for the invariant mass of the two particle system becomes

$$m^2 = (p_1 + p_2)^2 - (\vec{p}_1 + \vec{p}_2)^2 = 2p_1p_2(1 - \cos \Psi_{12}), \quad (2.2)$$



where  $\Psi_{12}$  is the relative angle between the two muons and  $p_1$  and  $p_2$  are the measured momenta of the muons, all in the laboratory frame. The contributions from momenta errors and uncertainties in the relative angle  $\Psi_{12}$  in the relative precision of the reconstructed invariant mass  $\Delta m/m$  are obtained by differentiation of equation 2.2:

$$\frac{\Delta m}{m} = \frac{1}{2} \frac{\Delta p_{1,2}}{p_{1,2}} \quad (2.3)$$

$$\frac{\Delta m}{m} = \frac{1}{2} \frac{1}{\tan(\Psi_{12}/2)} \Delta \Psi_{12}, \quad (2.4)$$

For a precision measurement of the Higgs mass, it is desirable to have the error on the reconstructed invariant mass of the same order or less than the natural width of the Higgs. Figure 1.4 shows that the natural width of the Higgs is less than 1% for Higgs masses up to  $m_H = 200 \text{ GeV}/c^2$ . For non-resonant background rejection in the Higgs decay via two real Zs to four leptons, a cut can be applied on the invariant mass of each lepton pair around the Z mass. See section 1.3.1 for a more elaborate discussion. The error in the invariant mass of the di-muon pairs has to be small or comparable to the natural width of the Z ( $\Gamma_Z = 2.5 \text{ GeV}/c^2$ ) to make full profit of this background reduction method. The above arguments show that a mass resolution for di-muons in the order of 1% is desirable.

The contributions to the error in the mass due to the uncertainties in the determination of the momenta dominate over that in the angle for the largest part of phase space. For high momentum particles the main error in the angle  $\Psi_{12}$  is due to the precision of the position determination of the first muon chambers at 4.5 m from the interaction point yielding  $\Delta \Psi_{12}$  of the order of  $4 \times 10^{-5}$  rad. For the largest part of the phase space the factor  $1/[2 \tan(\Psi_{12}/2)]$  is of such order that the error on  $\Psi_{12}$  results in  $\Delta m/m < 10^{-3}$ . For low momenta the main contribution to  $\Delta \Psi_{12}$  comes from multiple scattering in the calorimeters (about  $130 X_0$  at  $\eta = 0$ ) and is of the order of  $5 \times 10^{-3}$  rad for a  $20 \text{ GeV}/c$  muon. Here, the inner detector provides optionally an improvement of the measurement. The error due to the vertex spread of 5.5 cm (rms) cancels in first approximation in  $\Psi_{12}$ .

From equation 2.3 one can see that the error on the invariant mass is proportional to the error on the muon momenta. A muon momentum resolution in the order of 1% is therefore desirable. The dominant contributions to the error in the momentum measurements are energy loss fluctuations in the calorimeter for low momenta muons, multiple scattering in the precision and trigger chambers for intermediate momenta muons and the intrinsic resolution of the muon detector and alignment errors for high momenta muons. Those contributions will be discussed in detail in section 2.3.2. The error on the momentum measurement in the range from  $p = 20 \text{ GeV}/c$  to  $200 \text{ GeV}/c$  is between 1.8 and 2.5 %. For muons with momenta below  $25 \text{ GeV}/c$  the inner detector can optionally provide measurements of the muon momenta and  $\Psi_{12}$  which are then only limited by multiple scattering in the inner tracker.

## 2.3 The ATLAS muon spectrometer

The ATLAS detector is shown in figure 2.1. The inner detector is located in a solenoid, providing a 2 T field parallel to the beam axis. The charged particles are bent in the magnetic field and the curved tracks are measured by silicon tracking detectors. The inner detector is surrounded by the calorimeter, absorbing all particles except neutrinos and muons.

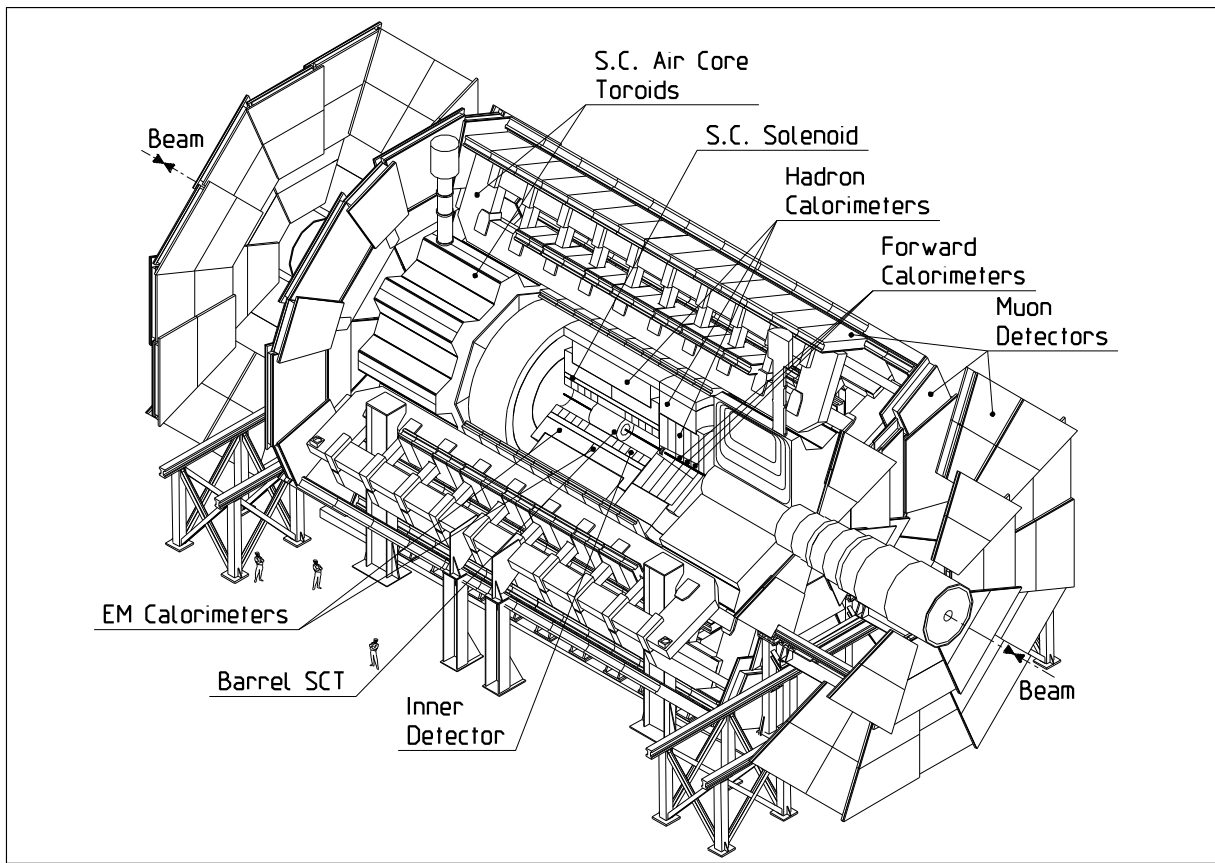


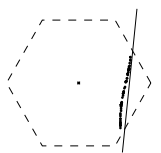
**Figure 2.1:** The ATLAS experiment.

The ATLAS muon spectrometer consists of three superconducting air core toroids, precision tracking detectors and dedicated trigger chambers. See section 2.3.1 for an elaborate description of the toroids. The choice of the (expensive) air core toroid for the barrel region as well as for the end caps reflects the ambitious approach of the ATLAS experiment with respect to the 'stand alone' performance of the muon spectrometer and muon trigger [1].

By having a toroidal field (instead of a solenoidal), the bending power of the field is conserved for muons produced at large rapidities. This allows to measure the momentum of muons with constant precision over the whole rapidity coverage of the detector ( $|\eta| < 2.8$ ).

By using superconducting coils and the magnetic field in air (instead of in iron), the amount of material in the spectrometer is minimised. Since multiple scattering is the dominant contribution to the error on the muon momentum measurement in the range from  $p=20$  GeV/ $c$  to 200 GeV/ $c$ , this magnet will improve the performance in this momentum interval.

During the design of the ATLAS muon spectrometer, large emphasis has been put on the so-called 'stand alone' performance of the spectrometer. This means that the spectrometer is optimised to trigger and reconstruct the interesting events which appear in the muon detectors without making use of the tracker in the inner detector. The layout of the chambers in the toroidal field is dominated by this requirement. The determination of the momenta of the muons is performed by a so-called 'sagitta measurement'. A muon track is bend in the magnetic field and the position of the track is measured at three positions. The sagitta  $s$  of a curved track segment between two points is defined as the maximum deviation of the curve from the straight line connecting these two points. This principle is shown in figure 2.2 where the layout of the barrel and forward muon stations is combined with an illustration of the definition of the sagitta  $s$ . The po-



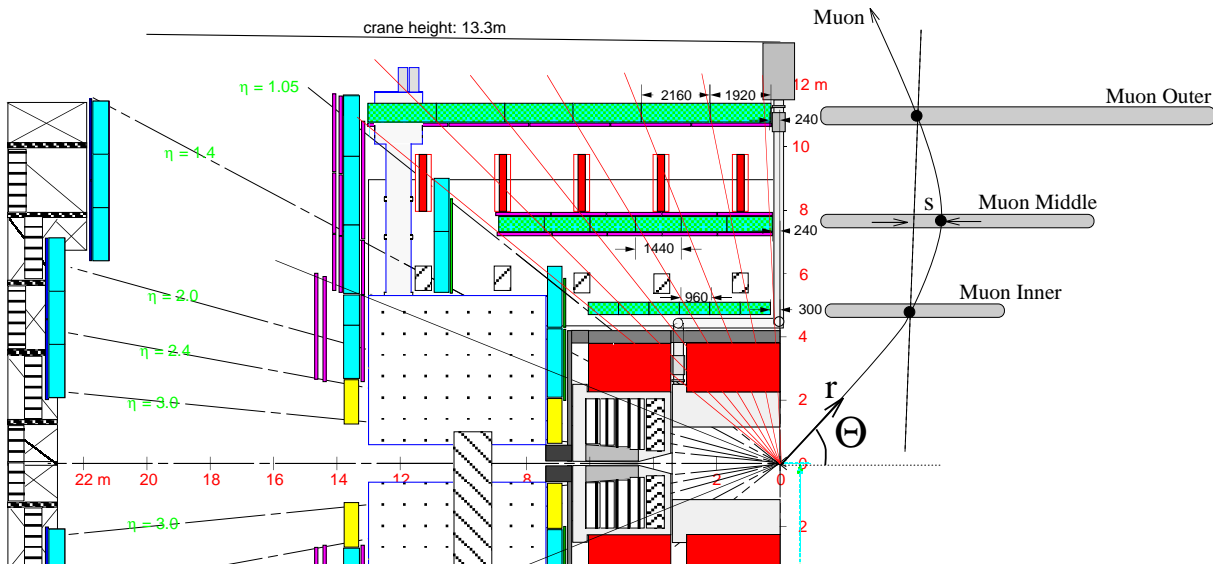


**Figure 2.2:** Side view of the ATLAS muon system showing the position of the muon chambers in a quarter of the experiment. In the right half of the figure the sagitta  $s$  is defined as measured in the inner, middle and outer muon stations.

lar coordinate system  $(r, \Theta, \Phi)$  to describe the experiment is also denoted, where  $\Phi$  (not shown) is the azimuthal angle defined with respect to the vertical.

If we assume that the strength of the magnetic field  $B$  is constant and perpendicular to the direction of the muon, we can express the momentum of the muon as function of the sagitta:

$$p = 0.3 \frac{BL^2}{8s}, \quad (2.5)$$

where  $L$  is the length of the track between the inner and outer muon stations. The track length  $L$  and sagitta  $s$  are expressed in metres, the magnetic field  $B$  in Tesla and  $p$  in GeV/c. In case of the ATLAS muon system, the average field strength is 0.6 T and the track length  $L$  is 5 m for  $\eta=0$ . This means that a muon with  $p=500$  GeV/c will have a sagitta of approximately 1 mm.

Two parameters have to be optimised for the muon momentum measurement. The most obvious one is the minimisation of the error on the momentum measurement. The second parameter is the geometrical coverage of the detector. The detector should cover the whole sphere inside  $|\eta| = 2.8$  without gaps.

The optimisation of the momentum resolution is done by measuring the two outer points of the muon as far separated as possible, while the middle measurement is done at the position where the deviation of the track from the straight lines connecting the measurements in the outer and inner stations is maximal. In a constant magnetic field this position is halfway the inner and outer muon station. In order to have equal contributions in the total uncertainty of the muon momentum for all three stations, the middle station should give the position of the muon twice as precise as the outer and inner station [2].

The hermetic coverage of the detector is obtained by having many partly overlapping chambers. The chamber layout of the precision chambers is shown in figure 2.3. The largest stations in the barrel have a length of 6 meter (in  $r\Phi$ ) and width of 2 meter (in  $z$ ). The spectrometer (barrel and end-cap and trigger chambers) will consist of approximately 700 chambers.



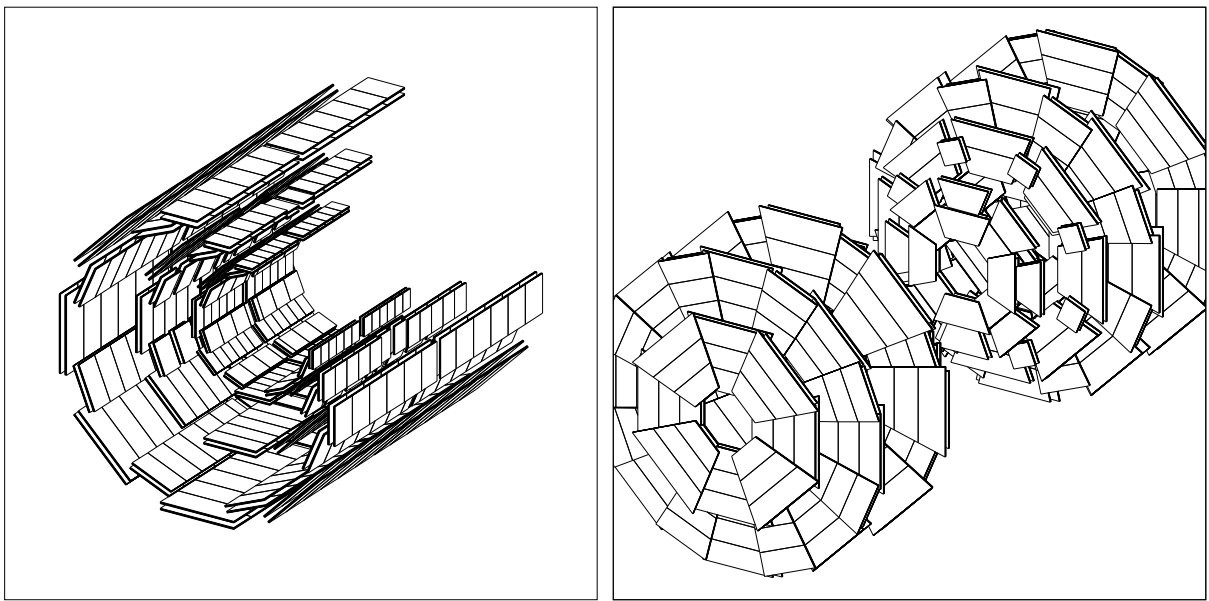


**Figure 2.3:** Layout of the muon stations in the barrel (left) and the end-caps (right). The configuration of stations is such that at least three point of the muon tracks are measured for  $|\eta| < 2.8$ .

### 2.3.1 The air core toroids

The total toroidal field will be produced by three toroids: one barrel (the largest) and two end cap toroids to produce bending power for large  $\eta$ .

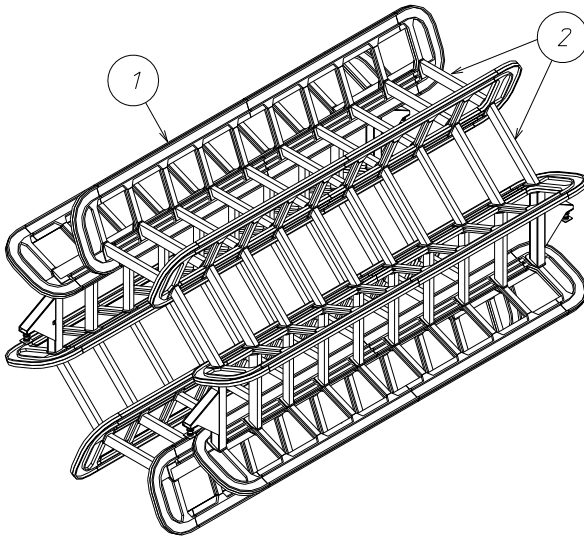


**Figure 2.4:** Cold mass of the barrel toroid. 1: coil; 2: voussoirs.

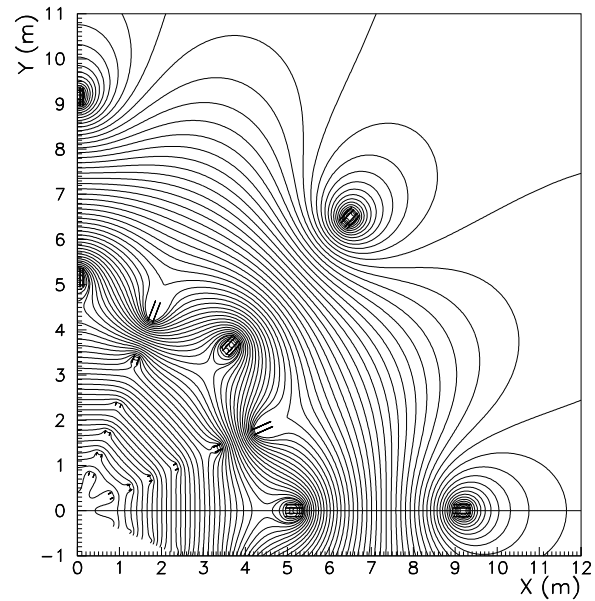
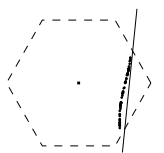


**Figure 2.5:** Magnetic field map in the barrel to end-cap transition region. The field lines are shown in a plane perpendicular to the beam axis in the middle of an end-cap toroid.

Figure 2.4 shows the cold structure of the barrel toroid. The length of the coils is 26 m, with an inner diameter of 9.4 m and outer diameter of 19.5 m. The two end-cap toroids have a length of 5.6 m and inner diameter of 1.3 m. The cold structure shown in figure 2.4 will be sufficiently



stiff to be supported separately from the warm vessel. Both the warm and cold mass will be supported by four legs. The total cold mass is 450 t and the total mass of the barrel toroid will be 1000 t. This structure has to support the additional 400 t of muon chambers.

The resulting field map of the combined end-cap and barrel toroid is shown in figure 2.5. It appears immediately that the field is quite inhomogeneous. This inhomogeneity has three severe consequences for the muon chambers. First, the relation between the measured sagitta and the muon momentum is far more complicated than suggested in equation 2.5. The field integral has to be calculated for each individual track. In order to suppress the error in the momentum resolution due to field uncertainties a precision of 2 cm is required on the position of the muon track in the non-bending plane ( $r - \Phi$ ). Secondly, the projective alignment scheme as described in section 2.5 is insensitive for correlated movement of a set of projective muon chambers. Therefore, some sort of absolute alignment system is needed in addition to the projective scheme. The third point is related to the technology of the precision chambers. For large scale detectors, drift chambers are the most preferable solution. The dependence of the drift of electrons on the magnetic field is characterised by the Lorentz angle (see section 3.4.2.3). This parameter will have impact on the performance of the detector. By placing drift chambers in strong inhomogeneous magnetic fields one has to verify that no loss in performance occurs due to the combination of the inhomogeneous field and the detection technology, e.g. by changes in the  $r(t)$  relation. In case of ATLAS the detection technology will be drift tubes with outer radius of 3 cm and operated at 3 bar gas pressure.

### 2.3.2 Spectrometer performance

The momentum resolution of the ATLAS spectrometer can be divided in three regions. Low momenta muons ( $p < 20$  GeV/ $c$ ) will be bent very strongly in the muon spectrometer and the error in the momentum measurement is dominated by fluctuations in the energy loss of the muon in the calorimeter. The bending of those muons in the solenoidal field in the inner tracker will provide a momentum measurement which is limited by multiple scattering. For 20 GeV/ $c$  muons the  $p_T$  resolution is 1.3 % averaged over the whole barrel.

The momentum resolution for very high momentum ( $p > 200$  GeV/ $c$ ) muons is dominated by the intrinsic precision of the muon chambers and alignment errors. This contribution can only be reduced by adding more precision chambers or by increasing the precision per measured hit. Both options have their consequences for the overall costs of the spectrometer. For the ATLAS spectrometer a total error on the sagitta measurement of 50  $\mu\text{m}$  (rms) is foreseen.

As mentioned before, in the intermediate momentum interval between 20 and 200 GeV/ $c$ , the momentum resolution is dominated by multiple scattering in support structures and the detectors themselves. In figure 2.6 the three contributions in the momentum resolution are shown together with the sum of all contributions as function of the muon momentum.

The momentum resolution will be a function of  $\eta$  due to the inhomogeneous distribution of material and variations in detector geometry. This dependence is shown in figure 2.7. Note the reasonable flat distribution up to  $\eta = 2.8$  due to the extended bending power in the toroids.

## 2.4 The HSC as muon detector in the ATLAS barrel

In this section some remarks will be made on the use of HSCs in the ATLAS barrel. The HSC is a two coordinate chamber with drift time measurement in one coordinate (anode wire readout) and

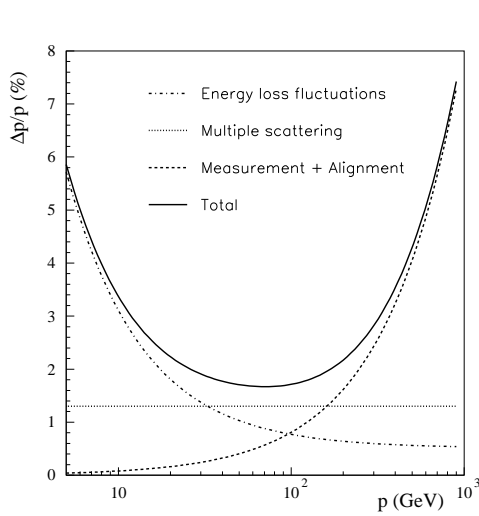


**Figure 2.6:** Atlas muon momentum resolution at zero rapidity. The figure shows the contributions as discussed in the text.

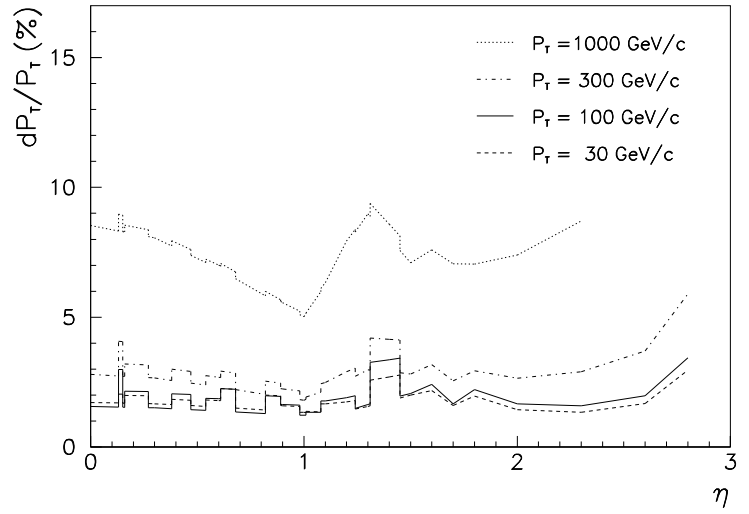


**Figure 2.7:** Transverse momentum resolution of the muon spectrometer as a function of  $\eta$ . The discontinuities are caused by the structural elements of the barrel toroid magnet.

charge distribution measurement (cathode strip readout) in the other (perpendicular coordinate).

Readout of the cathode strips with a pitch of 5 mm combined with the determination of a centre of gravity has shown to be a relatively simple method to obtain a resolution of 70  $\mu\text{m}$  per hit [3]. As will be shown, this is better than the best resolution (averaged over the cell) obtained with readout of the anode wire and 1 atmosphere gas pressure. Nevertheless, the HSC was optimised for ATLAS with the anode wire readout measuring the bending coordinate and the strips delivering an optional second coordinate.

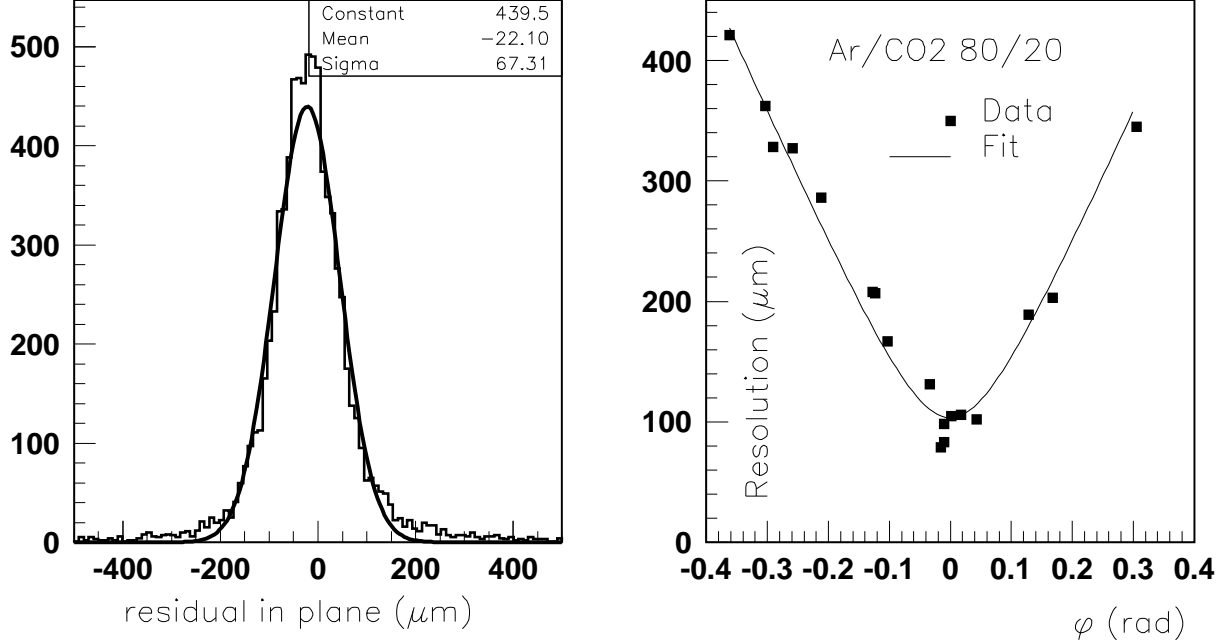
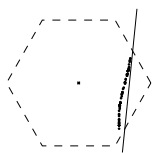


**Figure 2.8:** a) Measured residuals for the strip coordinate at  $\phi = 0^\circ$ ; b) Resolution of the strip coordinate versus the angle of incidence  $\phi$ .

In figure 2.8 the measured resolution of the strip readout is shown as function of the angle of



incidence  $\phi$ . The HSC coordinate system is shown in figure 3.1 The rapid increase in resolution is caused by the stochastic variation in the distance between, and size of the primary clusters in the gas.

In case the strips would measure the bending coordinate in ATLAS, this angle  $\phi$  is connected with the pseudo-rapidity  $\eta$ , increasing up to 800 mrad for  $\eta=1$ . The chambers can be tilted such that the angle of incidence for straight tracks from the vertex are perpendicular to the chamber. This tilt has to be adjusted to the local value of the Lorentz angle, which depends on the drift gas and the strength of the field. This makes a layout of tilted cathode chambers unlikely to be well adapted to the needs of ATLAS.

In addition, the time needed to get the hit information from the chamber is much shorter for the drift time readout than the cathode strip readout. In case of the wire readout, the current on the wire is measured, and the hit is detected within the maximum drift time. For a suitable signal to noise ratio on the charge measurement on the strips, a relatively long shaping time constant in the integrating circuit of the pre-amplifier is needed.

Measuring the bending of the muon with the anode wires offers the advantage of the (almost) constant resolution and  $r(t)$  of the detector for all angles of incidence. Since the largest chambers have wires of 6 m length, the angle of incidence in the  $\Phi$  direction will be limited to 300 mrad, which corresponds to a resolution of 400  $\mu\text{m}$ , more than sufficient for the second coordinate in ATLAS. Since the chamber is essentially made of plastic foils the multiple scattering contribution is very low, which matches the characteristics of the air core toroid well with the muon chambers. The slightly worse resolution of the drift time measurement ( $\sigma \approx 100 \mu\text{m}$ ) compared to the charge distribution measurement can well be compensated by adding more layers. In addition, this will improve the pattern recognition power.

## 2.5 Alignment

The measurement of the momenta of the muons in the muon spectrometer is performed by measuring its position in three muon stations at several metres distance. In order to benefit from the local precision in a station of approximately 30  $\mu\text{m}$  rms, the position of the stations with respect to each other has to be known with the same order of accuracy. The muon chambers in the ATLAS barrel will be supported by the toroid support structure. It has been calculated that this structure will show deformations in the order of 10 mm when the magnetic field is ramped up to full field. Therefore it is unavoidable that the muon chambers will show displacements of this magnitude. Furthermore, the thermal expansion of the chambers and their supports could also be in the millimetre range.

There are essentially two approaches to handle the alignment of large objects which move slowly in time. Both approaches need to monitor the amplitude and direction of the displacements of the objects. In the first approach one feeds the measured displacements back to actuators to stabilise the position of the chambers on-line. The ATLAS muon spectrometer will exploit the second approach where all displacements are measured and those measurements are used off-line to correct the data for systematic misalignments of the chambers. This method implies an important saving in the cost of the detector instrumentation.

Since the momentum measurement in the ATLAS muon spectrometer is a measurement of the sagitta of the bent muon track, it is sufficient to measure the relative position of the three muon stations which measure the muon. To first order, only the shift of the chambers perpendicular to the muon track and in the bending plane introduces a systematic error in the sagitta

measurement. Therefore the concept of projective alignment was developed [4].

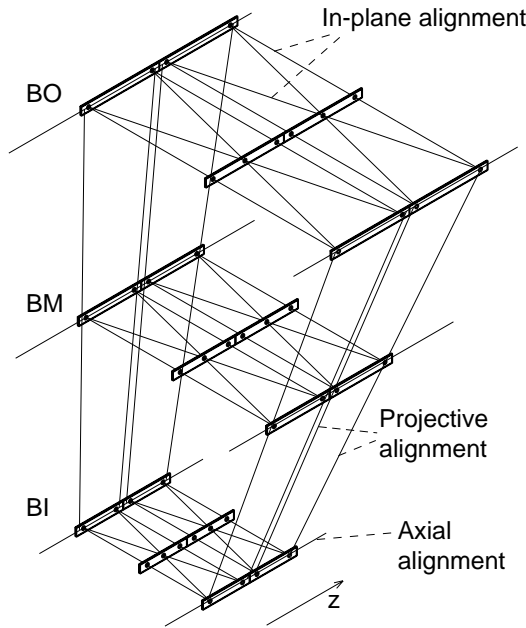


**Figure 2.9:** Arrangement of the alignment rays for two adjacent projective towers of the barrel spectrometer.

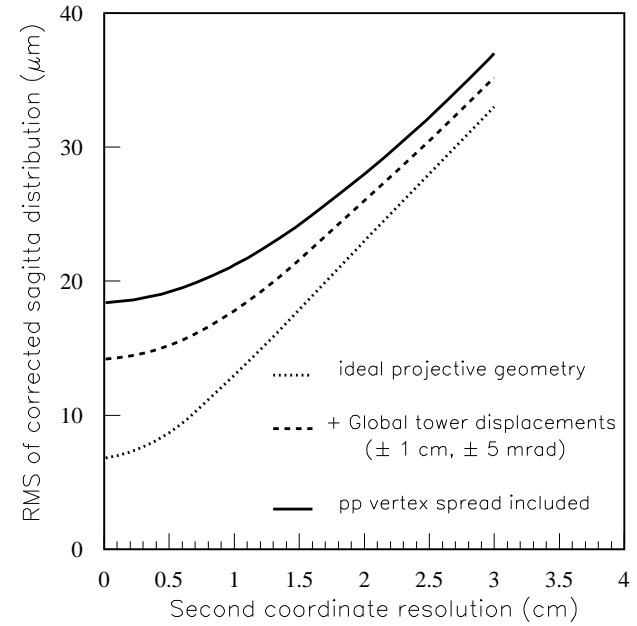


**Figure 2.10:** Width of the distribution of the corrected sagitta for infinite momentum tracks, averaged over the barrel region, as a function of the precision of the transverse track coordinate at the level of the middle layer for different assumptions on deviations from projective geometry.

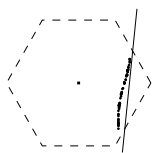
In figure 2.9 two adjacent projective tower are shown of the ATLAS muon barrel system. A projective tower consists of three muon detector stations which each measure the position of the muon in the bending plane with a local accuracy of  $30\ \mu\text{m}$ . The relative shifts of chambers is measured by four CCD/RASNIK systems mounted on the corners of the chambers and having their optical axis in the direction of the source of the muon: the interaction vertex (see appendix B).

Small deformations of individual chambers (curvature and torsion) are measured by a set of four, so-called, in-plane optical straightness monitors. Those systems will also consist of CCD/-RASNIK systems.

The position of the towers with respect to each other and to other sub-detectors is required to measure the production angle of the muons and thus to measure the invariant mass of a multi particle final state (e.g.  $H \rightarrow \mu^+ \mu^- \mu^+ \mu^-$  or  $H \rightarrow \mu^+ \mu^- e^+ e^-$ ). This position needs to be known in the centimetre range and is obtained by an external survey of the detector.

In figure 2.10 the resulting residual width of the error in the measured sagitta is shown for small deformations of the tower after correction. The error in the sagitta is shown as function of the precision of the second coordinate (in the non-bending plane). The error in the measured sagitta can not be reduced to zero with a projective alignment system because the system is insensitive for some deformations which affect the measured sagitta (e.g. a common rotation or translation of all three chambers). The error after alignment can be assigned to several sources:

- The precision of the optical sensors. In practise, the error in their relative position with respect to the anode wires of the chamber.



- The initial chamber positioning. For displacements of the order of several centimetres in translation, or milliradians in rotation, second-order effects dominate.
- Deviations from perfect projective geometry. This includes the spread of the interaction vertex in the bending plane ( $\approx 6$  cm).
- The precision of the coordinate of the muon in the direction along the wire. From figure 2.10 it can be seen that this precision has to be better than 10 mm in order to limit the total error to less than  $20 \mu\text{m}$ .

The dependence on the chamber positioning error will be reduced by an axial alignment system. Two axial light beams will connect all chambers of a layer within one octant. This additional alignment system will also add partial redundancy to the projective alignment systems.

## 2.6 Muon backgrounds

Background muons can be divided into two categories: real muons and other processes faking a muon track. Sources of real muons are K and  $\pi$  decay in front of the calorimeter and from hadronic punchthrough. A muon track can be faked by uncorrelated hits from neutron decays and hits from gammas. Furthermore, muon tracks can be obscured in the detector by electromagnetic secondaries induced by the high energetic muons themselves.

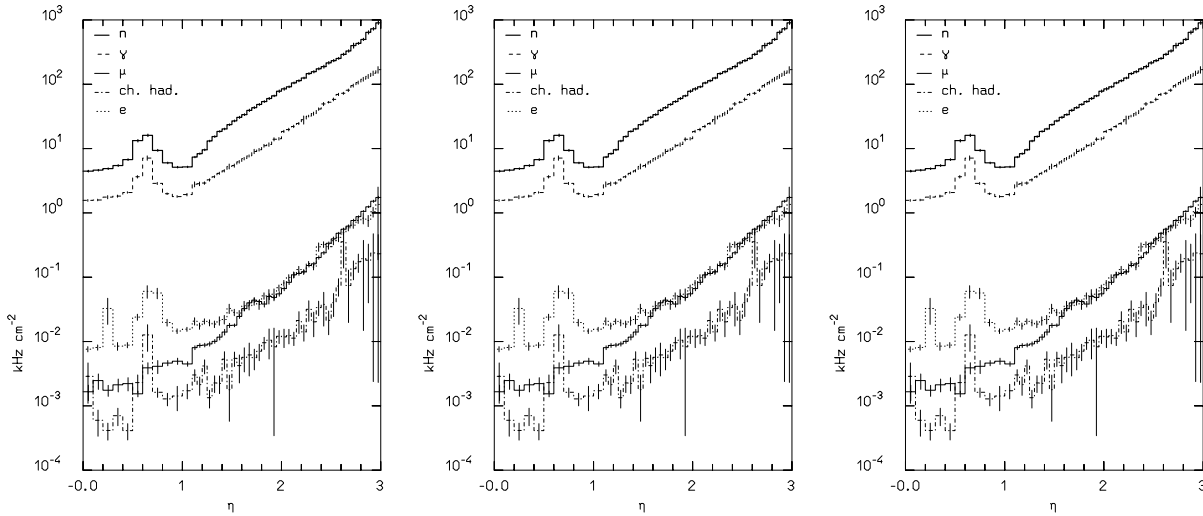


**Figure 2.11:** Total background in the inner (left) middle (middle) and outer (right) muon station as function of  $\eta$ . Fluence rates are shown for neutral particles, current rates for charged particles. The vertical lines in the middle and outer muon stations mark the end of the barrel and begin of the forward station.

In figure 2.11 the total background rates are shown in the three stations of the ATLAS muon system. The different background species have different detection probabilities in the muon chambers. While the response of the chambers to charged particles can be well approximated by one hit per particle, the effective sensitivity to neutral particles depends on both chamber composition and geometry and particle energy. For the ATLAS muon chambers the sensitivity to photons is larger than the one for neutrons. However, a significant component of the photon fluence is actually produced by inelastic neutron scattering and capture. Despite the low sensitivity, neutrons are the main source of uncorrelated background hits, where muon decay and punchthrough dominate the correlated muon background.

### 2.6.1 Decay muons and hadronic punchthrough

The source of decay muons is hadrons which emerge from the collision vertex and decay in flight before they reach the calorimeter. The majority of charged hadrons produced in p-p collisions are  $\pi$  and K mesons. The probability for a hadron to decay before reaching the calorimeter is proportional to the path length between the vertex and the calorimeter.

The majority of charged hadrons produced at the collision vertex will not decay in the central tracking volume, but will interact in the calorimeter. The interaction of hadrons with matter is characterised by the nuclear interaction length  $\lambda$ . This distance is the mean free path of the hadron before it initiates a hadronic cascade in a 'hard' interaction. The hadronic punchthrough consists of all hadronic shower debris which exit an absorber. This includes secondary muons which come from the decay of pions and kaons. For absorbers with thickness greater than  $10\lambda$  the muon constituent will dominate in the punchthrough particle types.

The total prompt muon rate for  $p_T > 20 \text{ GeV}/c$  and  $\eta < 2.2$  is a few kHz at nominal luminosity. This estimate has large uncertainties due to insufficient knowledge of the charm and beauty production cross-sections [1].

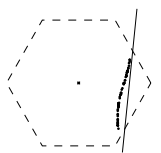
For  $\eta < 1.0$  the total flux of charged particles due to hadron decay in the inner detector and punchthrough is  $10 \text{ Hz}/\text{cm}^2$ , from which the muon contribution is 10%. In the region  $1.0 < |\eta| < 1.6$ , the total flux of charged particles due to those processes is  $11 \text{ Hz}/\text{cm}^2$ , where the muon contribution is 30 %. For  $|\eta| > 2$  the flux is dominated by muons and electrons and the rate of charged hadrons is a factor of three lower. The total particle flux increases rapidly as function of  $\eta$  for  $|\eta| > 1.2$  and the total rate in the first muon station due to charged particles is about  $1 \text{ kHz}/\text{cm}^2$  for  $\eta = 3$  [1].

### 2.6.2 Neutrons and gammas

The dominant source of backgrounds is induced by the hadrons produced in p-p collisions at the interaction vertex which interact in the calorimeter, the beam pipe and in a collimator which will shield the first quadrupole upstream of the experiments. The neutrons are a component of the hadronic shower. They can travel a long distance and lose their energy through numerous elastic collisions.

Neutrons can produce hits in gaseous detectors by scattering off light nuclei and by neutron capture, followed by gamma de-excitation. The gammas interact in the sensitive volume of the detector through photo-electron production, Compton scattering and  $e^+e^-$  pair production.

While the count rate in the barrel muon system and outer end cap station of ATLAS due to gammas and neutrons is reasonably low ( $< 10 \text{ Hz}/\text{cm}^2$ ), the count rate due to this source of background is much larger in the inner and middle end cap stations. In the inner endcap station the background count rate due to gammas and neutrons is the largest, depending on the rapidity up to  $900 \text{ Hz}/\text{cm}^2$  for  $\eta = 3.0$ .



## References

- [1] The ATLAS collaboration, ATLAS Technical Proposal, CERN/LHCC/94-43, LHCC/P2, 15 December 1994.
- [2] R.L. Gluckstern, Uncertainties in track momentum and direction, due to multiple scattering and measurement errors, Nucl. Instr. & Methods **24** (1963) 381–389.
- [3] H. van der Graaf *et al.*, The honeycomb strip chamber: the application in LHC/SSC experiments and the test results of a prototype, Nucl. Instr. & Methods **A307** (1991) 220.
- [4] C. Guyot and H. van der Graaf, ATLAS MUON NOTE, Alignment of the muon system. .



# Chapter 3

## The Honeycomb Strip Chamber

### Contents

---

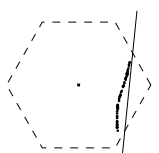
<b>3.1</b>	<b>Introduction</b>	<b>29</b>
3.1.1	The Proportional Counter	30
3.1.2	The Multi Wire Proportional Chamber and the Drift Chamber	30
3.1.3	The Honeycomb Strip Chamber	30
<b>3.2</b>	<b>The chamber principle</b>	<b>30</b>
<b>3.3</b>	<b>Constructed prototypes</b>	<b>32</b>
3.3.1	The 'Prototype 1' (P1) chamber	33
3.3.2	The TRACAL chambers	35
3.3.3	The 'Prototype 2' (P2) chambers	35
3.3.4	The 'Prototype 3' (P3) chamber	38
3.3.5	The 'Prototype 3 Aluminium' (P3A) chamber	39
<b>3.4</b>	<b>Charged particle detection with the HSC</b>	<b>40</b>
3.4.1	Energy loss of relativistic particles in matter	40
3.4.2	The drift of electrons in gases	46
3.4.3	The gas amplification process	51
3.4.4	The signal development: Drift of ions	54
3.4.5	Space charge effects	55
3.4.6	Electrostatic force on the wire	58

---

### 3.1 Introduction

**T**he Honeycomb Strip Chamber (HSC) combines the characteristics of the Proportional Drift Tube (PDT) and the Cathode Strip Chamber (CSC). The PDT is derived from the Proportional Counter, where the amount of collected charge on the wire is proportional to the amount of produced primary charge by the penetrating charged particle in the counter. The same process that creates the negative signal on the anode wire, induces a positive signal on the cathode planes. In a CSC the cathode plane of a PDT or Multi Wire Proportional Chamber (see section 3.1.2) is segmented into strips. By measuring the charge distribution over several adjacent strips, the position of the avalanche along the wire can be determined.

This chapter will describe briefly the history of drift tubes and their characteristics. The concept of the HSC will be introduced and an overview of the constructed prototypes will be given. Since the signal creation on the strips of the HSC is well understood (see e.g. [1]) a detailed description of the physics processes involved in the signal creation on the anode wires will be discussed.



### 3.1.1 The Proportional Counter

The Proportional Counter is a gas filled cylindrical metal tube at ground potential with a thin central anode wire at a positive potential  $V$ . The high voltage is applied via a high impedance resistor (typically 1 M $\Omega$ ). The signal on the wire is fed into a pre-amplifier via a decoupling capacitor of typical 1 nF. Energetic charged particles and photons traversing the tube may ionise the gas. The liberated primary and secondary electrons will drift towards the anode wire. Due to the high local electric field close to the wire ( $R < 30 \mu\text{m}$ ) a controlled amplification of charge of the order of  $10^5$  will occur. The gas amplification leads to a detectable signal.

### 3.1.2 The Multi Wire Proportional Chamber and the Drift Chamber

In a Multi Wire Proportional Chamber (MWPC), the single tube is replaced by a gas-filled box, with a grid of anode and field wires inside. The MWPC was introduced by Charpak in 1968 [2]. It had a typical spatial resolution for the position of the passage of the particle of 600 - 900  $\mu\text{m}$ , which was dominated by the digital readout and therefore by the wire pitch of the detector. Charpak introduced a new method by noticing that an increase in precision can be obtained by measuring the drift time of the electrons to the anode. This time can be converted into a distance perpendicular to the anode wire, if the drift velocity of the electrons is known.

First studies of a drift chamber were made by Bressani, Charpak, Rahm and Zupančič in 1969 [3]. Most of the effort went into the development of the front-end pre-amplifier and shaper to obtain the diffusion limited spatial accuracy.

Since 1969, drift chambers have been used in many experiments. A recent overview of design criteria of various types of drift chambers has been made by Blum and Rolandi [4].

### 3.1.3 The Honeycomb Strip Chamber

Experiments at the Large Hadron Collider (LHC) at CERN impose extreme conditions on track detectors compared to previous experiments (see chapter 1 and 2). Signal rates are very high and also the neutron and gamma background in the experimental hall is severe. Those neutrons are produced at the position of the beam pipe, but due to the long life time, the neutrons will decay throughout the whole experiment. The signals from those decaying neutrons will produce a random background of hits. This background leads to a high occupancy per unit length of the anode wire. This is the percentage of time that a signal is present on the anode wire.

NIKHEF is concerned with the development of muon detection systems for future LHC experiments. Prototypes have been designed and constructed according to the requirements of the ATLAS [5] muon detector. This means a minimisation of the number of readout channels, while the life-time, occupancy and pattern recognition efficiency remain within specifications. We think that HSCs with a maximum wire length of 6 metre and inner cell diameter of 20.0 mm are a suitable solution. In chapter 2 a more elaborate description is given of the optimisation of the chamber layout in ATLAS.

## 3.2 The chamber principle

In figure 3.1 the basic elements of the chamber are shown: each wire is surrounded coaxially by conducting hexagonal rings. Since the gap between the rings is small, the cell is essentially a drift tube. A muon passing through the volume produces ionisation clusters. The electrons

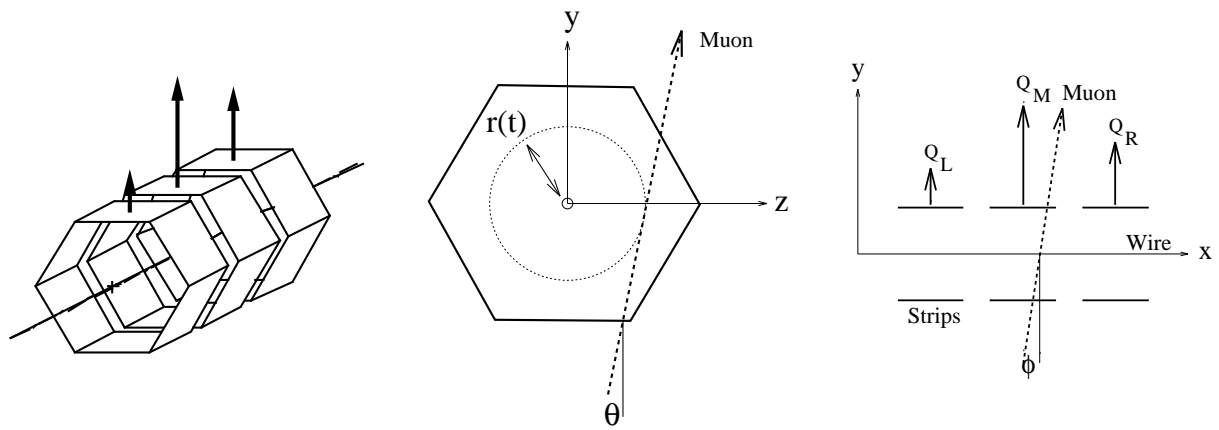


**Figure 3.1:** Principle of the Honeycomb Strip Chamber. The basic elements are shown in 3D and the projections perpendicular to the wire and perpendicular to the strips are shown. The coordinates  $(z, \theta)$  of the track as measured with the anode wires and  $(x, \phi)$  as measured with the cathode strips are indicated.

drift to the anode and cause an avalanche near the anode in the high electric field between anode and cathode. The separation of electrons and positive ions drifting in opposite direction in the electric field cause induced charges on the anode and cathode.

The negative charge signal from the wire equals the total positive charge signal from the rings at any time. The charge distribution over the rings is a function of the position of the drifting ion cloud and the geometry of the wires and rings. This is the well known principle used in 'segmented cathode strip readout' of MWPCs. By measuring the deposited charge on e.g. three adjacent strips (rings) it is possible to derive the position of the passing muon along the wire with high accuracy. The measurement of the drift time to the anode provides the position of the passage of the particle in a plane perpendicular to the anode wire.

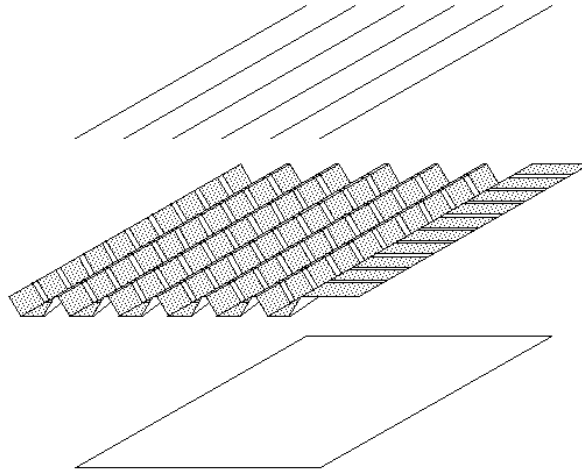
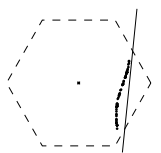


**Figure 3.2:** The construction elements. Two folded foils with conducting strips are interleaved with a wire plane, forming a monolayer (only the bottom foil is shown). A flat foil provides additional stiffness and supports the adjacent monolayer.

Figure 3.2 shows the construction elements of the chamber: anode wires, folded foils with a metallisation forming a strip pattern and a flat insulating foil. Two folded foils, interleaved with a wire plane, are glued or welded together to form a monolayer. An additional flat foil is glued on top of the hexagonal monolayer for more stiffness and it supports the adjacent monolayer. A



stack of these monolayers form a rigid and self-supporting multilayer. The wire tension is held by the cell walls.

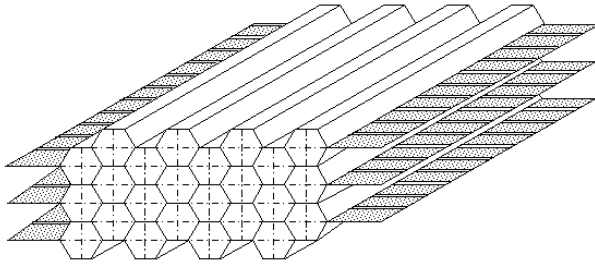


**Figure 3.3:** Genuine honeycomb structure. Strip readout for each cell is not possible because of too large capacitance between the strips of adjacent layers.

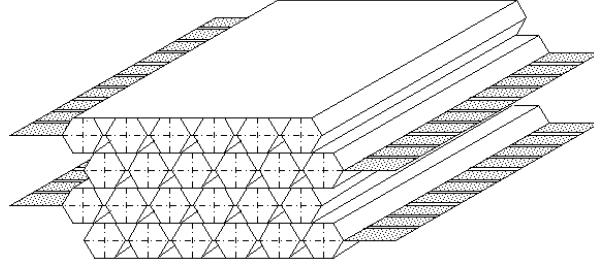


**Figure 3.4:** Honeycomb structure with insulating foils between the cell layers.

The geometry of figure 3.3 requires conducting strips at both sides of each foil. As a consequence, the mutual capacitance between a strip and its upper and lower neighbour is very high. Since each strip is virtually grounded by its amplifier, the source capacitances are very high and the signal/noise ratio poor. This problem is solved in the geometry of figure 3.4. Each layer of cells is covered with an insulating flat foil which acts as a base for the next layer. Odd and even planes are shifted relatively by half a cell pitch. In this geometry the 'vertical' capacity is much smaller than the unavoidable capacitance between 'horizontally' neighbouring strips. The distance between two neighbouring cells is as small as mechanically possible, minimising the insensitive area of a monolayer.

### 3.3 Constructed prototypes

Three generations of prototypes have been built: P1, P2 and P3(A), and a set of monolayers used for TRACAL. Table 3.1 gives a summary of the chamber characteristics.

The P1 (Prototype 1) chamber is a  $30 \times 30 \text{ cm}^2$  8-layer prototype. The strip foils are Kapton/copper laminated foils. The strip pattern is etched using standard flexible printed circuit board technology. The folds in the foils are made by thermic treatment in an oven. The cell diameter is 11.54 mm. Two different wire diameters, 20  $\mu\text{m}$  and 30  $\mu\text{m}$ , are used for testing purposes. This chamber is still in use anno 1995.

The TRACAL chambers are genuine monolayers. They have been built for the RD5 TRAcking CALorimeter. The folded foil is now made of a copper sputtered melinex sandwich. Because the copper was sputtered on the insulating foil (instead of laminated), less copper could be applied than for the P1 foils, resulting in a layer of 0.3  $\mu\text{m}$ . This reduction of applied copper reduced also the amount of etch-material used during etching of the strips. The foils are folded on a specially developed folding machine which is used for all subsequent chambers. TRACAL consists of 25 monolayers interleaved with 4 or 8 cm stainless steel plates, forming a calorimeter of 9.6 interaction lengths. Each monolayer is surrounded by a  $70 \times 100 \text{ cm}^2$  brass frame providing stiffness. Wire and strip signals are read out. The calorimeter was positioned in a 3 T superconducting magnet.

The P2 chambers are enlarged P1 chambers. The wires (strips) are 3 (10) times longer than for P1. The folded foil was made of copper sputtered Mylar. Three chambers have been con-

Characteristics	P1	TRACAL	P2	P3	P3A
year	1990	1991	1992/93	1993	1994
# constructed	1	25	3	1	1
# wires/layer	24	48	255	8	8
# strips/layer	54	192	192	–	–
# layers/chamber	8	1	8	8	8
outer cell radius (mm)	5.77	5.77	5.77	11.54	11.54
wire length (m)	0.3	0.8	1.0	5.7	5.7
wire diameter ( $\mu\text{m}$ )	20/30	30	30	50	50
wire pitch (mm)	12.7	12.7	12.7	25.4	25.4
strip length (m)	0.3	0.6	3.2	–	–
strip pitch (mm)	5.08	5.08	5.08	–	–
plane pitch (mm)	10.7	–	10.64	20.0	20.0
folded insulating foil thickness ( $\mu\text{m}$ )	Kapton 100	melinex 75	Mylar 75	Mylar 75	– –
flat insulating foil thickness ( $\mu\text{m}$ )	Kapton 100	Mylar 75	Mylar 75	Kapton 100	– –
folded conductor thickness ( $\mu\text{m}$ )	copper 17	copper 0.3	copper 0.8	copper 0.8	aluminium 50
flat conductor thickness ( $\mu\text{m}$ )	– –	– –	– –	copper 17	aluminium 50

**Table 3.1:** Characteristics of the HSC prototypes.

structed and tested in the RD5 muon beam.

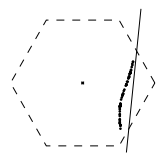
The P3 and P3A chambers are prototype modules of the large ATLAS muon chambers with HSC technology. In ATLAS, the 2<sup>nd</sup> coordinate will be delivered by the strip readout of trigger chambers (RPC or TGC) [5]. All strips (foils) were grounded in P3 (P3A). The cathode foils are now made from copper sputtered Mylar (P3) or plain aluminium (P3A) foil. In order to minimise the required number of readout channels, the cell size was doubled to 23.08 mm outer-diameter. The 64 anode wires are 6 m long and are additionally supported by a middle comb. The flat supporting foil between the monolayers is made of Mylar/copper (P3) or aluminium (P3A) and put on ground potential to prevent cross-talk between the layers

In the following section, the production procedure of each prototype will be described individually.

### 3.3.1 The 'Prototype 1' (P1) chamber

This chamber is made from Kapton/copper laminated foil. The strip pattern is etched using standard flexible printed circuit board technology [1]. A precision of 0.1 mm on the position of the strip edges was obtained. The foils (flat dimensions  $400 \times 600 \text{ mm}^2$ ) were folded by means of a template. The foil was fixed in the template by bolting hexagonal bars onto each half cell of the template, starting from one side. The template was then put in an oven and heated at 305 °C for 30 minutes. The thermo-plastic properties of Kapton foil were such that the foil kept its 'ribbon' shape.

In figure 3.6 the production of a monolayer is shown. Two templates were made to hold a



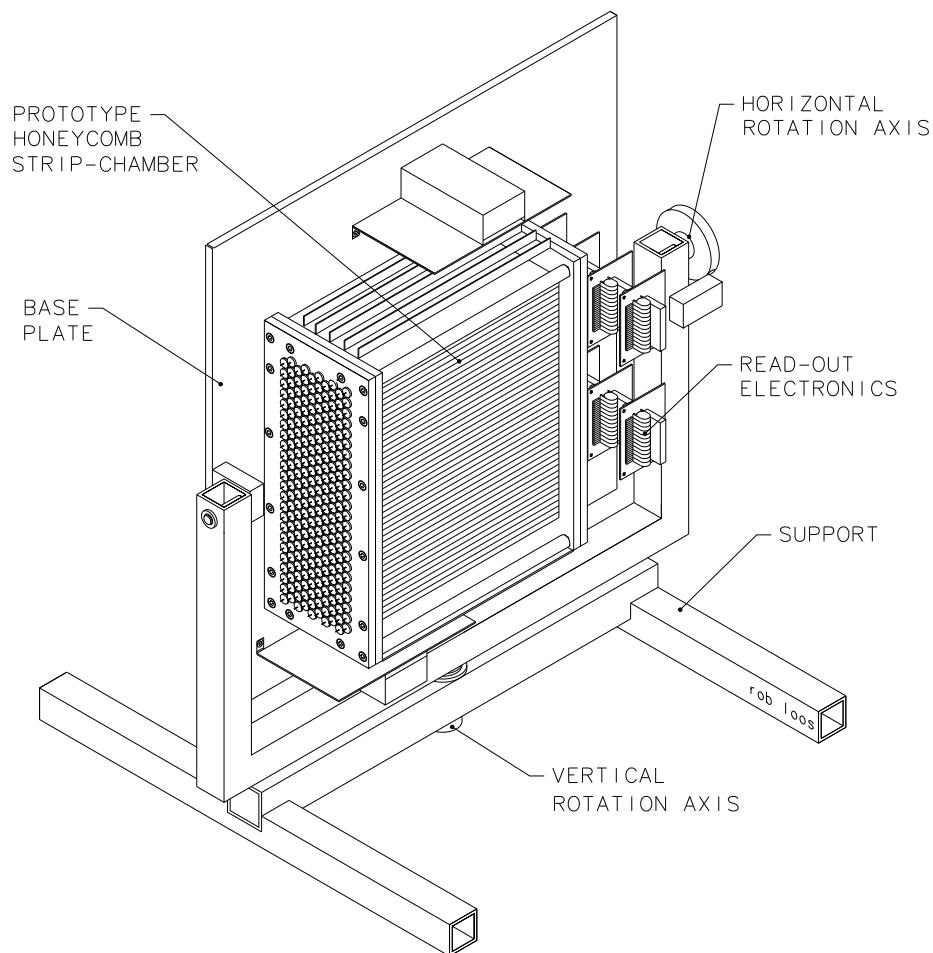


**Figure 3.5:** P1 prototype and its support. The wires are strung horizontally. The signals on the strips are read out on top (bottom) for the even (odd) layers.

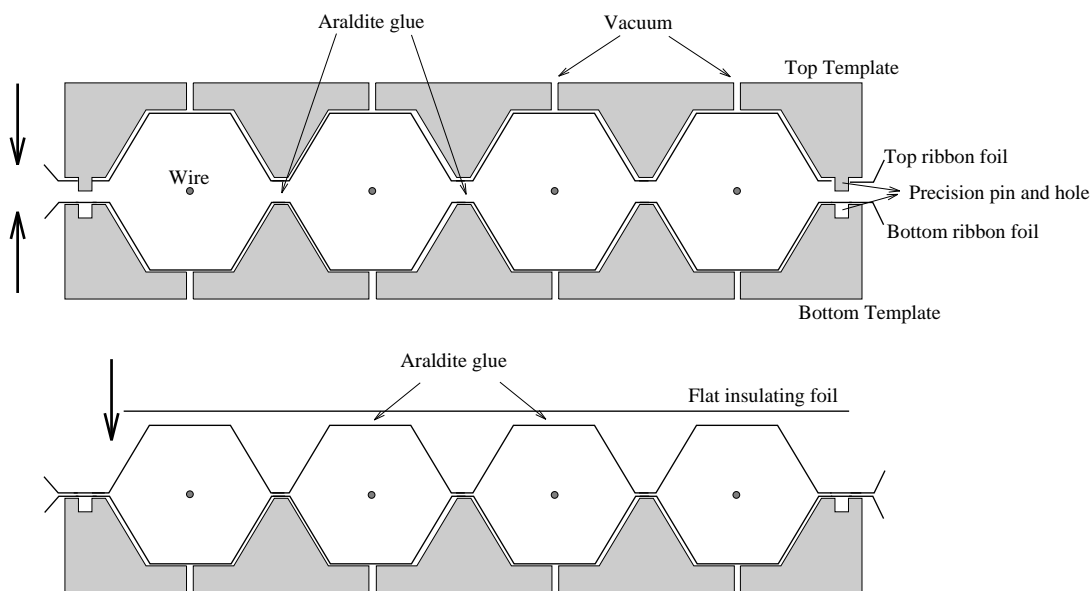


**Figure 3.6:** Production of a monolayer for the P1 chamber (see text).

ribbon foil in position by applying a vacuum. Araldite glue was applied on the narrow flat area between two cells. Then the templates with the foils were placed facing each other. The templates were aligned with precision pins and holes. After the glue had hardened, one template was removed. A flat Kapton foil (without copper) was then glued onto the cell layer, forming a monolayer stiff enough to be handled. At each cell-end a nylon plug was inserted. The nylon plugs fitted into an aluminium gas distribution box in which the wires were fixed. The completed chamber was fixed onto an aluminium base plate supported by a stand which allowed the chamber to be rotated over two angles (see figure 3.5).

### 3.3.2 The TRACAL chambers

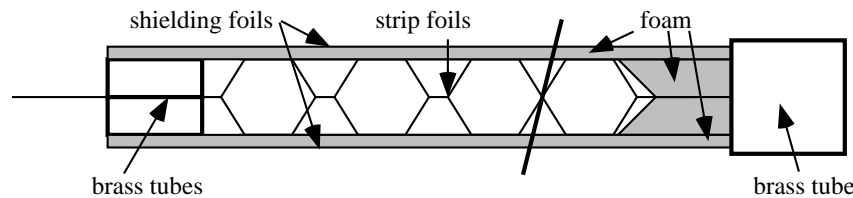


**Figure 3.7:** Cross section of a TRACAL monolayer.

The construction of these chambers is described in detail in [6] and [7](see figure 3.7). The copper sputtered melinex foil was folded on a folding machine developed and built at NIKHEF. This machine transported the foil with two pneumatically driven shuttles. After each transport of the foil, a fold was made by rolling a plastic cylinder along a 'fold-knife'. The folds were parallel to each other within  $10\ \mu\text{rad}$ .

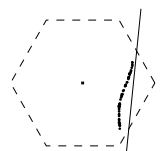
In total 25 TRACAL chambers are produced and were operational in the RD5 experiment at CERN from 1991 – 1993.

### 3.3.3 The 'Prototype 2' (P2) chambers

These chambers were constructed in order to study the strip readout in the case of long strips (3.25 m) and to gain experience with building large HSC units. Given the larger length of the foils (5 m), the perpendicularity between the folds and the strips had to be even better than for the TRACAL chambers. The total misalignment over the chamber length of 3 metre was less than 0.2 mm. This was achieved by active stabilisation of the foil position on the folding machine. The foil transport mechanism, previously made up of two pneumatically driven shuttles, was replaced by two high-precision linear motors with a step resolution better than  $1\ \mu\text{m}$ . The position of the foil was monitored by four optical systems, based on the RASNIK [8] which measured the angle between the folding edge and the strips, as well as the translation of the foil perpendicular to the strips (see figure 3.8).

The bottom and top templates were made on a precision milling-machine at NIKHEF. All tolerances on the reference holes for wire positioning were smaller than  $20\ \mu\text{m}$ . In the top template, 6000 additional holes (beside the vacuum holes) were drilled for the ultrasonic welding machine to weld the bottom foil to the top foil.

A folded foil was put on the bottom template and vacuum was applied (see figure 3.9). Then, at the cell edges, mold-injected precision plastic 'Lego' blocks were glued on the foil (see figure 3.10). The blocks were positioned by pins on the template and attached 8 adjacent wires. The blocks had an 8-fold hexagonal shape at one side to define the foil geometry at the chamber



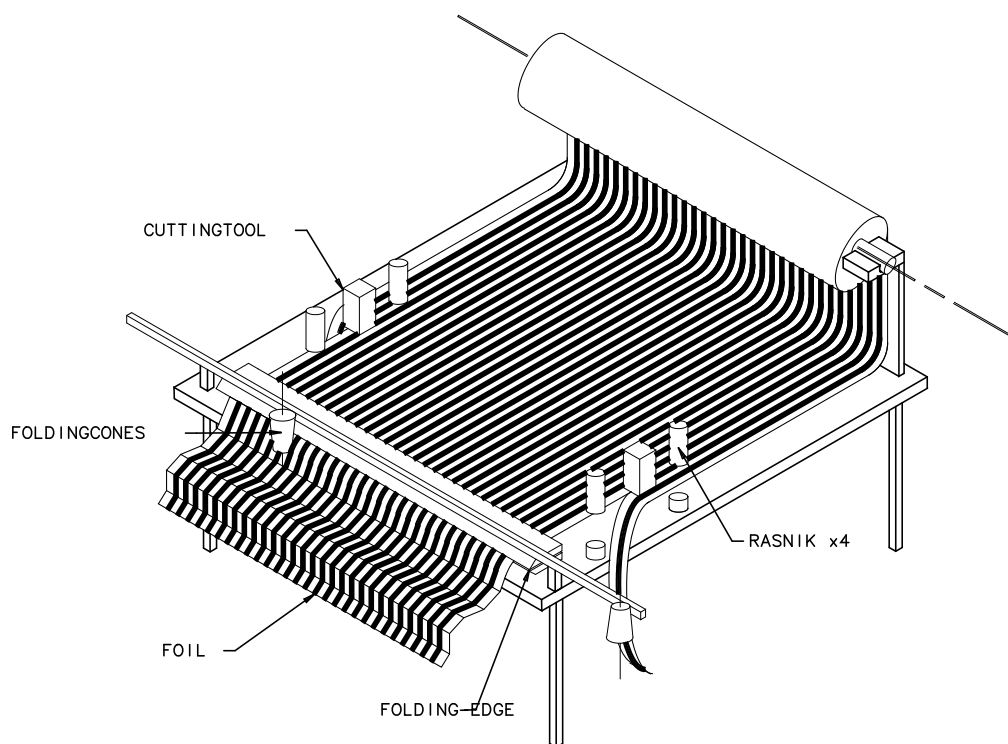


**Figure 3.8:** The folding machine. The foil is transported from right to left.

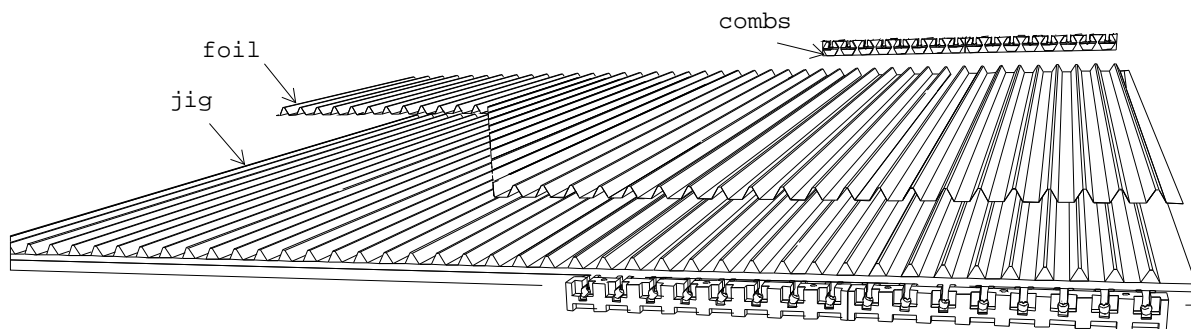


**Figure 3.9:** Schematic assembly of a monolayer. The foil-template and end-combs are shown.

edge. On the other side, Cu/Te blocks with a slit in which a wire could be fixed by crimping were glued [9]. The position of the wire in horizontal and vertical direction was defined by a precision V-formed slit in the Lego-block.

The Au/W wires with a diameter of  $30\text{ }\mu\text{m}$  were tensioned with 50 g in groups of 72 on a special wire frame. So in total 64 Lego blocks were positioned on the bottom template and 256 wires were crimped.

The top foil was positioned by the top-template which was lowered on the bottom template. The foils were fixed together by means of ultrasonic welding. This method of merging two foils (instead of gluing) allowed to automate this step in the production process. Over the course of one night, a pattern of 6000 spots of one monolayer was welded automatically. The top template was then lifted from the bottom template, and a flat foil was glued onto the cell layer. An auxiliary frame was mounted on the monolayer, which was then removed from the bottom template, while keeping its shape due to the stiffness of the frame.



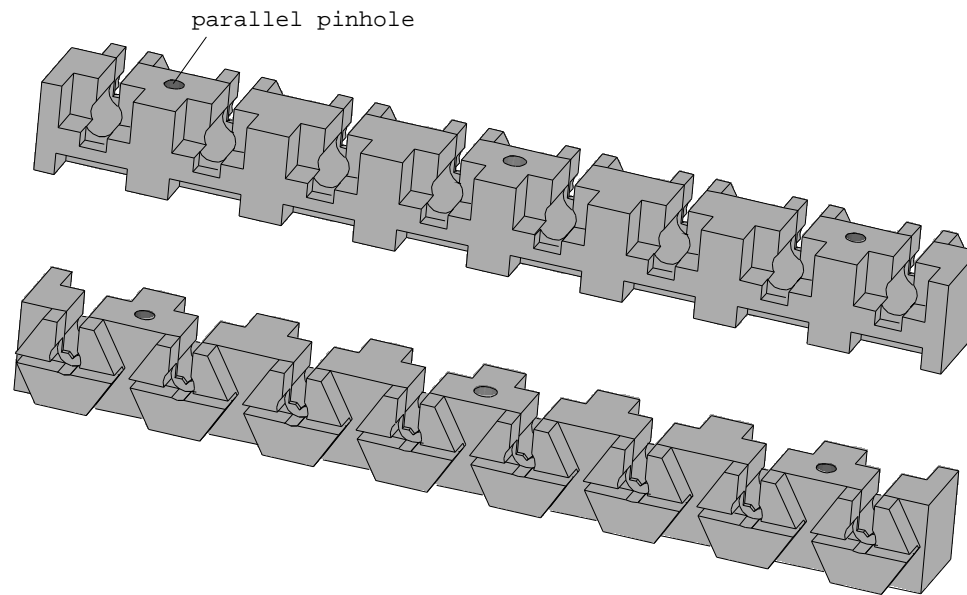


**Figure 3.10:** The plastic mould-injected edge blocks. Top: outer side (the Cu/Te blocks with the slits for wire fixation are not in place). Bottom: inner side; the hexagonal shape of the individual cell is clearly visible.

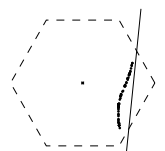
The chamber was assembled by fixing the first monolayer onto a flat aluminium table. Then the next monolayer (kept in shape by the auxiliary frame) was glued onto the previous one. The monolayers were aligned with respect to each other by precision holes in the top and bottom of the Lego-blocks (see figure 3.10). After the 10<sup>th</sup> monolayer, the chamber was covered on both sides with an aluminium sheet (0.5 mm) to provide stiffness and shielding. The 1<sup>st</sup> and 10<sup>th</sup> monolayer were assembled for shielding and stiffness purposes and produced without anode wires.

At the 'Lego' block sides of the chamber, printed circuit boards were mounted with pins sticking into the holes of the Cu/Te crimping blocks (see figure 3.11). These boards act as gas seal, HV distributors and signal feed-through. The space between the boards and the 'Lego' blocks serves as a gas distributor. By placing the gas input and output diagonally opposite on the chamber, a reasonable homogeneous flow through the cells was obtained.

After the production of the first monolayers of the P2 chamber, the wire positions of all 256 wires were measured with a microscope. This measurement was possible because the Mylar foil was transparent, so the wire could be seen in the gap between two adjacent strips. All wires were indeed positioned (horizontally) within 20  $\mu\text{m}$  (rms) with respect to each other.

The last P2 chamber (P2-3) was produced after P2-1 and P2-2 were tested in cosmic rays and testbeams. In testbeams it appeared that the strips of 5 metre length had many micro-breaks. Those breaks were caused by the folding machine where the folding mechanism was damaging the copper strips. This production problem caused that strips did not give a signal in case such a micro-break was present between the position where the signal was created and the pre-amplifier.

During production of the P2-3 chamber, the resistivity of the strips of all monolayers was measured. In case of a break in a strip, this was repaired by applying conductive glue on the strip. The break in a strip between the position of the signal origin and the electronics also has a negative influence on the wire readout. For optimal use of proportional counters it is required that the cathode is grounded or virtually on ground via a pre-amplifier. Since this is not the case for broken strips, this will give rise to an efficiency loss, noise and a deterioration of the resolu-



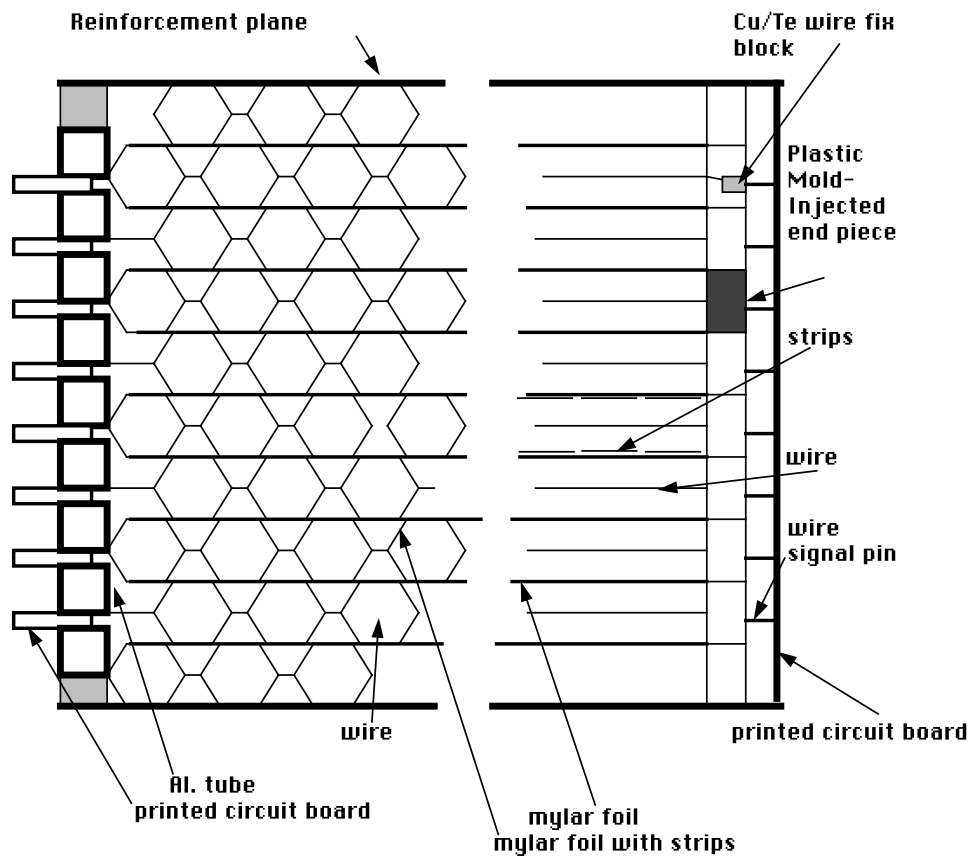


**Figure 3.11:** Cross section of P2: Left) perpendicular to the wires. Right) perpendicular to the strips.

tion.

### 3.3.4 The 'Prototype 3' (P3) chamber

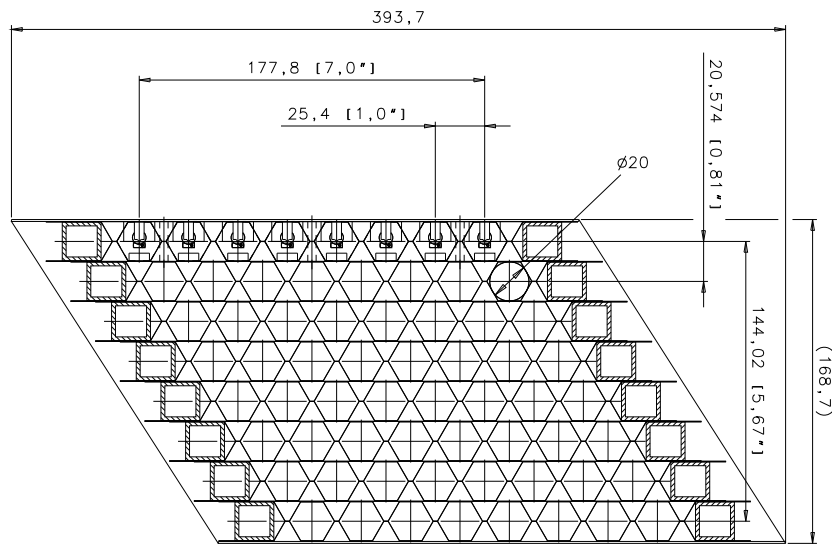


**Figure 3.12:** Cross section of P3 perpendicular to the wires.

The P3 chamber (see figure 3.12) has a wire length of 5.5 m, and a cell radius twice as large as the previous chambers. It has a middle wire support to maintain the distance between the wire position and the cell axis. The width of the chamber was limited to eight cells for economical reasons. Later, it appeared that a stack of  $8 \times 8$  tubes is about the optimum size of a module for the ATLAS muon spectrometer. So, this chamber could also be regarded as a prototype of a module for the outer muon chambers in the ATLAS barrel.

The foil was folded on the same machine as used for the P2 chambers: the linear motors were computer controlled so the geometry of the ribbon foil is programmable. The dead zone between two cells was minimised and held to 1 mm. The construction of the monolayers was similar to that of the P2 chambers. The top and bottom templates were made by an industrial firm. Two ribbon foils were glued together, instead of ultrasonically welded. As flat foil a Kapton-copper laminate was chosen in order to limit crosstalk between two monolayers. Since the second co-ordinate was not required, all strips were connected to ground at the chamber edge.

The wires were supported by machined Lego-blocks. Those Lego-blocks were equal in shape to the ones used for P2, but scaled up by a factor 2 to fit the doubled cell size. The Lego-blocks formed three combs, two at the ends and one in the middle of the wire. The signal, HV and gas feed through was done by double printed circuit boards at each side. The first printed circuit board was in the gas volume and distributed the high voltage.

The outer printed circuit board fed the signals through the gas seal. Leakage currents due to moisture at the outside of the inner printed circuit boards were thus prevented. This leakage of current through a moisture film on large area printed circuit boards (in open air) from high voltage spots to ground spots had been a serious problem for the P2 chambers.

### 3.3.5 The 'Prototype 3 Aluminium' (P3A) chamber

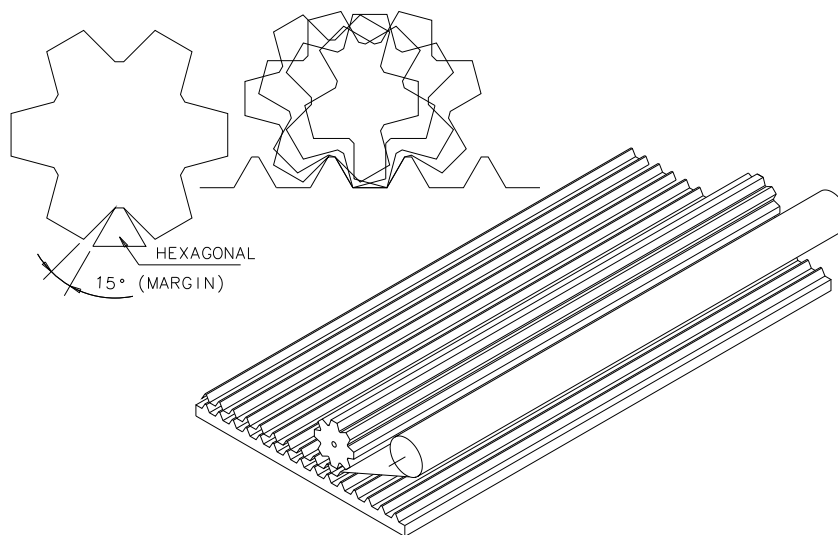
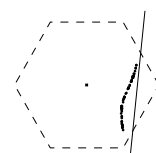


**Figure 3.13:** Reel and template used to fold aluminium foils.

The geometry of the chamber was identical to the P3 chamber. If a second coordinate is not needed, aluminium foil has the advantages that it is much cheaper than the sputtered or laminated foils and it can be folded simply by rolling a reel over the bottom template (see figure 3.13).

Monolayers were constructed from 1 metre wide folded  $50 \mu\text{m}$  thick aluminium foil. Adja-



cent foils of 1 metre were glued together forming the 5.77 m length. The same aluminium foil was used between two monolayers.

Since it was unlikely that muon chambers constructed with HSC technology would be used in ATLAS at the moment P3A was finished, only cosmic ray tests were done with this prototype.

## 3.4 Charged particle detection with the HSC

As for all particle detectors, the detection of passing or stopped particles is based on its interaction with matter. In case of a drift tube, the interacting particle will ionise the gas molecules with a given probability. The liberated electrons will drift towards the anode wire, generate a signal on the wire and the inverted signal on the cathode strips. All relevant processes will be discussed.

### 3.4.1 Energy loss of relativistic particles in matter

The production of ion-electron pairs happens instantaneously when a charged fast particle traverses the tube. What remains after the passage of the particle is a trail of electrons starting to drift towards the anode and ions drifting to the cathode.

For a better understanding of the chamber performance, it is important to get a good insight in the process of ionisation.

#### 3.4.1.1 Primary ionisation

It is well known that the ionisation along a particle track does not appear as randomly distributed ion-electron pairs. On the contrary: the electron-ion pairs are grouped together in ionisation clusters. Each cluster is produced by a primary ionisation. The clusters are indeed randomly distributed along the track. Three possible scenarios are possible after this first interaction. First, the energy of the primary electron is below the ionisation potential of the gas (15.7 eV for Argon). In this case the cluster consists of only one electron. Second, the energy of the primary electron is larger than the lowest ionisation potential. The primary electron has sufficient energy to ionise one or more additional atoms. This can result in a cluster size larger than one, where the final size of the cluster depends on the kinematics of the individual collisions between the electrons and gas atoms. The third option is that more electrons are ejected from a single atom, e.g. by the Auger effect.

The number of primary interactions follows Poisson-like statistics, i.e. if  $N$  is the average number of primary interactions, the probability of having  $k$  in one event is  $P_k^N = \frac{N^k}{k!} e^{-N}$ . The number of electrons per cluster may vary from  $n=1,2,3,\dots$  up to very large values. In the latter case it is more appropriate to speak of  $\delta$ -rays, since the energy transferred to the primary electron is large enough to let the cluster evolve into a track.

#### 3.4.1.2 Relativistic rise

In the late 60's and early 70's the theoretical framework was set up to calculate the cluster size distribution for bubble chambers and the relation between cluster size and particle velocity [10].

Jackson notes that the mean energy loss of high velocity charged particles in thin absorbers is a function of the velocity ( $\beta$ ) of the particle and not of its mass [11]. In fact it is more convenient to consider its dependence on  $p/mc = \beta(1-\beta^2)^{1/2} = \beta\gamma$ . Three clear regions can be distinguished

in the behaviour of the energy loss versus  $p/mc$  (see figure 3.14). First, in the non-relativistic

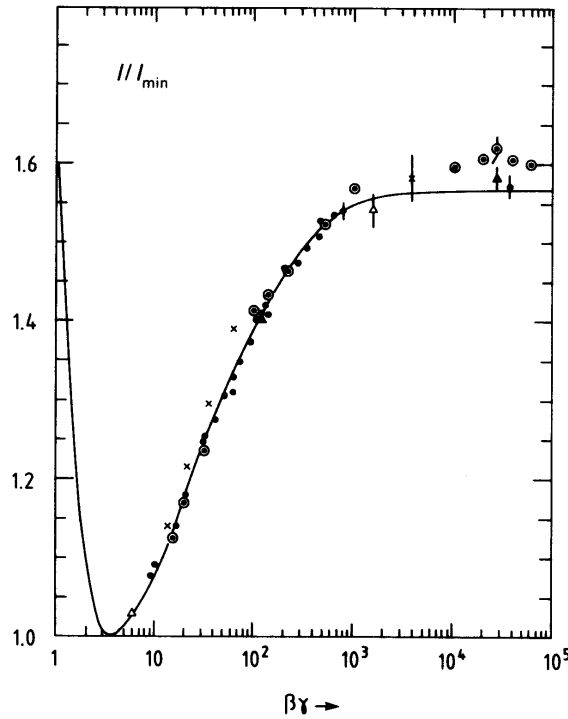


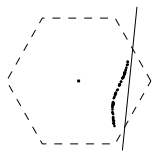
**Figure 3.14:** Measured values of the most probable energy loss in an Ar + methane mixture as function of  $\beta\gamma$ , compared with the photo-absorption model of Allison and Cobb for Ar [4, 12].

case, the mean value of the energy loss is proportional to  $\beta^{-2}$ , (classical Bohr limit). The value of  $dE/dx$  stabilises for  $\beta\gamma = 4$ . Then for  $\beta\gamma > 4$  a slow logarithmic increase occurs (relativistic rise). For highly relativistic particles, a plateau will be reached which is called the Fermi plateau. The value of the plateau and the value of  $\beta\gamma$  for which it occurs depends on the gas (or liquid) material.

The relativistic rise can be understood by considering the electromagnetic field of a relativistic charged particle. The interaction of virtual longitudinal photons represents the instantaneous Coulomb interaction and is effectively constant at high velocities [13]. The increase in range of the transverse photons is responsible for the relativistic rise. The saturation on the Fermi plateau is explained by the effect that the transverse dimension of the field of a relativistic particle can not expand infinitely in matter. The effect of the medium may be described by a screening length, which prohibits the transverse field to interact with electrons at large distance [14].

### 3.4.1.3 $dE/dx$ distribution for thin gas layers

The main features of energy loss distributions are the most probable value  $\Delta_{mp}$  corresponding to the maximum of the energy loss distribution and the relative width  $\delta$ . This is the full width at half-maximum, fwhm, divided by  $\Delta_{mp}$ . Many experiments with proportional detectors showed that  $\delta$  values are considerably greater than the Landau theory [15] predicts (see figure 3.15). Ispirian was the first who showed quantitatively where the Landau solution gives problems in thin gas layers [19]. First, the Landau solution is only applicable for energies above the binding energies where the scattering cross section is determined by Rutherford scattering and the atomic structure can be ignored. So, Ispirian worked with a (simple) model which took the atomic form



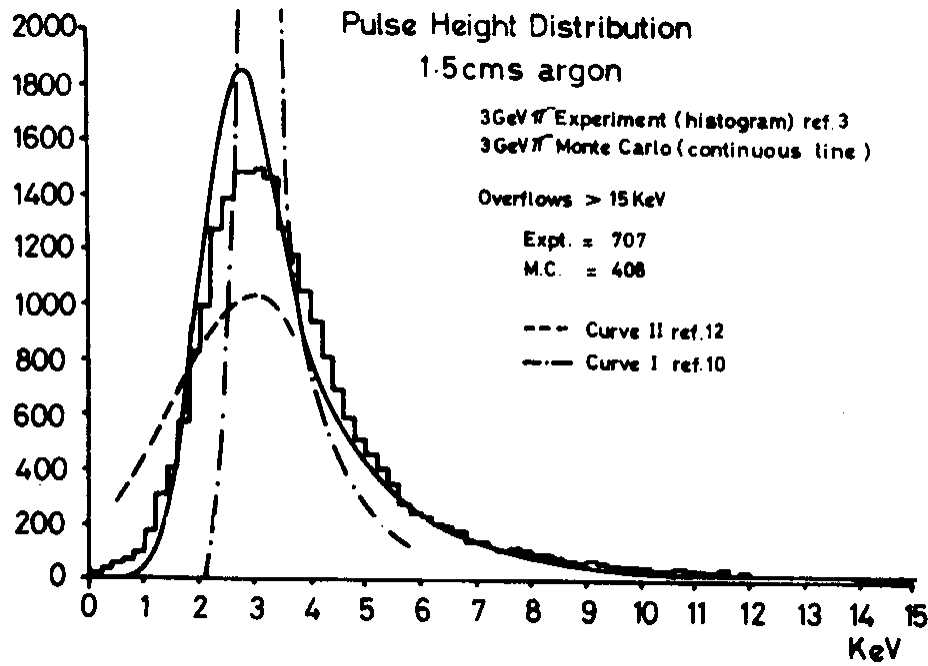


**Figure 3.15:** Experimental pulse height distribution in 1.5 cm of argon (histogram) [16, 17]. The dot-dashed curve represents the original Landau theory [15] which fits extremely bad to the experimental distribution. The solid curve is computed by Cobb et al. [14] and the dashed curve represents an alternative theory by Blunck and Leisegang [14, 18].

factors and polarisation effects into account. Secondly, due to the small number of interactions of the primary particle with the gas atoms (about 30/cm), the continuous integral over all possible collisions had to be replaced by a summation over discrete energy losses by a Monte Carlo (MC) method. The work of Ispirian was continued by Cobb and Ermilova who were able to simulate with a MC model realistic  $dE/dx$  distributions and the relativistic rise [14, 20]. As a result of the simulations they found that the Landau solution is only valid for gas detectors with lengths  $x(\text{cm}) \gg 2\beta^2Z$ , which means  $x \gg 40$  cm for argon.

#### 3.4.1.4 From $dE/dx$ to primary ionisation fluctuations

Since it was noticed in the late 70's that the Poisson-like behaviour of cluster counting provides significantly smaller fluctuation than the Landau fluctuations in the same gas layer thickness, techniques were developed to use this advantage for particle identification. Lapique and Piuz have used the model of Chechin [10] to calculate the variation of the number of primary clusters as a function of  $\gamma$  together with the cluster size distribution, given in number of electrons [21]. The main results of this study are summarised in figure 3.16 and table 3.2. The most remarkable phenomenon is the stabilisation of the relativistic rise of the primary ionisation at  $\gamma = 200$ , while the curves for the mean energy loss and most probable energy loss continue to rise, up to values of  $\gamma = 10^4$  (see figure 3.16). From this, one can conclude that the number of energy transfers from the relativistic particle to the gas atoms saturate around  $\gamma = 200$ , while the transferred energy continues to increase. This increase of the transferred energy for large  $\gamma$  values can be recognised in table 3.2, where a small shift is visible towards higher cluster sizes for  $\gamma = 1000$  with respect to  $\gamma = 4$ .

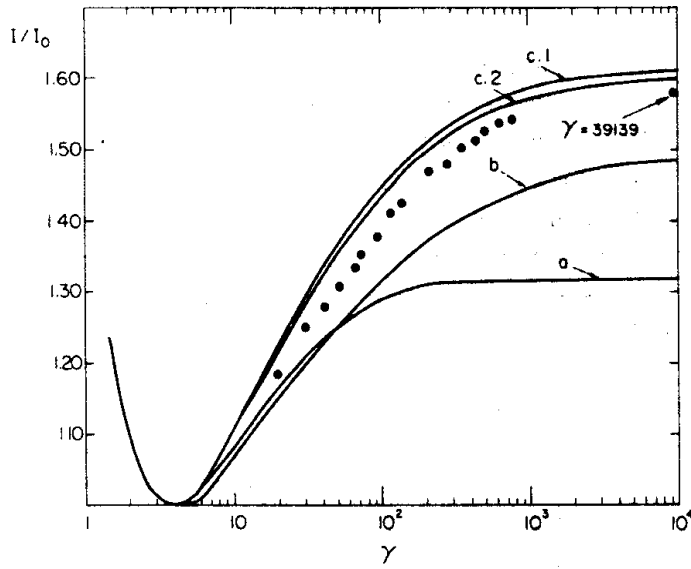


**Figure 3.16:** Relativistic rise of the ionisation in a 10 mm layer of argon: (a) Number of primary clusters. (b) Mean number of deposited electrons. (c) Most probable number of deposited electrons. Dots: most probable  $dE/dx$  measurement [21].

Cluster size (number of electrons)	$\gamma = 4$ (%)	$\gamma = 1000$ (%)
1	80.2	78.2
2	7.7	7.4
3	2.0	2.1
4	1.3	1.4
5	0.8	0.8
6	0.6	0.7
7	0.5	0.6
$\Sigma 8 - 20$	5.3	6.9
$\Sigma > 20$	1.4	1.65
overflow	0.2	0.25

**Table 3.2:** Cluster size distribution for minimum ionising and 'on the Fermi plateau' particles [21].

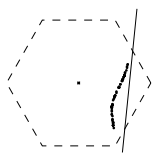
Cluster size n (number of electrons)	Ar measured (%)	fit (%)	CO <sub>2</sub> measured (%)	fit (%)
1	65.6 $\pm$ 1.58	65.6	73.0 $\pm$ 2.8	72.50
2	14.8 $\pm$ 0.67	15.0	16.2 $\pm$ 1.2	14.00
3	6.49 $\pm$ 0.45	6.4	4.80 $\pm$ 0.4	4.20
4	3.37 $\pm$ 0.25	3.5	2.00 $\pm$ 0.3	2.20
5	2.44 $\pm$ 0.19	2.25	1.10 $\pm$ 0.20	1.40
6	1.41 $\pm$ 0.14	1.55	1.47 $\pm$ 0.26	1.00
7	0.78 $\pm$ 0.10	1.05	0.60 $\pm$ 0.14	0.75
$\Sigma 8 - 18$	3.73 $\pm$ 0.23	3.50	3.31 $\pm$ 0.37	2.88
$\Sigma > 18$		21.6/ $n^2$		14.9/ $n^2$

**Table 3.3:** Cluster size distribution for argon and CO<sub>2</sub> [22].

### 3.4.1.5 Experimental cluster size distributions

For a long time, the Monte Carlo calculation of Lapique was the only input for drift chamber simulation programs. The Heidelberg group has presented measured cluster size distributions for the most used drift gases (Ar, He, CH<sub>4</sub>, C<sub>2</sub>H<sub>6</sub>, C<sub>3</sub>H<sub>8</sub>, i-C<sub>4</sub>H<sub>10</sub> and CO<sub>2</sub>) for values of  $\beta \approx 0.8$ – $0.97$  (see table 3.3) [22].

A significant deviation of the Lapique distribution was found and could be explained by fine tuning the atomic model in the Monte Carlo simulation. For all simulation studies in this thesis I will use the measured cluster size distributions of the Heidelberg group. For an evaluation of the impact of the range of  $\delta$ -rays on the spatial resolution, I have to use the simulation of Lapique since no experimental data exists.



Energy transfer (eV) between	$\gamma = 4$ (%)	$\gamma = 1000$ (%)	Energy transfer (eV) between	$\gamma = 4$ (%)	$\gamma = 1000$ (%)
15–30	70.9	69.3	225–240	0.1	0.1
30–45	14.1	13.7	240–255	0.4	0.5
45–60	1.9	1.7	255–270	0.6	0.8
60–75	1.6	1.5	270–285	0.6	0.7
75–90	1.1	1.2	285–300	0.5	0.6
90–105	0.9	0.9	300–315	0.4	0.5
105–120	0.7	0.8	315–330	0.3	0.4
120–135	0.5	0.6	330–345	0.3	0.4
135–150	0.4	0.5	345–360	0.3	0.3
			360–375	0.2	0.3
			>375	3.2	4.3

**Table 3.4:** Primary ionisation energy transfer distribution in steps of 15 eV for argon. The values are computed for minimum ionising particles and for particles 'on the Fermi plateau' [21].

For a gas mixture, the total primary ionisation density and the cluster size distributions are calculated by a weighted sum of the numbers for the individual gases. The weighting is done with the relative volumes of each gas component in the mixture (partial pressure). This method does not take into account that secondary ionisation in gas mixtures may involve physical processes which are absent in the corresponding pure gases.

#### 3.4.1.6 The range of $\delta$ -electrons

Since the primary electron is produced with some finite energy, it will travel through the gas and ionise more atoms, until its energy is below the lowest ionisation potential. The distance the primary electron can travel and still is able to produce a secondary electron will be called the 'range'. The value of the range of primary electrons is one of the contributions to the spatial resolution of a drift tube. We will estimate the number of high energetic long range primary electrons ( $\delta$ -electrons) from the simulation by Lapique. The energy transfer of the relativistic particle to the primary electron is tabulated for pure argon in table 3.4.

Primary electrons are emitted almost perpendicularly to the track of the fast particle. This transverse direction of the primary electron is immediately randomised by the scattering with the gas molecules. In the literature, a practical range  $R$  can be found by the empirical relation:

$$R(E) = AE(1 - \frac{B}{1 + CE}), \quad (3.1)$$

with  $A = 5.37 \times 10^{-4} \text{ g cm}^{-2} \text{ keV}^{-1}$ ,  $B = 0.9815$ ,  $C = 3.1230 \times 10^{-3} \text{ keV}^{-1}$  and  $E$  in keV [4]. It is shown that this parametrisation is applicable to all materials with low and intermediate atomic number  $Z$  [23]. This relation is shown in figure 3.17. For argon  $1 \text{ g/cm}^2$  is equivalent with 562 cm.

From table 3.4 and figure 3.17, we can estimate the fraction of primary electrons with an energy and range above a threshold value. Further, it is assumed that the cross-section above 375 eV is Rutherford-like. So, the following equation is used to calculate the probabilities in



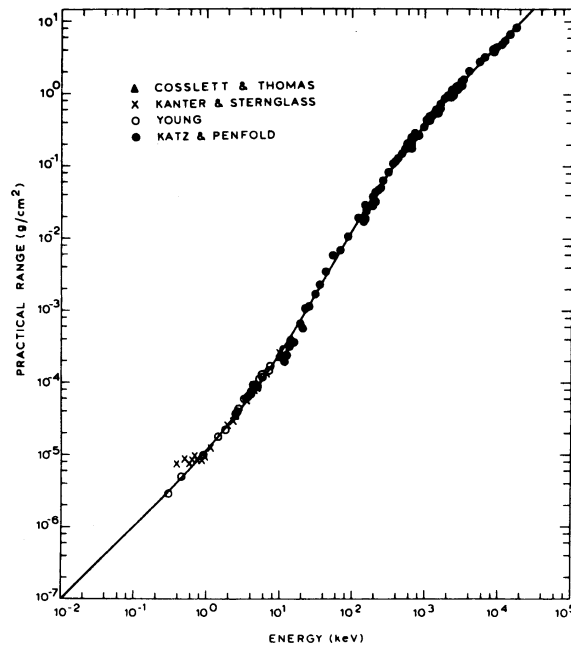


**Figure 3.17:** Practical range versus kinetic energy for electrons in aluminium. The solid curve represents the parametrisation according to equation 3.1 [4].

Probability $E > E_0$ (%)	$E_0$ (keV)	Range (g/cm <sup>2</sup> )	Range (mm)
1.0	1.60	$2.0 \times 10^{-5}$	0.11
0.1	16.0	$5.6 \times 10^{-4}$	3.2
0.01	160	$3.0 \times 10^{-2}$	170

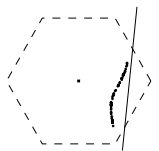
**Table 3.5:** Probability for the creation of a primary electron above energy  $E_0$  per primary interaction for relativistic particles ( $\gamma = 1000$ ). The probabilities are computed using equation 3.2 and the range is computed using equation 3.1. The range in mm is for argon N.T.P.

table 3.5:

$$P(E > 375\text{eV}) = \int_{375\text{eV}}^{\infty} \frac{C}{E^2} dE = 4.3\%, \quad (3.2)$$

giving  $C=1.6 \text{ keV}^2$ .

The probability of a high energetic  $\delta$ -electron in this calculation is significantly higher than quoted by Blum and Sauli [4, 24]. Blum gives (without derivation) a number of 0.05% probability for an electron of 10 keV or higher. According to the above calculation (based on the work of Lapique) this probability is  $\approx 0.16\%$ . Sauli gives a number of one out of twenty minimum ionising particles ejecting a 3 keV electron [24]. For minimum ionising particles ( $\gamma = 4$ ), the factor  $C$  in equation 3.2 becomes  $1.2 \text{ keV}^2$ . We find for argon (29 primary ionisations per cm) that every 9 cm an electron with 3 keV or more ( $R > 250 \mu\text{m}$ ) is produced. The range quoted by Sauli ( $100 \mu\text{m}$  for a 3 keV electron in pure argon) is rather small.



### 3.4.2 The drift of electrons in gases

Liberated electrons will start drifting towards the wire under influence of the electric (and if present magnetic) field. The drift behaviour of individual electrons can be described by the following properties: drift velocity, diffusion (longitudinal and transverse), attachment and the Lorentz angle. All those quantities are functions of the following variables: the gas composition, electric field (or normalised field  $E/p$ ), the magnetic field, temperature and pressure. In the following the relevant dependencies of the gas properties on the variables will be discussed.

#### 3.4.2.1 The electric field

By applying a high voltage (order 2.5 kV) on the conducting wire in the drift tube an electric field is created radially around the wire with field lines ending on the cathode. The field close to the hexagonal cathode can locally be very low (order 100 V/cm) and inhomogeneous. Close to the wire the field has perfect cylinder symmetry and will reach values of several thousands V/cm in the avalanche region. The shape of the field depends only on the ratio of the wire diameter and the tube diameter:

$$E(r) = \frac{V}{\ln(r_b/r_a)} \frac{1}{r}. \quad (3.3)$$

Since the strength of the electric field varies radially, the interaction between the drifting electron and the gas will also continuously change. This situation is significantly different with respect to planar drift chambers, where the drift region can be divided in two regions: the drift region with constant electric field (typical several 100 V/cm) and the multiplication region with cylindrical field. One of the consequences of this non-homogeneous field in drift tubes will be that the diffusion contribution in the resolution will NOT be proportional to the square root of the drift distance anymore. This will be discussed later in this section.

#### 3.4.2.2 The drift velocity

For detailed calculations of the transport parameters, the Boltzmann transport equation, which will be discussed later, has to be solved. In order to get some insight in the dependence of the transport parameters on the  $E$ -field, pressure, gas components and  $B$ -field, the classical theory of electron drift in gases will be followed. This theory is derived in appendix A, starting with the equation of motion of a free electron in perpendicular  $E$  and  $B$  fields. The main results will be quoted and some side remarks will be made.

The electrons that drift through the gas are scattered off the gas molecules. The direction of motion of the drifting electron is randomised in each collision. We can use a classical treatment of the scattering process between the electron and gas molecules if the mean free path between two collisions is much larger than the Compton wavelength. This is true for gas pressures up to approximately 100 atm.

If no force is applied on a free electron by an electric field, the electron will move randomly with an average energy of  $\frac{3}{2}kT$ . This thermal diffusion of an electron cloud will be referred to as the 'thermal limit' of diffusion.

If an electric field is applied, the free electron will continue to have a non-directional velocity  $v_0$ , but also a macroscopic mean drift velocity  $u$  along the field direction. In case also a magnetic field  $B$  is applied with some component perpendicular to  $E$ , the mean drift velocity will not anymore be parallel to the electric field lines. This effect appears on macroscopic scale as

the Lorentz angle  $\alpha_L$ . It is important to keep in mind that the non-directional velocity  $v_0$  is much higher than the mean velocity  $u$ .

In order to find the relationship between the drift velocity  $u$  and the random velocity  $v_0$ , we introduce the fractional energy loss per collision  $\lambda$  and the average free time of an electron between two collisions  $\tau$ . The extra energy the electron extracts from the  $E$ -field is, on the average, lost in the collision through recoil or excitation. Therefore there is a balance between the energy gain in the field and the energy loss in the collisions.

In appendix A it is found that the macroscopic (drift) velocity  $u$  and the non-directional velocity  $v_0$  are:

$$u^2 = \frac{\varepsilon^2 \tau^2}{1 + \omega^2 \tau^2}, \quad (3.4)$$

$$v_0^2 = \left( \frac{1}{\lambda} - 1 \right) \frac{2\varepsilon^2 \tau^2}{1 + \omega^2 \tau^2} + \frac{2kT}{m}, \quad (3.5)$$

$$\lambda \rightarrow 1 \quad v_0^2 = \frac{2kT}{m} \quad (\text{thermal limit}) \quad (3.6)$$

$$\lambda \rightarrow 0 \quad v_0^2 = \frac{2}{\lambda} \frac{\varepsilon^2 \tau^2}{1 + \omega^2 \tau^2} \quad (\text{hot gas}), \quad (3.7)$$

where  $\tau$  is the mean free time of drift between two collisions. Here,  $\varepsilon = eE/m$  is the reduced electric field and  $\omega = eB/m$  the reduced magnetic field and  $m$  and  $e$  are the mass and charge of the electron. One finds in the literature most of the gas properties tabulated as a function of normalised electric field  $E/p$  with  $p$  the absolute gas pressure. This normalisation is based on the observation that the mean time of drift  $\tau$  is proportional to the gas pressure. If  $\varepsilon$  appears always in combination with  $\tau$  in the formulas, one is allowed to use normalised units for the electric field. For the drift velocity  $u$  this is only true for  $\omega\tau \ll 1$ . We will see that this is equivalent to a Lorentz angle  $\alpha_L \approx 0$ .

In a gas mixture composed of two or more components  $i$  with volume densities  $n_i$ , the effective cross section  $\sigma(v_0)$  and the effective fractional energy loss per collision  $\lambda(v_0)$  can be computed from the properties of the individual components:

$$\begin{aligned} \sigma(v_0) &= \sum n_i \sigma_i(v_0)/N, \\ \lambda(v_0) \sigma(v_0) &= \sum n_i \lambda_i(v_0) \sigma_i(v_0)/N, \\ N &= \sum n_i. \end{aligned} \quad (3.8)$$

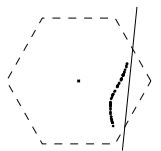
### 3.4.2.3 The Lorentz angle $\alpha_L$

In appendix A the macroscopic drift direction is derived from the microscopic electron transport theory. In case of a  $B$ -field perpendicular to the  $E$ -field, the macroscopic drift velocity  $u$  can be described by a component parallel to the  $E$  field  $u_{\parallel}$  and a component perpendicular to  $E$  and  $B$ :  $u_{\perp}$ . The Lorentz angle  $\alpha_L$  is defined as:

$$\tan \alpha_L = \frac{u_{\perp}}{u_{\parallel}} = \omega\tau. \quad (3.9)$$

### 3.4.2.4 Longitudinal and transverse diffusion

The diffusion is a measure of the width of an initially point-like cloud of electrons after a drift over distance  $x$ . In case a magnetic field is applied, the distance along the trajectory of the electrons will be called  $x$  and the projection of  $x$  on the electric field line will be called  $x_{\parallel}$ . Since



diffusion is a Gaussian process, the square of the width of the cloud will be proportional to the distance  $x_{||}$ :

$$\sigma_x^2 = D^2 x_{||}, \quad (3.10)$$

here  $D^2$  is the proportionality constant.  $D$  is often given in units of  $\sqrt{\text{cm}}$  and can be regarded as the width of a point-like cloud after 1 cm of drift. From the classic theory of drift it appears that:

$$D^2 = \frac{v_0^2}{\varepsilon}, \quad (3.11)$$

which means for the 'hot gas' limit where  $kT$  can be neglected:

$$D^2 = \frac{2}{\lambda} \frac{\varepsilon \tau^2}{1 + \omega^2 \tau^2}, \quad (3.12)$$

where  $1/(1 + \omega^2 \tau^2)$  is the diffusion compression factor. See appendix A for more details. In the thermal limit one finds:

$$D^2 = \frac{2kT}{m\varepsilon}, \quad (3.13)$$

which is independent of the magnetic field. In figure 3.18 the value of the diffusion is plotted

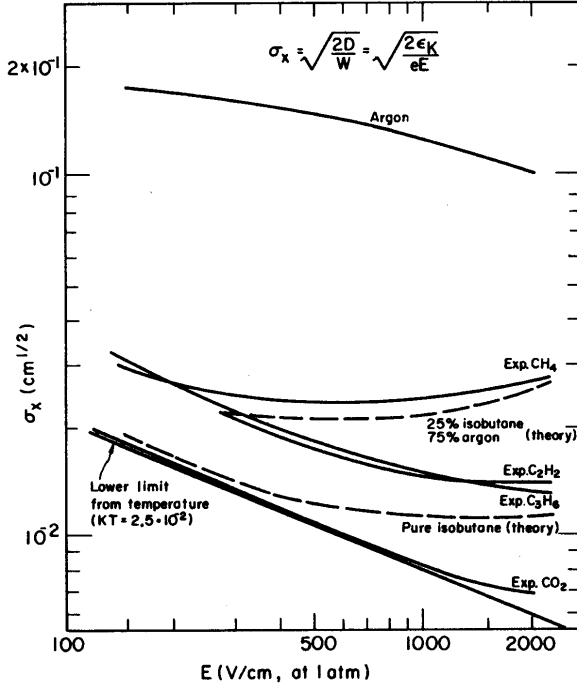


**Figure 3.18:** Width of an initially point-like cloud of electrons after 1 cm of drift in different gas mixtures. The solid lines represent data, while the dashed curves represent a simulation [25].

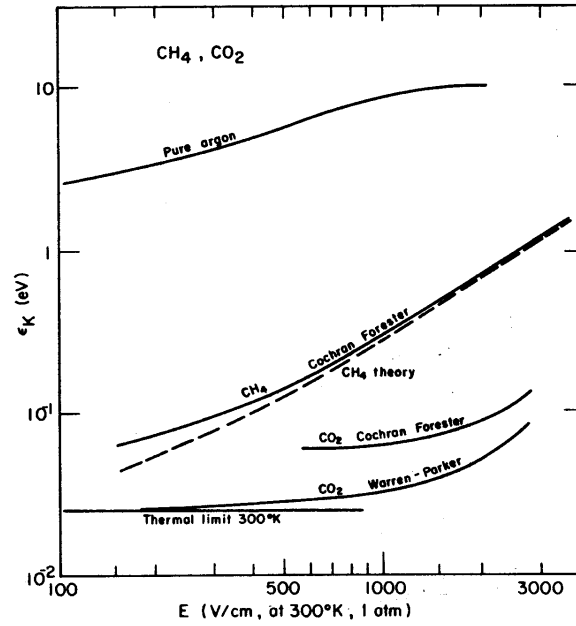


**Figure 3.19:** Experimental value of the characteristic energy  $\varepsilon_k$  for different gases. The dashed curve is a simulation for methane [25].

for cool gases like  $\text{CO}_2$  and hot gases with argon as its prime example.

By analogy with  $kT$  in equation 3.13 one can define the 'characteristic energy'  $\varepsilon_k$ :

$$D^2 = \frac{2\varepsilon_k}{m\varepsilon}. \quad (3.14)$$

In figure 3.19  $\varepsilon_k$  is shown for some commonly used drift gases. Regarding the diffusion, small additions of argon, with its high characteristic energy, will dominate the spatial contribution. We will see, however, that we can not ignore argon because it is fast, cheap, inflammable and has good primary ionisation, attachment and gas amplification characteristics.

Since 1967 it is known that there is an anisotropy in the diffusion in the direction of the electric field [26]. This means that the diffusion in the direction of the  $E$ -field has another value than the diffusion perpendicular to the field. The basic argument for this anisotropy is the difference in mobility of the electrons in the leading edge and the trailing edge of the cloud. Since the electron energy  $\varepsilon$  depends on the mobility, all properties related to  $\varepsilon$  will also be functions of the position of the electron in the cloud. The value of the transverse diffusion can be lower or higher than the longitudinal diffusion.

Care should be taken in using equation 3.14 to compute the spatial resolution obtained with a real drift chamber. All numbers quoted are for single electrons. In general one will never detect single electrons, but some average number. A careful optimisation has to be made between information loss due to primary ionisation uncertainties and reduction of diffusion by triggering on some average number of electrons instead of triggering on the first electron arriving in the avalanche region.

Also, care should be taken when applying equation 3.14 in an inhomogeneous  $E$ -field (like the drift tube) to compute the diffusion contribution to the spatial resolution. In a homogeneous drift field (like in the traditional drift chamber) the spatial resolution due to diffusion can be computed by a quadratic summation over the diffusion coefficient  $D$ :

$$\sigma_x^2 = \int_0^x D^2 dx' = D^2 x, \quad (3.15)$$

with  $D$  the diffusion contribution in  $\sqrt{\text{cm}}$  and constant over the whole integral.

In an inhomogeneous drift field, the diffusion  $D$  and the drift velocity  $u$  will depend on  $x$ . Equation 3.15 will give an erroneous result if we replace  $D$  by  $D(x)$ . Instead, we have to integrate quadratically over the width of the electron cloud in **time** and to multiply the result of this integral with the local drift velocity  $u$ . In an inhomogeneous  $E$ -field and  $\alpha_L = 0$  equation 3.15 becomes:

$$\sigma_x^2 = \left[ \int_0^x \frac{D^2(x')}{u^2(x')} dx' \right] u^2(x). \quad (3.16)$$

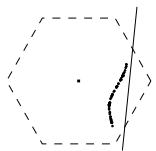
This equation is equal to equation 3.15 in case  $u$  is constant. In case  $\alpha_L$  is non-zero, the situation becomes a little more complicated.

### 3.4.2.5 Attachment

Electron attachment in gases occurs when free electrons encounter molecules which somehow capture them. Two processes can be distinguished: electro-affinity and molecular dissociation [27].

The basic process of electron attachment depends in first order on the mean energy  $\varepsilon$  of the free electrons. If  $\varepsilon$  is close to or above the threshold for molecular dissociation (4.6 eV for  $\text{O}_2 \rightarrow \text{O}^- + \text{O}^+$  and 5.5 eV for  $\text{H}_2\text{O} \rightarrow \text{H}^+ + \text{OH}^-$ ), the free electron gets easily absorbed by the positive ions and one observes a rapid increase of the attachment cross section with increasing electric fields. This process is dominant close to the anode wire where very high fields are present.

For electron energies below 1 eV the electron attachment process occurs by electron-affinity. During this process, a negative ion is created in an excited state. From this situation, different



scenarios are possible. The negative ion can reach its ground state by emission of a photon or the electron can be released again. Also, all sort of interactions occur between the excited negative ion and the gas molecules. Sometimes this may lead to a stable negative ion, which means that the electron is lost for detection.

Whereas the noble gases and most organic molecules can form only negative ions at collision energies of several electron-volts (which is higher than the energy reached during most of the drift in drift tubes), there are some molecules that are capable of attaching electrons at much lower electron energies. The largest electro-affinities are found with the halogenides and oxygen, therefore, we have to consider contamination with air and water, but also drift gas components like  $\text{CF}_4$  and  $\text{CO}_2$ .

It is highly desirable to actually measure the attachment coefficient in the working point of the detector in which a specific gas is to be applied. If a number of electrons is deposited at time  $t=0$  in a gas, the time evolution of the number of free electrons will follow:

$$N(t) = N(t=0)e^{-At}, \quad (3.17)$$

where  $A$  is the attachment rate in  $1/\text{s}$  and is a function of the  $E$ -field. For drift chamber applications, one also defines the attachment rate in units of  $1/\text{cm}$ .

### 3.4.2.6 The Boltzmann transport equation

As mentioned before, the classical theory of drift of electrons in gases can give good insights in the elementary processes at the microscopic level. But in order to calculate quantitative results, one has to solve the Boltzmann transport equation, which expresses the conservation of the number of electrons. If one introduces the distribution function  $f(\vec{v}, \vec{r}, t)$  of electrons at point  $\vec{r}$ ,  $\vec{v}$  of phase space at time  $t$ , the equation reads [25]:

$$\frac{\partial f}{\partial t} + \frac{\partial f}{\partial \vec{r}} \frac{\partial \vec{r}}{\partial t} + \frac{\partial f}{\partial \vec{v}} \frac{\partial \vec{v}}{\partial t} - \frac{\partial f}{\partial t} \Big|_{\text{via collisions}} = 0. \quad (3.18)$$

In the stationary case (without  $\vec{r}$  and  $t$  dependence), the distribution function  $F(\varepsilon, \cos \theta)$  can be used, where  $\theta$  is the angle between the direction of motion of the electron and the  $E$ -field and  $\varepsilon = \frac{1}{2}mv^2$  the energy of the electron.  $F(\varepsilon, \cos \theta)$  is normalised by:

$$\int_{-1}^1 \int_0^{\varepsilon_{\max}} F(\varepsilon, \cos \theta) d\varepsilon \frac{d \cos \theta}{2} = 1. \quad (3.19)$$

In order to solve equation 3.18, all terms are expressed in terms of the electric field  $E$ , the electron energy  $\varepsilon$ , the momentum transfer mean free path  $l_e(\varepsilon)$ , the mean free path  $l_h(\varepsilon)$  for excitation of the  $h^{\text{th}}$  level of energy  $\varepsilon_h$ . Further on  $F(\varepsilon, \cos \theta)$  is expressed in Legendre polynomials. The number of terms taken into account is one of the limiting factors in the finally achieved accuracy of the calculation. Writing down the first two terms:

$$F(\varepsilon, \cos \theta) = F_0(\varepsilon) + F_1(\varepsilon) \cos \theta + \dots, \quad (3.20)$$

one can solve the resulting coupled differential equations with numerical methods. In this thesis, the programme MAGBOLTZ will be used which solves the Boltzmann equation, using Legendre polynomials to the third order [28, 29, 30, 31, 32].

### 3.4.3 The gas amplification process

In a proportional counter or drift tube, the process of multiplication is restricted to the area very close to the wire, due to the high local  $E$  field which has a  $1/r$  dependence. In order to achieve a clear spatial separation of the drift region and multiplication region, the wire has to be as thin as possible. By applying a wire of typically 30  $\mu\text{m}$  diameter, the multiplication region can be limited to a diameter of 50 to 100  $\mu\text{m}$ .

#### 3.4.3.1 Photons in the gas amplification process

The physical processes inside a so called 'avalanche' are quite complicated, as they involve ionisation, excitation, recombination and energy transfer by collisions. The gas amplification properties of a proportional counter are dominated by the produced photons. They are produced as often as secondary electrons, but have a larger mean free path. Some photons will be energetic enough to ionise the gas. Some photons may even reach the cathode and produce free electrons by the photo-electric effect. It has been reported that the use of plastic cathodes reduces this effect compared with aluminium cathodes [33]. It is because of this far-travelling photons that an organic quench gas has to be added to noble gases. Those organic molecules with their many degrees of freedom, have large photo-absorption coefficients over a wide range of wavelengths.

#### 3.4.3.2 The amplification factor: Gain

The amplification amplitude can be derived from the first Townsend coefficient  $\alpha$ . This coefficient describes the increase in the number of free electrons over a path length  $dr$ :

$$\frac{dN}{N} = \alpha dr. \quad (3.21)$$

The coefficient  $\alpha$  is determined by the excitation and ionisation cross sections of the electrons. Since these quantities depend in a complicated manner on the electron energy distributions and thus on the electric field and gas mixture, no fundamental expression can be given for  $\alpha$ . To determine the total gas gain ( $N/N_0$ ) one has to measure  $\alpha$  for a large range of  $E$ -fields and to calculate the following integral for a specific geometry:

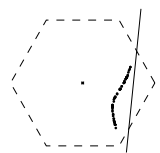
$$\frac{N}{N_0} = \exp \left[ \int_{r_a}^{r_{\min}} \alpha(r) dr \right] = \exp \left[ \int_{E(r_a)}^{E_{\min}} \frac{\alpha(E)}{dE/dr} dE \right], \quad (3.22)$$

where  $r_{\min}$  the distance from the wire where the field ( $E_{\min}$ ) is high enough to produce secondary electrons by ionisation and  $r_a$  is the wire diameter. The electric field at radius  $r$  in a tube geometry with the cathode at radius  $r_b$  and a potential difference  $V$  between wire and cathode is given in equation 3.3:

$$E(r) = \frac{V}{\ln(r_b/r_a)} \frac{1}{r}. \quad (3.23)$$

In this special geometry we can express the gain  $G$  (total amplification) in terms of  $\alpha(E)$ ,  $V$ , the geometry and an integral over the electric field:

$$\ln(G) = \ln \left( \frac{N}{N_0} \right) = \int_{E_{\min}}^{E(r_a)} \frac{V}{\ln(r_b/r_a)} \frac{\alpha(E)}{E^2} dE. \quad (3.24)$$



From measurements and first order considerations  $\alpha$  can be assumed to be proportional with  $E$ . Diethorn was the first to derive an expression for the gain with this simplified model [34]. We introduce  $\beta$  with  $\alpha = \beta E$ , evaluate equation 3.24 and obtain:

$$\ln(G) = \beta E(r_a) r_a \ln \left( \frac{E(r_a)}{E_{\min}} \right), \quad (3.25)$$

which gives the basic dependence of  $G$  on the experimental conditions.

It is often assumed that near the anode wire, the effective ionisation coefficient is proportional to the pressure and a function of the reduced field  $E/p$ . In the Diethorn approximation this reduces to:

$$\frac{\alpha}{p} = \beta \frac{E}{p}. \quad (3.26)$$

In this approximation, the first Townsend coefficient is independent of the gas density. The total gain  $G$  depends on the gas density because the lower limit of the integration interval scales with the pressure according to:

$$E_{\min}(p) = E_{\min}(p_0) \frac{p}{p_0}, \quad (3.27)$$

with  $E_{\min}(p_0)$  and  $p_0$  the field and gas pressure in the reference situation and  $E_{\min}(p)$  the lower limit of the integration interval in case of pressure  $p$ . Substituting equation 3.27 into equation 3.25 gives the following expression for the gain:

$$\ln(G) = \beta E(r_a) r_a \ln \left( \frac{E(r_a)}{E_{\min}(p_0) \frac{p}{p_0}} \right). \quad (3.28)$$

This equation can be found in the literature in a more general form as (see e.g. [35]):

$$\frac{\ln(G)}{K} = f \left( \frac{E(r_a)}{p} \right), \quad (3.29)$$

where  $K = \beta E(r_a) r_a$ . It depends on the specific parameterisation of  $\alpha$  as function of the E-field, which expression will be found for  $f$ . From equation 3.28 one can derive the increase in high voltage to achieve a constant gain in case of increasing pressure. This equation can also be used to estimate the high voltage of a new detector with a known gas, but changed cathode diameter and/or wire diameter.

Some authors have tried to simulate in detail the multiplication process by a Monte Carlo method, taking the excitation and ionisation cross sections into account [36, 37, 38]. Figure 3.20 is a three dimensional display of an event. The problem in those simulations are the photons, which behaviour is difficult to simulate. In practise one will use the measured gain as a function of high voltage in similar circumstances to get an idea of the high voltage setting of a new detector, or for a new gas filling. In case this data is not available one has to use measured  $\alpha$  coefficients for the gas of choice and perform the integration of equation 3.24. Figure 3.21 gives an example of the measured  $\alpha/p$  for various Ar/CO<sub>2</sub> mixtures.

### 3.4.3.3 Variations in the gain

Since the amplification process is a stochastic process, variations are to be expected in the total amplification factor between individual events. Assuming that the probability of ionisation per unit path length of an electron depends only upon the field strength and does not depend on the



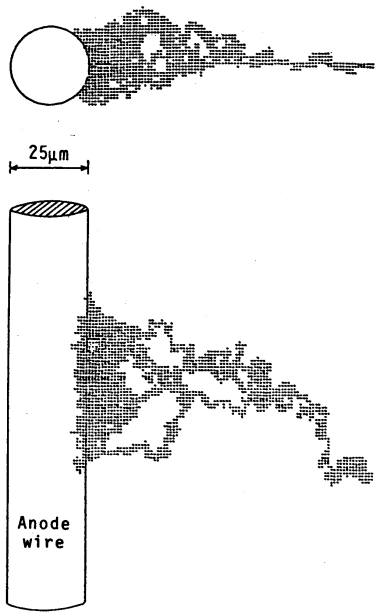


**Figure 3.20:** Three dimensional display of a simulated electron avalanche [37].

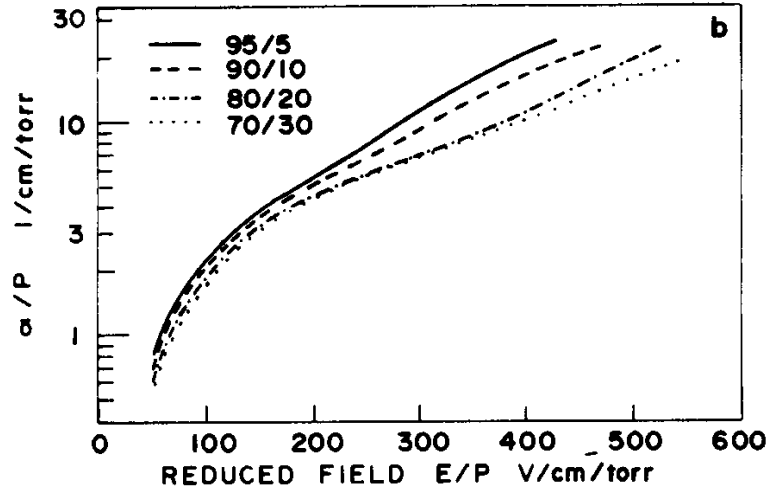


**Figure 3.21:** The reduced Townsend ionisation coefficient,  $\alpha/p$ , obtained from the fits to the gas gain data as a function of the reduced anode electric field for Ar/CO<sub>2</sub> gas mixtures [35].

history of the electron, one can compute that the distribution of the amplification factor is of exponential form:

$$p\left(\frac{K}{\bar{K}}\right) = p(z) = e^{-z}, \quad (3.30)$$

where  $\bar{K}$  is the average multiplication factor, better known as the gain  $G$  and  $K$  the number of electrons per single avalanche. From experiments with proportional counters, the avalanche size distribution appears to have a clear maximum and is described by Curran by the experimental distribution [39]:

$$p(z) = 3\sqrt{3/2\pi} \sqrt{z} e^{-\frac{3}{2}z}. \quad (3.31)$$

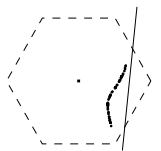
To explain the experimental results of Curran and Byrne [39, 40], Lanciart and Morucci have proposed a model, in which the probability for an electron to ionise depends on the total number of electrons already produced in the avalanche [41]. By using the following value  $a(\xi)$  for the probability of ionisation per unit path-length  $\xi$ :

$$a(\xi) = \begin{cases} 0, & \text{for } \xi < U_0/E, \\ a = \alpha(1 + \mu/K), & \text{for } \xi \geq U_0/E, \end{cases} \quad (3.32)$$

with  $U_0$  approximately the first ionisation potential,  $\alpha$  the first Townsend coefficient and  $\mu$  an empirically defined parameter, they arrive at the Polya distribution:

$$p_m(z) = \frac{m^m z^{m-1}}{\Gamma(m)} e^{-mz}, \quad (3.33)$$

in which  $m = 1 + \mu$ . In the particular case, that  $m = 3/2$ , this distribution is equal to the experimentally found Curran distribution. Note that the Polya distribution describes the avalanche size well for a proportional tube with a  $1/r$  field dependence. In case of a uniform electric field, the Polya distribution is not valid [42].



### 3.4.4 The signal development: Drift of ions

The whole multiplication process happens in a fraction of a nanosecond. The negative current signal seen at the input of the pre-amplifier has, nevertheless, a long duration of hundreds of ns. This typical current signal from a proportional counter is explained by the drift behaviour of the positive ions.

The deposited charge on the wire  $Q_e$  can be split in two components: the first is the negative charge seen by the pre-amplifier at the end of the wire  $Q_w$  and a part of the charge that remains at the position of the avalanche due to induction of the positive ion cloud:  $Q_i$ . So we can write for the charge flowing to the pre-amplifier:

$$Q_w = Q_e - Q_i, \quad (3.34)$$

with negative signs for all charges. We now have to evaluate the relation between  $Q_i$  and the position of the ion cloud to find an expression for  $Q_w$ . The ion cloud is assumed to be point-like at a distance  $r$  from the anode. It can be shown that (see e.g. [43]):

$$Q_i(r) = Q_e \left( 1 - \frac{\ln(r/r_a)}{\ln(r_b/r_a)} \right), \quad (3.35)$$

where  $r_a$  and  $r_b$  are the wire and tube radii [24]. Together with equation 3.34 the total charge seen at the input of the pre-amplifier becomes:

$$Q_w(r) = Q_e \frac{\ln(r/r_a)}{\ln(r_b/r_a)}. \quad (3.36)$$

By extracting the time behaviour of the cloud, we can describe the time dependence of  $Q_w$ . Making use of the  $E$ -field in a circular tube (equation 3.3) and the ion mobility:

$$\frac{dr}{dt} = \mu E, \quad (3.37)$$

we find the following relation between the position  $r$  of the ion cloud and the time since the avalanche:

$$r^2 = \frac{2\mu V}{\ln(r_b/r_a)} t + r_a^2. \quad (3.38)$$

By substitution of this relation in equation 3.36 the charge signal seen by the pre-amplifier becomes:

$$Q_w(t) = \frac{Q_e}{\ln(r_b/r_a)} \ln \left( \sqrt{\frac{2\mu V}{r_a^2 \ln(r_b/r_a)} t + 1} \right). \quad (3.39)$$

The current signal can now be obtained by computing the first derivative of the charge signal:

$$i(t) = \frac{Q_e}{2t \ln(r_b/r_a) + \frac{r_a^2 \ln^2(r_b/r_a)}{\mu V}}. \quad (3.40)$$

From equation 3.40 it can be observed that the shape of the signal has a  $1/(1 + t/\tau)$  shape with the time constant  $\tau$  given by:

$$\tau = \frac{r_a^2 \ln(r_b/r_a)}{2\mu V}. \quad (3.41)$$

For a typical tube of wire radius  $r_a = 25 \mu\text{m}$ , tube diameter  $r_b = 10 \text{ mm}$ , ion mobility  $\mu = 1.5 \text{ cm}^2\text{V}^{-1}\text{s}^{-1}$  and high voltage  $V = 2500 \text{ V}$  one finds a characteristic time of 5 ns.

### 3.4.5 Space charge effects

We have seen that after the avalanche, the electrons are collected on the wire and the ions start to drift from the avalanche region, following a field line, towards the cathode. Due to the very low mobility of the ions with respect to the mobility of the electrons, the ion cloud will be present in the tube long after the avalanche has been measured.

In the following, I will discuss the additional effects of the presence of the ion cloud on the behaviour of the drifttube. The positive ions can contribute to a distorted behaviour of the detector in three ways:

- The positive ions will shield the ground potential with respect to the anode potential close to the wire. This will result in a reduction of the  $E$ -field in the avalanche region and a reduction in gas-gain.
- The positive ions will distort the  $1/r$  electric field and thereby the drift behaviour of the electrons.
- Drifting electrons from later tracks can recombine with the space charge to form stable atoms.

#### 3.4.5.1 Reduction of the gas gain

For a study of the reduction of the electric field close to the wire, due to space charge, a simple model will be introduced. The space charge will be described by an infinitely long cylindrical sheet with charge density  $\lambda_p$ . This sheet of charge is moving away from the anode with velocity  $u$ :

$$u = \mu E, \quad (3.42)$$

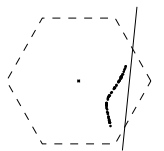
with  $E$  given by equation 3.3. For simplicity, we have assumed the avalanche to be cylindrically symmetric around the wire, which is not necessarily the case. Simulations and measurements have shown that the shape of the avalanche is not cylindrical and the direction distribution of the drifting ions is clearly peaked around the direction of the original electron with an rms width depending on the gas gain [43]. The model also assumes the avalanche to have a finite width  $L$  along the wire, which is typical a few mm, and determines the charge density by:

$$\lambda_p = \frac{Ne}{L}, \quad (3.43)$$

with  $N$  and  $e$  respectively the number of positive ions created in the avalanche and the electron charge. The model will describe the local field distortion on the wire as a function of time after an avalanche and is only valid in case the distance of the space charge from the wire is small with respect to the lateral length of the avalanche  $L$ . The value of  $L$  depends strongly on the angle between the track and the wire. We will assume that  $L$  has a lower limit of 1 mm for perpendicular tracks.

The charge density on the wire due to the high voltage is  $\lambda_L$ . Given the potential difference  $V$  between the anode and cathode and the space charge density, we can compute the electric field by the following set of equations:

$$\begin{aligned} E(r) &= \frac{\lambda_L}{2\pi\epsilon_0} \frac{1}{r}, & r < R, \\ E(r) &= \frac{\lambda_L + \lambda_p}{2\pi\epsilon_0} \frac{1}{r}, & r > R, \end{aligned} \quad (3.44)$$



$$V = \int_{r_a}^{r_b} E(r) dr = \int_{r_a}^{R(T)} \frac{\lambda_L}{2\pi\epsilon_0} \frac{1}{r} dr + \int_{R(T)}^{r_b} \frac{\lambda_L + \lambda_p}{2\pi\epsilon_0} \frac{1}{r} dr,$$

where  $r_a$  and  $r_b$  are the wire and tube radii and  $R(T)$  the position of the ion cloud at time  $T$  after the avalanche has occurred. Assuming that the field disturbance from the space charge is small with respect to the case without space charge, we can use equation 3.3 to describe the electric field and the relation between the position of the ion cloud and time,  $R(T)$ , becomes:

$$R^2 = r_a^2 + \frac{2\mu VT}{\ln(r_b/r_a)}. \quad (3.45)$$

From this equation we learn that for a tube with wire radius  $r_a = 25 \mu\text{m}$ , tube radius  $r_b = 1.0 \text{ cm}$ , high voltage  $V = 2500 \text{ V}$  and a typical ion mobility of  $\mu = 1.5 \text{ cm}^2\text{V}^{-1}\text{s}^{-1}$ , the drift time for ions to reach the cathode becomes  $800 \mu\text{s}$ . This is about 1600 times larger than the typical drift time of the electrons from the cathode to the wire ( $\approx 500 \text{ ns}$ ).

Solving equation 3.45 gives the following values for the  $E$ -field at radii smaller and larger than  $R(T)$ , where, given the model, only the solution for  $r_a < r < R$  and  $R < L$  is meaningful:

$$\begin{aligned} E(r) &= \left[ V - \frac{\lambda_p}{2\pi\epsilon_0} \ln\left(\frac{r_b}{R(T)}\right) \right] \frac{1}{\ln(r_b/r_a)r}, \quad r < R(T), \\ E(r) &= \left[ V + \frac{Q_\lambda}{2\pi\epsilon_0} \ln\left(\frac{R(T)}{r_a}\right) \right] \frac{1}{\ln(r_b/r_a)r}, \quad r > R(T). \end{aligned} \quad (3.46)$$

The above obtained results will be discussed by an example, where the above defined tube will be applied in the ATLAS muon spectrometer. The maximum expected rate will be  $400 \text{ Hz/cm}^2$ , the gas will contain mainly argon and the chamber will be operated at N.T.P. with a gain of  $2 \times 10^5$ . Assuming that all tracks are MIPs and using a total ionisation of  $94/\text{cm}$ , we expect a total of  $3.8 \times 10^7$  ions per track, which is equivalent to  $6.0 \times 10^{-12} \text{ C}$ . We assume the ion cloud to have a width  $L = 5 \text{ mm}$  along the wire, resulting in a charge density  $\lambda_p$  of  $1.2 \times 10^{-11} \text{ C/cm}$ . From equation 3.46 we can see that the field inside the space charge shield can be described by the unperturbed field and a shielding factor of the space charge.

In figure 3.22 the shielding voltage and position of the ion shield are shown versus the time after the avalanche. After  $800 \mu\text{s}$ , the ions have arrived on the cathode and the shielding is reduced to zero. As an example, the average fraction of time that the shielding potential exceeds the value of  $10 \text{ V}$  will be computed in case a tube with  $2 \text{ cm}$  diameter is radiated with  $400 \text{ Hz/cm}^2$ . The shielding voltage is for  $T > 300 \mu\text{s}$  below  $10 \text{ V}$ . With  $400 \text{ Hz/cm}^2$  on a  $2 \text{ cm}$  tube diameter, this means that there will be a hit on the same spot of the wire every  $1/400 \text{ s} = 2500 \mu\text{s}$  (assuming that the width of the ion cloud along the wire is  $5 \text{ mm}$ ). This means that in a substantial fraction of the hits (11 %) there will be a shielding potential that exceeds  $10 \text{ V}$ .

### 3.4.5.2 The drift field

For a study of the impact of space charge on the  $r(t)$  relation, we can only use the described theory in case the space charge is located close to the wire compare with the lateral length of the cloud. Even in this limited region, the shielding voltage as shown in figure 3.22 can only be applied in case the drifting electron is between the wire and the space charge. In order to compute the distortion of the  $E$ -field in the outer regions, we have to use a different approach.

We will assume that the positive charge is created in a continuous process, all along the wire. The wire can be regarded as a source of charge and after some time the amount of charge generated will be equal to the amount of charge being neutralised at the cathode. We will compute

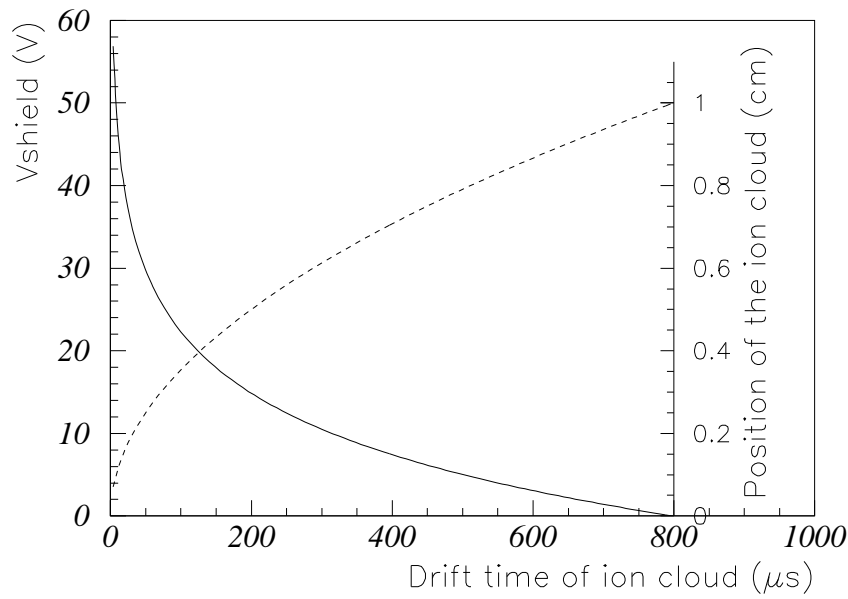


**Figure 3.22:** Effect of space charge on the field near the wire. The reduction of the electric field is presented as a shielding voltage. The position of the ion cloud is also given (right hand scale).

the charge density in this equilibrium and the resulting distortion on the  $E$ -field without space charge. Since the perturbation of the  $E$ -field is (assumed to be) small, the influence of the space charge on the drift velocity of the ions will be neglected. This last condition means that relation 3.45 is still valid.

The charge density will be computed in a numerical example where the same numbers are taken for gas gain, tube geometry and occupancy as in the above calculation. Given the amount of  $6.0 \times 10^{-12}$  C of produced charge per track and an occupancy of 400 Hz/cm<sup>2</sup> on a tube with 2 cm diameter, the strength  $F$  of the ion source located on the wire will be  $4.8 \times 10^{-9}$  Ccm<sup>-1</sup>s<sup>-1</sup>. This number is in agreement with a life time of the wire of 12 years (2400 days equivalent) if we assume a maximum load of 1 C/cm on the wire before deterioration of the gain occurs due to aging.

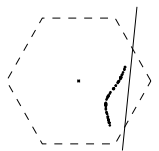
The charge density  $\rho$  can now be computed by using that the charge flow through every arbitrary closed surface around the wire is equal to the source strength  $F$ :

$$\rho(r) = \frac{F \ln(r_b/r_a)}{2\pi\mu V}. \quad (3.47)$$

This result is indeed independent of  $r$ , resulting in a homogeneous charge distribution in a cylindrical geometry. In our example  $\rho$  equals  $1.2 \times 10^{-12}$  C/cm<sup>3</sup>. This result has a more general meaning. One can proof that a constant charge density is the only possible solution of the Maxwell equations in case of a stable charge distribution in time ( $d\rho/dt = 0$ ) and the velocity of the charge is given by equation 3.42. This is of course only valid if the drift field in equation 3.42 is the unperturbed field and thus if the perturbation of the  $E$ -field due to space charge is small with respect to the field without space charge.

The electric field at any position in the tube due to space charge can easily be computed because of the cylinder symmetry of the electrostatic problem:

$$E(r) = \frac{\rho}{2\epsilon_0} \left( r - \frac{r_a^2}{r} \right), \quad (3.48)$$



where the field is directed radially outwards. The strength of the space charge field has a maximum at the cathode ( $r = 1\text{cm}$ ) and yields in our example  $6.7\text{ V/cm}$ . This value is indeed small compared with the field at the position of the cathode without space charge:  $E = 420\text{V/cm}$ . Because the equipotential lines in a hexagonal cell have a shape between a circle and hexagon, the electric field due to space charge in a cell with  $2\text{ cm}$  inner diameter was computed by a computer programme. The field due to space charge showed to have the same maximum value as for the round tube. The electric field due to the high voltage on the anode, however, shows an angular dependency. The field on the cathode has a maximum for  $\theta = 30^\circ$  (where the distance between cathode and wire has a minimum) of  $500\text{ V/cm}$ . For  $\theta = 10^\circ$  the field is still  $360\text{ V/cm}$  and even in the most outer corner of the hexagon for  $\theta = 1^\circ$ , the field on the cathode is far above the field due to space charge:  $150\text{ V/cm}$ . From this exercise it can be concluded that space charge will not be a problem in this specific situation. However, due to the simple model, no hard conclusion can be made and a Monte Carlo approach with a more detailed description of the physical processes in the tube should give more insight in the fraction of spoiled hits in the tube. This study is beyond the scope of this thesis.

### 3.4.5.3 Recombination

Considering the question of recombination we can be very brief. In the above example where the maximum rate in ATLAS is considered, the space charge density will be  $1.0 \times 10^7\text{ ions/cm}^3$ . The total gas density is  $1.3 \times 10^{22}\text{ atoms/cm}^3$ . If one uses the simplified model that recombination occurs in case of a collision of an electron with an ion and never occurs in case of a collision with an atom and one uses an average momentum transfer cross section for argon of  $10^{-16}\text{ cm}^2$ , it can be simply seen that the probability on recombination per cm drift is  $10^{-8}$ . This is far too low to be of any importance.

### 3.4.6 Electrostatic force on the wire

Until now, we have assumed the anode wire to be perfectly aligned with the central axis of the drift tube. Due to gravitational forces and misalignments of anode and cathode during chamber construction, the wire will be off-axis. The amplitude of the wire displacement is amplified by the electric field. It will be shown that this amplification by the electric field can even lead to a situation of electrostatic instability of the position of the wire.

In the following, the wire with length  $L$  will be positioned horizontally and perfectly centred at its end points:  $\Delta(z = 0) = 0, \Delta(z = L) = 0$ , where  $\Delta(z)$  is the displacement of the wire perpendicular to the cell axis and  $z$  is the coordinate along the wire. At each point of the wire, three forces are acting on it: the gravitational, the electrostatic and the restoring force due to the tension of the wire.

If  $T$  is the mechanical tension of the wire, the restoring force per unit length will be:

$$F_T = T \frac{d^2 \Delta}{dz^2}. \quad (3.49)$$

The electrostatic force  $F_E$  will be directed outwards from the tube axis and follows from the change in the capacitance between the tube and the wire by a displacement of the wire. The force per unit length can be found to be [4]:

$$F_E = K \Delta, \quad \text{with} \quad K = 2\pi\epsilon_0 \frac{V^2}{[r_b \ln(r_b/r_a)]^2}, \quad (3.50)$$

Material	Critical tension (kg/mm <sup>2</sup> )	Density (kg/m <sup>3</sup> )	Sag over 100 cm (μm)
W/Au	270	$19.3 \times 10^3$	9.0
Cu/Be HS	114	$8.25 \times 10^3$	9.0
Cu/Be HC	75	$8.62 \times 10^3$	14.4

**Table 3.6:** The critical wire tension  $T_c/\sigma$ , density  $\rho$  and sagitta  $S_g$  for a wire of 100 cm length of different materials.

with  $r_a$  and  $r_b$  the wire and tube radii and  $V$  the high voltage on the wire. The gravitational force  $F_G$  per unit length is simply given by the product of the mass per unit length and the gravitational acceleration constant:

$$F_G = g\rho\sigma, \quad (3.51)$$

where  $g = 9.8 \text{ m/s}^2$ ,  $\rho$  the density and  $\sigma$  the cross section of the wire. In case of equilibrium we can write:

$$T \frac{d^2\Delta}{dz^2} + K\Delta + g\rho\sigma = 0. \quad (3.52)$$

In order to study the effect of gravity alone we solve 3.52 in the special case  $K = 0$ , which can be compared with the situation with the high voltage switched off:

$$\Delta(z) = \frac{1}{2} \frac{g\rho\sigma}{T} (zL - z^2). \quad (3.53)$$

The sagitta of the wire is defined as the maximum displacement which is equal to the displacement at  $z = L/2$ :

$$\Delta(L/2) = S_g = \frac{L^2 g\rho\sigma}{8T}. \quad (3.54)$$

So, the wire sag due to gravity can be reduced by increasing the tension of the wire. But, increasing the tension can only be done up to a critical value with the risk of breaking the wire when increasing the tension further. Unfortunately, the critical tension is also proportional with the wire cross section  $\sigma$ , which means that the sag of the wire is determined by its total length, the critical tension and its density. In table 3.6 the critical tension ( $T_c/\sigma$ ), density ( $\rho$ ) and wire sag ( $S_g$ ) for a wire with  $L = 100 \text{ cm}$  are given.

Including the electrostatic force in equation 3.52 gives the following solution:

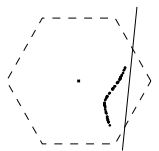
$$\Delta(z) = \frac{8S_g T}{L^2 K} \left( \frac{\cos[\sqrt{K/T}(z - L/2)]}{\cos[\sqrt{K/TL}/2]} - 1 \right), \quad (3.55)$$

where the displacement of the wire is expressed in terms of  $S_g$ . By analogy with equation 3.54 the sagitta of the wire under the combined effect of electrostatic and gravitational forces is:

$$S = \Delta(L/2) = S_g \frac{8T}{L^2 K} \left( \frac{1}{\cos[\sqrt{K/TL}/2]} - 1 \right). \quad (3.56)$$

This result can be evaluated for two limits. In the limit of a small value of  $\sqrt{K/TL}/2$  equation 3.56 becomes:

$$S = S_g \frac{1}{1 - KL^2/8T}, \quad (3.57)$$



where the second term clearly denotes an amplification term of the gravitational sag due to the electrostatic force. Another limit is the critical limit. Here the value of  $\sqrt{K/TL}/2$  approaches the value of  $\pi/2$  which means that  $S$  becomes infinite. This critical limit can be written down as a fundamental relationship which has to hold (with a safety margin) for all drift tube designs. The dimensionless expression of Ahlen gives good insight in the relation between the critical situation and the fundamental tube parameters [44]:

$$V < 3611 \sqrt{\frac{T}{300}} \frac{r_b}{2L} \ln(r_b/r_a), \quad (3.58)$$

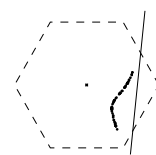
with  $V$  in Volt, the tension on the wire  $T$  in gram, the tube radius  $r_b$  in cm and the length of the wire  $L$  in metre. According to this equation, the critical voltage for the above discussed ATLAS tube of 6 metre length with one additional spacer in the centre and a W/Au wire at 80 % of its critical tension is 17 kV.

## References

- [1] H. van der Graaf *et al.*, The honeycomb strip chamber: the application in LHC/SSC experiments and the test results of a prototype, Nucl. Instr. & Methods **A307** (1991) 220.
- [2] G. Charpak, R. Bouclier, T. Bressani, J. Favier and Č. Zupančič, Nucl. Instr. & Methods, **62** (1968) 262.
- [3] T. Bressani, G. Charpak, D. Rahm and Č. Zupančič, Track localization by means of a drift chamber, Proc. Dubna Meeting *Filmless and streamer chambers*, April 1969.
- [4] W. Blum and L. Rolandi, Particle detection with drift chambers, Accelerator Physics, Springer-Verlag, 1993, ISBN 3-540-56425-X.
- [5] The ATLAS collaboration, ATLAS Technical Proposal, CERN/LHCC/94-43, LHCC/P2, 15 December 1994.
- [6] F. Bakker *et al.*, The construction and performance of single-layer honeycomb strip chambers in the TRACAL detector of RD5, Nucl. Instr. & Methods **A330** (1993) 40.
- [7] R. Bergman, Thesis on the TRACAL detector in RD5, Title to be announced, University of Nijmegen, PhD Thesis, 1996, Nijmegen.
- [8] P. Duinker *et al.*, Some methods and tools for testing and optimizing proportional wire chambers, Nucl. Instr. & Methods **A273** (1988) 814–819.
- [9] R. Bock *et al.*, Wire fixation for proportional and drift chambers using a Cu-Te alloy, Nucl. Instr. & Methods **A336** (1993) 128, I. Physikalisches Institut, Rheinisch-Westfälische Technische Hochschule, Aachen, Germany.
- [10] V.A. Chechin, L.P. Kotenko, G.I. Merson, V.C. Yermilova, The relativistic rise of the track density in bubble chambers, Nucl. Instr. & Methods, **98** (1972) 577–587.
- [11] J.D. Jackson, Classical Electrodynamics, John Wiley & sons, Second Edition, 1975, ISBN 0-471-43132-X.
- [12] W.W.M. Allison and J.H. Cobb, Relativistic charged particle identification by energy loss, Ann. Rev. Nucl. Sci. **30** (1980) 253.
- [13] U. Fano, Ann. Rev. Nucl. Sci., **13** (1963) 1.
- [14] J.H. Cobb, W.W.M. Allison and J.N. Bunch, The ionisation loss of relativistic charged particles in thin gas samples and its use for particle identification; Theoretical predictions, Nucl. Instr. & Methods, **133** (1976) 315–323.
- [15] L. Landau, J. Phys. (USSR) **8** (1944) 201.
- [16] F. Harris *et al.*, Nucl. Instr. & Methods, **107** (1973) 413.
- [17] J.H. Cobb, D. Phil. thesis (Univ. of Oxford, 1975). Available from Rutherford as HEP/T/55.
- [18] O. Blunck and S. Leisegang, Z. Physik **128** (1950) 500.
- [19] K.A. Ispirian, A.T. Margarian and A.M. Zverev, A monte-carlo method for calculation of the distribution of ionization losses, Nucl. Instr. & Methods **117** (1974) 125–129.
- [20] V.C. Ermilova, L.P. Kotenko and G.I. Merzon, Fluctuations and the most probable value of relativistic charged particle energy loss in thin gas layers, Nucl. Instr. & Methods, **145** (1977) 555–563.
- [21] F. Lapique and F. Piuz, Simulation of the measurement by primary cluster counting of the energy lost by a relativistic ionizing particle in argon, Nucl. Instr. & Methods, **175** (1980) 297–318.
- [22] Hansjörg Fischle, Joachim Heintze and Bernard Schmidt, Experimental determination of ionization cluster size distributions in counting gases, Nucl. Instr. & Methods, **A301** (1991) 202–214.
- [23] E.J. Kobetich and R. Katz, Energy deposition by



- electron beams and delta rays, *Phys. Rev.* **170** (1968) 391.
- [24] F. Sauli, Principles of operating of MultiWire Proportional and Drift Chambers, CERN 77-09, 1977.
- [25] V. Palladino and B. Sadoulet, Application of classical theory of electrons in gases to drift proportional chambers, *Nucl. Instr. & Methods* **128** (1975) 323–335.
- [26] E.B. Wagner, F.J. Davies and G.S. Hurst, Time-of-flight investigations of electron transport in some atomic and molecular gases, *J. Chem. Phys.* **47** (1967) 3138.
- [27] M. Huk, P. Igo-Kemenes and A. Wagner, Electron attachment to oxygen, water and methanol, in various drift chamber gas mixtures, *Nucl. Instr. & Methods* **A267** (1988) 107–119.
- [28] S. Biagi, MAGBOLTZ source code, CERN, obtained by private communication, Biagi@cernvm.cern.ch for information.
- [29] L.C. Pitchford, S.V. O'Neil and J.R. Rumble Jr., Extended Boltzmann analysis of electron swarm experiments, *Phys. Rev. A* **23-1** (1981) 294–304.
- [30] S.F. Biagi, Accurate solution of the Boltzmann transport equation, *Nucl. Instr. & Methods* **A273** (1988) 533–535.
- [31] S.F. Biagi, A multiterm Boltzmann analysis of drift velocity, diffusion, gain and magnetic-field effects in argon-methane-water-vapour mixtures, *Nucl. Instr. & Methods* **A283** (1989) 716–722.
- [32] K.F. Ness, Multi-term solution of the Boltzmann equation for electron swarms in crossed electric and magnetic fields, *J. Phys. D: Appl. Phys.* **27** (1994) 1848–1861.
- [33] G. Battistoni *et al.*, Influence of gas mixture and cathode material on limited streamer operation, *Nucl. Instr. & Methods* **217** (1983) 433–439.
- [34] W. Diethorn, A methane proportional counter system for natural radiocarbon measurements, US-AEC report (1956) NY06628, Also doctoral dissertation, Carnegie Inst. of technology (1956).
- [35] J.C. Armitage, S.P. Beingsner, R.K. Carnegie, E.F. Ritchie and J. Waterhouse, A study of the effect of methane and carbon dioxide concentration on gas amplification in argon based gas mixtures, *Nucl. Instr. & Methods* **A271** (1988) 588–596.
- [36] J. Grog, E. Schenuit and H. Spitzer, Computer simulation of the electron avalanche in cylindrically symmetric electric fields, *Nucl. Instr. & Methods* **A283** (1989) 730–734.
- [37] M. Matoba, T. Hirose, T. Sakae, H. Kametani, H. Ijiri and T. Shintake, Three dimensional Monte Carlo simulation of the electron avalanche around an anode wire of a proportional counter, *IEEE Transactions on Nuclear Science* **NS-32 1** (1985) 541–544.
- [38] R. Bellazzini and M.A. Spezziga, Electric field, avalanche growth and signal development in Micro-Strip Gas Chamber and Micro-Gap Chamber, INFN internal note INFN PI/AE 94/02, INFN-Pisa and University of Pisa, June 1994, Paper submitted for publication in *La Rivista del Nuovo Cimento*.
- [39] S.C. Curran, A.L. Cockroft and J. Angus, *Phil. Mag.* **40** (1949) 929.
- [40] J. Byrne, *Proc. Roy. Soc. Edinburgh* **A66** (1962) 33.
- [41] A. Lansart and J.P. Morucci, *J. Phys. Radium* **23** (1962) 102A, suppl. no 6.
- [42] G.D. Alkhazov, Statistics of electron avalanches and ultimate resolution of proportional counters, *Nucl. Instr. & Methods* **89** (1970) 155–165.
- [43] H. van der Graaf, Signal development and processing in Multi Wire Proportional Chambers, University of Technology, PhD Thesis, 19 June 1986, Delft.
- [44] S. Ahlen, A. Marin and B. Zhou, Basic information relating to Use of PDT's: specification for wire/wall a-concentricity, PDT/BU Memo no. 2, February 1992, SSC-note.





# Chapter 4

## Simulation methods of the HSC wire and strip readout

### Contents

---

<b>4.1</b>	<b>Introduction</b>	<b>63</b>
<b>4.2</b>	<b>The gas properties: MAGBOLTZ</b>	<b>64</b>
<b>4.3</b>	<b>Detailed drift cell simulation: GARFIELD</b>	<b>66</b>
<b>4.4</b>	<b>Front-end electronics simulation</b>	<b>66</b>
4.4.1	The input	67
4.4.2	The wire	67
4.4.3	Noise	68
4.4.4	The amplifier	68
4.4.5	The shaper	69
4.4.6	The discriminator	69
4.4.7	The TDC	69
4.4.8	Some results	69
<b>4.5</b>	<b>Simulation of the strip response of the HSC</b>	<b>71</b>
4.5.1	Determination of the second coordinate $x$ from $Q_L/Q_M$ and $Q_R/Q_M$	73

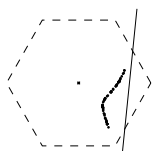
---

### 4.1 Introduction

**I**n this chapter we will describe the software tools used for simulating the behaviour of the HSC. The main emphasis will be on a detailed description and simulation of the creation of the signal on the anode wire and processing of this signal by the front-end electronics. Those tools were developed for helping to interpret the measured characteristics of the various prototypes (see chapter 6). In figure 4.1 the various modules with their input and output data flows are schematically shown.

A global overview will be given of the MAGBOLTZ [1] and GARFIELD [2] packages as well as a detailed description of the simulation of the front-end electronics.

A brief overview will be given of the signal development on the strips. No detailed study or optimisation of the cathode strip readout of the HSC is performed in this thesis. The process of signal creation and analysis is performed according to the algorithm described in [3, 4].



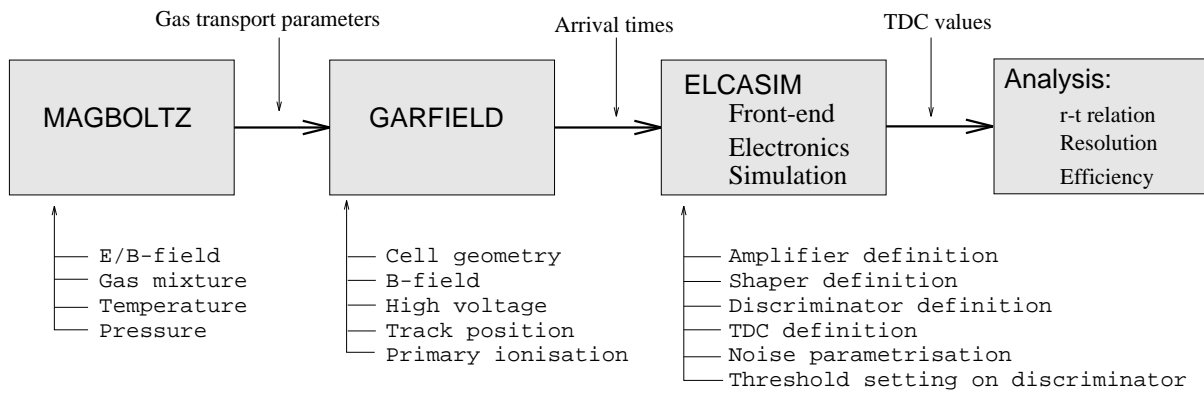


**Figure 4.1:** Block diagram of the software tools used in the simulation of the wire response of a proportional drift tube.

## 4.2 The gas properties: MAGBOLTZ

The MAGBOLTZ programme was written by Biagi and computes for a large variety of gases, and mixtures of gases, the gas transport parameters [1]. The programme is based on the numerical solution of the Boltzmann transport equation. In table 4.1 the main input and output parameters and the set of known gases are summarised. The result of the calculation of the drift

Input parameters	Output parameters	Gases
E-field	Drift velocity	Ar, CH <sub>4</sub> , N <sub>2</sub> ,
B-field	Longitudinal diffusion	H <sub>2</sub> O, CO <sub>2</sub> , <sup>3</sup> He,
Angle between E and B	Transverse diffusion	<sup>4</sup> He, Xe, Ne,
Gas-components	Lorentz angle	C <sub>2</sub> H <sub>6</sub> , i-C <sub>4</sub> H <sub>10</sub> , CH <sub>3</sub> OH,
Gas component fractions	Attachment coefficient	C <sub>3</sub> H <sub>8</sub> , C <sub>5</sub> H <sub>12</sub> , Kr,
Temperature	Townsend coefficient	CF <sub>4</sub> , O <sub>2</sub> , DME,
Pressure		C <sub>2</sub> H <sub>4</sub> , C <sub>2</sub> H <sub>2</sub>
Cut off for electron velocity		

**Table 4.1:** Input and output parameters and a list of available input gases of the MAGBOLTZ programme.

velocity, diffusion and Lorentz angle are in general better than five percent, but depend on the accuracy of the cross section data of the specific gas. The attachment and Townsend coefficients have to be used as crude indications and not to be taken too literally. Especially the value of the attachment coefficient is subject to large uncertainties due to the large impact of trace elements of polluting gas components on the attachment.

In figure 4.2 the predictions of MAGBOLTZ are shown for four gases. The results represent the drift parameters for  $B = 1.0$  T,  $T = 20$  °C and  $p = 1$  atm. The range of the electric field in a drifttube is from 400 V/cm at the cathode up to approximately  $2 \times 10^5$  V/cm at the wire.

Since the field in the tube is in general below  $5 \times 10^3$  V/cm, we can state from the drift velocity plot that the Ar/CO<sub>2</sub> 50/50 mixture will show the slowest drift properties and the Ar/CO<sub>2</sub>/CF<sub>4</sub> 68/17/15 will be a so called 'fast gas' (small drift times).

Both the longitudinal ( $D_L$ ) and transverse diffusion ( $D_T$ ) are plotted. The terms 'longitudinal' and 'transverse' are related to the direction of drift of the electron. Only the diffusion perpendicular to isochrones will contribute to the spatial resolution. In case the Lorentz angle is zero, the

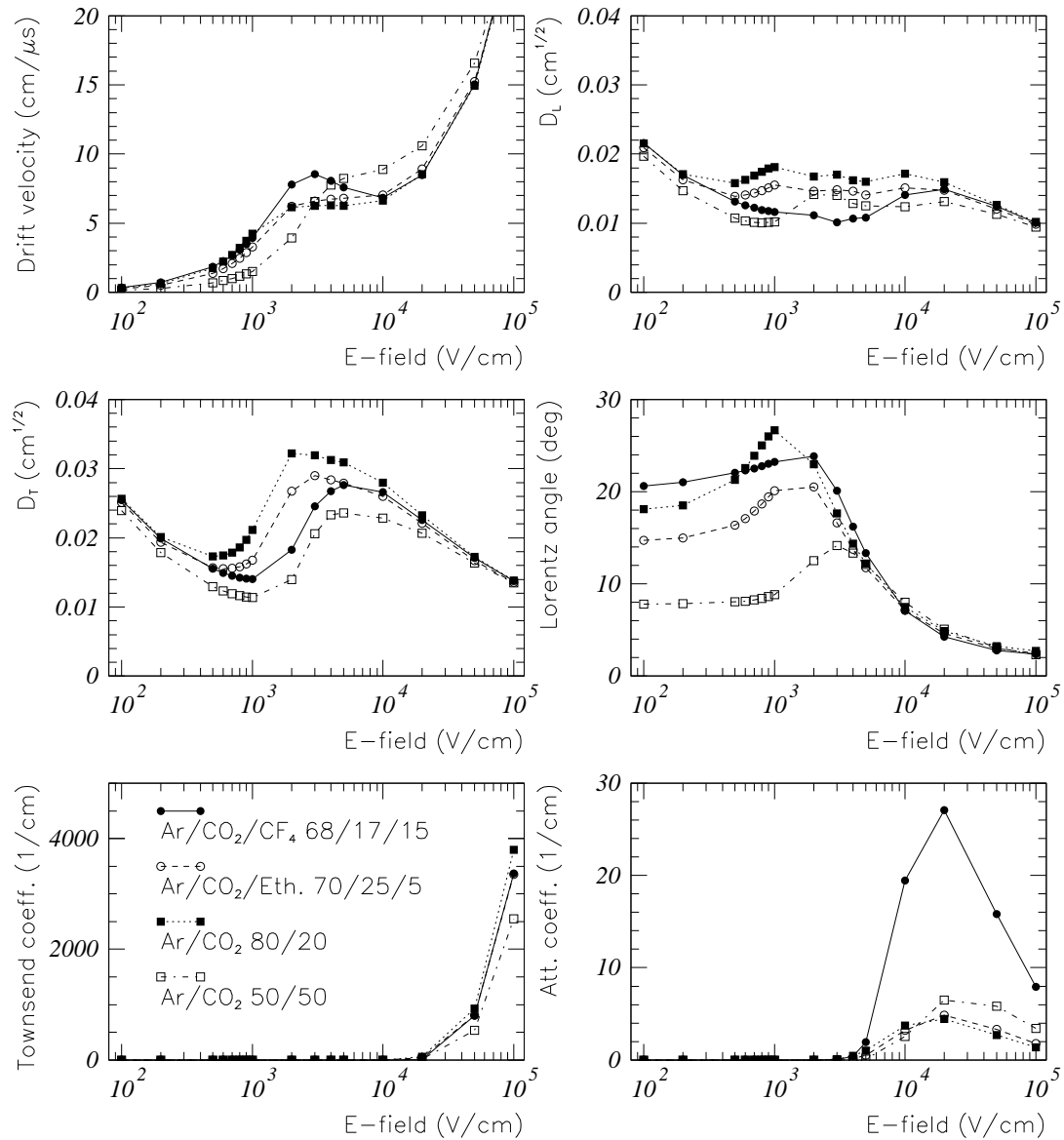
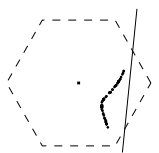


**Figure 4.2:** MAGBOLTZ output for four commonly used gases during testbeam experiments with the HSC prototypes.

longitudinal diffusion will dominate over the transverse diffusion. In case of a non-zero Lorentz angle, the diffusion perpendicular to the isochrones will be a vector sum of the longitudinal and transverse diffusions.

The Lorentz angle curves show that a slow gas like Ar/CO<sub>2</sub> 50/50 has a smaller Lorentz angle than faster gases.

Since the Townsend coefficient is low for gases containing a large percentage of CO<sub>2</sub>, the high voltage on the wire will be high compared with gases containing a small fraction of CO<sub>2</sub>. Further, it is interesting to see that the drift-velocity, diffusion and Lorentz angle have a tendency to converge for large values of the electric field. Also the very high attachment coefficient of CF<sub>4</sub>



based gases is clearly visible.

### 4.3 Detailed drift cell simulation: GARFIELD

GARFIELD is a drift chamber simulation programme written by Veenhof [2]. The programme was originally set up to simulate large conventional drift chambers with many wires. The author has added the cylindrical tube geometry and all sorts of polygonal tube geometries with the wire parallel to the tube, but not necessary centred at the tube axis.

The programme starts with computing the electric field in the tube for the given tube geometry, wire position, wire thickness and high voltage on the wire. The drift parameters are read in as function of  $E/p$  and are computed using MAGBOLTZ. One can also compute drift parameters for commonly used gases with GARFIELD, but with a dedicated programme like MAGBOLTZ one can achieve a much better accuracy. At this stage one can define to what detail one likes to simulate the drift behaviour of the electrons (or ions) in the drift tube. A simple  $r(t)$  (distance to the wire versus time) relation can be calculated and the integrated diffusion over the drift path can be computed. More advanced simulation requires the cluster input data (e.g. from [5]). The arrival time distributions of the first, second, ..., last electron can be obtained by a Monte Carlo approach. Actually, an interpolation table is made which connects the position of the primary ionisation on the track with the arrival time. The width of the electron cloud is evaluated over the 'ideal' drift path. The Monte Carlo programme is in this case just a random generation of cluster position and size and generating random time uncertainties from the integrated diffusion.

In case of an additional magnetic field and a non-zero Lorentz angle at the position of the primary ionisation and avalanche region, the simulation of the diffusion contribution due to the longitudinal and transverse width of the electron cloud is not so straightforward, especially close to the wire, where the cloud becomes very asymmetric in the inhomogeneous electric field. Therefore I have checked the GARFIELD results with a real Monte Carlo programme, which is an extension to the GARFIELD programme and actually tracks all electrons from its point of creation to the wire, applying the longitudinal and transverse diffusion locally. All results presented in this thesis, which are based on GARFIELD calculations, will use this level of detail. Finally, by taking the first Townsend coefficient into account one can calculate the shape of the signal at the pre-amplifier. I have not used this part of GARFIELD and have used the arrival times of individual electrons in a dedicated gas-gain and front-end simulation programme.

### 4.4 Front-end electronics simulation

The front-end simulation package (ELCASIM) was written by myself with input from Rewiersma (NIKHEF). The programme starts with the creation of the signal on the wire, taking Curran fluctuations into account (see section 3.4.3.3). The current signal is then transported over the wire (attenuation) to the pre-amplifier, shaper and discriminator, and finally digitised in the TDC.

After analysing typically 1000 tracks at various distances of the wire, one can reconstruct the  $r(t)$  relation, fit the spatial resolution and derive the inefficiency of the tube. In addition one can trigger on the trailing edge of the pre-amplifier output. The last trailing edge can be assigned to the last arriving electron on the wire. This electron will be produced close to the cathode and the drift time will be constant and equal to the maximum drift time. This measurement delivers a method to identify the bunch crossing to which the hit belonged.

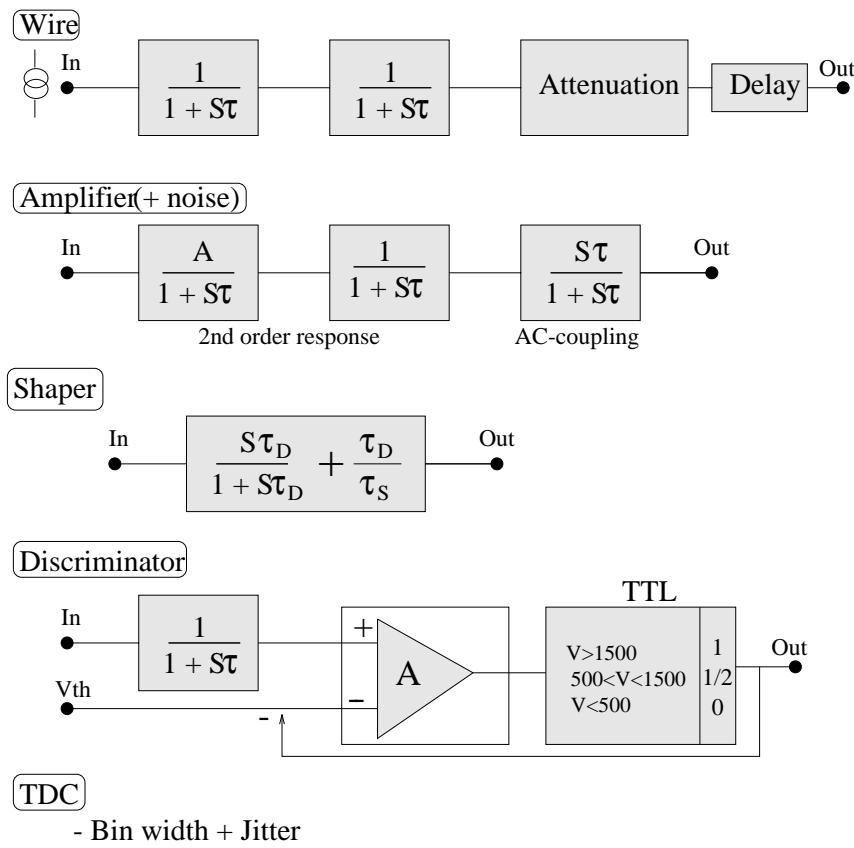


**Figure 4.3:** Schematic description of the electronic response of the components in the front end simulation ELCASIM. The simulation starts with feeding the current signal in the wire response functions (top) and finally a leading or trailing edge TDC value is returned.

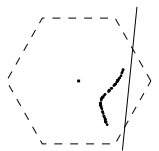
In figure 4.3 a schematic overview is shown of the simulation model. The behaviour of all electronic components is described by transfer functions in the frequency domain  $S$  indicated in the boxes. The shaper was pole-zero cancelling (PZC). This is a differentiator with a proportional feedback of the output of the shaper on the input of the shaper. All calculations are done in the time domain with a fixed bin width of 0.1 ns. All individual subsystems will be described.

#### 4.4.1 The input

The programme needs the arrival times of individual electrons from one track through the cell. Those arrival times are computed by the drift cell simulation programme GARFIELD. In order to create the signal from one electron one has to define the E-field and ion mobility. The total current signal on the wire is then computed by a superposition of all individual contributions of all electrons multiplied with the gas gain and Curran fluctuation.

#### 4.4.2 The wire

The dominant effect in the wire is the attenuation and delay which are a function of the position of the creation of the signal along the wire. Also some dispersion will occur, which can be described by two simple integrators. The integrator can be described by a very simple transfer function in the frequency domain:  $1/(1 + S\tau)$ . The time constant  $\tau$  is typical less than 0.1 ns and a function of the position of the avalanche along the wire.



	Input parameters	Default value
Wire	Wire radius	25 $\mu\text{m}$
	Tube radius	1.0 cm
	High voltage on wire	2500 V
	Ion mobility	0.2 $\mu\text{m}^2/(\text{ns V})$
	Gas gain	50000
	Position along wire	0 m
	Dispersion	0 ns/m
Noise	Equivalent input noise	40 nA
Amplifier	Rise time	5.0 ns
	AC-coupling time	1000.0 ns
	Gain	25 mV/ $\mu\text{A}$
Shaper (pole-0)	Differentiator time	5.0 ns
	Proportionality factor	0.5
Discriminator	Rise time	1.0 ns
	Gain	400
	Threshold	20.0 mV
	Hysteresis	2.0 mV
TDC	Bin width	1.0 ns
	Bin accuracy	0.2 ns

**Table 4.2:** Parameters to tune the front end electronics response.

In table 4.2 the parameters to define the wire response have been summarised.

### 4.4.3 Noise

The white noise of an amplifier is normally defined in terms of Equivalent Input Noise (EIN). This is the hypothetic rms value of the current at the input of the amplifier with an infinite bandwidth in case of output noise with an rms of  $A \times \text{EIN}$ , where  $A$  is the gain of the amplifier in volt/ampere. Since the bandwidth of the amplifier is limited (given by the rise time), the simulated input noise is larger than the EIN and can be calculated taking the rise time into account. The white noise is superimposed on the signal (in bins of 0.1 ns) by generating random current values from a Gaussian distribution.

### 4.4.4 The amplifier

The amplifier is AC-coupled and consists of a second order integrator with gain  $A$ , and a differentiating circuit with a long RC time (typically 1  $\mu\text{s}$ ). For a good timing of the first electron it is important to have a fast rise time ( $< 10$  ns) and high enough gain to discriminate the signal as fast as possible above a fixed threshold. With the tunable parameters in table 4.2 one can study the dependencies of the resolution and efficiency on those parameters.



#### 4.4.5 The shaper

The shaper as applied in the pre-amplifier of drift tubes is mainly there to cut off most of the tail of the signal. The time constant  $\tau_s$  of this tail at the output of the amplifier is dominated by the current signal on the wire and thus by the ion mobility and drift field in the tube (see section 3.4.4).

The length of the tail is reduced by differentiating the signal with a time constant  $\tau_D$ . This operation on the signal will indeed reduce the length of the tail, but will also produce an undershoot of the signal. This undershoot is caused by the differentiation operation on a decaying signal. In order to compensate for the undershoot and to minimise pile up in a high occupancy environment, a fraction of the signal after the differentiation is fed back to the input of the shaper. This scheme of shaping (tail cancellation and undershoot compensation by proportional feedback) is called pole-zero cancellation (PZC). The fraction of the signal that is fed back to the input is given in first order by the time constants  $\tau_s$  and  $\tau_D$ :  $fr = \tau_D/\tau_s$ , where  $fr$  is a number between zero and one.

This scheme has an optimum for signals with a tail of exponential form:  $\exp(-t/\tau_s)$ . As mentioned in section 3.4.4 the tail is of the form  $1/(1+t/\tau)$ , for which the PZC is less effective, nevertheless, the best scheme available. PZC is done to achieve a good trailing edge timing. If only the leading edge is recorded, no shaping is required and no amplitude of the signal is lost.

#### 4.4.6 The discriminator

The discriminator in this simulation is a first order integrator with a very short rise time ( $< 1$  ns) and high gain ( $\approx 400$ ). The signal from the amplifier is compared with a threshold and converted to a TTL logic signal. Some negative hysteresis of the output to the threshold is added to assure a stable output signal.

#### 4.4.7 The TDC

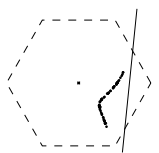
The TDC discriminates the TTL signal and digitises it in TDC counts. The bin-width can be varied and some jitter on the border between two bins can be added. Out of the simulation come the TDC counts for all leading and trailing edges for one track.

#### 4.4.8 Some results

In figure 4.4 the response to a single electron avalanche ( $G = 10^5$ ) is shown in the various stages of the simulation process. The simulation is performed with realistic settings for the ion drift process: HV=2475 V, wire diameter=50  $\mu\text{m}$ , tube diameter=2.0 cm and the ion mobility=0.2  $\mu\text{m}^2/(\text{nsV})$ .

One can observe that the signal on the wire from an avalanche with  $10^5$  electrons is still very small ( $< 0.5\mu\text{A}$ ), which results in a signal of 4 mV after a typical pre-amplifier with a gain of 25 mV/ $\mu\text{A}$  and a rise time of 5 ns. The shaper performs a good tail cancellation, but the price is a loss of pulse height. This will be more obvious when the total signal of a minimum ionising track will be studied. Due to the low signal from one electron, no threshold is crossed in the discriminator and the logic out (TTL) remains zero.

A simulation of the front end response is performed for a realistic test setup. The above mentioned tube is filled with an Ar/CO<sub>2</sub>/C<sub>2</sub>H<sub>6</sub> mixture (70/25/5). Using GARFIELD, the individual



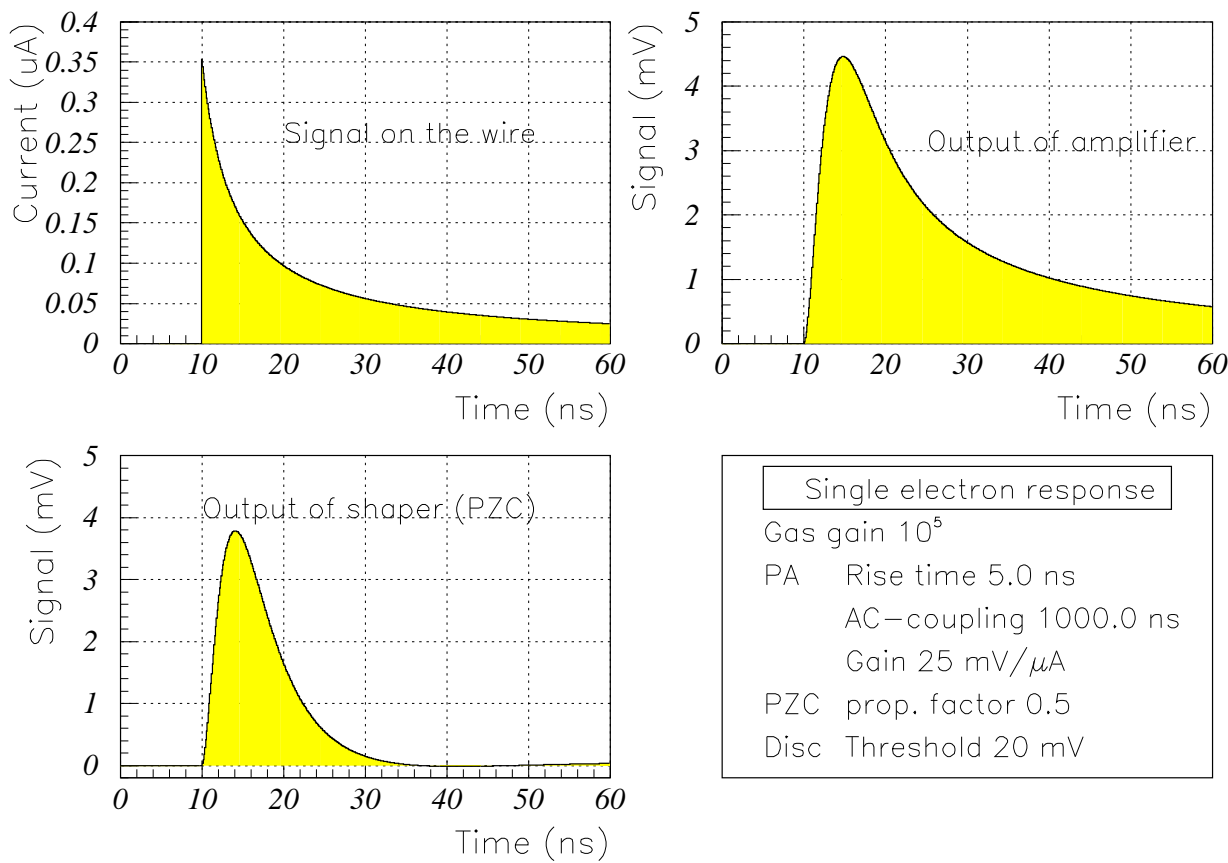


**Figure 4.4:** Signal shapes in the various steps of the electronic processing. The current signal on the wire and resulting output signals are shown for the detection of a single electron, resulting in an avalanche of  $10^5$  ionisations.

arrival times of all created electrons are computed for a track passing through the tube at 5 mm from the wire. After applying the Curran fluctuations on the gas gain, all individual signals on the wire are superimposed.

In figure 4.5 the various stages of the simulation are shown for a track. The signal on the wire (before adding the white noise) reflects the drift time of the first electron ( $\approx 100$  ns) and the last electron ( $\approx 650$  ns).

The shaping reduces the amplitude of the signal significantly and the threshold has to be lowered or the total signal increased to perform a proper trailing edge measurement. The detection of the trailing edge of the signal will offer a method to compute the arrival time of the last electron on the wire. This electron will be created very close to the cathode, independent of the distance between the track and the wire. The time interval between the arrival time and the moment of passage of the muon will be constant and primary ionisation statistics and diffusion will dominate the fluctuations on this time interval. Thus, trailing edge detection offers a method to measure the time of passage of the particle and thus the bunch to which it belonged. In order to have a good trailing edge determination of the signal, the threshold crossing should be as fast as possible and a strong tail cancellation should be performed. In our example in figure 4.5, the trailing edge cancellation was too strong and no threshold crossing was detected at 650 ns.

In case no bunch cross identification by a trailing edge determination is needed, a minimum of shaping should be performed. In a high occupancy environment where successive hits on the wire can show pile up due to the long tail, shaping will be applied to reduce this effect.

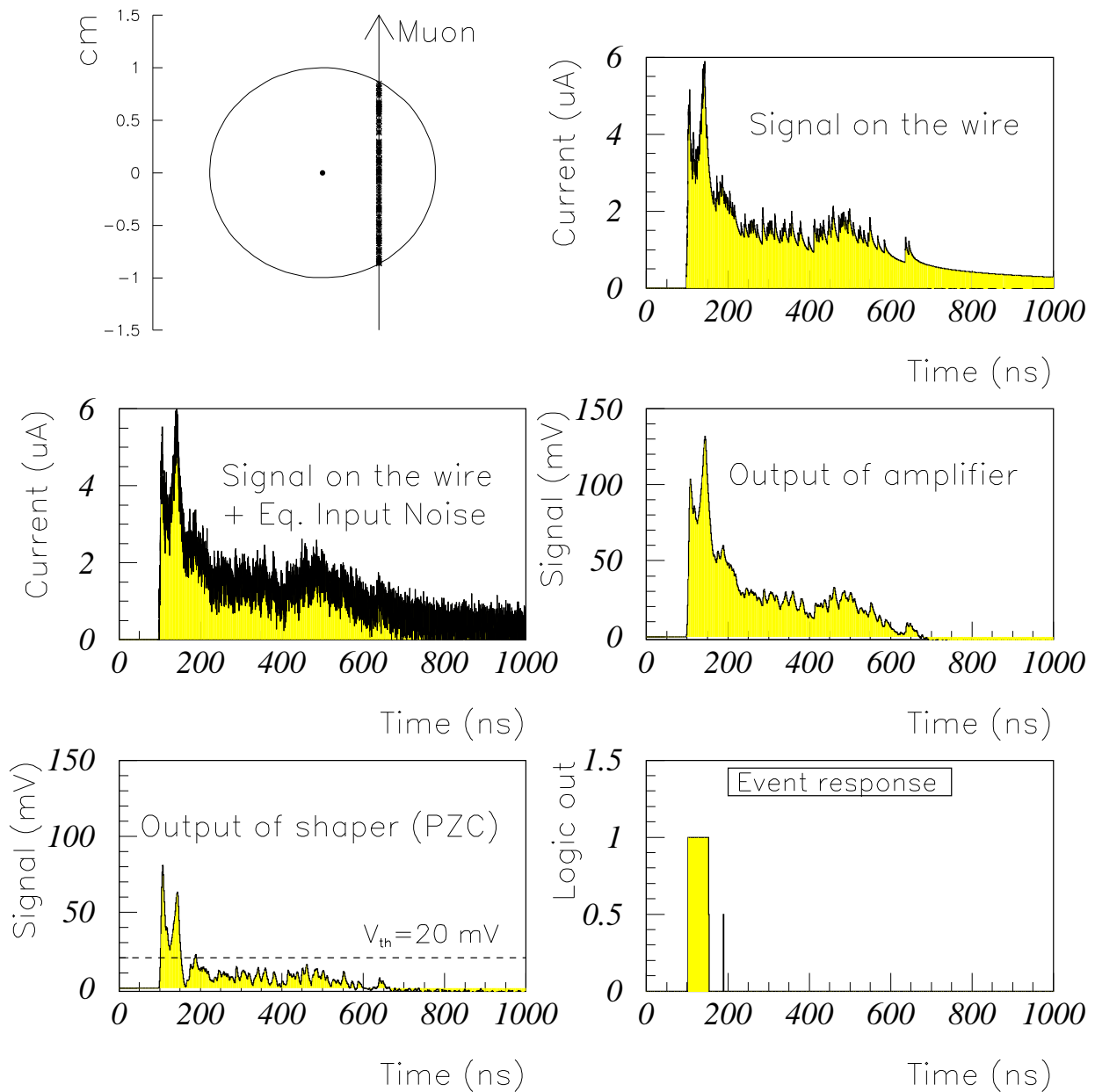
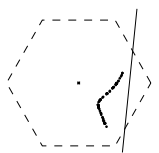


**Figure 4.5:** Current and voltage signals on the wire and after the various steps in the electronic processing. Due to the strong tail cancellation in the shaper, the maximum amplitude of the signal will only amount to 80 mV after shaping.

In the last plot of figure 4.5 the logic signal is shown that is fed in the TDC. A leading edge is (correctly) detected at  $t = 100$  ns and the first trailing edge is detected far too early at  $t = 150$  ns. At  $t = 190$  ns a logic value of  $\frac{1}{2}$  was fed in the TDC and it depends on the type of TDC if this small spike in the logic signal will be detected or not. Unfortunately, the shaping was too strong or the signal too low to detect the arrival time of the last electron at  $t = 650$  ns.

## 4.5 Simulation of the strip response of the HSC

The coordinate along the wire can be measured by cathode strips, perpendicular to the wires on the cathode foil. The distribution of the induced charge on the cathode strips is equal to the distri-



bution of the induced charge on a continuous conductor. The gap between the strips is neglected and the charge on each individual strip is computed by integrating the charge on the area of the continuous cathode which is covered by the strip.

The position of an ionising particle can be derived from the measured charges on three adjacent strips. The segmented strip readout can deliver the longitudinal coordinate along the wire with a precision of less than 50  $\mu\text{m}$  (rms) [6]. This coordinate is often called the 'second coordinate'. In order to achieve this precision with a strip pitch of 100 times this value, it is not sufficient to compute a weighted average of the position of three adjacent strips, but one has to take the charge distribution over the strips into account [7, 8].

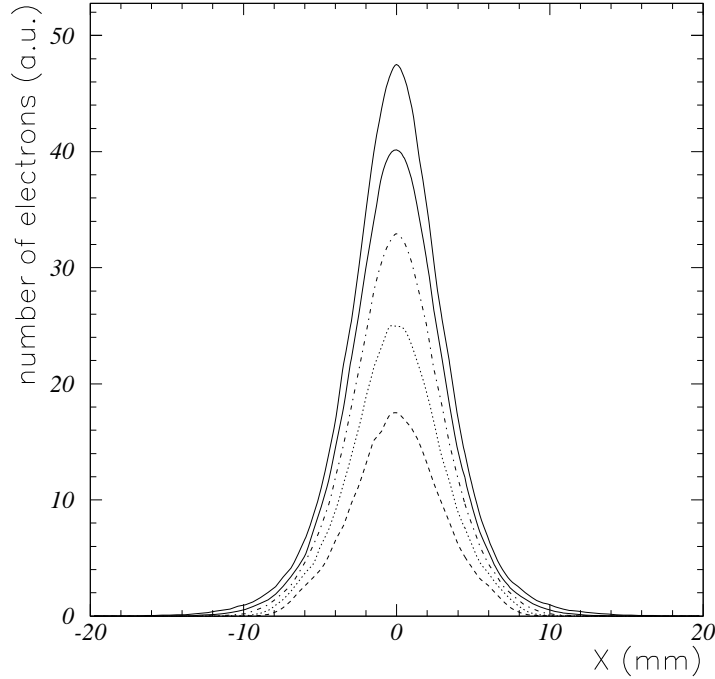


**Figure 4.6:** The density of electrons on the cylindrical cathode of a counting tube as a function of  $x$  (direction along the wire). The curves show the distribution for different positions of the ion cloud:  $R_{\text{cloud}} = 50$  (inner curve), 100, 200, 400 and 800  $\mu\text{m}$  (outer curve) [3].

In figure 4.6 the charge distribution is shown on a cylindrical cathode for various positions of the ion cloud. The charge distribution is calculated using a multi-particle approach described in [3, 9].

The normalised charge distribution  $\Gamma(\lambda)$  is often described by the empirical single parameter expression of Gatty and Mathieson [10, 11]:

$$\Gamma(\lambda) = K_1 \frac{1 - \tanh^2(K_2 \lambda)}{1 + K_3 \tanh^2(K_2 \lambda)}, \quad (4.1)$$

where

$$\lambda = x/R, \quad (4.2)$$

$$K_1 = \frac{K_2 \sqrt{K_3}}{2 \arctan(\sqrt{K_3})}, \quad (4.3)$$

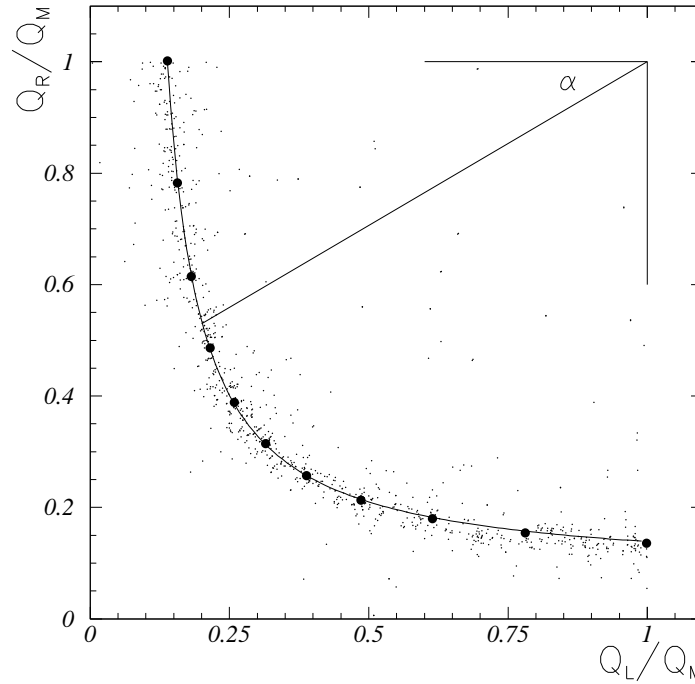
$$K_2 = \frac{\pi}{2} \left( 1 - \frac{1}{2} \sqrt{K_3} \right). \quad (4.4)$$

Here  $R$  is the radius of the tube and  $K_3$  the single parameter which has to be fitted to the numerically found charge distribution and  $x$  is the coordinate along the wire. For the P1 and P2 HSC prototypes with an inner tube radius of 5 mm and a strip pitch of 5 mm, the parameter  $K_3$  is 0.01969.

Equation 4.1 is used with this parameter to simulate the basic charge distribution over the strips for a point charge at  $x = 0$ . The total charge on the strips is a summation of all individual charges induced by the avalanches of all primary electrons. In the simulation of the charge distribution over the strips, the Poisson distribution of the primary clusters along  $x$ , Curran fluctuations, diffusion and pre-amplifier noise are taken into account.

#### 4.5.1 Determination of the second coordinate $x$ from $Q_L/Q_M$ and $Q_R/Q_M$

The charges on three adjacent strips are called Q-left ( $Q_L$ ), Q-middle ( $Q_M$ ) and Q-right ( $Q_R$ ). In



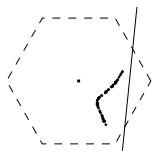
**Figure 4.7:** The ratio  $Q_R/Q_M$  plotted versus  $Q_L/Q_M$ . The  $x$  coordinate of the track is a function of the angle  $\alpha$ . The solid curve is a fit through the thick points for  $x = -2.5$  to  $x = +2.5$  mm in steps of 0.5 mm which have been calculated using the multi-particle method. The dots are from real events measured with the P1 prototype [3].

figure 4.7 the ratio  $Q_R/Q_M$  is plotted versus the ratio  $Q_L/Q_M$ , both for the calculation and test beam data with perpendicular tracks. The  $x$  coordinate of a track is a function of the position of the points along the drawn curve. The curve can be approximated by a function via the angle  $\alpha$ , shown in figure 4.7,

$$\alpha(x) = \arctan \left[ \left( 1 - \frac{Q_L}{Q_M} \right) / \left( 1 - \frac{Q_R}{Q_M} \right) \right]. \quad (4.5)$$

The  $x$ -coordinate is fitted with respect to  $\alpha$  with the following two parameter function,

$$x = A \arctan \left[ B \left( \alpha - \frac{1}{4}\pi \right) \right]. \quad (4.6)$$



From the fit we found that  $A = 2.4065$  and  $B = 2.0995$ . Equation 4.6 is used in the analysis to calculate the centre of the charge distribution, relative to the centre of the strip carrying the largest signal.

## References

- [1] S. Biagi, MAGBOLTZ source code, CERN, obtained by private communication, Biagi@cernvm.cern.ch for information.
- [2] Rob Veenhof, GARFIELD, a drift-chamber simulation program, User's guide, CERN, Version 5.05, 3 November, 1994.
- [3] H. van der Graaf *et al.*, The honeycomb strip chamber: the application in LHC/SSC experiments and the test results of a prototype, Nucl. Instr. & Methods **A307** (1991) 220.
- [4] H. van der Graaf, Signal development and processing in Multi Wire Proportional Chambers, University of Technology, PhD Thesis, 19 June 1986, Delft.
- [5] Hansjörg Fischle, Joachim Heintze and Bernard Schmidt, Experimental determination of ionization cluster size distributions in counting gases, Nucl. Instr. & Methods, **A301** (1991) 202–214.
- [6] E. Gatti, A. Longoni, H. Okuno and P. Semenza, Optimum geometry for strip cathodes or grids in MWPC for avalanche localization along the anode wires, Nucl. Instr. & Methods **163** (1979) 83–92.
- [7] F. Piuze, R. Roosen and J. Timmermans, Evaluation of systematic errors in the avalanche localization along the wire with cathode strips read-out MWPC, Nucl. Instr. & Methods **196** (1982) 451–462.
- [8] J. Chiba *et al.*, Study of position resolution for cathode readout MWPC with measurement of induced charge distribution, Nucl. Instr. & Methods **206** (1983) 451–463.
- [9] H. van der Graaf and J.P. Wagenaar, A calculation in three dimensions of the induced charge on the electrodes of an MWPC, Nucl. Instr. & Methods **217** (1983) 330–334.
- [10] J.S. Gordon and E. Mathieson, Cathode charge distributions in multiwire chambers; I. Measurement and theory, Nucl. Instr. & Methods **227** (1984) 267–276.
- [11] J.R. Thompson, J.S. Gordon and E. Mathieson, Cathode charge distributions in multiwire chambers; B. Distribution in anode wire direction, Nucl. Instr. & Methods **A234** (1985) 505–511.

# Chapter 5

## Autocalibration of the relation between drift distance and drift time

### Contents

---

<b>5.1</b>	<b>Introduction</b>	<b>75</b>
<b>5.2</b>	<b>Determination of the initial <math>r(t)</math></b>	<b>76</b>
<b>5.3</b>	<b>The autocalibration algorithm</b>	<b>78</b>
5.3.1	The track fit	78
5.3.2	Correcting the $r(t)$ relation	80
5.3.3	An example: autocalibration of simulated data with a large and small angular distribution	83
<b>5.4</b>	<b>The MSGC/P1 experiment</b>	<b>89</b>
5.4.1	Introduction	89
5.4.2	The experimental setup	89
5.4.3	The analysis	92
5.4.4	Results	93

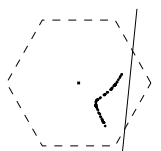
---

### 5.1 Introduction

**T**he determination of the relation between the measured drift time and the minimum distance between the anode wire and muon track is one of the major tasks for track reconstruction in drift-tubes.

The drift-distance versus drift-time  $r(t)$  relation is a function of many parameters. This relation is determined by the characteristics of the drift of ionised electrons in the gas, the electric field configuration, and thus of the geometry of the drift cell. The electrons drift along the electric field lines. If a magnetic field is present, the path of the drift deviates from the electric field lines by the Lorentz angle. Then the 'track distance to the wire' and the 'drift-distance' are no longer equal. Since we are only interested in the relation between the track distance to the wire and the measured drift-time, we will call this relation the  $r(t)$  relation.

The relation between the measured drift-time and the distance between a relativistic charged particle to the anode wire is *not* equal to the relation between the time of drift of a single electron and its distance from the wire at the moment of the ionisation. The charged relativistic particle causes a distribution of ionisation clusters. The measured drift-time to the anode wire depends on the superposition of the signal from individual drift-electrons arriving in the avalanche region, and on the threshold setting of the electronic detection circuit, on the characteristics of the pre-amplifier, shaper and discriminator. These effects are important in view of our aim to reach a



precision on the  $r(t)$  relation of  $20\text{ }\mu\text{m}$  (rms). In case of the P3 chamber, this implies a relative accuracy of 0.2 %.

There are in principle three different methods to obtain the  $r(t)$  relation. The first method uses only the theoretical knowledge of simulation programs like MAGBOLTZ, GARFIELD and a dedicated electronics simulation programme. The present absolute precision of these programs is more than a factor 5 worse than required. The second method obtains the  $r(t)$  relation with high precision reference chambers, e.g. Micro Strip Gas Counters (MSGCs). All experimental parameters are varied and the measured drift-time in the tube is correlated with the distance between the track and the wire as given by the reference chambers. This measurement has been done with the P1 chamber in a cosmic ray setup. The results of this experiment are described in section 5.4. The third method is an in-situ calibration method which makes use of the data redundancy of the measured muon tracks. The  $r(t)$  relation is determined in an iterative process, where a fit to the reconstructed hits is used to improve the  $r(t)$  relation. We will refer to this process as 'the autocalibration procedure'.

Autocalibration has many advantages because no precise knowledge is needed of any theory, B-field or gas-parameters. For a successful use of this method one has to apply the autocalibration mechanism on data taken in a region of the detector with stable parameters, such that the maximum rms-error in the measured drift distance is smaller than  $10\text{ }\mu\text{m}$ .

One can also consider a mixture of the mentioned methods to find the  $r(t)$  relation. Especially, the use of simulations (to predict local dependencies of the main disturbing parameters) in combination with autocalibration shows promising possibilities [1].

Driven by the success of autocalibration of  $r(t)$ , we have also tried to find corrections on the individual positions of the wires and to find corrections on the individual  $T_0$ s of the wires, induced by differences in signal delay in the electronics. The definition of the  $T_0$  will be given in section 5.2. Those values can indeed be fitted using muon track data, however, the precision in the calibration of all parameters depends on the geometrical layout of the drift cells and the topology of the data sample. The term autocalibration is strictly reserved, in this chapter, for in-situ calibration of the  $r(t)$  relation where all wire positions and  $T_0$ s are assumed to be perfectly known.

In this chapter a fast autocalibration algorithm will be derived and the feasibility of autocalibration will be discussed. By means of a verification experiment with a setup consisting of MSGCs and the P1 chamber it will be proven that autocalibration indeed works.

## 5.2 Determination of the initial $r(t)$

In the next section we will derive an algorithm to compute  $r(t)$ . During this derivation we will assume that we have an approximate  $r(t)$  to start the iterative process and that the drift times are correctly measured. We will see that the measured time on the TDC has to be corrected before we have the drift time and a method will be introduced to compute an initial  $r(t)$ .

In figure 5.1 the relation is given between the measured time difference on the TDC ( $T_{\text{Stop}} - T_{\text{Start}}$ ) and the drift time in the cell ( $T_{\text{Drift}}$ ). As is indicated in the figure, both 'Start' and 'Stop' signals are subject to delay. Delay  $T_1$  is caused by trigger signal cables and logic units and is common for all channels. Delay  $T_2$  is caused by the read-out front-end electronics and read-out cables and has to be determined for all channels individually. In practise it is impossible to calculate the values of  $T_1$  and  $T_2$  from the specifications of the trigger and read-out electronics. We are only interested in the difference between  $T_1$  and  $T_2$  and this value is called the  $T_0$  and can



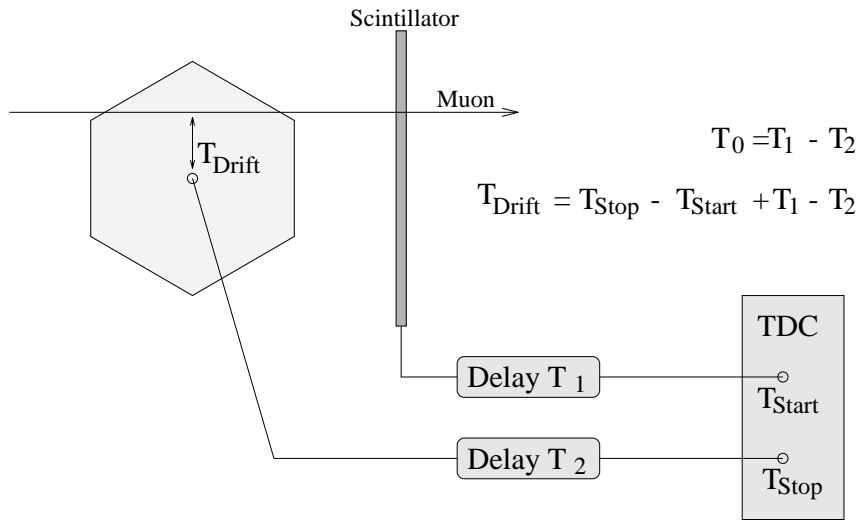


**Figure 5.1:** The drift time  $T_{\text{Drift}}$  is indicated in the drift cell. On the TDC the time difference between the 'Start' and 'Stop' Signal is measured. This time difference is proportional to  $T_{\text{Drift}}$ , but shows an offset which is equal to  $T_1 - T_2$ .

be extracted from the data.

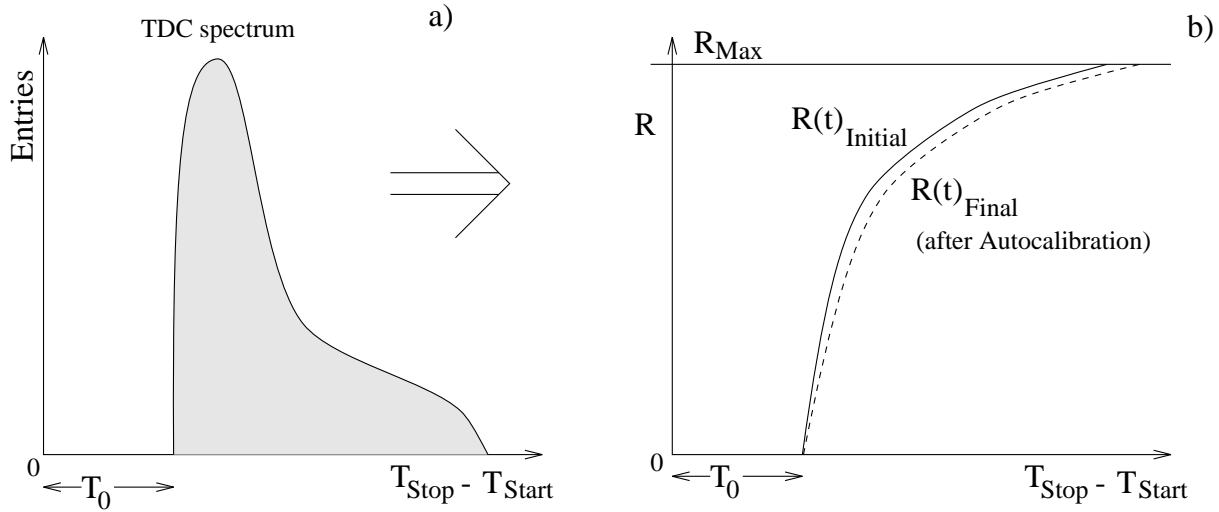
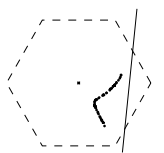


**Figure 5.2:** a) Schematic distribution of the measured TDC values. The distribution shows an offset on the time axis which is equal to  $T_0$ . b) In case we assume that the TDC values in a) are measured by radiating the tube homogeneously, we can compute a good approximation of  $r(t)$  from the measured TDC spectrum.

In case a drift tube is homogeneously radiated we can plot the distribution of measured TDC values. This distribution is schematically shown in figure 5.2. The value of  $T_0$  is equal to the lowest drift-time measured. Since the value of  $T_0$  depends on the channel number, we have to determine all  $T_0$ s for all channels individually.

From the TDC spectra, we can also compute a good approximation for  $r(t)$ . Assuming that the tube is homogeneously radiated,  $r(t)$  can be reconstructed with a deviation less than 5 % from the final  $r(t)$  after autocalibration. This difference between the true  $r(t)$  and the  $r(t)$  based on the normalised TDC spectrum is induced by the (in)efficiency of the drift-tube for tracks close to the cathode, by the noise hits and by systematics in the topology of the data sample.



## 5.3 The autocalibration algorithm

In-situ calibration of the  $r(t)$  relation or 'autocalibration' is based on the assumption that a straight-line track fit to  $N$  wires will give a better estimate for the distance between a track and the wire than an individual hit. By comparing the difference between the measured distance with the fitted distance of the track to the wire, a correction of  $r(t)$  can be obtained. In order to compute the correction on  $r(t)$ , the individual track fit and the fit of  $r(t)$  will be discussed.

### 5.3.1 The track fit

The projection of a straight track onto a plane perpendicular to the wires can be parameterised as a line with the general equation in two dimensions:

$$z = ay + b, \quad (5.1)$$

with  $a$  and  $b$  the track parameters of the track to be fitted. This situation is schematically shown in figure 5.3.

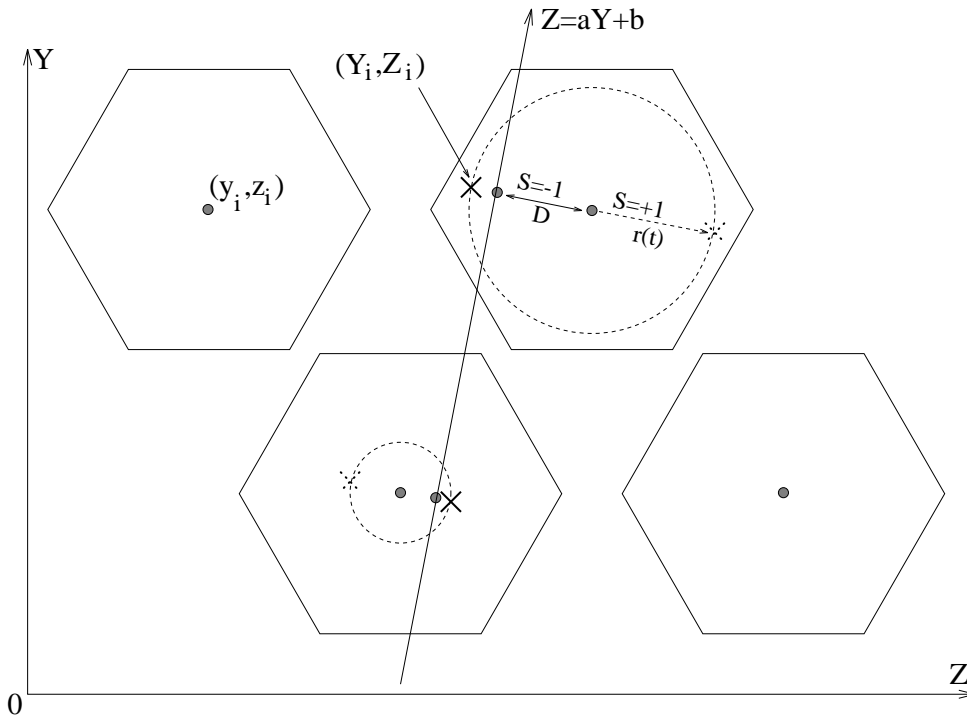


**Figure 5.3:** Definition of parameters used for the track fit and the autocalibration procedure.

Assume a track with  $L$  hits and the wires at position  $(y_i, z_i)$ , for  $i = 1 \dots L$ . The distance between the track and wire  $i$  is given by:

$$D_i = \frac{ay_i - z_i + b}{\sqrt{a^2 + 1}}, \quad (5.2)$$

where  $D_i$  has opposite sign for tracks at opposite sides of the wire. The track parameters  $a$  and  $b$  follow from the minimisation of the  $\chi^2$  function:

$$\chi^2 = \frac{1}{L-2} \sum_{i=1}^L W_i^2 [D_i - S_i r_i]^2 = \frac{1}{L-2} \sum_{i=1}^L W_i^2 \left[ \frac{ay_i - z_i + b}{\sqrt{a^2 + 1}} - S_i r_i \right]^2, \quad (5.3)$$

with weights  $W_i$  equal to the inverse of the estimated resolutions,  $S_i$  equal to plus or minus one, depending on the left-right ambiguity of the hit and  $r_i$  the measured distance between wire and track as given by the current  $r(t)$  (see figure 5.3). The values of  $a$  and  $b$  can be computed by solving the two differential equations:  $\partial\chi^2/\partial a = 0$  and  $\partial\chi^2/\partial b = 0$ . This set of equations can not be solved directly and has to be computed by an iterative method. This is done by writing equation 5.3 as:

$$\chi^2 = \frac{1}{L-2} \sum_{i=1}^L W_i^2 \left[ \frac{aY_i - Z_i + b}{\sqrt{a^2 + 1}} \right]^2, \quad (5.4)$$

where the wire coordinates  $(y_i, z_i)$  are replaced by the coordinates of the hit  $(Y_i, Z_i)$  on the track.  $Y_i$  and  $Z_i$  are given by:

$$\begin{aligned} Y_i &= y_i - S_i r_i \frac{a_0}{\sqrt{a_0^2 + 1}}, \\ Z_i &= z_i + S_i r_i \frac{1}{\sqrt{a_0^2 + 1}}, \end{aligned} \quad (5.5)$$

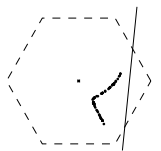
where  $a_0$  is the initial best estimate for the value of  $a$ . Minimisation of equation 5.4 will result in a solution of the parameters  $a$  and  $b$ :

$$\begin{aligned} a &= \frac{-\beta + \sqrt{\beta^2 + 4\alpha^2}}{2\alpha}, \\ b &= \frac{E - aD}{C}, \end{aligned} \quad (5.6)$$

with:

$$\begin{aligned} C &= \sum_{i=1}^L W_i^2, \\ D &= \sum_{i=1}^L W_i^2 Y_i, \\ E &= \sum_{i=1}^L W_i^2 Z_i, \\ F &= \sum_{i=1}^L W_i^2 Y_i^2, \\ G &= \sum_{i=1}^L W_i^2 Z_i^2, \\ H &= \sum_{i=1}^L W_i^2 Y_i Z_i, \\ \alpha &= H - \frac{DE}{C}, \\ \beta &= F - G - \frac{D^2}{C} + \frac{E^2}{C}. \end{aligned} \quad (5.7)$$

The value of  $a_0$  is in the iterative process replaced by the value of  $a$ . The starting value of  $a_0$  is zero. The track parameters  $a$  and  $b$  are stable after three iterations.



### 5.3.2 Correcting the $r(t)$ relation

We assume that the initial  $r(t)$  allows to perform track recognition on a set of hits and that the track recognition routine will return the correct hits on a track with the correct values of  $S_i$ . In case the initial  $r(t)$  relation deviates from the true  $r(t)$ , the fitted parameters  $a$  and  $b$  for individual tracks will deviate from the real track parameters.

An algorithm will be presented to compute the corrections on  $r(t)$  from the fitted residuals and a method will be described to monitor the precision of the obtained result.

#### 5.3.2.1 Definition of the $r(t)$ relation

We will present the  $r(t)$  relation by a limited number of  $(t, r)$  points. All other points on the curve can be reconstructed by an interpolation algorithm. The number of 'master points' to define  $r(t)$  is chosen large enough that the maximum deviation between the true  $r(t)$  and interpolated  $r(t)$  is smaller than  $10 \mu\text{m}$  for all drift times. On the other hand, the number is limited by the amount of statistics needed to compute a correction on the  $r$  value more precise than  $10 \mu\text{m}$ . In practice a total number of points  $N_p$  between 10 and 30 will give satisfactory results. The master points of  $r(t)$  will be distributed over the  $t$ -axis such that a homogeneous distribution in the  $r$  domain is created. In that case, the same amount of statistics is accumulated for each master point if the tubes are homogeneously irradiated.

#### 5.3.2.2 Correction of the $r(t)$ relation

Since we have defined the  $r(t)$  as an interpolation between a limited number of master points, we can as well define the corrections on the  $r(t)$  by the same limited number of values. We will derive an algorithm to find the corrections  $\vec{\Delta}$  on the  $r$  values of the master points. During the autocalibration process, we will assign to all drift times in a time bin  $j$  a constant correction  $\Delta_j$  on  $r(t)$ . In total  $N_p$  time bins are defined with the same number of  $\Delta$  values. So, we will *not* interpolate the  $(t, \Delta)$  values, but from the measured drift time  $t_i$ , each hit will be assigned to an element of  $\vec{\Delta}$ . This will be done such that  $\Delta_1$  represents the correction on  $r(t)$  for the smallest drift times and  $\Delta_{N_p}$  represents the corrections on  $r(t)$  for the longest drift times.

#### 5.3.2.3 Definition and minimisation of the error function

In order to compute  $\vec{\Delta}$  we have to write down the relation between  $\vec{\Delta}$  and the total error function  $F$ . The total error function is defined as the sum over the  $\chi^2$  values of equation 5.4 of all tracks. Here we replace the current  $r(t)$  by  $r(t) + \Delta(t_i)$ .

$$F(\vec{a}, \vec{b}) = \sum_{n=1}^N \frac{1}{L-2} \sum_{i=1}^L W_i^2 \left[ \frac{a_n y_i - z_i + b_n}{\sqrt{a_n^2 + 1}} - S_i(r_i + \Delta(t_i)) \right]^2, \quad (5.8)$$

where  $t_i$  is the measured drift time and  $N$  is the total number of events. Our task is now to solve all  $a_n$ ,  $b_n$  and  $\vec{\Delta}$  by minimisation of  $F$ . The standard procedure exists of solving the set of equations  $\partial F / \partial a_n = 0$ ,  $\partial F / \partial b_n = 0$  and  $\partial F / \partial \Delta_j = 0$ , where  $j = 1 \dots N_p$ , representing the time bins. This procedure will lead to  $2N + N_p$  equations with the same number of variables and thus will give a unique solution.

### 5.3.2.4 Linearisation of the error function

In case we use equation 5.8 to write down all derivatives  $\partial F/\partial a_n$ ,  $\partial F/\partial b_n$  and  $\partial F/\partial \Delta_j$ , we obtain a set of equations which is not linear in  $a_n$  due to the  $\sqrt{a_n^2 + 1}$  term in the denominator. Since a set of linear equations is easy to solve with linear algebra, we will rewrite equation 5.8 such that all derivatives  $\partial F/\partial a_n$ ,  $\partial F/\partial b_n$  and  $\partial F/\partial \Delta_j$  are linear in  $a_n$ ,  $b_n$  and  $\vec{\Delta}$ .

The term between square brackets in equation 5.8 is the difference between the measured and fitted drift distance  $V_i$ :

$$F(\vec{a}, \vec{b}) = \sum_{n=1}^N \frac{1}{L-2} \sum_{i=1}^L W_i^2 V_i^2, \quad (5.9)$$

with,

$$V_i(a_n, b_n, \vec{\Delta}) = \frac{a_n y_i - z_i + b_n}{\sqrt{a_n^2 + 1}} - S_i(r_i + \Delta(t_i)). \quad (5.10)$$

This distance  $V_i$  will be written as a linear function of the variables  $a_n$ ,  $b_n$  and  $\vec{\Delta}$  by a Taylor expansion in  $a_n$  and  $b_n$ .

$$V_i(a_n, b_n) \approx V_i(\bar{a}_n, \bar{b}_n) + (a_n - \bar{a}_n) \frac{\partial V_i}{\partial a_n} \Big|_{\bar{a}_n, \bar{b}_n} + (b_n - \bar{b}_n) \frac{\partial V_i}{\partial b_n} \Big|_{\bar{a}_n, \bar{b}_n} + \dots \quad (5.11)$$

Introducing equation 5.10 into the Taylor expansion gives the following result:

$$V_i(a_n, b_n) \approx \frac{\bar{a}_n y_i - z_i + \bar{b}_n}{\sqrt{\bar{a}_n^2 + 1}} - S_i(r_i + \Delta(t_i)) + \frac{a_n - \bar{a}_n}{(\bar{a}_n^2 + 1)^{3/2}} (y_i + \bar{a}_n z_i - \bar{a}_n \bar{b}_n) + \frac{b_n - \bar{b}_n}{\sqrt{\bar{a}_n^2 + 1}}. \quad (5.12)$$

Now we have expanded  $V_i(a_n, b_n)$  around the working point  $(\bar{a}_n, \bar{b}_n)$  and write the above definition of  $V_i(a_n, b_n)$  in a simplified way:

$$V_i(a_n, b_n) \approx A_i + E_n B_i + G_n - S_i \Delta(t_i), \quad (5.13)$$

where  $A_i$  and  $B_i$  are given by given by:

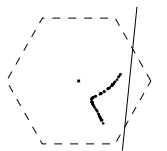
$$\begin{aligned} A_i &= \frac{\bar{a}_n y_i - z_i + \bar{b}_n}{\sqrt{\bar{a}_n^2 + 1}} - S_i r_i, \\ B_i &= y_i + \bar{a}_n z_i - \bar{a}_n \bar{b}_n, \end{aligned} \quad (5.14)$$

and the new variables  $E_n$  and  $G_n$  given by:

$$\begin{aligned} E_n &= \frac{a_n - \bar{a}_n}{(\bar{a}_n^2 + 1)^{3/2}}, \\ G_n &= \frac{b_n - \bar{b}_n}{\sqrt{\bar{a}_n^2 + 1}}. \end{aligned} \quad (5.15)$$

The error function  $F$  transforms to:

$$F(\vec{a}, \vec{b}) \approx \sum_{n=1}^N \frac{1}{L-2} \sum_{i=1}^L W_i^2 [A_i + E_n B_i + G_n - S_i \Delta(t_i)]^2, \quad (5.16)$$



In the first step  $\vec{a}$  and  $\vec{b}$  are approximated by assuming that  $\vec{\Delta} = \vec{0}$ . Using equation 5.6 for a fit of the individual tracks we compute  $(\vec{a}, \vec{b})$ . The second step consists of solving the remaining  $N_p$  equations  $\partial F / \partial \Delta_j = 0$  with the condition that also  $\partial F / \partial a_n$  and  $\partial F / \partial b_n$  remain zero. This is now straightforward since all derivatives are linear in  $E_n$ ,  $G_n$  and  $\Delta_j$ . The equations  $\partial F / \partial E_n = 0$  and  $\partial F / \partial G_n = 0$  can be solved:

$$\begin{aligned} \frac{\partial F}{\partial E_n} = 0 &\Rightarrow K_n + E_n M_n + G_n N_n - \sum_{i=1}^L W_i^2 S_i B_i \Delta(t_i) = 0, \\ \frac{\partial F}{\partial G_n} = 0 &\Rightarrow R_n + E_n N_n + G_n P_n - \sum_{i=1}^L W_i^2 S_i \Delta(t_i) = 0, \end{aligned} \quad (5.17)$$

with

$$\begin{aligned} K_n &= \sum_{i=1}^L W_i^2 A_i B_i, \\ M_n &= \sum_{i=1}^L W_i^2 B_i^2, \\ N_n &= \sum_{i=1}^L W_i^2 B_i, \\ R_n &= \sum_{i=1}^L W_i^2 A_i, \\ P_n &= \sum_{i=1}^L W_i^2. \end{aligned} \quad (5.18)$$

From equations 5.17 the variables  $E_n$  and  $G_n$  can be solved straightforward:

$$\begin{aligned} E_n &= \frac{1}{N_n^2 - P_n M_n} \left( \sum_{i=1}^L W_i^2 S_i \Delta(t_i) [N_n - P_n B_i] + P_n K_n - N_n R_n \right), \\ G_n &= \frac{1}{N_n^2 - P_n M_n} \left( \sum_{i=1}^L W_i^2 S_i \Delta(t_i) [N_n B_i - M_n] + R_n M_n - N_n K_n \right). \end{aligned} \quad (5.19)$$

Two remarks have to be made about this result. First, one has to observe that  $E_n$  and  $G_n$  depend only in first order on  $\Delta_j$ . Second, since  $E_n$  and  $G_n$  are zero in case  $\vec{\Delta} = \vec{0}$ , the terms  $[P_n K_n - N_n R_n]$  and  $[R_n M_n - N_n K_n]$  in equation 5.19 will be zero. In order to compute  $\vec{\Delta}$ , we have to write down the set of  $N_p$  linear equations  $\partial F / \partial \Delta_j = 0$ :

$$\frac{\partial F}{\partial \Delta_j} = \sum_{n=1}^N \frac{1}{L-2} \sum_{i=1}^L W_i^2 [A_i + E_n B_i + G_n - S_i \Delta(t_i)] S_i \delta_{ij} = 0, \quad (j = 1 \dots N_p), \quad (5.20)$$

where  $\delta_{ij} = 0$  in case the measured drift time of hit  $i$  is *not* inside the time window covered by master-point  $j$ ,  $\delta_{ij} = 1$  in case the drift time of hit  $i$  is inside the time window covered by master point  $j$ . By inserting the expressions for  $E_n$  and  $G_n$  found in equation 5.19 in equation 5.20 we find the final set of  $N_p$  equations:

$$\sum_{n=1}^N \frac{1}{L-2} \sum_{i=1}^L W_i^2 S_i A_i \delta_{ij} - \sum_{n=1}^N \frac{1}{L-2} \sum_{i=1}^L W_i^2 \delta_{ij} \Delta(t_i) +$$

$$\sum_{n=1}^N \frac{1}{L-2} \frac{1}{N_n^2 - P_n M_n} \sum_{i=1}^L W_i^2 B_i S_i \delta_{ij} \sum_{k=1}^L W_k^2 S_k \Delta(t_k) [N_n - P_n B_k] + \sum_{n=1}^N \frac{1}{L-2} \frac{1}{N_n^2 - P_n M_n} \sum_{i=1}^L W_i^2 S_i \delta_{ij} \sum_{k=1}^L W_k^2 S_k \Delta(t_k) [N_n B_k - M_n] = 0, \quad (j = 1 \dots N_p). \quad (5.21)$$

Here  $\Delta(t_i)$  and  $\Delta(t_k)$  are the elements of  $\vec{\Delta}$  to be used to compute the correction on  $r(t)$  for hit  $i$  and  $k$ . Since we have found  $N_p$  equations with  $N_p$  unknowns ( $\Delta_j$ ) and all equations depend in first order on  $\Delta_j$  we can solve this set using the theory of linear algebra.

### 5.3.2.5 Writing $N_p$ equations in matrix notation

The set of equations in 5.21 can be written in matrix form:

$$[A]\vec{\Delta} = \vec{c}, \quad (5.22)$$

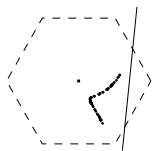
where  $[A]$  represents a square  $N_p \times N_p$  matrix,  $\vec{\Delta}$  is a column vector of dimension  $N_p$  with the values of  $\Delta_j$  and  $\vec{c}$  is also a column vector of dimension  $N_p$ . The solution of  $\vec{\Delta}$  can be found by inverting matrix  $[A]$  and computing  $\vec{\Delta} = [A^{-1}]\vec{c}$ . The value of the matrix elements can be simply extracted from equation 5.21.

We use the theory of linear algebra to get an indication of the stability of the derived solution. The theory says that a solution can only be found in case that matrix  $[A]$  is not singular. The algorithm is unstable in case a small variation at the input side of the algorithm causes large deviations in the output. The stability of the solution depends on how non-singular the matrix  $[A]$  is. The singularity of the matrix (and thus of our problem) can be detected by computing the determinant of  $[A]$ . If the determinant is zero (or close to zero) then the solution of the matrix equation will be unstable. In practise an unstable problem will be caused by a strong coupling of the linear equations which are represented by matrix  $[A]$ . The coupling of the linear equations is strong in case the off-diagonal elements of  $[A]$  are large compared with the diagonal elements.

In order to give a meaningful value to the determinant of  $[A]$ , the rows of  $[A]$  are normalised such that all diagonal elements of  $[A]$  will be one. The determinant of  $[A]$  will now range between zero (unstable solutions) to one (stable solutions). We will see that autocalibration will give a stable  $r(t)$  in case a data sample with a large range of track parameters  $a_n$  and  $b_n$  is used. In case we have to work with a data sample of a limited range of the track parameters, the determinant will in general be very small ( $< 0.1$ ) and no unique  $r(t)$  relation can be found.

### 5.3.3 An example: autocalibration of simulated data with a large and small angular distribution

The above described autocalibration algorithm will be demonstrated in a case study. I will show the behaviour of the algorithm in case of a wide angular distribution of tracks (section 5.3.3.3) and in case the data consists of (nearly) parallel muon tracks (section 5.3.3.4). We will see that autocalibration in the first case will convert faster and gives a more stable result. All computations are performed on simulated data in order to be able to compare the computed  $r(t)$  with the input  $r(t)$ .



### 5.3.3.1 The setup

Simulated data is used with well known characteristics of an individual tube, like  $r(t)$ , resolution, efficiency and probability on correlated and random noise hits. Also the spatial and angular distribution of the track sample was varied to study the behaviour of the algorithm. The geometry of the simulated chamber was chosen to be equal to that of the P3 chamber with a maximum cell radius of 11.5 mm. The  $r(t)$  and resolution characteristics were calculated by a MAGBOLTZ and GARFIELD simulation for an Ar/CO<sub>2</sub>/C<sub>2</sub>H<sub>6</sub> 70/25/5 gas mixture with 2475 V on the 50  $\mu$ m diameter anode wire. This gas is known to have a very non-linear  $r(t)$  relation and the algorithm has to perform well to reconstruct the correct  $r(t)$  over the whole time range. During all simulations a total of 10,000 events are produced. No angular dependence (in  $\theta$ ), due to the hexagonal shape of the cell, of  $r(t)$  is taken into account.

### 5.3.3.2 The analysis

The simulated data is analysed with a  $r(t)$  relation which deviates by 5 percent from the real  $r(t)$ . The ambiguities are supposed to be known to speed up the track-fitting algorithm, so no pattern recognition was performed in this analysis. The autocalibration algorithm as described should provide a correct  $r(t)$  in one iteration. This is only true if the corrections on the  $r(t)$  are small, since we have linearised all equations around a working point.

I will compare the described autocalibration algorithm with a more simple and widely used algorithm, where the off-diagonal elements of the matrix equation are ignored, which means that the measured systematic residual shifts are fed back straightforward to the current  $r(t)$  to achieve an improved  $r(t)$ .

### 5.3.3.3 Data with a Gaussian angular distribution of 200 mrad (rms)

In figure 5.4 the front view of the P3 chamber is shown with 100 muon tracks overlayed. This selection of tracks represents very well the spatial distribution of the simulated data sample and the width of the angular distribution (Gaussian with an rms of 200 mrad). The initial  $r(t)$  devi-

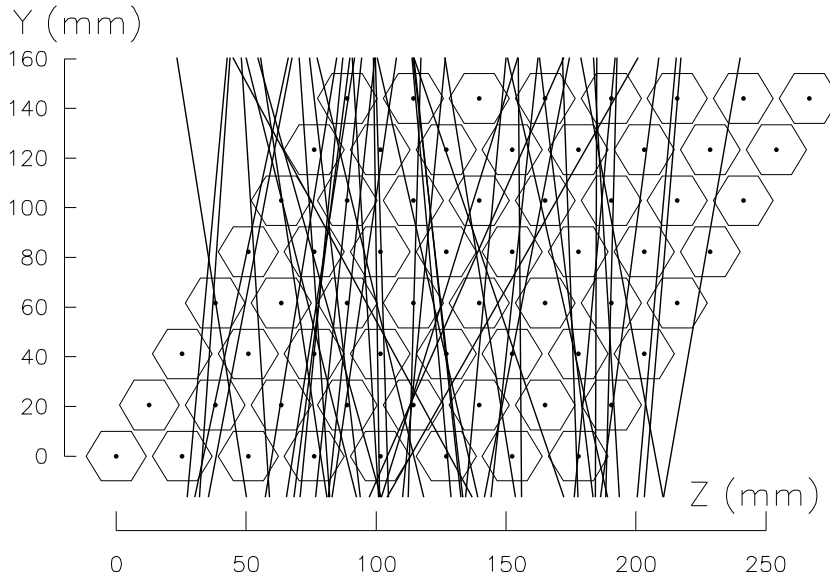


**Figure 5.4:** Impression of a data sample with a wide angular distribution in the P3 chamber, 100 tracks are shown.



ates 5 % from the true  $r(t)$  over the whole drift time range. The residuals of these fits are shown in figure 5.5a as function of the distance of the fitted track to the wire. The centre of gravity of

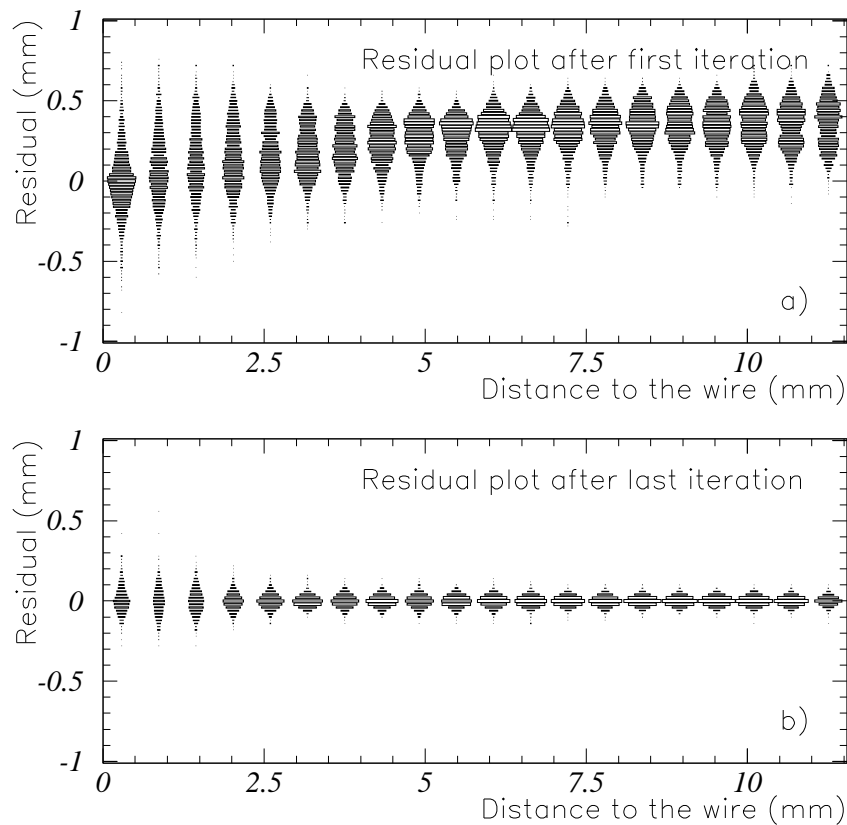


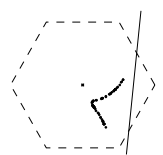
**Figure 5.5:** Residual plot as function of the distance of the track to the wire. a) First iteration with 5 % wrong  $r(t)$ . b) Last iteration with autocalibrated  $r(t)$ .

the residuals can be computed for all 20 slices. These values form together the vector  $\vec{c}$  in equation 5.22. In total 5 iterations are performed and as a result after the last iteration the residuals are shown in figure 5.5b. The resulting residuals are centred around zero, and are closely related to the intrinsic resolution of the detector.

In order to show the behaviour of the  $r(t)$  during the sequence of iterations, the  $r(t)$  curve and error with respect to the real  $r(t)$  are plotted in figure 5.6 and 5.7. Figure 5.6 shows the very fast convergence of the algorithm. The correct  $r(t)$  is reconstructed essentially over the whole time scale in one iteration. The maximum error in the  $r(t)$  appears at very short drift distances. This error in the reconstructed  $r(t)$  can be explained by the non-Gaussian shape of the residuals for tracks close to the wire, where the limited number of clusters per unit track length dominates the resolution. Since the weights  $W_i$  in the track fit are the inverse of the resolutions of the measurements, these hits close to the wire will have a very low weight in the fit.

Figure 5.7 shows the error in the  $r(t)$  in case the  $r(t)$  is straightforward corrected with the fitted residuals. This simple autocalibration procedure shows the disadvantage that more iterations are needed and no handles are available to check the confidence in the final result.

As a final check of the quality of the reconstructed  $r(t)$  we can compare the track definition of the simulated data with the fitted track parameters. Also the input resolution in the simulation has to be well reconstructed. In figure 5.8 the intrinsic resolution of a single wire is given as computed by the GARFIELD programme, with a realistic threshold on the fifth electron. This relation is indicated by the dashed curve with the black dots. The reconstructed resolution after



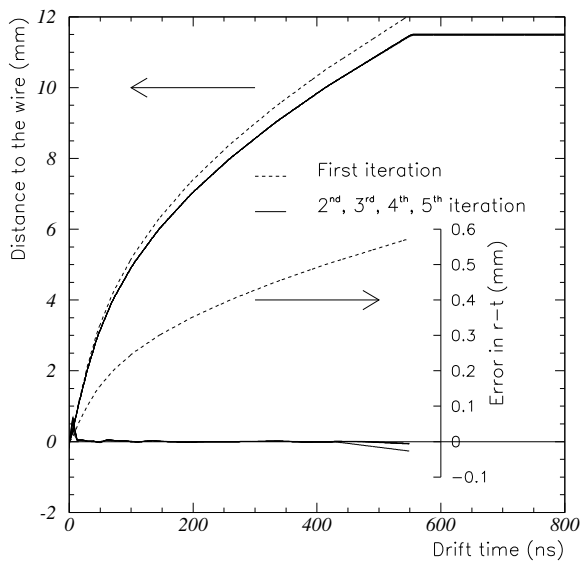


**Figure 5.6:**  $R(t)$  relation and error on the  $r(t)$  ( $10 \times$ , right hand scale). While the error in the first iteration has a maximum of  $600 \mu\text{m}$ , this is reduced to zero over the whole time axis in the second iteration. The algorithm of equation 5.21 is used.

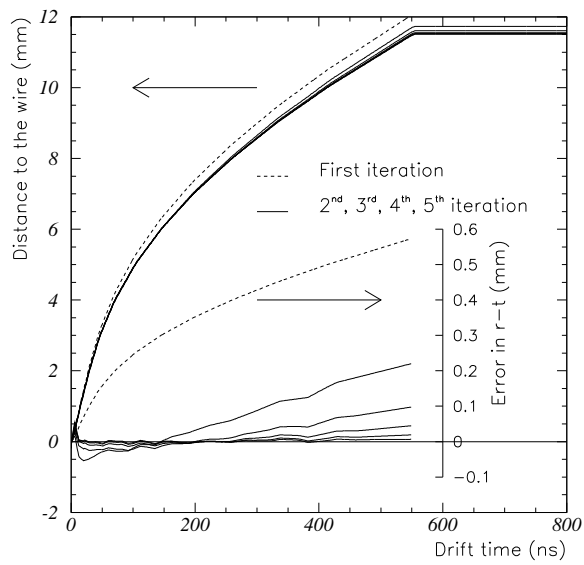


**Figure 5.7:** Same as figure 5.6, but the off diagonal elements in equation 5.21 are set to zero, i.e. the correction on the  $r(t)$  is equal to the measured residual shift.

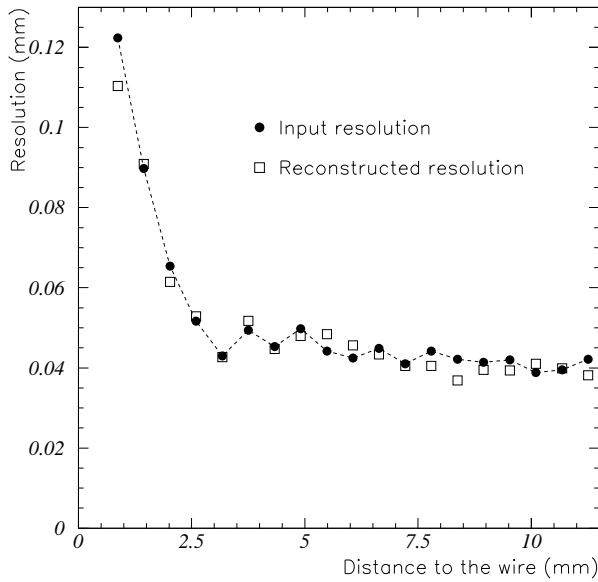


**Figure 5.8:** The dashed line and black dots represent the input resolution in the simulation programme. The open boxes are the fitted resolution after autocalibration.

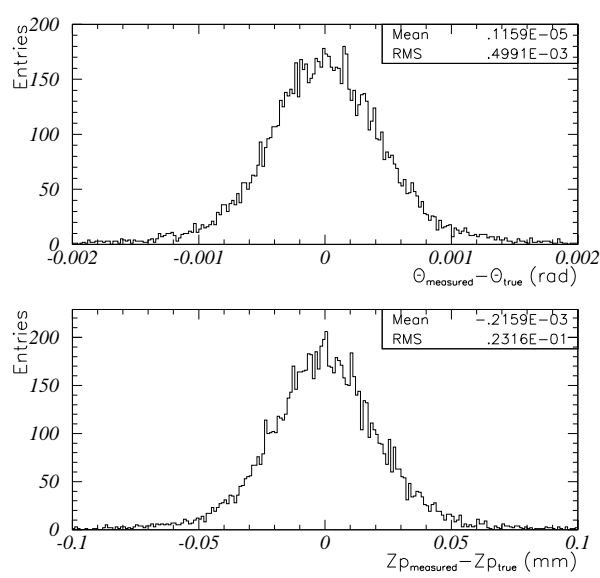


**Figure 5.9:** Angular residual and spatial residual in the  $z$  plane. The angular resolution of  $0.5 \text{ mrad}$  and spatial resolution of  $23 \mu\text{m}$  are well in agreement with an eight-layer HSC with  $60 \mu\text{m}$  resolution per wire.

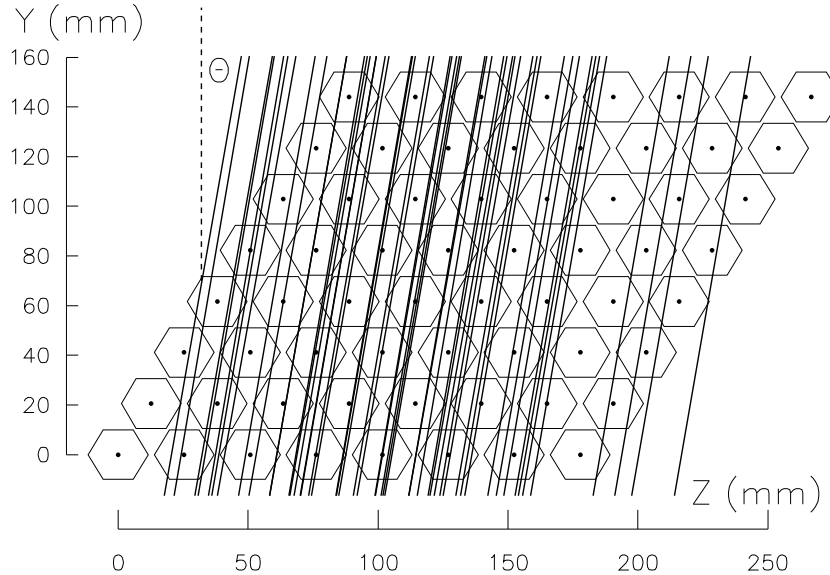
the last iteration is given by the open boxes. The agreement is good and one can conclude that the contribution of the autocalibration to the resolution is negligible for this data sample with a wide angular distribution. As a final proof that the track fit reconstructs the correct tracks, I have plotted in figure 5.9 the distributions of the angular error and the spatial error in the  $z$ -plane. The distributions are well centred around zero and the width of the distributions are in agreement with

a mean number of 7 hits per track and  $60\text{ }\mu\text{m}$  resolution for each wire, resulting in  $60\text{ }\mu\text{m}/\sqrt{7}=23\text{ }\mu\text{m}$  resolution for the track position.

#### 5.3.3.4 Data with an angular distribution of 2, 20 and 100 mrad (rms)

In real applications, the angular distribution of the data will be limited. The most extreme case is a parallel beam as delivered in a test beam facility with a Gaussian angular distribution with an rms of 2 mrad. I will study the consequences of this type of data and I will study two intermediate cases between a beam with an rms=2 mrad and a wide angular distribution (e.g. rms=200 mrad). The problem of a dataset with (nearly) parallel tracks can be understood best for a beam with incident angle at  $30^\circ$ . In this case the tracks are parallel to a wire plane (like a matrix axis). The drift times of all wires will be equal for this type of tracks. This means that no information can be extracted from the residuals and every arbitrary  $r(t)$  will give the same residuals, centred around zero. In case of a beam perpendicular to the wire planes ( $\theta = 0^\circ$ ), autocalibration will fail for similar reasons. An important question is how such a singularity can be detected and (if possible) avoided. Since the correction on the  $r(t)$  is given by equation 5.22, the determinant of matrix  $[A]$  will be correlated with the singularity of the autocalibration process.

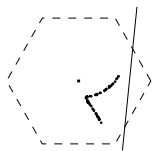
In figure 5.10 hundred tracks are shown with a angular distribution of 2 mrad (invisible by eye in the figure) around a mean angle of incidence of 200 mrad.



**Figure 5.10:** Impression of a parallel data sample in the P3 chamber. 100 tracks are shown with the angle of incidence  $\theta = 200 \pm 2\text{ mrad}$ .

The determinant of the matrix  $[A]$  of equation 5.22 is computed for three widths of the beam (2, 20 and 100 mrad) with incident angles between 0.0 and 1.0 rad ( $57^\circ$ ). The value of the determinant will be a value between 0.0 and 1.0, where a 'very small' determinant will indicate a nearly singular matrix  $[A]$  and thus a nearly singular problem. The value of the determinant is shown in figure 5.11. From this figure it appears that the singularity of the autocalibration algorithm is the largest for narrow beams. Even for a beam with an angular width of 20 mrad, the determinant of  $[A]$  is nearly zero at the predicted problematic areas of 0 and 540 mrad. But also at 200 and 900 mrad a clear drop in the determinant can be observed.

One can make a crude estimation of the minimum angular width of the beam in order to



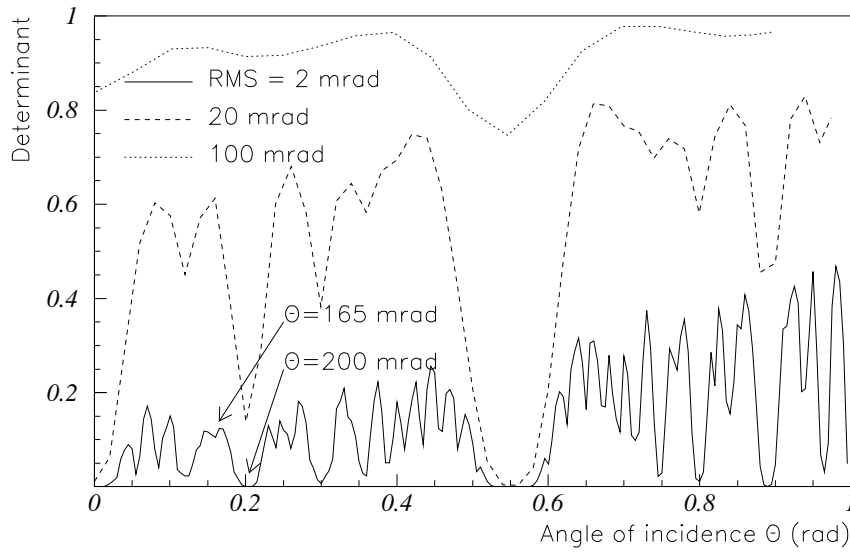


**Figure 5.11:** Determinant of matrix  $[A]$  in equation 5.22 as function of the mean angle of incidence  $\theta$ . The angular width of the beam is small (2 mrad), intermediate (20 mrad) and large (100 mrad). A clear drop of the determinant at 0 and 540 mrad can be observed. For very low determinants, the autocalibration problem becomes singular.

have a guaranteed good convergence of the autocalibration algorithm. This estimation is based on the empirical knowledge that autocalibration converges if there exist tracks in the data sample which connect every random drift distance at a random wire with every random drift distance at a different wire. Note that this case corresponds too a matrix  $[A]$  where none of the elements is empty (and thus zero). The minimum angular width will show a maximum at  $\theta = 0^\circ$  and is given by the geometry of the detector:  $\theta_{\text{rms}} = R_{\text{cell}}/D_{\text{chamber}}$ , where  $D_{\text{chamber}}$  is the thickness of the detector. In case of P3 is the cell diameter  $R_{\text{cell}}$  10 mm and  $D_{\text{chamber}}$  150 mm, which makes the minimum angular beam width  $\theta_{\text{rms}}$  for guaranteed convergence over the whole  $\theta$  range equal to 70 mrad.

The relation between the determinant and the mean angle of incidence for a beam with an angular width of 2 mrad is fluctuating surprisingly fast. The knowledge of this curve is of great importance when data is taken in a test beam and the angle of incidence  $\theta$  can be varied freely.

In the following the result of the autocalibration process will be shown for two simulated test beam runs with the P3 chamber for  $\theta = 165 \pm 2$  mrad (determinant = 0.1234) and for  $\theta = 200 \pm 2$  mrad (determinant = 0.0009). A badly converging autocalibration process can be expected in the last case. In figure 5.12 and 5.13 the different steps of the autocalibration algorithm are shown, assuming again an initial  $r(t)$  curve which deviates by 5 % from the true  $r(t)$ . In case of a determinant of 0.1234 the convergence of the algorithm is as good as for a cosmic data sample. In case of the data sample simulated at  $\theta = 200$  mrad the  $r(t)$  will converge to a stable curve, but this is not the real  $r(t)$ . Note that the outer curve (most wrong) is the result of the last iteration. Note also the so called 'nodes' at 100 and 300 ns where all curves during all iterations cross the 'zero-error' line (figure 5.13).

In figure 5.14 and 5.15 the reconstructed resolution as function of drift distance are compared with the input resolution in the simulation. In spite of the error of 100  $\mu\text{m}$  in  $r(t)$ , no significant worsening of the reconstructed resolution is observed for the  $\theta = 200$  mrad case with respect to the  $\theta = 165$  mrad case. But we will see that an erroneous  $r(t)$  will lead to large systematic errors in the reconstructed track  $z$ -coordinate.

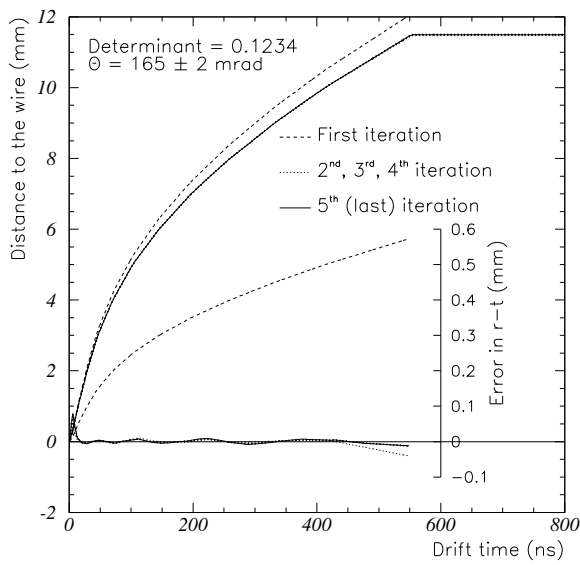


**Figure 5.12:** As figure 5.6, instead of a cosmic data sample, the tracks are parallel ( $\theta = 165 \pm 2$  mrad), and the determinant is 0.1234, resulting in a well defined autocalibration problem.

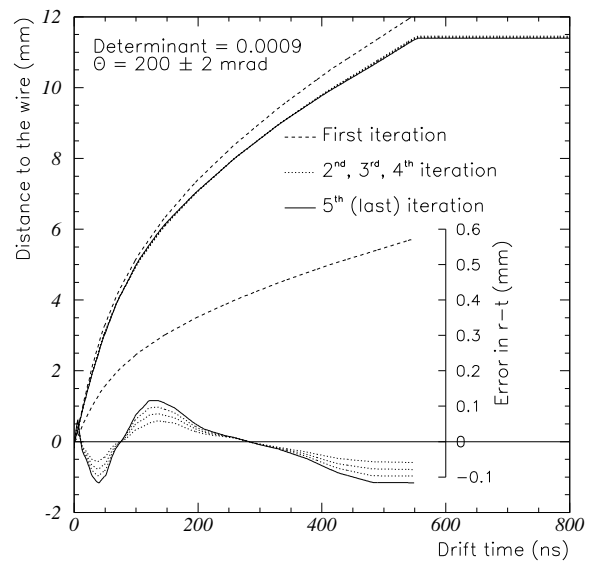


**Figure 5.13:** As figure 5.12, and the determinant of the parallel beam ( $\theta = 200 \pm 2$  mrad) is 0.0009. This results in a singular problem and an erroneous  $r(t)$  is found.

In figure 5.16 and 5.17 the reconstructed track parameters  $\theta$  and  $Z_P$  are compared with the true track parameters. The results of the track fit with the autocalibrated  $r(t)$  with data at  $\theta = 165$  mrad agrees well with that of a wide angle data sample (see figure 5.9). We see for the data sample at  $\theta = 200$  mrad a small asymmetry in the error of the reconstructed angle of incidence. But the systematic error of the reconstructed position of the track in the detector is much worse. A worsening of the resolution from 21  $\mu\text{m}$  (rms) to 65  $\mu\text{m}$  is the result.

## 5.4 The MSGC/P1 experiment

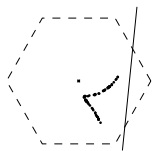
### 5.4.1 Introduction

The autocalibration method as described above has been tested with real muon data by a so called 'reference experiment'. In this experiment,  $r(t)$  has been determined by autocalibration as well as by making use of a totally independent set of reference detectors. The two obtained  $r(t)$  relations have been compared in order to study the consistency of the methods. A more detailed description of the setup and analysis can be found in [2].

The reference detectors were Micro Strip gas Counters (MSGCs) of  $10 \times 10 \text{ cm}^2$ , which gave a track definition completely independent of the Honeycomb chamber. In order to define a track with MSGCs, two detection planes are required. For redundancy reasons and pattern recognition, four planes are used: two planes close above and two planes below the chamber. The Honeycomb chamber in this experiment was the P1 chamber (see section 3.3).

### 5.4.2 The experimental setup

A schematic cross section of the experiment is shown in figure 5.18. The P1 chamber is shown with the four MSGC planes which are put into two gas envelopes. The different components of the experiment will be described in more detail.



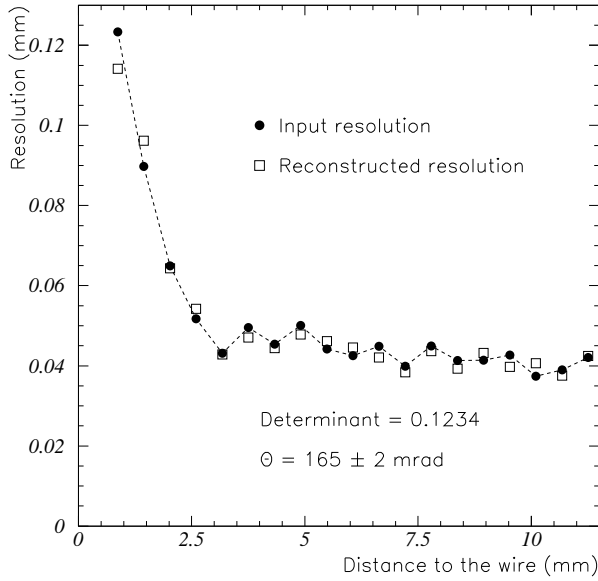


**Figure 5.14:** As figure 5.8, the data sample consists of parallel tracks with  $\theta = 165 \pm 2$  mrad and a determinant of 0.1234. The resolution is well computed and equals the input resolution in the simulation.

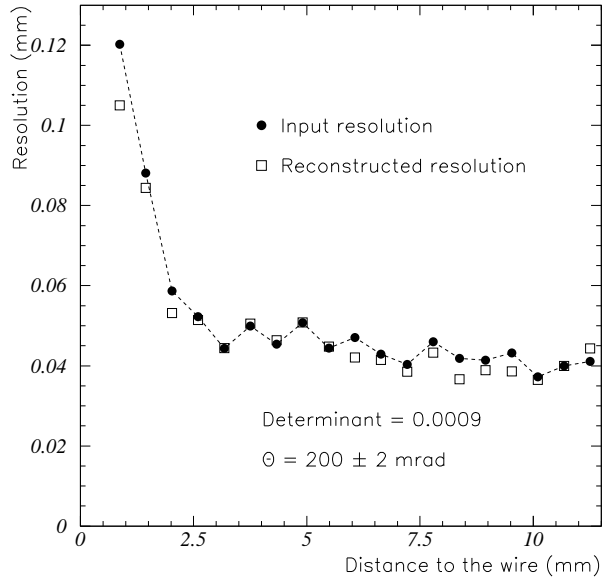


**Figure 5.15:** As figure 5.14, but  $\theta = 200 \pm 2$  mrad and the determinant is 0.0009. The  $r(t)$  is wrongly reconstructed. The resolution, however, is not influenced (open boxes) which is an indication that the minimum of function  $F$  (equation 5.8) is indeed very shallow for small perturbations on the correct  $r(t)$ .

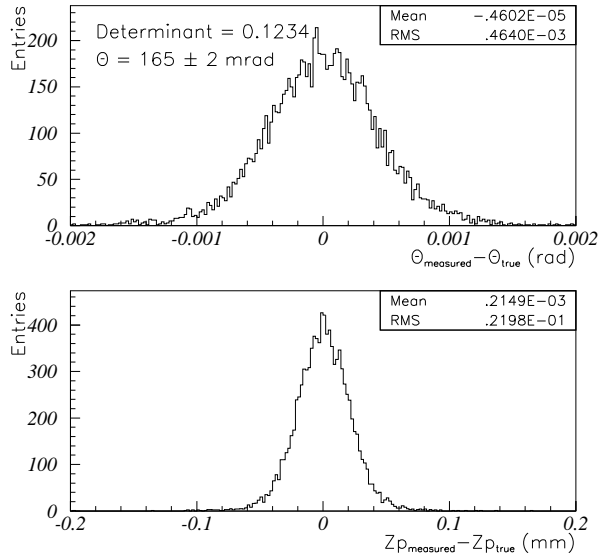


**Figure 5.16:** As figure 5.9 for a data sample with nearly parallel tracks and a large determinant. The spatial and angular (stochastic) errors have the same value as for a data sample with a broad angular distribution.

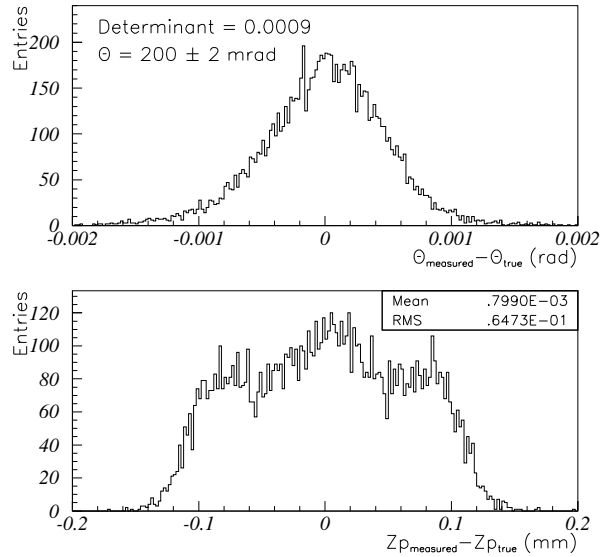


**Figure 5.17:** As figure 5.16 for a data sample with nearly parallel tracks and a small determinant and erroneously reconstructed  $r(t)$ . The rms value of the  $z$ -distribution is three times as large as for the data sample with a determinant of 0.1234 instead of 0.0009.

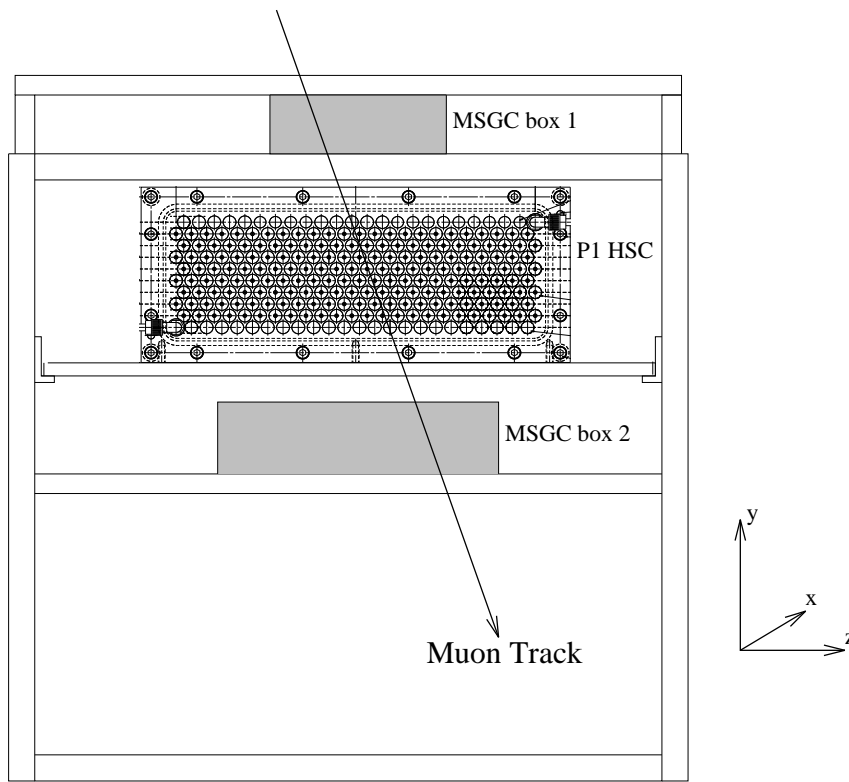


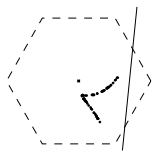
**Figure 5.18:** Schematic view of the test setup with the wires of P1 and strips of the MSGCs along the  $x$ -axis. Each MSGC box contained two  $10 \times 10 \text{ cm}^2$  counters and 40 wires of the P1 chamber were equipped with electronics.

#### 5.4.2.1 The P1 HSC

In this experiment a total of 40 wires were read out. The anode wires had a diameter of  $30 \text{ }\mu\text{m}$  and were grouped in eight planes of five wires. With an outer cell radius of  $5.773 \text{ mm}$ , a wire pitch of  $12.4 \text{ mm}$ , and a wire length of  $300 \text{ mm}^2$ , an area of  $70 \times 300 \text{ mm}^2$  was covered for vertical tracks.

The cathode strips of four planes (16 strips per plane) were read out for optional alignment corrections. The coordinate of the tracks along the wires was needed in case the wires of the HSCs were not well aligned with the strips of the MSGCs (worse than  $0.1 \text{ mrad}$ ). In the analysis it turned out that the alignment of the MSGCs with respect to each other did not contribute to the internal MSGC resolution, nor did the alignment of the MSGC system with respect to the P1 wires contribute to the P1 single wire resolution. For this reason, the information of the second coordinate (along the wire) was not included in the analysis.

The chamber was flushed with premixed  $\text{Ar}/\text{CO}_2$  80/20 gas. The anode wires were put on  $1850 \text{ V}$  and read out with a standard L3 pre-amplifier, L3 discriminator and 4208 Le Croy TDCs with  $1 \text{ ns}$  binning [3, 4, 5]. The high voltage on the wires was moderate, resulting in a low gas gain (a few times  $10^4$ ). The level of the threshold setting was dominated by pick up by the pre-amplifier of high frequent signals induced by the digital controller of the MSGCs and had to be set relatively high. The combination of low gain and high threshold resulted in a resolution of only  $150 \text{ }\mu\text{m}$  (rms).



### 5.4.2.2 The Micro Strip Gas Counter

The MSGC is essentially a miniaturised MWPC. Because electrostatic forces between field, anode and cathode wires will not allow a straightforward reduction of the wire pitch, the anode wires and cathode strips are etched on a glass substrate. The substrate with anode and cathode is separated by a gaseous layer from the conducting drift plane (see figure 5.19).

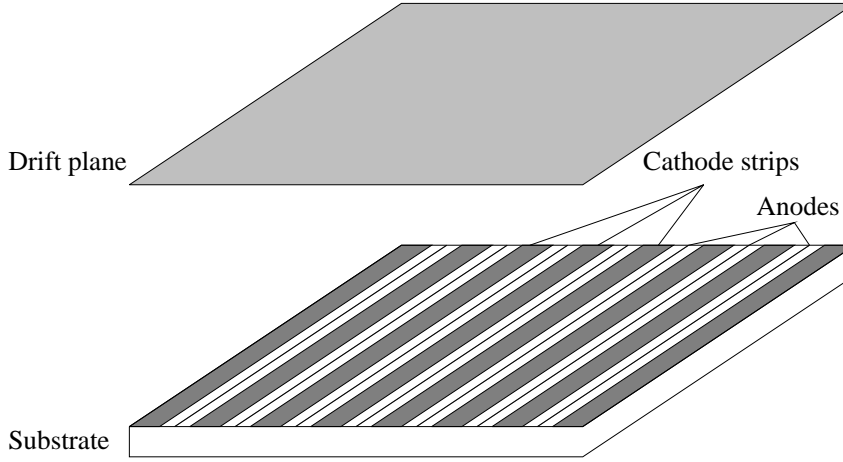


**Figure 5.19:** Outline of the MSGC detector: a substrate carrying conductive strips is positioned in a gas volume, covered by a conductive drift plane [6].

The drift plane (or 'cathode plane') is on negative high voltage, the cathode strips are also on (a different) high voltage, while the anode strips are on ground potential, which allows to feed the signals from the anode directly into a charge sensitive pre-amplifier. The MSGC in this experiment had an anode pitch of  $200\text{ }\mu\text{m}$  and consisted of 512 anodes of each  $100\text{ mm}$  length, making an active surface of  $10 \times 10\text{ cm}^2$ . The principles of ionisation, drift and signal amplification are very similar to the processes in a drift tube, with the difference that due to the small dimensions no drift-time has to be measured and a simple centre of gravity algorithm on a cluster of hits in a plane can give a spatial resolution of  $30\text{ }\mu\text{m}$  for perpendicular tracks[6].

The MSGCs were positioned in gas volumes in two pairs. The drift gas was DME/CO<sub>2</sub> 50/50. The drift planes were at  $-2130\text{ V}$  and the cathode strips at  $-650\text{ V}$ . The signals on the 2048 strips were pre-amplified in groups of 128 by an MX5 chip. The chips were serially read out and for each layer of 512 channels a Sirocco flash ADC unit was used for analogue to digital conversion.

## 5.4.3 The analysis

Two analysis methods are performed on the same data set. In the first analysis, the  $r(t)$  relation is derived by autocalibration as described before. In the alternative analysis, the  $r(t)$  relation is derived by matching of the measured drift times in P1 with the track position in the chamber as given by the MSGCs.

### 5.4.3.1 Reference chamber analysis

The main problem in the reference chamber analysis is the determination of the positions of the four MSGC planes with respect to each other and the P1. These positions are fitted in an iterative method, using the cosmic tracks through both P1 and the MSGCs as alignment lines.



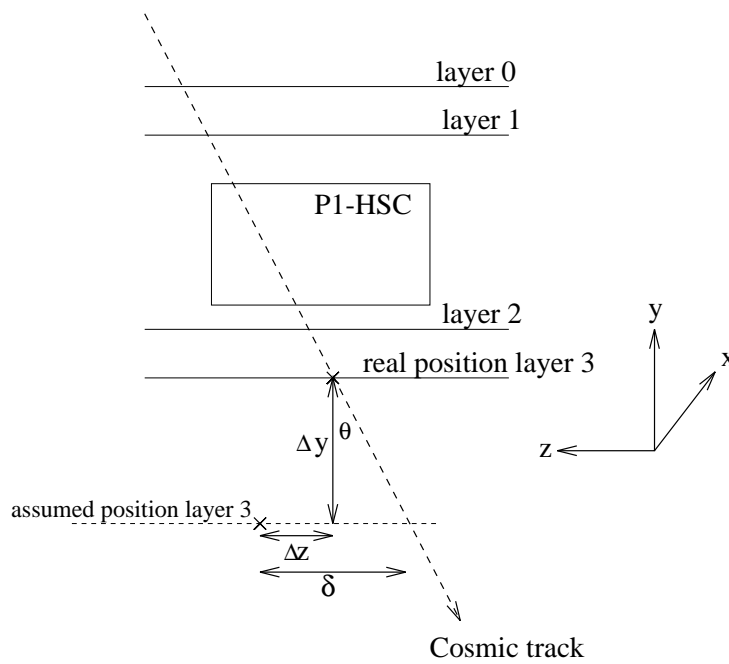


**Figure 5.20:** Schematic cross section of the experiment with all relevant geometric parameters indicated. MSGC-3 is assumed to be misaligned in  $z$  and  $y$  direction. A track through the P1 chamber with angle of incidence  $\theta$  will show a systematic shift of the residuals  $\delta$ . In case  $\delta$  is measured over a range of  $\theta$  values, the  $z$ -shift  $\Delta z$  and  $y$ -shift  $\Delta y$  can be computed unambiguously for all 4 MSGC planes. The wires of P1 and the strips of the MSGCs run in the  $x$ -direction.

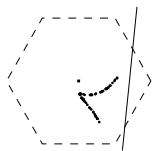
The situation is schematically drawn in figure 5.20. The strips of the four MSGC planes are well aligned (error  $< 0.1$  mrad) with the wires of the P1. The geometry can now be fitted in two dimensions. The strips in the MSGCs and wires in P1 are perpendicular to the paper. Further, we aligned the MSGCs and P1 in the  $x$ - $z$  plane. This means that no angular errors between the counters and P1 have to be determined. The only remaining error is the relative position of all four counters with respect to a reference point of the P1. These errors are indicated in figure 5.20 for MSGC-3 by the parameters  $\Delta y$  (vertical) and  $\Delta z$  horizontal. This gives a total of eight degrees of freedom to be fitted.

All the MSGC positioning parameters are derived from the residuals, being the difference between the  $z$ -coordinate as measured on the MSGC and the predicted  $z$ -coordinate as predicted by an extrapolation of the track through the P1 chamber. This residual is indicated in figure 5.20 for MSGC-3 where a geometry error  $\Delta z$  is introduced and the residual is indicated by  $\delta$ .

Given the mean position of the residuals as function of the track angle  $\theta$ , one can compute straightforward the corrections  $\Delta y$  and  $\Delta z$ , where the precision of  $\Delta y$  depends on the angular width of the cosmic data sample.

#### 5.4.4 Results

The results of the reference chamber analysis and the autocalibration analysis will be presented. The final result will be a comparison of the two independently derived  $r(t)$  relations.



#### 5.4.4.1 Reference chamber

In figure 5.21 an example is given of a reconstructed event. The four MSGC counters are shown with crosses representing the positions of the hits. The cells of P1 which were equipped with electronics are indicated with a dotted line, while the hits are indicated with solid circles around the wires. The radii of the circles are obtained from the  $r(t)$  relation. The track fits perfect to the HSC hits as well as to the MSGC hits.

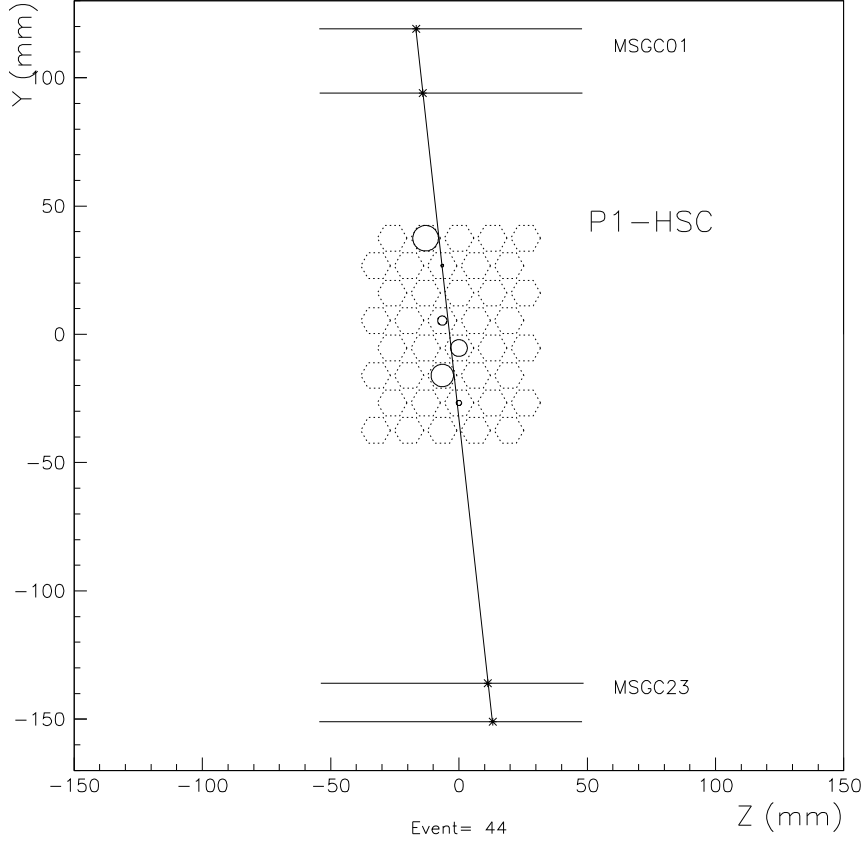


**Figure 5.21:** Event display of a well fitted event. All four hits in the MSGC match the track which is also well reconstructed in the HSC. The circles indicate the drift distance computed from the drift time with the current  $r(t)$  relation.

A total of 4,500 clean events have been selected for further analysis out of a total of 56,000. This severe cut in the data allowed us to select clean data with exactly one cluster of hits per MSGC and a low fraction of noise hits in the P1 chamber. No pattern recognition is thus needed in the MSGC setup, while the result of the analysis (a correct  $r(t)$ ) is not influenced by background.

#### 5.4.4.2 $r(t)$ determination

The positions of the MSGCs are determined in 10 iterations. After the last iteration the residual width of the MSGC hits was  $50 \mu\text{m}$ , giving a spatial resolution per MSGC of  $69 \mu\text{m}$ . The stability of the positions of all four planes was after 10 iterations better than the convergence criteria:  $|\Delta z| < 1.5 \mu\text{m}$  and  $|\Delta y| < 5.0 \mu\text{m}$ .

The result of the  $r(t)$  determination is shown in figure 5.22 after the last iteration. The combined spatial uncertainty of the P1 wires and MSGC strips is indicated in the two dimensional

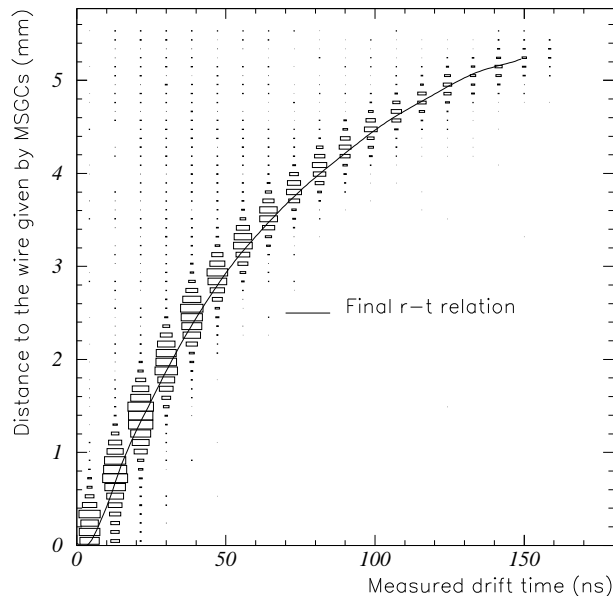


**Figure 5.22:** Scatter plot between the distance of the track to the P1 wire as given by the MSGC fit (vertical) and drift time as measured by the P1 chamber (horizontal). The solid curve indicates a fit through the scatter-plot and represents the  $r(t)$  relation as measured by the reference system.

density plot. This density distribution shows the measured distance between wire and track as given by the MSGCs versus the measured drift time measured by the indicated wire. The solid line in figure 5.22 is a fit through the scatter plot and represents the final  $r(t)$  as determined by the reference experiment.

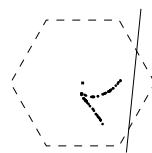
#### 5.4.4.3 Autocalibration

The dataset for the autocalibration algorithm was identical to the data used for the analysis including the reference detectors. A cut was applied on the angle of incidence  $\theta$  of  $\pm 250$  mrad to keep deviations of the  $r(t)$  as function of  $\theta$  within limits due to the hexagonal shape of the cathode. This effect is, however, only of concern for very large  $r$  ( $r > 5$  mm).

The angular width of the 11,000 analysed tracks was 126 mrad (rms), resulting in a determinant of 0.95, close to unity for a perfect cosmic (random) data sample. The reduction of the raw dataset to the quoted number of 11,000 was due to the mentioned  $\theta$ -cut and a limit on the maximum number of 'noise' hits (hits on wires which are not in the track fit).

In figure 5.23 the residuals are shown after the first and last (fifth) autocalibration iteration. The initial  $r(t)$  gives a good approximation of the final  $r(t)$  and only a small correction is needed, as can be seen in figure 5.24. Due to electronic pick-up of a signal approximately 150 ns after passage of the particle (produced by the digital controller of the MSGCs), it was not possible to reconstruct the  $r(t)$  for radii larger than 5.2 mm.

In spite of the small corrections of the  $r(t)$  with a maximum shift of 200  $\mu\text{m}$ , the single wire resolution improves significantly, as can be seen from the residual width in figure 5.23 after the last iteration. The final single wire resolution is 220  $\mu\text{m}$  (rms) close to the wire and 100  $\mu\text{m}$  between  $r = 4$  and 5 mm.



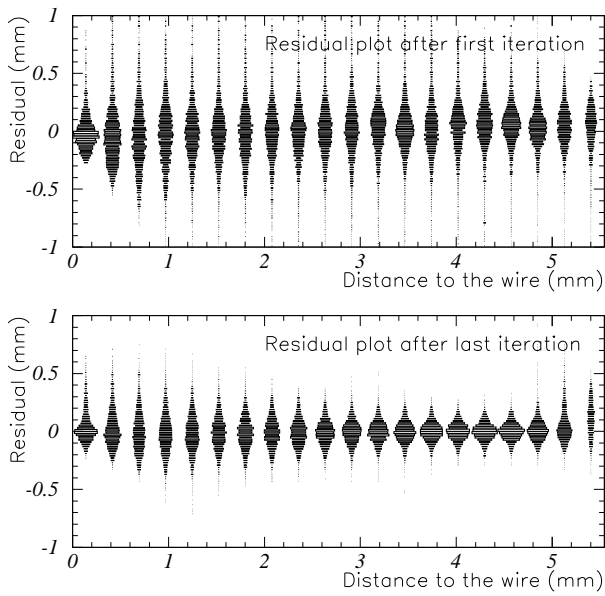


**Figure 5.23:** Residual plot as function of the distance from the track to the wire after the first and last (fifth) iteration. The initial  $r(t)$  is a good approximation and only small corrections on the  $r(t)$  have to be applied. Nevertheless, a clear decrease of the residual width can be observed.

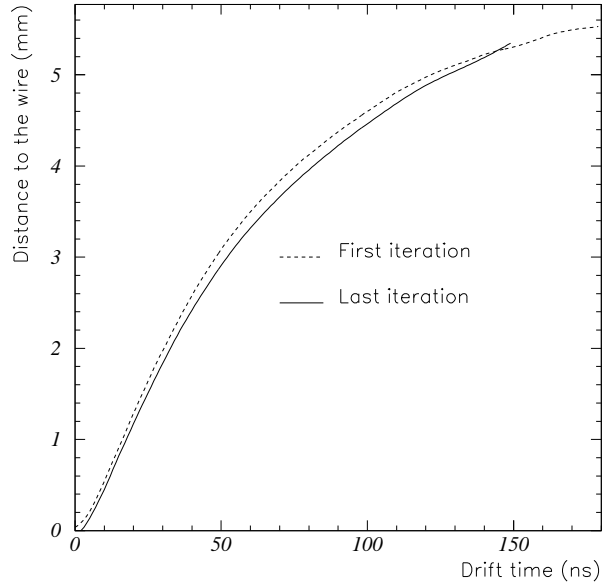


**Figure 5.24:** Initial and final  $r(t)$  relation after five iterations. The maximum time of drift was 150 ns due to pick up of the electronics.

#### 5.4.4.4 Comparison and conclusion

The  $r(t)$  curves in figure 5.22 and figure 5.24 have been merged and subtracted. This is done in figure 5.25 where the scale of the subtracted curve is magnified by a factor 10 (right hand scale).

The agreement between the two methods is very good in the region where the single wire resolution is minimal. Since the disagreement between the two methods for large drift times is everywhere smaller than  $30 \mu\text{m}$ , this can be neglected. For small drift times, the deviation between the two methods is nowhere larger than  $75 \mu\text{m}$  and in general much smaller. One has to compare this error with the stochastic error which exceeds  $200 \mu\text{m}$  rms.

One can understand the systematic deviation as shown in figure 5.25 by regarding the non-Gaussian shape of the residuals for small radii (due to the primary ionisation contribution in the resolution). Since the autocalibration algorithm (indirectly) works with the mean value of residual distributions, and the analysis of the reference experiment with Gaussian fits to the residuals, a systematic error can be expected.

One can conclude that this experiment gives confidence in autocalibration of  $r(t)$ . The algorithm should be handled with care. The determinant of  $[A]$  is a strong indicator of the confidence level of the result.

## References

- |  |  |
|--|--|
| <p>[1] G. Viehhauser, Detector Physics of the ATLAS MDT muon precision chambers, University of Vienna, PhD Thesis, 1996, Vienna, CERN.</p> <p>[2] A.P. Colijn, Cosmic ray and beam tests with the Honeycomb Strip Chamber, Master thesis, University of Utrecht, The Netherlands, November 21, 1994.</p> | <p>[3] P.R. Rewiersma, Internal Documentation EA, NH 19-6523, NIKHEF-H, Amsterdam, 1986.</p> <p>[4] P.R. Rewiersma, Internal Documentation EA,</p> |
|--|--|

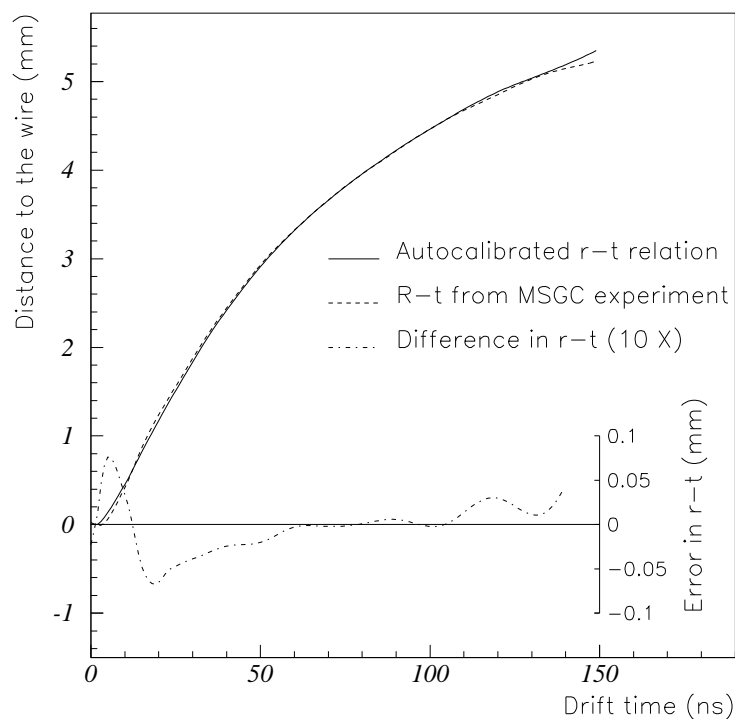
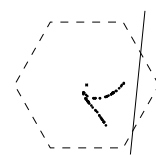


**Figure 5.25:** Comparison of the  $r(t)$  relations obtained with the reference experiment (dashed curve) and by autocalibration (solid curve). The difference between the two curves is indicated by the dot-dashed curve ( $10 \times$ , right hand scale).

NH 19-6121, NIKHEF-H, Amsterdam, 1986.

- [5] LeCroy Model 4208 8-channel wide range real time TDC, User's manual, Geneva, 1982.
- [6] J. Schmitz, The Microstrip Gas Counter and its ap-

plication in the ATLAS inner tracker, University of Amsterdam, PhD Thesis, 14 October 1994, Amsterdam.





# Chapter 6

## Detector performance

### Contents

---

<b>6.1</b>	<b>Introduction</b>	<b>99</b>
<b>6.2</b>	<b>Experimental setup</b>	<b>99</b>
6.2.1	Cosmic muon setup	100
6.2.2	The RD5 test facility	101
<b>6.3</b>	<b>Results from chamber tests</b>	<b>104</b>
6.3.1	Drift gas mixture	104
6.3.2	High voltage and threshold settings	111
6.3.3	The angle of incidence $\theta$	113
6.3.4	Primary ionisation density	115
6.3.5	The segmentation of the cathode in strips	118
6.3.6	The coordinate along the wire	119
6.3.7	$B$ -field study	121
6.3.8	P3 versus P3A	127
<b>6.4</b>	<b>Conclusions and outlook</b>	<b>128</b>

---

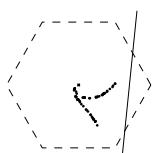
### 6.1 Introduction

**I**n this chapter the performance of the HSC prototypes will be discussed. Since many experiments have been done with three generations of prototypes (P1, P2, P3) in cosmic rays as well as in muon beams at CERN, the results will be ordered according to a specific study instead of chronological or per prototype. Therefore, I will start with a description of the cosmic ray facility in Amsterdam and a description of the RD5 experiment at CERN where all muon beam experiments have been performed.

### 6.2 Experimental setup

Since June 1992, the P1, P3 and P3A chambers have been tested in a cosmic ray setup at NIKHEF. The trigger, muon momentum filter and readout will be described in this section.

At CERN, several test beam experiments have been done with the P1, P2 and P3 chambers. The experiments have been done with and without magnetic field. The chamber read-out was integrated in the RD5 data acquisition (DAQ) and used the RD5 trigger system.



### 6.2.1 Cosmic muon setup

The P1 and P3 chamber have been tested in a cosmic muon setup. The muons have their origin in showers developed by high energetic pions and protons in the atmosphere. The momentum distribution of the muons peaks at sea level at approximately 1 GeV/c with a long tail to high momenta. Due to the origin of the muons, their angle of incidence distribution is peaked around the vertical direction. In order to have a maximum flux, the geometric acceptance was optimised for vertical muons.

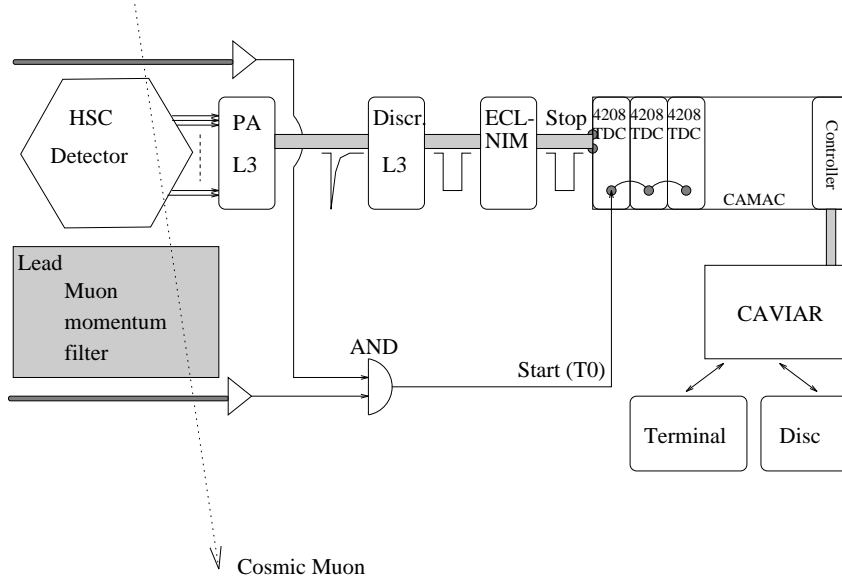


**Figure 6.1:** Experimental setup of the experiments in cosmic rays. The trigger and  $T_0$  are defined by two scintillators. The L3 pre-amplifier was mounted on the detector as close to the anode wires as possible. The signals from the pre-amplifiers are fed in the discriminators. The ECL signals were converted in standard NIM pulsed and fed in the LeCroy 4208 TDCs which were operated in common start mode.

In figure 6.1 the setup and readout chain of the cosmic ray experiments is shown. The angular acceptance of the setup is determined by the positions of the scintillators. Due to the presence of low energetic muons in cosmic rays, a momentum filter is used to absorb all low momentum muons. A cutoff energy of 1 GeV can be achieved with 40 cm of lead. GEANT simulations have shown that 40 cm of lead will result in a maximum contribution of 10  $\mu\text{m}$  in the resolution of the HSC due to multiple scattering. A higher muon momentum cut-off will only reduce the flux further and is thus unfavourable.

The current signals on the wires are amplified as close to the chamber as possible. The pre-amplification of the signal is done with the L3 pre-amplifier. This very fast (rise time 5 ns) pre-amplifier is designed and used for the L3 barrel muon chambers. Of these, 48 amplifiers are mounted on one board. The analogue bipolar signals are transported to the discriminator by twisted pair shielded cables of approximately 15 m length. The signals are fed into a discriminator with variable threshold setting. The discriminator was also designed and used for the L3 barrel muon chambers and were mounted in groups of 48 on one board. The discriminator is designed around the LeCroy MVL407 quad ultrafast voltage comparator. The discriminator driver produced a bipolar ECL time over threshold signal which is converted in a standard NIM signal in an ECL to NIM converter. Finally the standard NIM signals are fed into an 8-channel LeCroy 4208 TDC with a binning of 1 ns.



The trigger and start signal are obtained from a logic AND gate of the two scintillators, where the upper scintillator delivered the timing of the signal to minimise jitter on the  $T_0$ . Data acquisition is done by a CAVIAR computer. The CAVIAR read the data from the TDCs in a continuous loop and wrote the drift times to disk for off-line analysis.

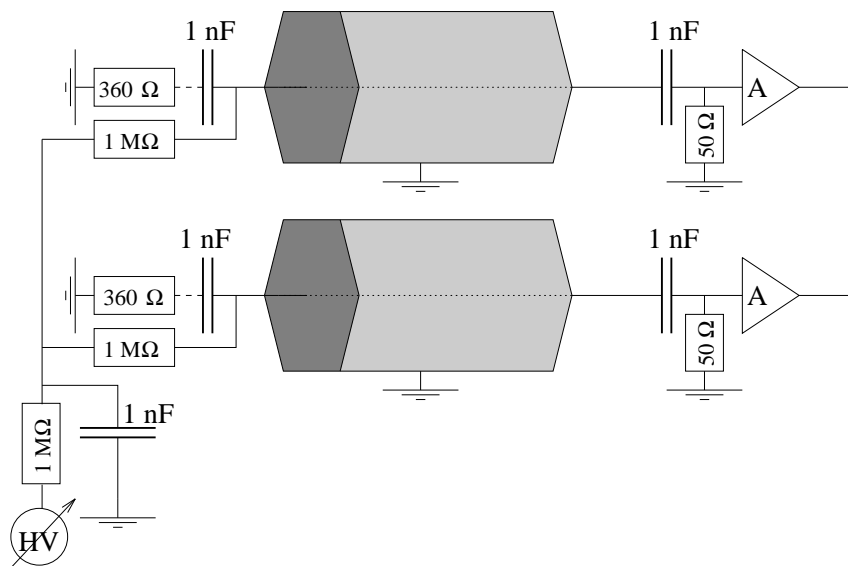


**Figure 6.2:** Electronic layout of the HSC as a drift tube. The high voltage distribution, optional terminating resistances and pre-amplifier connections are indicated.

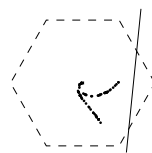
Figure 6.2 shows how the anode voltage is put onto the wires via a low pass filter (RC-time 1 ms). The wires of all individual tubes are connected to the HV supply via 1 MΩ resistors. At the side of the pre-amplifiers, the high voltage is decoupled via a 1 nF capacitor. The signals are fed into the pre-amplifier at a typical impedance of 50 Ω. This scheme is repeated for all HSC detectors, with the exception of the P3 chambers where the wire is terminated at the HV side with the characteristic impedance of 360 Ω. This optional terminating resistor is indicated in figure 6.2 with a dashed line.

## 6.2.2 The RD5 test facility

The RD5 experiment is situated at the H2 beam of the SPS North Area at CERN. The RD5 programme covers several topics related to muon detection at LHC: punchthrough measurements, trigger studies, muon momentum measurements, and tests of various types of large area muon chambers [1].

The experimental setup is shown in figure 6.3. The experiment consists of two magnets, a superconducting air core solenoid with 3 T maximum field (the former EHS magnet) and an iron core magnet producing a 1.5 T field. This so-called 'absorber magnet' provides 10  $\lambda$  addition interaction lengths, thus simulating a calorimeter for the muon chambers down-stream the experiment (see figure 6.3). The scintillator counters S1 to S7 are used to define the trigger. As indicated in figure 6.3 various beam types were available. In all our experiments we only used  $\mu^-$  beams in the momentum range between 100 and 300 GeV/c.

NIKHEF has participated with the HSC in RD5 in the physics programme and with muon chamber tests. The TRACAL (TRACKing CALorimeter) detector was located in the EHS magnet from 1991 until 1994 and consisted of 25 HSC monolayers, interleaved with stainless steel



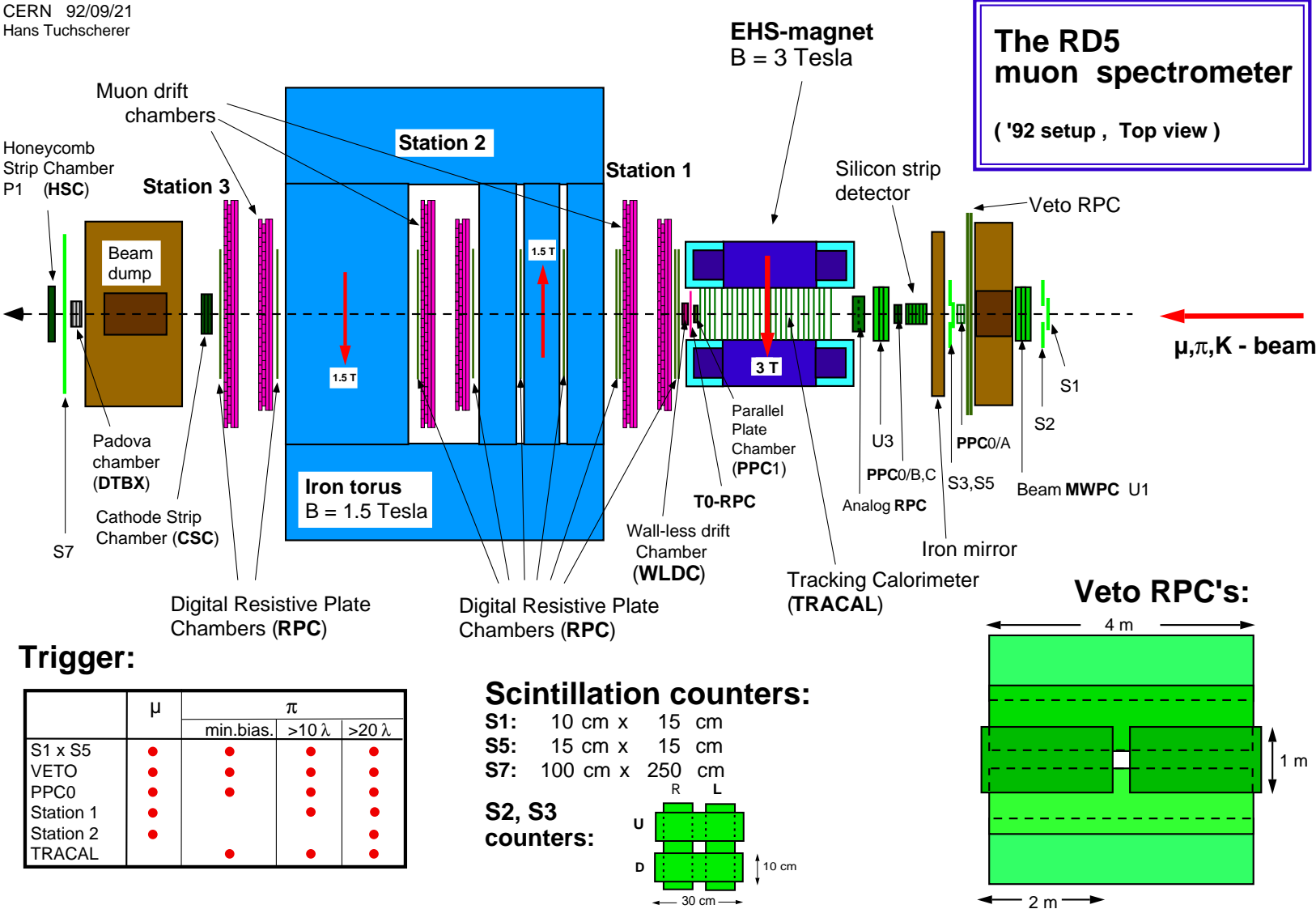


**Figure 6.3:** The RD5 experiment. The P1 and P3 detector have been tested inside the 3 T EHS magnet. In the drawing P1 is positioned downstream of the experiment for additional measurements without magnetic field.

absorbers. The TRACAL detector was used to perform the extensive muon punchthrough programme [2, 3]. Since 1992, all multilayer HSCs were tested in the RD5 experiment. All studies with the P2 chambers and studies with P1 without magnetic field were performed downstream of the experiment. The P1 and P3 chamber were also tested inside the 3 T EHS magnet.

The HSCs were tested independent from other tracking chambers. This means that no global trackfit through the whole experiment was performed. All test-results in this chapter are therefore based on in-situ consistency of the measured muon position. The main advantage of experimenting in RD5 were (beside the use of the magnet) the infra-structural facilities like DAQ, on line monitoring, gas systems and the use of common facilities like mechanical designers, engineers and their workshops.

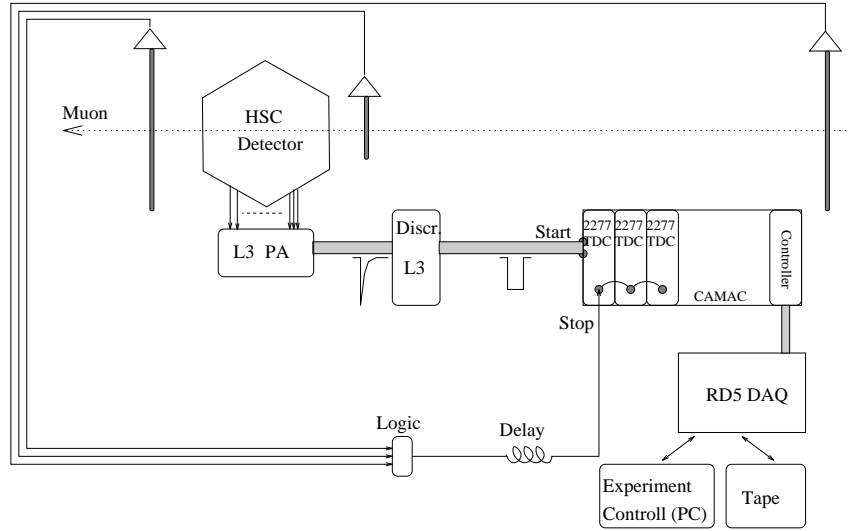
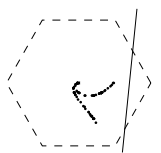


**Figure 6.4:** Experimental setup in the RD5 muon beam. The trigger is defined by a set of scintillators. The pre-amplifier and discriminator have also been used in the cosmic ray experiments. The ECL signals from the discriminator are directly fed in the LeCroy 2277 TDCs. The TDCs were operated in common stop mode.

In figure 6.4 the setup and readout chain of the experiments with the P1, P2 and P3 chamber are shown. The trigger and  $T_0$  are defined by a set of scintillators and logic units. Due to the delays in cables and units of the trigger electronics, it was not possible to deliver the  $T_0$  signals before the first signals from the anode wires arrived at the TDCs. Therefore we used the 'common stop' mode. This means that the signals on the anode wires start the time measurement and the stop is delivered after the last signal has arrived. In this case the  $T_0$  has to be delayed with a constant amount of time. This delay is between 500 ns and 2  $\mu$ s depending on the maximum drift time.

The LeCroy 2277 TDC has 16 bipolar ECL inputs which matches with the 16-channel outputs of the L3 discriminator. The 2277 TDC has multi-hit capacity per channel per event [4]. The 2277 TDCs are located in a CAMAC crate and read out by the RD5 DAQ system. The data is written on 200 Mbyte cartridges in ZEBRA format and on-line histogramming is done to obtain fast feedback about the status of the detector.



## 6.3 Results from chamber tests

The data from cosmic ray experiments and beam-tests is analysed with a FORTRAN77 programme HGANA. This programme was initially written in 1991 to study autocalibration on simulated drift-time data. Today, HGANA has evolved into an allround drift tube analysis programme. The programme performs track pattern recognition on wire data as well as on strip data. The  $r(t)$  relation can be obtained as described in chapter 5. Optionally, the relative position of the monolayers (and even individual wires) can be fitted. See appendix C for more details on HGANA.

Study	Section	Detectors
Drift gas mixture	6.3.1	P1
HV/ $V_{th}$	6.3.2	P3
Angle of incidence $\theta$	6.3.3	P1/P3
Primary ionisation density	6.3.4	P1
Segmented cathode (strips)	6.3.5	P2
The coordinate along the wire	6.3.6	P3
$B$ -field	6.3.7	P1/P3
Aluminium versus Mylar/Cu cathode	6.3.8	P3/P3A

**Table 6.1:** Experimental programme.

Since a large amount of data (and thus results) from chamber tests is available, the presentation of these results has to be as compact as possible. For this reason, the results of the measurements and simulations will be presented in separate 'studies'. Those studies are indicated in table 6.1. For all studies is indicated which prototypes were used.

### 6.3.1 Drift gas mixture

The characteristics of a drift tube are dominated by the choice of the drift gas. Most commonly used drift gases contain a large fraction of argon and some sort of quencher like  $CO_2$  or hydrocarbons like methane, ethane or iso-butane. Those quenching molecules have large cross-sections for the absorption of photons, produced in the amplification process. The absorption of those photons is required to prevent gas gain instability and possibly high voltage break down.

Recently, the use of  $CF_4$  as gas component has become popular in straw tubes because it shows high electron drift velocities and (in some cases) good ageing properties. Most of the HSC tests are performed with Ar/ $CO_2$  mixtures. Some tests are done with Ar/ $CO_2$  and a small fraction of  $CF_4$  added.

In this section, the performance of the P1 prototype will be discussed with Ar/ $CO_2$  80/20 and 50/50 gas mixtures. Finally, fractions of 15% and 30% of  $CF_4$  were added to a pre-mixed Ar/ $CO_2$  80/20 mixture.

All results from simulations are computed as described in chapter 4. For all simulations, 10,000 tracks have been produced, randomly distributed over the volume of the cell.

In figure 6.5 the simulated and experimental TDC spectra as measured with P1 are shown for Ar/ $CO_2$  80/20. The maximum drift time in the simulation is 220 ns, while the measured TDC spectrum shows a tail up to 280 ns. This difference in the spectra for large drift times corresponds

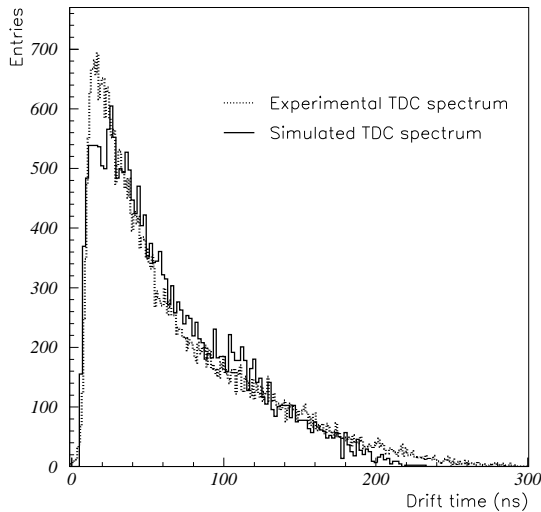


**Figure 6.5:** Measured and simulated TDC spectra of the P1 detector with Ar/CO<sub>2</sub> 80/20 drift gas. The anode wire diameter was 20  $\mu\text{m}$  and 1700 V was put on the wire.

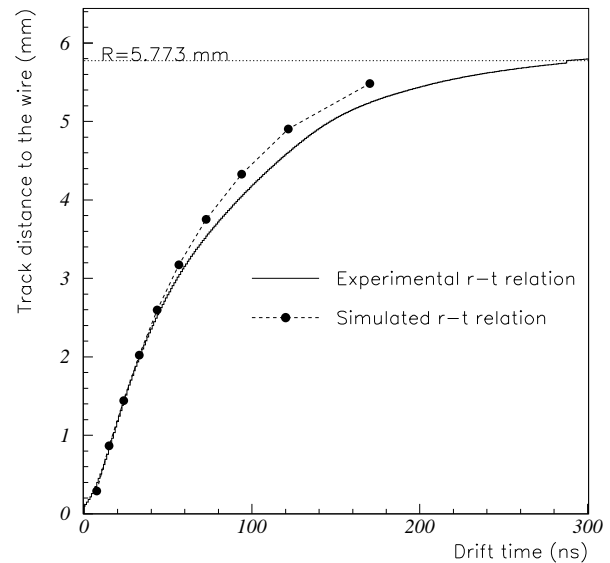


**Figure 6.6:** Measured and simulated  $r(t)$  for the same experimental situation as in figure 6.5. The angular  $\theta$  distribution of the cosmics was centred around  $0^\circ$ .

to the difference between the simulated  $r(t)$  and autocalibrated  $r(t)$  in figure 6.6. The agreement between the simulated and measured  $r(t)$  is good for drift distances up to  $r = 3$  mm. For  $r > 3$  mm the curves start to deviate. This is an ever present effect when comparing many simulated and measured  $r(t)$  relations.

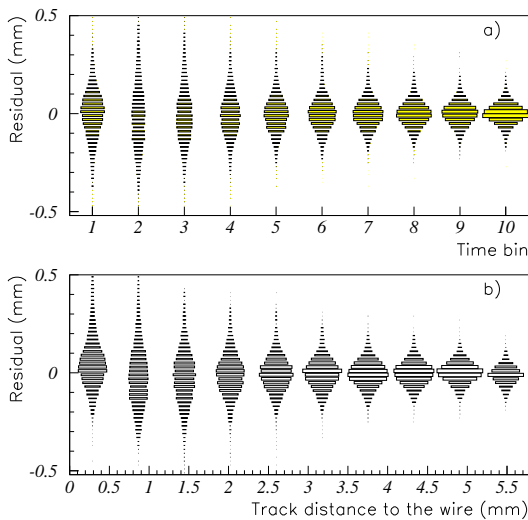


**Figure 6.7:** Measured residual distributions. The hits are binned according to the measured drift time (a) and according to the fitted track distance to the wire (b).

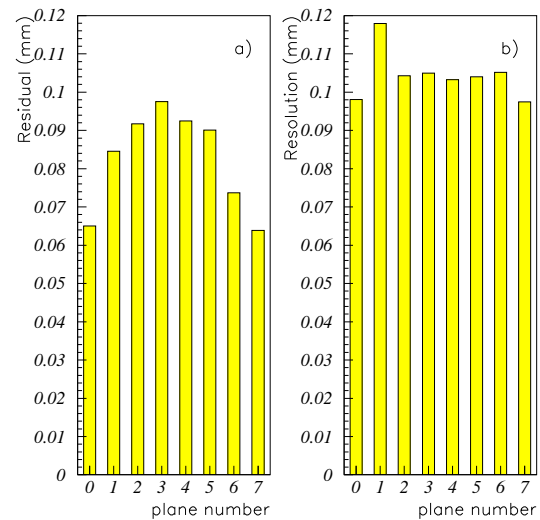
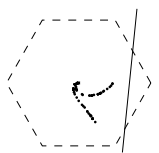


**Figure 6.8:** a) Measured residual width per plane. The experimental situation is described in figure 6.5; b) The resolution per plane as derived from the residuals and corrected for systematic errors in the track fit.



Some attention will be given to the details of the analysis of the Ar/CO<sub>2</sub> 80/20 data of P1. In the remainder of this chapter, many graphs will be shown of the resolution of the drift cell versus the track distance to the wire. Several problems have to be solved before those plots can be produced. In figure 6.7 the residuals are plotted in 10 bins. The first problem is: how to define the bins? In the upper residual plot the bins represent time intervals from  $t = 0$  for the left edge of the first bin to  $t = T_{\max}$  for the right edge of the tenth bin. The  $r(t)$  relation is corrected using the residual shifts of those 10 bins, resulting in a  $10 \times 10$  autocalibration-matrix (see chapter 5). Figure 6.7a shows the residuals after the last iteration and all residuals are centred around zero. In case the residuals are plotted in bins of  $r$ , covering the whole cell from  $r = 0$  to  $r = R_{\max}$ , the residuals appear as in figure 6.7b. A problem arises for small  $r$  (or small  $t$ ). It can clearly be seen in figure 6.7b that the first residual shows a systematic shift upwards. This effect is due to the non Gaussian residuals for small drift distances. The resolution is dominated by primary ionisation statistics, resulting in an asymmetric drift time distribution for tracks passing the wire at a fixed distance. Since the residuals are not Gaussian in this region close to the wire, a fundamental choice has to be made. Does the  $r(t)$  relation describe the  $\bar{r}(t)$  or  $r(\bar{t})$ ? The last definition assigns to a value  $r$  the mean of the measured drift times corresponding to the distance  $r$ . I have used the first definition of  $r(t)$ , where the mean of the fitted  $r$  values is assigned to the measured  $t$ . The definition of  $r(t)$  as  $\bar{r}(t)$  has a good reason. Imagine tracks passing the wire at  $r = 0$ . The mean measured drift times for those tracks will be non-zero and positive. In the definition of  $r(t)$  as  $r(\bar{t})$ , this means that for  $r = 0$  the corresponding  $t$  value is larger than zero. What to do with smaller drift times? In our definition where  $r(t)$  is defined as  $\bar{r}(t)$  this problem does not occur. In case  $t = 0$  is measured, the distance from the track to the wire has to be *exactly* 0 mm. The  $r(t)$  relation will cross ( $t = 0, r = 0$ ) per definition.

Once the method of binning of the residuals is defined we can compute them from the data. In figure 6.8a the residual widths are plotted per plane. The widths of the residuals depend on the plane number. This effect is well understood and is due to the effect that the hit which residual is computed is used to define (fit) the track. The true resolution is under-estimated and the amount of 'underestimate' is a function of the position of the hit on the track with respect to the positions of the other hits. For hits in the middle of the track it is harder to influence the position of the track than for hits at the end of the track. As an alternative, one can exclude the hit, which residual is computed, from the fit. In this case the true resolution will be over-estimated. Since this effect is well known, one can compute correction factors per plane to compute from the residual width the single wire resolution. The resolution per plane is shown in figure 6.8b where the average resolution per plane is 105  $\mu\text{m}$ . The average residual width is computed by a Gaussian fit to the residuals of all hits in a plane, irrespective of the drift distance.

In figure 6.9 the measured resolution is shown versus the distance of the track to the wire. Without any cuts on the data a resolution of 100  $\mu\text{m}$  is achieved at  $r = 5$  mm. In figure 6.10a the angular distribution of the tracks is shown. This distribution is slightly asymmetric due to the positioning of the scintillator counters. The distribution is also very wide with respect to the  $2\pi/6$  periodicity of the honeycomb cell. The honeycomb cell causes the  $r(t)$  relation to be a function of the angle  $\theta$ . This dependence is small for small drift radii, but is relevant in the outer corners of the cell. After applying a cut on  $\theta$  of  $\pm 100$  mrad, the resolution improves to 80  $\mu\text{m}$  at  $r = 5$  mm.

In addition, I have tried to fit the individual positions of the wires. The mechanical precision was very good and the wires were at their positions within 30  $\mu\text{m}$ . The single wire resolution, with the cut on  $\theta$  and fit of the wire positions, is shown in figure 6.9. In this figure the result of the simulated resolution is also plotted. In the simulation, a gain of  $2 \times 10^5$  was assumed and the

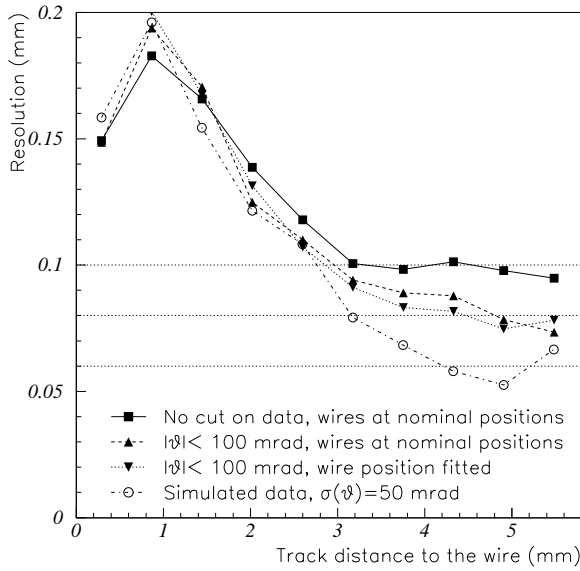


**Figure 6.9:** Measured resolution of the P1 cell with Ar/CO<sub>2</sub> 80/20, HV=1700 V and 20 mV threshold on the discriminator. The resolution is shown for different cuts on the accepted angle of incidence  $\theta$ . The apparent improvement of the resolution for small track distances is due to the non Gaussian shape of the residual in this region of the cell. The result of the simulated resolution (as described in chapter 4) is also shown.

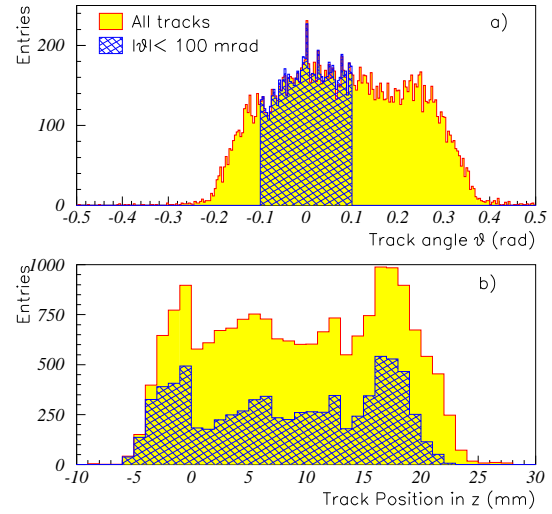
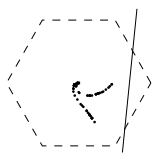


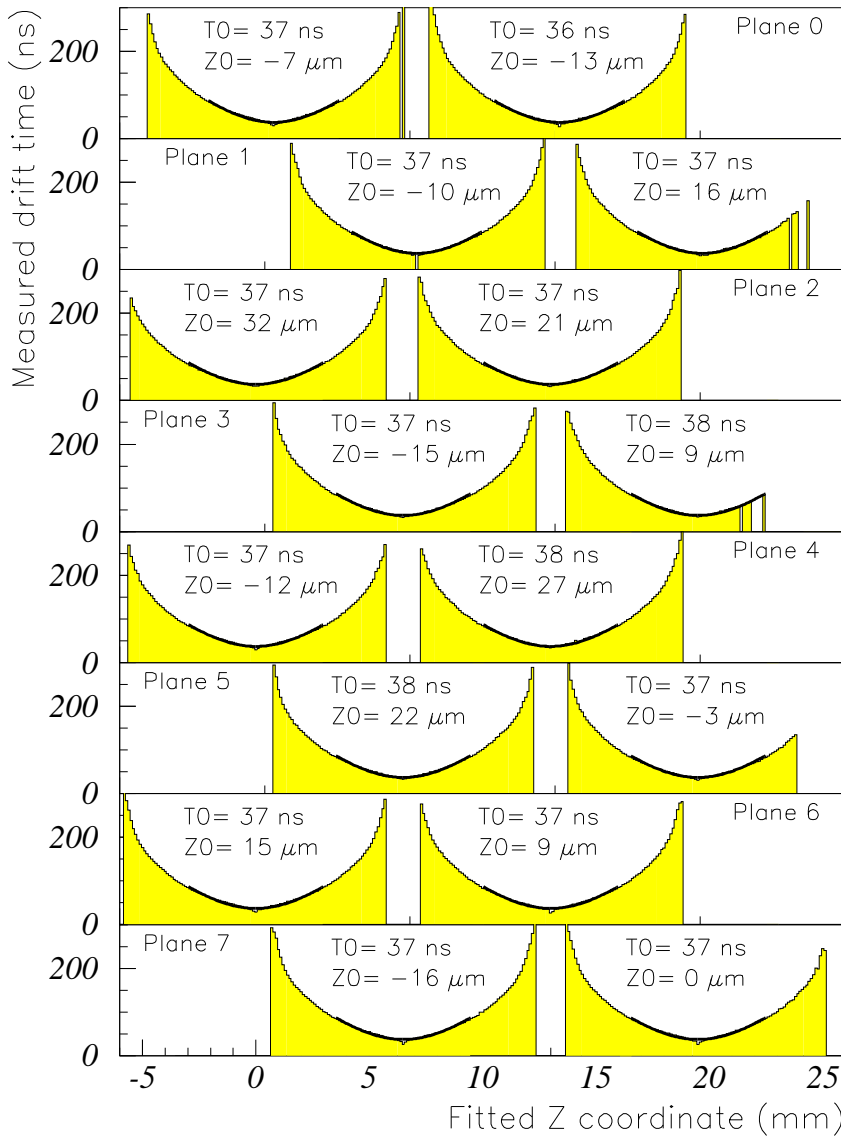
**Figure 6.10:** a)  $\theta$  distribution of the cosmic data sample. The cut as used in figure 6.9 is indicated; b) Reconstructed  $z$  coordinate (perpendicular to the wire-plane, see figure 3.1) of the tracks in case no cut is applied and in case  $|\theta| < 100$  mrad.

threshold of the discriminator was 20 mV, as in the experiment. The agreement with the data is good up to drift radii of 3 mm and then the simulation shows systematically better performance as measured. We will see this is all simulations. The combined effect of primary ionisation and gas gain is well simulated. At the end of the cell (where diffusion, the hexagonal geometry and possibly cathode positioning errors become dominant) the simulated resolution is systematically lower than the measured one.

Figure 6.11 demonstrates how the fit of the  $T_0$  per wire and the fit of all individual wire positions is performed. In the figure the fitted distance from the track to the wire is shown versus the measured drift time on the wire. This is done for two wires per plane and in total eight planes. Tracks passing the wire at the left side appear with negative sign for the drift distance and tracks at the right side with positive sign. This results in two nearly symmetric  $r(t)$  relations for each wire. In the region  $\pm 2$  mm around the wire, a parabolic fit is performed on the double- $r(t)$ . The minima of the parabola represent the relative correction on the individual  $T_0$  and the horizontal shift of the parabola represents the relative shift of the wire in the  $z$  direction. The values of the relative  $T_0$  and  $z$  shifts are indicated in figure 6.11 for each wire individually.

The experiment with the P1 detector was continued by adding more CO<sub>2</sub> to the gas mixture. The chamber was operated with Ar/CO<sub>2</sub> 50/50. From figure 3.18 and 3.19 we see that the diffusion characteristics of CO<sub>2</sub> approach the thermal limit, so a better spatial resolution can be expected. Adding more CO<sub>2</sub> leads also to lower drift velocities. Notwithstanding the increase in high voltage from 1700 V for Ar/CO<sub>2</sub> 80/20, to 2100 V for Ar/CO<sub>2</sub> 50/50, maintaining the gain at  $2 \times 10^5$ , the maximum drift time increases from 280 ns to 500 ns. This can be seen in





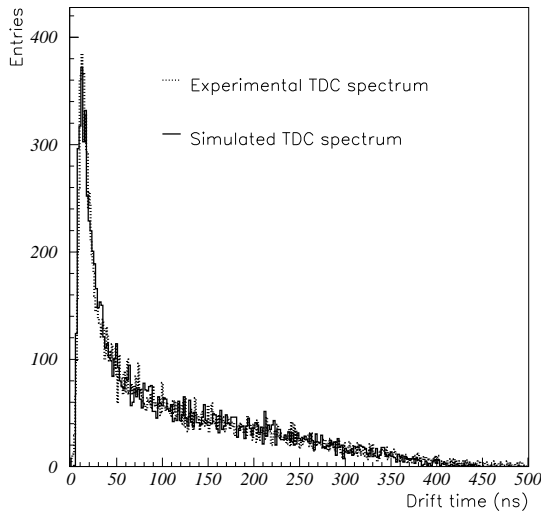
**Figure 6.11:** Measured drift time versus the fitted  $z$  coordinate for 16 wires distributed over eight planes. The measured curves are fitted by parabolas, indicated by the thick solid lines. In the analysis, all wires were positioned at their nominal positions. A relative vertical shift of the fitted parabola indicate the error on the  $T_0$  of the wire and a horizontal shift of the parabola indicates the mis-alignment of the wire.

figure 6.12 where the simulated and measured TDC spectra are plotted.

As in figure 6.9, the reconstructed resolution for all data without any cuts is plotted and the measured resolution after a cut on the angle of incidence  $\theta$  is applied. The resolution at  $r = 5$  mm equals  $60 \mu\text{m}$ , where the simulation predicts  $40 \mu\text{m}$ .

During test beam experiments with P1 in RD5, different gas mixtures have been tested. The 'standard' Ar/CO<sub>2</sub> 80/20 and 50/50 mixtures have been used and two mixtures with CF<sub>4</sub>, Ar/CO<sub>2</sub>/CF<sub>4</sub> 68/17/15 and 56/14/30, have been tested. Some changes were made with respect to the cosmic ray experiment. The wire diameter was changed from  $20 \mu\text{m}$  diameter to  $30 \mu\text{m}$ ; the





**Figure 6.12:** Measured and simulated TDC spectra for the P1 chamber with Ar/CO<sub>2</sub> 50/50 drift gas and operated at 2100 V.

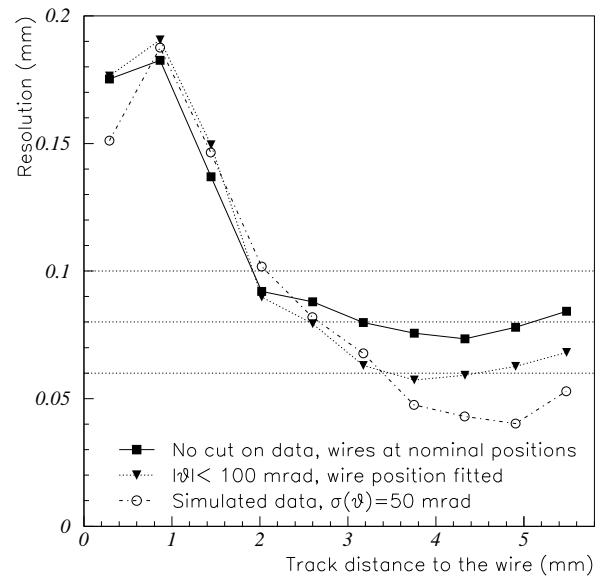


**Figure 6.13:** Measured and simulated resolution of the P1 cell with the experimental conditions as in figure 6.12. The threshold on the discriminator was 20 mV.

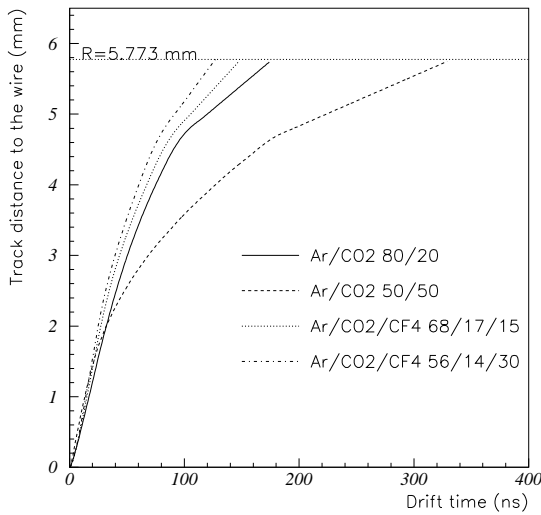


**Figure 6.14:** Simulated  $r(t)$  relations for four different gas mixtures in the P1 cell with 30  $\mu$ m wire diameter. The drift fields had the same value as during the measurements in figure 6.15.

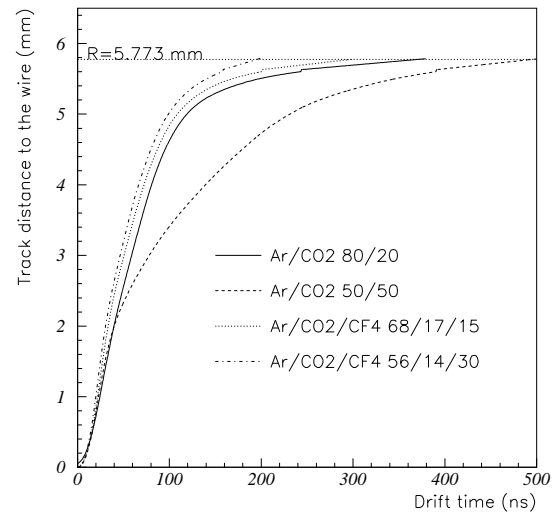
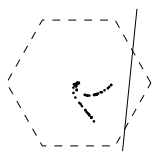


**Figure 6.15:** Measured  $r(t)$  relations for four gas mixtures. The high voltage on the anode wires is for each gas as indicated in figure 6.17.

chamber was rotated over 90° to have the planes perpendicular to the beam, and the LeCroy 4208 TDC was replaced by the LeCroy 2277 TDC. The threshold of the discriminator had to be put at 30 mV due to the increased noise level in the RD5 environment with respect to the situation in the cosmic ray test. From all HSC prototypes the P1 detector was the most sensitive for pick-up noise since no additional shielding was provided around the detector. The P2 and P3 detectors



were all designed as Faraday cages, minimising electro-magnetic leakage from the outside into the interior of the detector.

The simulated  $r(t)$  relations for the above mentioned gases are shown in figure 6.14. The addition of 15% and 30%  $\text{CF}_4$  to the  $\text{Ar}/\text{CO}_2$  80/20 mixture causes a reduction of the drift times. In figure 6.15 the measured  $r(t)$  relations are shown. The agreement with the simulation in figure 6.14 is good for  $r < 5$  mm. The gases containing  $\text{CF}_4$  are only marginally faster than  $\text{Ar}/\text{CO}_2$  80/20.

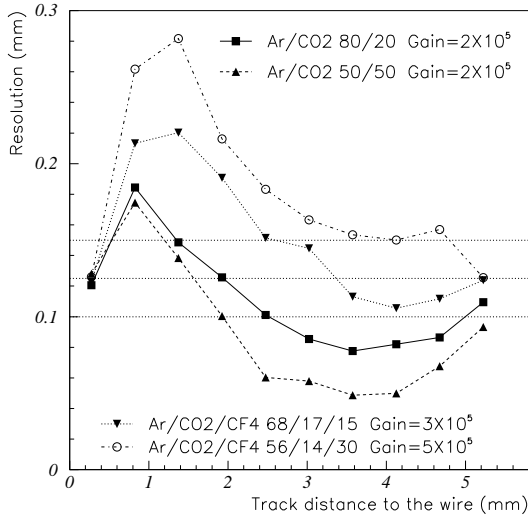


**Figure 6.16:** Simulated resolution for the same gas mixtures as discussed in figure 6.14. The gain has been increased for the gases containing  $\text{CF}_4$  with respect to the  $\text{Ar}/\text{CO}_2$  mixtures because of the large attachment effects in gases containing  $\text{CF}_4$ . The simulation was performed for  $\theta = 15^\circ$ .

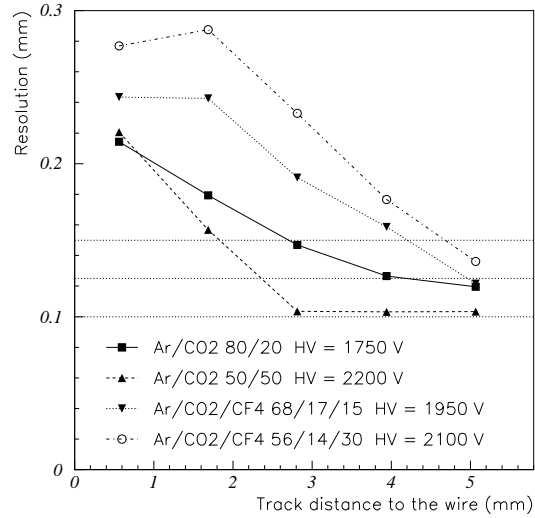


**Figure 6.17:** Measured resolution for the same gases as simulated in figure 6.16. The operation high voltage on the anode wires is indicated in the figure.

Although the  $r(t)$  relations for  $\text{Ar}/\text{CO}_2$  80/20 and the tested  $\text{Ar}/\text{CO}_2/\text{CF}_4$  mixtures are quite similar, the performance of the gases is very different. This can be seen in figure 6.16 where the resolution is simulated for the four gases. Note the high gain of  $3 \times 10^5$  and  $5 \times 10^5$  for the gases containing  $\text{CF}_4$ . This gain was chosen in view of the simulation to have the simulated resolutions in the same order of magnitude as the measured ones. In figure 6.17 the measured resolutions are shown. No absolute gain measurement is done during the experiments. Therefore, the gain used in the simulation was based on the shape of the measured resolution curve. Especially the radius where the primary ionisation contribution to the resolution is not longer dominant is a strong function of the gain.

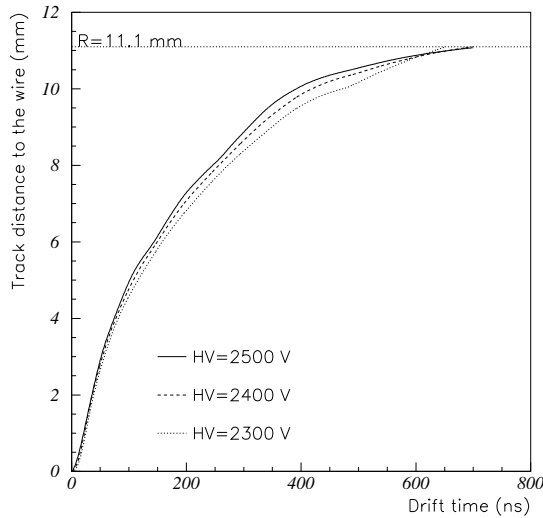
It can be seen in figure 6.16 and 6.17 that the simulated and measured resolutions are poor for the  $\text{CF}_4$  containing gas mixtures. This is due to the attachment of drifting electrons close to the amplification region. From MAGBOLTZ calculations we find that the attachment probability for an electron drifting from the point of ionisation to the wire is 65% for  $\text{Ar}/\text{CO}_2/\text{CF}_4$  68/17/15 and 80% for  $\text{Ar}/\text{CO}_2/\text{CF}_4$  56/14/30.

The measured resolution curves for  $\text{Ar}/\text{CO}_2$  80/20 and 50/50 gases show minima at 120  $\mu\text{m}$  and 100  $\mu\text{m}$  with approximately the same gain as during the cosmic ray experiments, in which a resolution of less than 100  $\mu\text{m}$  was obtained. This deterioration of the performance is probably

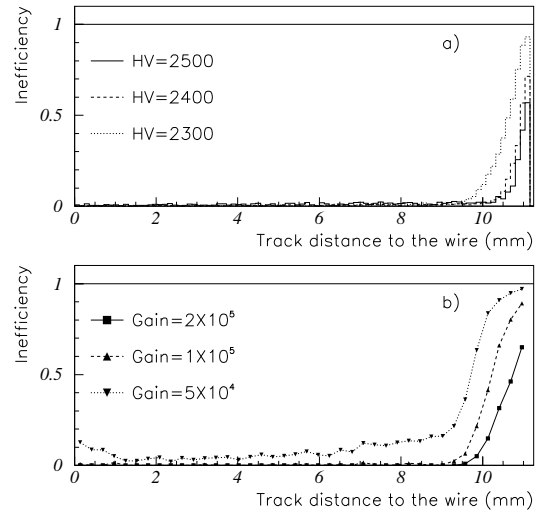
due to pick-up on the wires of all sorts of electro-magnetic signals. The effects of this type of contribution in the resolution is very hard to simulate if the characteristics of the superimposed signals are unknown. Therefore, no attempt has been made in this study to simulate this type of backgrounds.

### 6.3.2 High voltage and threshold settings

For drift tubes operated at 1 bar pressure and with a diameter smaller than 2 cm, the detection of the first electron out of the primary ionisation arriving at the wire provides the best position measurement of the track. This means that the gain has to be as high as possible and the discriminator level as low as possible. During all experiments the values of the high-voltage on the anode wires and the threshold on the discriminator were determined by cross-talk considerations. In practice this means a gain of approximately  $2 \times 10^5$ , equivalent to 12 mV output signal from the L3 pre-amplifier for single electrons. In testbeam situations the threshold on the discriminator was between 20 and 30 mV. This shows that it is difficult to trigger on the first arriving electron. From the experiments we learned that triggering on the third to the tenth electron is more realistic.



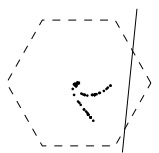
**Figure 6.18:** Measured  $r(t)$  curves for the P3 chamber with  $\text{Ar}/\text{CO}_2/\text{C}_2\text{H}_6$  70/25/5 for different high voltages on the anode wires. The angle of incidence  $\theta$  of the tracks was  $15^\circ$ .



**Figure 6.19:** Measured (a) and simulated (b) inefficiency as function of the high voltage (a) or gain (b).

The high-voltage does not only affect the gain, but also the  $r(t)$  relation. This is demonstrated in figure 6.18 where three  $r(t)$  curves are shown as measured in the P3 chamber in the RD5 experiment with  $\text{Ar}/\text{CO}_2/\text{C}_2\text{H}_6$  70/25/5. The increase of the drift velocity with increased electric field strength is obvious. The gain does also affect the efficiency of the tube. In figure 6.19a the inefficiency of the tube to detect a fitted track is shown for different settings of the high voltage in the experiment. In figure 6.19b is the inefficiency shown as function of the the gain in the simulation. All data is produced for tracks with angle of incidence  $\theta$  of  $15^\circ$ . The inefficiency in the corner of the hexagonal cell is due to the decreased length of the track-path inside the cell.

Figures 6.20 and 6.21 show the measured and simulated resolution for the same high voltage



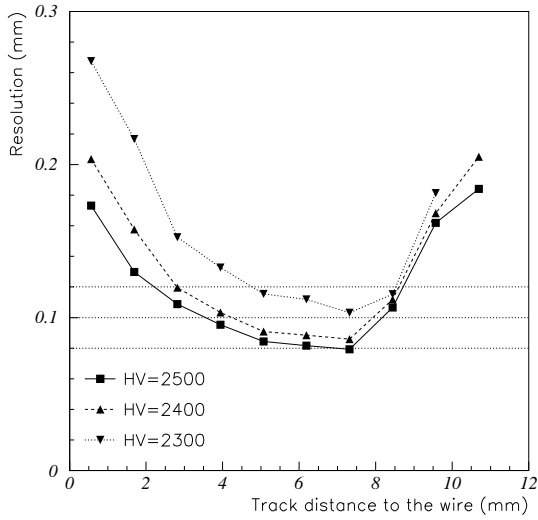


**Figure 6.20:** Measured resolution for different high voltages on the anode wire of the P3 cell with  $\text{Ar}/\text{CO}_2/\text{C}_2\text{H}_6$  70/25/5 drift gas,  $\theta$  was  $15^\circ$  and the threshold on the discriminator was set to 20 mV.

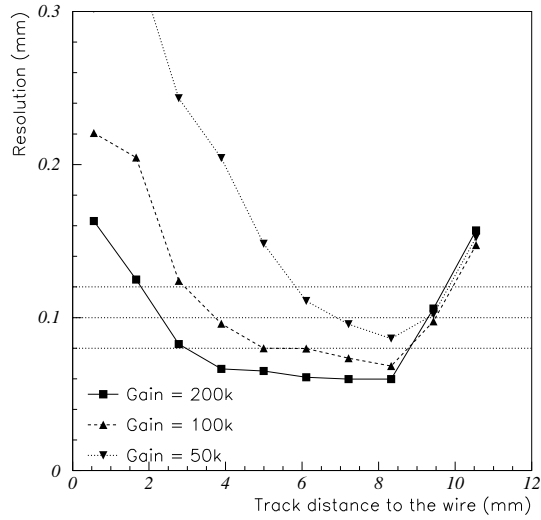


**Figure 6.21:** Simulated resolution for different settings of the gain. The simulated conditions were as described in figure 6.20.

and gain settings as in figures 6.18 and 6.19. The measurement and simulation show both a deterioration of the resolution for lower gains. The impact on the resolution is the largest for small drift distances and is negligible for  $r > 8$  mm where the hexagonal shape of the cell dominates the resolution. The effect of the hexagonal shape of the cell on the resolution will be further discussed in sections 6.3.3 and 6.3.7.

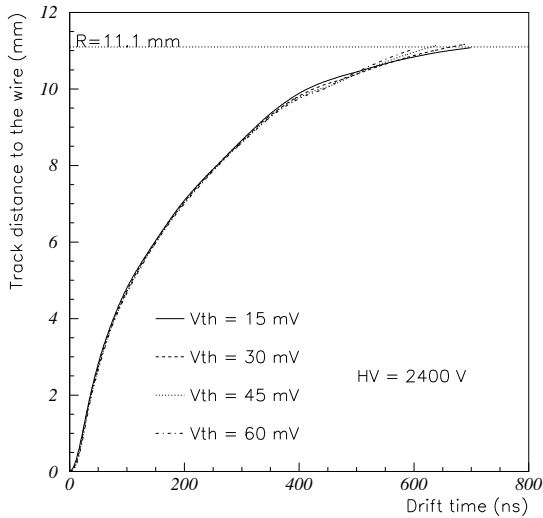


**Figure 6.22:** Measured  $r(t)$  curves for the P3 chamber with  $\text{Ar}/\text{CO}_2/\text{C}_2\text{H}_6$  70/25/5 for different thresholds on the discriminator. The high voltage was 2400 V and  $\theta = 15^\circ$ .

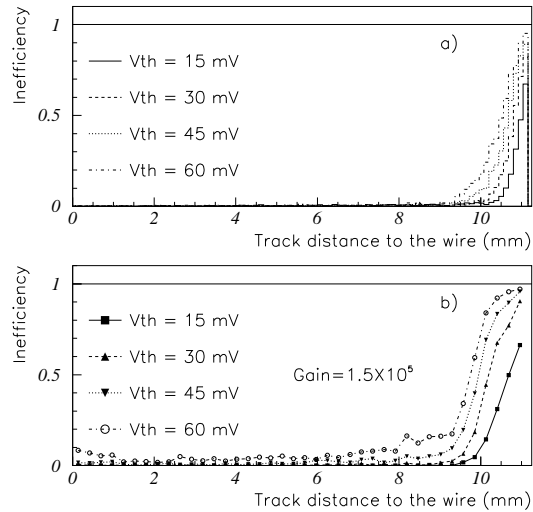


**Figure 6.23:** Measured (a) and simulated (b) inefficiency curves for the same experimental setup as described in figure 6.22.

The effect of the value of the threshold of the discriminator on  $r(t)$  is negligible, as can be seen in figure 6.22. In this figure the measured  $r(t)$  relations are shown for the same experimental conditions as for the high voltage scan. In figure 6.23a the inefficiency is shown as measured for a fixed high voltage of 2400 V and four different threshold levels, and as simulated (figure 6.23b) with a fixed gain of  $1.5 \times 10^5$  and the same threshold levels.

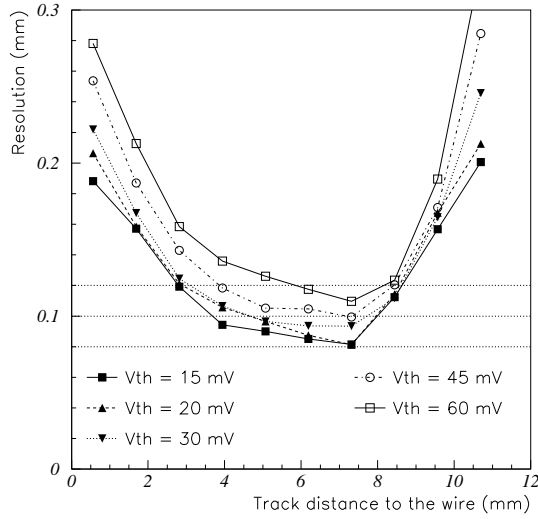


**Figure 6.24:** Measured resolution for different values of the threshold setting on the discriminator. Experimental settings are as described in figure 6.22.

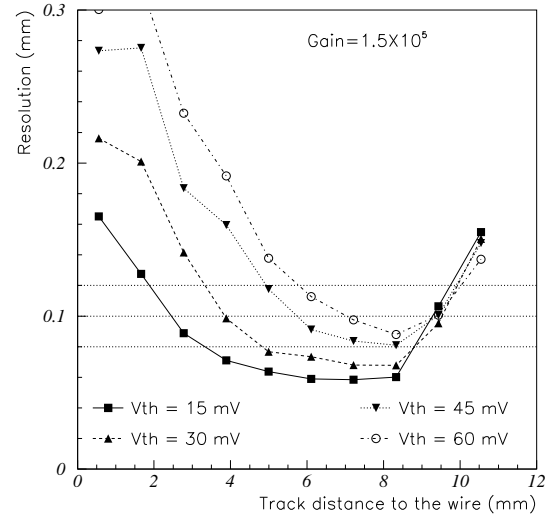


**Figure 6.25:** Simulated resolution for different levels of the discriminator threshold. The simulation is performed for the P3 cell and the settings are as the measurement in figure 6.24. The gain was put at  $1.5 \times 10^5$ .

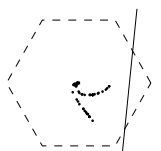
The measurement of the resolution of the P3 cell shows a strong dependence on the setting of the discriminator threshold (figure 6.24). Not only does the resolution for tracks close to the wire deteriorate for larger thresholds, but this is also the case for large drift distances. Figure 6.25 shows the resolution as simulated. The gain was fixed at  $1.5 \times 10^5$  and two remarks can be made. Firstly, the deterioration of the resolution close to the wire is much more apparent in the simulation than in the data. Secondly, where the simulation shows an improvement of the resolution for larger thresholds for large drift distances, the measurements show in the same region of the cell a worsening of the resolution. The improvement in the simulation in the outer corner of the cell is due to the better timing of multiple electrons in the diffusion dominated situation. The deterioration of the measured resolution in the same situation has not yet been explained.

### 6.3.3 The angle of incidence $\theta$

The maximum measurable track distance to the wire is equal to the outer radius for tracks perpendicular to the chamber ( $\theta = 0^\circ$ ) and equal to the inner radius for tracks entering the detector at  $\theta = 30^\circ$ . In general, the maximum measurable track distance  $R_{\max}$  is given by:

$$R_{\max} = R_{\text{outer}} \cos \theta, \quad (6.1)$$

with  $R_{\text{outer}}$  the outer radius of the cell and  $\theta$  the angle of incidence of the tracks in the range  $-\pi/6 < \theta < \pi/6$  with  $2\pi/6$  periodicity.



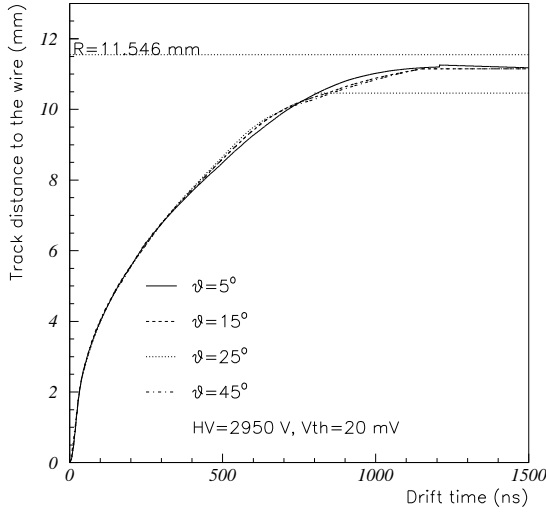


**Figure 6.26:** Measured  $r(t)$  for four angles  $\theta$  in the P3 chamber with Ar/CO<sub>2</sub> 50/50 drift gas. The high voltage on the anode wires was 2900 V and the threshold on the discriminator was 20 mV.

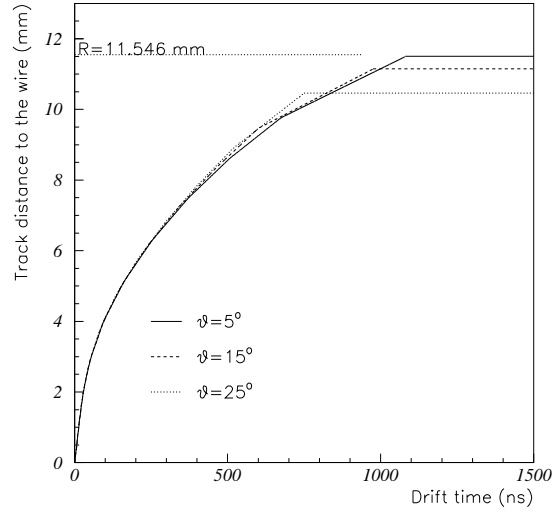


**Figure 6.27:** Simulated  $r(t)$  for three angles  $\theta$  in the P3 chamber. The simulated settings are as during the measurement shown in figure 6.26.

Besides the maximum measurable track distance,  $r(t)$  will also change under a rotation of the tracks. The average electric field will be relatively low for drifting electrons produced with tracks at  $\theta = 0^\circ$  compared to electrons produced by tracks at  $\theta = 30^\circ$ . This effect has been measured in the P3 detector in Ar/CO<sub>2</sub> 50/50. The chamber was rotated in the RD5 testbeam along the axis parallel to the wires. In figure 6.26 the measured  $r(t)$  relations for  $\theta = 5^\circ, 15^\circ, 25^\circ$  and  $45^\circ$  are shown. Although the effects are marginal,  $r(t)$  for  $\theta = 25^\circ$  shows indeed the fasted drift properties. Note that the measured  $r(t)$  at  $\theta = 15^\circ$  corresponds indeed with the curve for  $\theta = 45^\circ$  as is expected from the periodicity of the cell. In figure 6.27 the simulated  $r(t)$  dependencies are shown for  $\theta = 5^\circ, 15^\circ$  and  $25^\circ$ . The agreement in the relative positions is good up to  $r = 10$  mm.

Because electrons drifting to the anode wires with different angles  $\theta$  experience different electric field configurations, also the resolution will be affected by this angle  $\theta$ . The measured resolution of the P3 cell for different angles of incidence is shown in figure 6.28. The resolution close to the wire is, as expected, not influenced by the angle  $\theta$  of the tracks. We see that the resolution in the outer regions of the cell deteriorates in case  $\theta$  changes from  $5^\circ$  to  $15^\circ$  and deteriorates more after changing  $\theta$  from  $15^\circ$  to  $25^\circ$ . The observed deterioration of the resolution for increasing angle of incidence  $\theta$  can in principle be due to mechanical geometry errors of the detector in the direction perpendicular to the planes (y-direction, see figure 3.1). Those errors appear only in the spatial resolution for inclined tracks with respect to the normal of the detector. In order to exclude this type of errors, the resolution is also measured for  $\theta = 45^\circ$ . In this situation, the resolution improves with respect to the  $\theta = 25^\circ$  situation and the same resolution curve is measured as for  $\theta = 15^\circ$ . This confirms the suggestion that the measured dependence of the resolution on the angle  $\theta$  of the tracks is due to the hexagonal shape of the honeycomb cell.

In figure 6.29 the resolution curves are simulated for the same experimental situations as in the measurements described above. Here, the  $\theta = 15^\circ$  situation is by definition equal to the

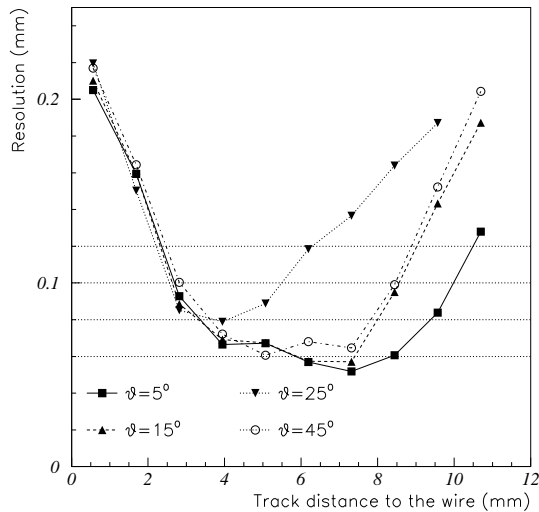


**Figure 6.28:** Measured resolution of the P3 cell for four angles  $\theta$ . The experimental parameters are described in figure 6.26.

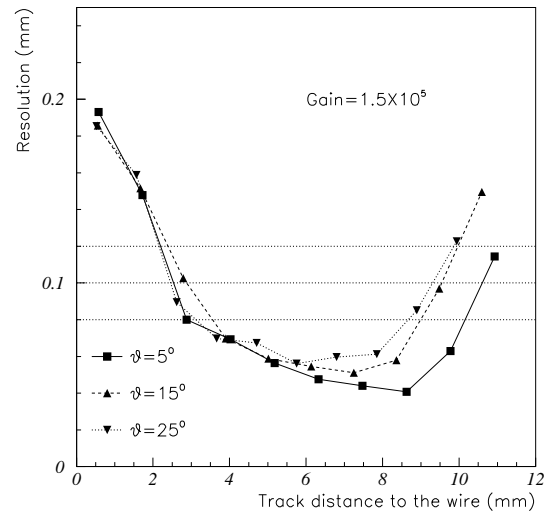


**Figure 6.29:** Simulated resolution according to the measurements shown in figure 6.28.

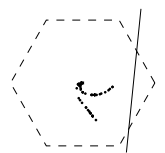
$\theta = 45^\circ$  situation. The deterioration of the resolution for tracks at  $\theta = 15^\circ$  with respect to tracks at  $\theta = 5^\circ$  is well simulated, although in the simulation a little less outstanding. The measured dramatic deterioration of the resolution for tracks at  $\theta = 25^\circ$  is not reproduced by the simulation. Most likely a different process dominates the resolution for this type of tracks. For tracks at  $\theta = 25^\circ$  the measured drift times in adjacent planes is nearly equal due to the geometry of the wires, which are in a plane for  $\theta = 31^\circ$  (see e.g. figure 5.10). This nearly simultaneous signal on all wires might contribute in a negative way to the resolution due to cross-talk effects.

The above described measurement of the resolution of the P3 cell as function of the angles of incidence  $\theta$  of the tracks has been repeated with the P1 chamber. In figure 6.30 the different measured  $r(t)$  curves are shown. The measured  $r(t)$  for tracks at  $\theta = 25^\circ$  shows the fastest drift properties, as expected from the electric field configuration in the cell. The measured resolution curves for different  $\theta$  are shown in figure 6.31. Regarding the resolution at the end of the cell, the same tendency in the resolution versus  $\theta$  can be observed as in the P3 cell, but less pronounced. Especially, the deterioration of the resolution for  $\theta = 25^\circ$  is relatively modest and seems thus to be an artefact of the P3 detector.

More measurements and simulations on the  $\theta$  dependence of the P3 performance will be given in section 6.3.7.

### 6.3.4 Primary ionisation density

The primary ionisation density (mean distance between ionisation clusters) is first of all a function of the composition of the drift gas. For a given drift gas, the ionisation density is proportional to the gas pressure. The gas pressure is, however, not a free parameter for the HSC. As described in section 3.4.1 the energy loss of relativistic muons in matter depends on the momentum of the muon. From figure 3.16 we see that the ionisation density shows a minimum for  $\beta\gamma = 4$ . For muons, this is equivalent to  $p=0.4$  GeV/c. This value is close to the most probable momentum ( $p=0.6$  GeV/c) of vertical cosmic muons. Thus, cosmic muons can be considered as genuine



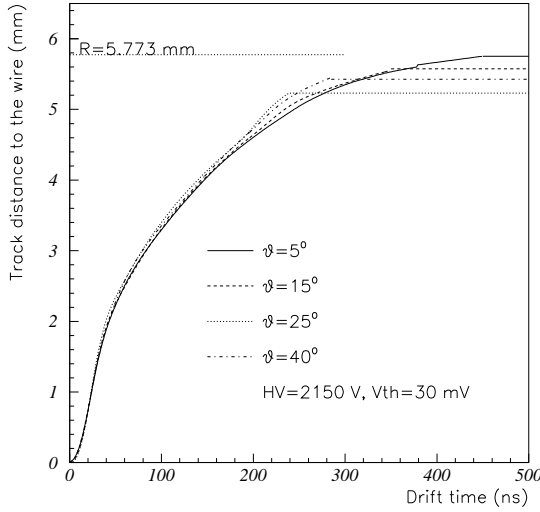


**Figure 6.30:** Measured  $r(t)$  for four angles  $\theta$  in the P1 chamber with Ar/CO<sub>2</sub> 50/50 drift gas. The high voltage on the anode wires was 2150 V and the threshold on the discriminator was 30 mV.

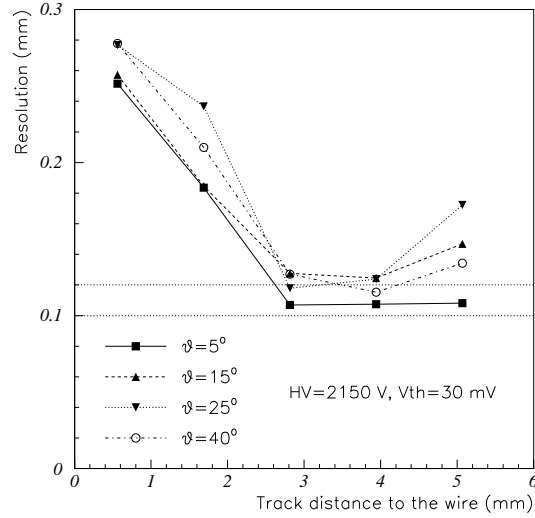


**Figure 6.31:** Measured resolution curves for the same experimental situations as described in figure 6.30.

Minimum Ionising Particles (MIPs). From figure 3.16 we see that the number of primary cluster density reaches a level of 1.3 times the value for MIPs on the relativistic plateau. This value is reached for  $\beta\gamma = 200$ , equivalent to muons of  $p=20$  GeV/c. Since all testbeam results are obtained with beam momenta between 100 and 300 GeV/c, we will consider the primary clustering to be on the relativistic plateau. The increased mean cluster size for muons on the relativistic plateau with respect to MIPs is accounted for in the simulations by a relative increase of the primary clustering density to 1.4 (instead of 1.3), while leaving the mean cluster size unchanged.

An other increase in the 'visible' ionisation density can be obtained by rotating the muon tracks around an axis parallel to the strips (angle  $\phi$ , see figure 3.1). All simulations are performed in the situation where the muons are perpendicular to the wire ( $\phi = 0^\circ$ ). In case the directions of the wire and muon are not perpendicular this will result for the muon in an increased path length in the gas volume of the cell. For the wire, the primary cluster density projected onto the plane perpendicular to the wires will be larger. The electrons from tracks with  $\phi \neq 0^\circ$  will arrive at different positions along the wire. The additional delay of the signal due to this effect is negligible due to the large signal velocity on the wire ( $\approx 0.2$  m/ns).

Since the experimental conditions in the RD5 testbeam and cosmic ray experiment were very different, no direct comparison can be made between the response of the HSC on minimum ionising cosmics and highly relativistic muons. The angle of incidence  $\phi$  has only been studied in the limited range from  $0^\circ$  to  $20^\circ$ . In figure 6.32 two  $r(t)$  relations are shown, measured with the P1 chamber in RD5. The angle of incidence  $\theta$  was put to  $5^\circ$  and  $\phi$  was  $0^\circ$  and  $20^\circ$ . In figure 6.33 the resolution curves are plotted for the same experimental settings as in figure 6.32. No difference can be observed between the two measurements.

In figure 6.34 and 6.35 the simulated resolution curves are shown as computed for the P1 detector operated at  $10^5$  and  $2 \times 10^5$  gain. The resolution curves are computed for MIPs (relativistic rise = 1.0) and for higher values of the primary ionisation density. The performance of the tube depends strongly on the primary ionisation density. No data with the HSCs is available



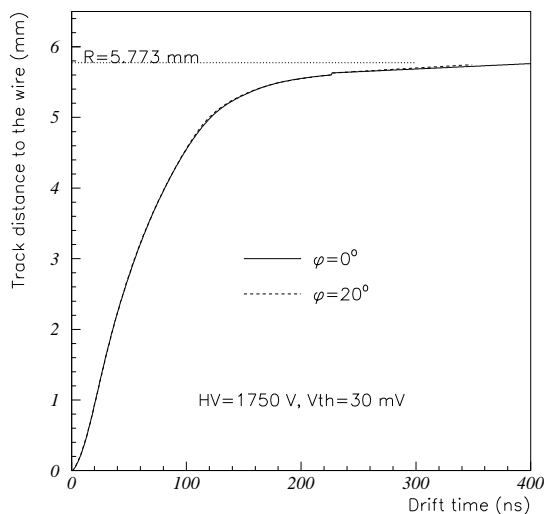


**Figure 6.32:** Measured  $r(t)$  curves of the P1 cell with Ar/CO<sub>2</sub> 80/20 drift gas. The angles of incidence  $\phi$  are set at  $0^\circ$  and  $20^\circ$ . The angle  $\theta$  was fixed at  $5^\circ$ .

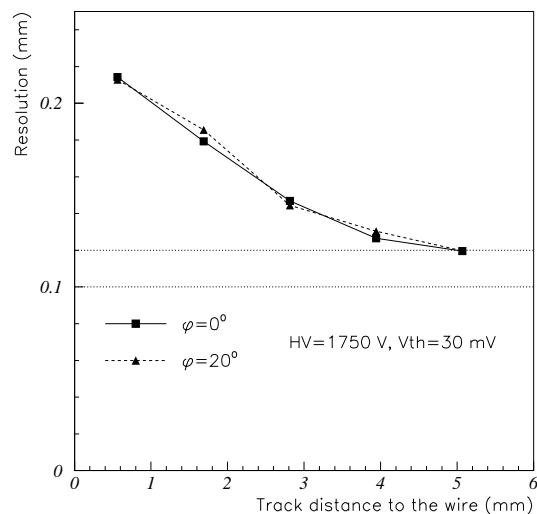


**Figure 6.33:** Measured resolution for two angles  $\phi$  as in figure 6.32.

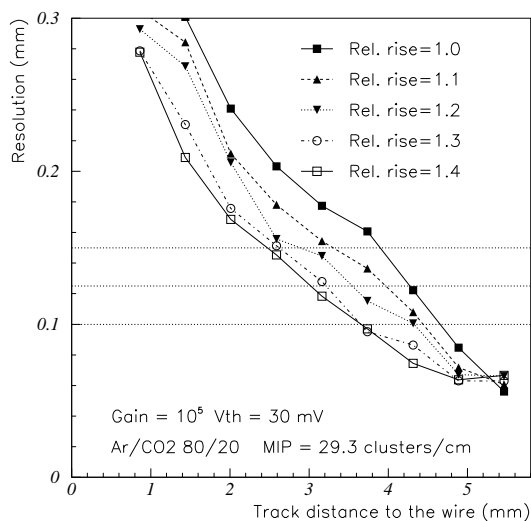


**Figure 6.34:** Simulated resolution curves for different values of the relativistic rise in the primary ionisation density. The P1 cell is simulated with Ar/CO<sub>2</sub> 50/50 drift gas and the anode wires at 1750 V. The simulations are performed for a gain of  $10^5$ .

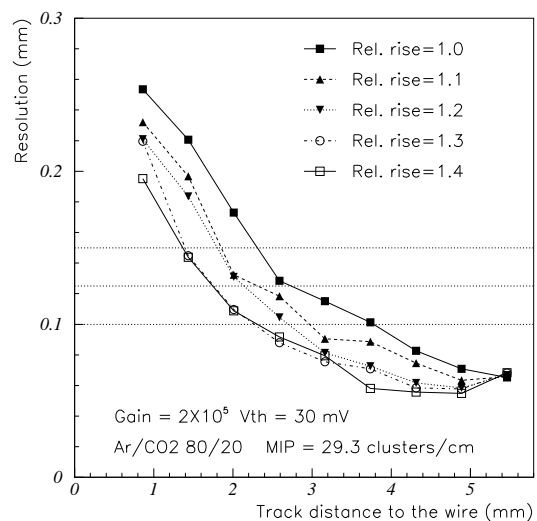
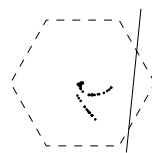


**Figure 6.35:** As figure 6.34, with a gain of  $2 \times 10^5$ .

to verify the simulations.



### 6.3.5 The segmentation of the cathode in strips

The cathode of the HSC is segmented in strips. The copper strips have a pitch of 5.04 mm and are individually separated by a gap of 1 mm. The segmentation of the cathode will affect the electric (drift) field in the tube. The effect on the resolution of this disturbance will show a maximum in the outer region of the cell for tracks which pass the cell exactly in the insulating gap between two strips.

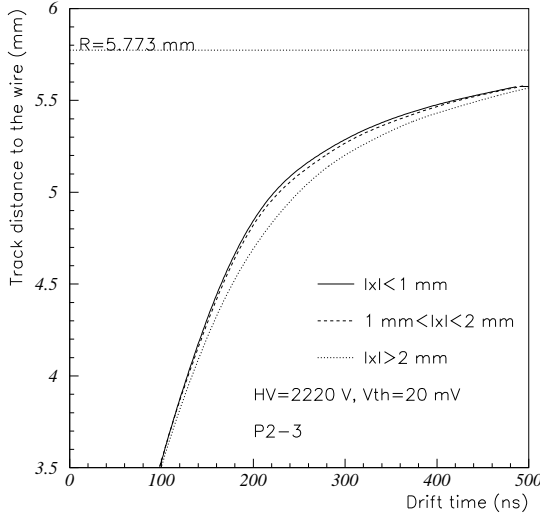


**Figure 6.36:** Measured  $r(t)$  curves for tracks passing the drift cells at different positions of the cathode strips. The data is obtained with the P2 chamber. The angle  $\phi$  was  $0^\circ$  and  $\theta$  was  $12^\circ$ . The strips were divided in three regions as indicated in the figure. The value of  $x$  is defined with respect to the centre of the strip.

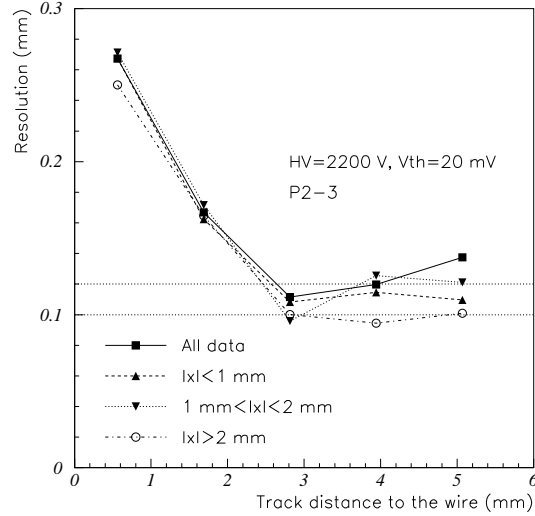


**Figure 6.37:** Measured resolution for tracks passing the cell in the three regions indicated in the figure. The resolution of all tracks without cuts is also shown.

The effect of the  $x$  position of the track along the wire (see figure 3.1) has been measured with one of the P2 chambers in RD5. The anode wires are perpendicular to the beam ( $\phi = 0^\circ$ ) and  $\theta$  is  $12^\circ$ . In this situation the strips on all planes are hit at the same position, while the measured drift distances are distributed randomly from plane to plane. In appendix C an event of this measurements is displayed in both the wire and strip projection (figures C.1 and C.2).

The drift-time data sample was separated in three samples. The first sample consisted of tracks passing the middle of the strips ( $|x| < 1$  mm). The second sample covered tracks on the border of the strips, but still entering the cell at the position where conductive copper was applied ( $1 \text{ mm} < |x| < 2$  mm). The third category of data consisted of tracks which entered the cells at the position of the insulating gap between the cells ( $2 \text{ mm} < |x| < 2.5$  mm). The measured  $r(t)$  for the three samples are shown in figure 6.36. The tracks entering the cell in the insulating gap between two cells show longer drift times than tracks passing a region of the cell with copper applied. In figure 6.37 the measured resolutions are shown for the three data samples and the average resolution is shown when all data is super-positioned. The resolution curve for tracks passing the cell in the insulating gap is better than in the other two regions. Since the total effect of the segmentation on the resolution is only marginal, no further studies are done to cathode

segmentation effects on the drift tube performance.

### 6.3.6 The coordinate along the wire

The P3 detector has six meter long wires. The wires are fixed at the end-combs of the chamber and additionally supported by a middle bridge halfway the chamber to prevent excessive sag of the wire. The six meter length of the wire cause a maximum delay of 60 ns between the direct detection of the signal and the detection of the signal reflected at the opposite end of the wire. In order to prevent the shape of the signal to be a function of the position of the hit along the wire, the wires are terminated at the high voltage side with a characteristic impedance of  $360 \Omega$ . The performance of the P3 chamber has been measured at different positions along the wire in the RD5 muon beam. The support of the chamber was put on two sets of wheels, such that the chamber could be translated perpendicular to the beam over 2.5 m.

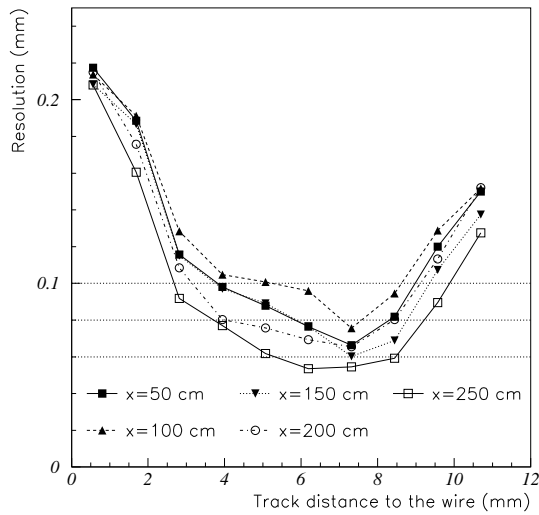


**Figure 6.38:** Measured resolution of the P3 cell for five different positions along the wire between the middle-comb ( $x=0$  cm) and the end-comb ( $x=265$  cm). The drift gas was Ar/CO<sub>2</sub> 50/50, the angle  $\theta$  of the beam was  $5^\circ$ , the high voltage was 2950 V and the threshold on the discriminator was 20 mV.

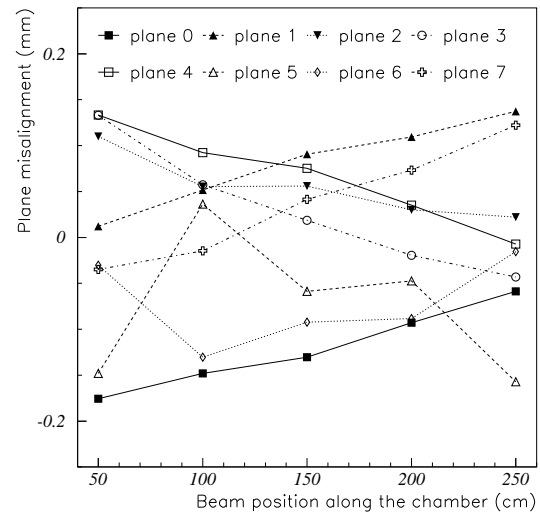
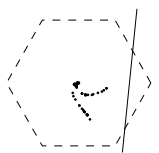


**Figure 6.39:** Fitted position of the eight planes of P3 in the  $z$  direction as function of the position along the wire ( $x$ ). The offset and rotation of six planes could be well reconstructed. Only plane 5 and 6 give non-consistent results.

The P3 chamber was tested in the region between the middle-comb ( $x=0$  cm) and the end-comb at the pre-amplifier side ( $x=265$  cm). So the minimum delay between the direct and reflected signal (if any, due to the termination of the wire) was 30 ns and the maximum delay was 60 ns. The minimum delay of 30 ns of the reflected signal prevented that any problems could be expected from reflections. Figure 6.38 shows the resolution as measured at five different positions along the wire. The drift-gas was Ar/CO<sub>2</sub> 50/50. The best resolution is measured close to the end-comb and the pre-amplifier ( $x=250$  cm). The resolution deteriorates for measurements at  $x=200$  cm and  $x=150$  cm and for  $x=100$  cm the resolution is even  $40 \mu\text{m}$  worse for all drift distances with respect to the resolution for  $x=250$  cm. At 50 cm from the middle-comb the resolution recuperates to only  $20 \mu\text{m}$  degradation with respect to the resolution at  $x=250$  cm. Possibly, the positions of the wires are badly defined between the combs due to variations in the wire ten-



sion. Due to the small angular distribution of the beam with respect to the experiments in cosmic rays, the positions of the wires could not be fitted individually as described in section 6.3.1.

On the other hand, the positions of the planes with respect to each other had to be fitted before the resolutions as shown in figure 6.38 could be measured. The monolayers were aligned during construction in the  $x-z$  plane with 100  $\mu\text{m}$  tolerance. This large value of the tolerance on the fitting of the 'precision' pins in the 'precision' holes was needed in the direction along the wire ( $x$ ) in order to mount the 6 m long layers without stress. Instead of milling a slit at the position of the precision holes with 20  $\mu\text{m}$  tolerance in  $z$  and 100  $\mu\text{m}$  tolerance in  $x$ , a hole was drilled with 100  $\mu\text{m}$  in both the  $x$  and  $z$  directions.

The relative positions of all monolayers of P3 were fitted using muon tracks. The plane misalignment of all eight planes is shown in figure 6.39 as function of the muon beam position along the chamber. The misalignments are all relative and all values are thus with respect to the mean position of all other planes. The rotations and offsets of the different planes with respect to each other are well measured. The alignment of the monolayers with muon tracks is for P3 only possible in the  $z$  and  $y$  directions, perpendicular to the wires, since no precision coordinate ( $x$ ) is measured along the wire.

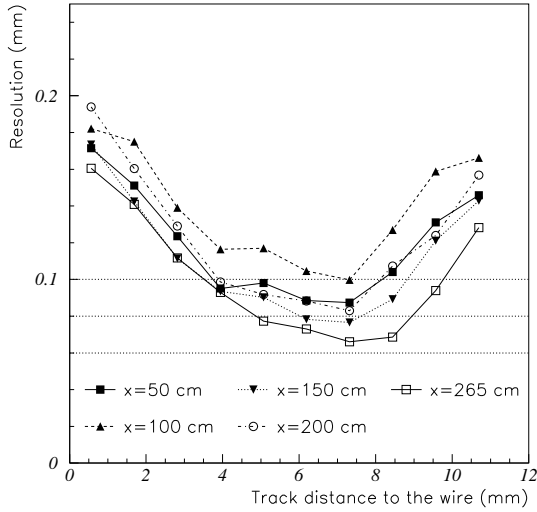


**Figure 6.40:** As figure 6.38, the drift gas was  $\text{Ar}/\text{CO}_2/\text{C}_2\text{H}_6$  70/25/5 and the high voltage was 2475 V.

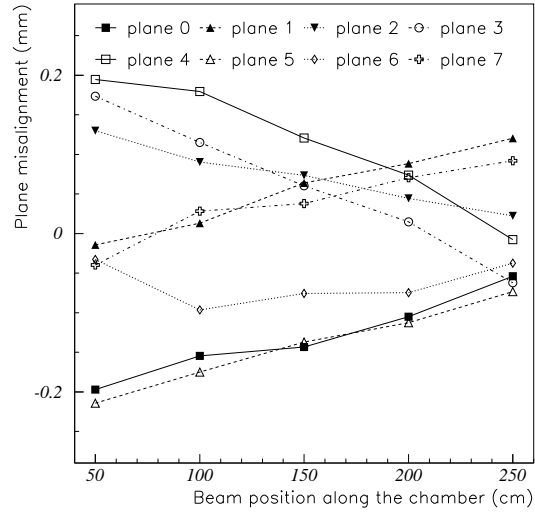


**Figure 6.41:** As figure 6.39, all positions of all planes are reconstructed well.

The above described measurements have been repeated with the  $\text{Ar}/\text{CO}_2/\text{C}_2\text{H}_6$  70/25/5 gas mixture. In figure 6.40 the resolution curves are shown for the same five positions along the chamber. The measurement close to the end-comb is performed 15 cm closer to the end-comb at  $x=265$  cm. The dependence of the resolution on the position along the chamber is equal to the measurements with  $\text{Ar}/\text{CO}_2$  50/50. The overall deterioration of the resolution with respect to the previous measurements is due to the increased diffusion in case the drift-gas is  $\text{Ar}/\text{CO}_2/\text{C}_2\text{H}_6$  70/25/5 instead of  $\text{Ar}/\text{CO}_2$  50/50.

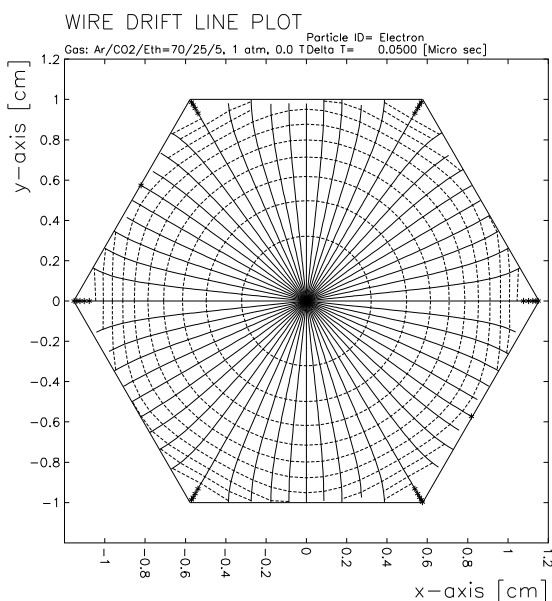
The positions of all eight planes are well reconstructed in this run for all values of the beam position (see figure 6.41). The results of the previous run are well reproduced within 20  $\mu\text{m}$  precision. In section 6.3.8 the plane positions of P3 will be measured again at the position of the

end-combs with cosmic muons in a different experiment.

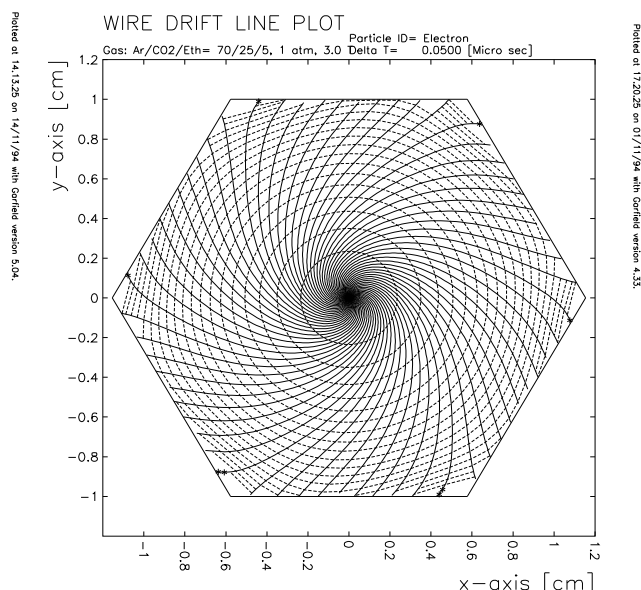
### 6.3.7 B-field study

The R&D on the HSC was guided by the future application of the HSC in the ATLAS muon spectrometer. As described in chapter 2, the ATLAS muon spectrometer will consist of three air core toroid magnets and three layers of muon detectors. The middle muon chambers will be put in the full field ( $B \approx 0.6$  T) with the anode wires parallel to the field lines. The outer and inner muon stations will be positioned in the stray fields which are in general weaker than 0.6 T. Some chambers, however, will experience the very strong inhomogeneous fields close to the coils. Those regions are identified in figure 2.5 by the locally increased density of magnetic field lines.

The P1 and P3 chambers have been tested in the 3 T superconducting EHS magnet in the RD5 muon beam. The magnetic field was horizontally oriented and perpendicular to the muon beam. The anode wires of the detectors were parallel to the magnetic field and thus perpendicular to the beam, as would be the case in the ATLAS muon spectrometer.



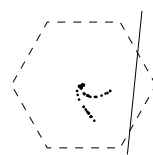
**Figure 6.42:** GARFIELD computation of the drift lines and isochrones of the P3 cell operated with Ar/CO<sub>2</sub>/C<sub>2</sub>H<sub>6</sub> 70/25/5 drift gas without magnetic field. The spacing of the isochrones is 50 ns. Note the  $2\pi/6$  periodicity in the shape of the isochrones in the outer regions of the cell.



**Figure 6.43:** As figure 6.42, the magnetic field is 3 T parallel to the anode wire. The electrons spiral around the wire due to the Lorentz force. Note the decreased spacing of the isochrones, implying an increase of the drift times with respect to the  $B = 0$  T situation.

In figure 6.42 and 6.43 the drift lines and isochrones (in steps of 50 ns) are shown for the P3 chamber with and without magnetic field. Due to the Lorentz force on the drifting electrons, the drift lines 'spiral' around the wire in figure 6.43. As result of this effect the density of isochrones increases which means that the drift times of the electrons increase with respect to the field-free case in figure 6.42. More details about drift of electrons in crossed electric and magnetic fields can be found in section 3.4.2 and appendix A.

The Lorentz angle is a function of the gas mixture and the strength of electric and magnetic



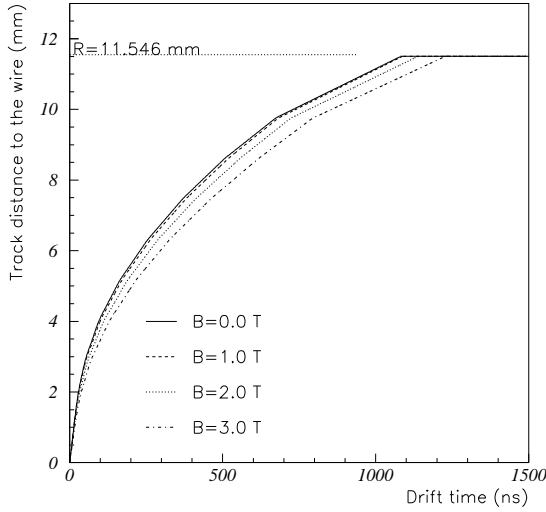


**Figure 6.44:** Simulation of the  $r(t)$  curves for the P3 cell operated with Ar/CO<sub>2</sub> 50/50 drift gas at different values of the magnetic field.

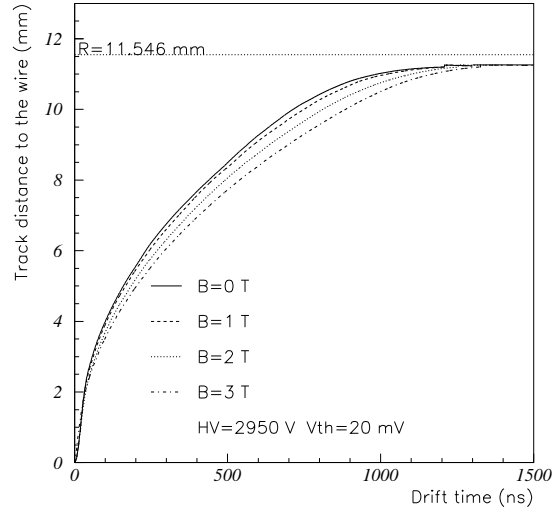


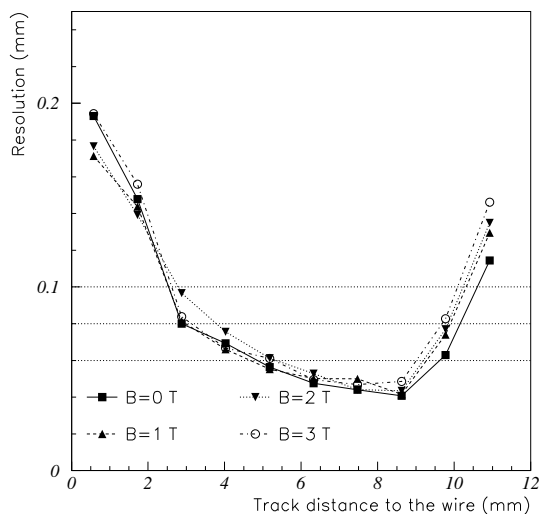
**Figure 6.45:** Measured  $r(t)$  curves for the same situation as simulated in figure 6.44. The high voltage on the anode wires was 2950 V.

fields. We will only consider the case where the electric and magnetic fields are perpendicular. In figure 4.2 the Lorentz angles are shown as function of  $E/p$  for four gases. In general one can state that the higher the drift velocity, the higher the Lorentz angle will be. This relation between the drift velocity  $u$  and Lorentz angle  $\alpha_L$  can be seen by combining equation 3.4 with equation 3.9. Since Ar/CO<sub>2</sub> 50/50 is known as a gas with low drift velocities for electrons, the Lorentz angle will be moderate, even for  $B$  up to 3 T. In figure 6.44 the simulated relations are shown in the P3 cell between the measured drift time and distance of the track to the wire ( $r(t)$ -relation) for different values of the  $B$  field. In case of a non-zero Lorentz angle the difference between 'drift distance' and 'distance of the track to the wire' is obvious. For the highest field of 3 T the Lorentz angle is approximately  $23^\circ$  over most of the drift path and shows a maximum of  $36^\circ$  at 1.3 mm from the wire. The simulated dependence of the  $r(t)$  on the magnetic field is well reproduced by the measurements shown in figure 6.45.

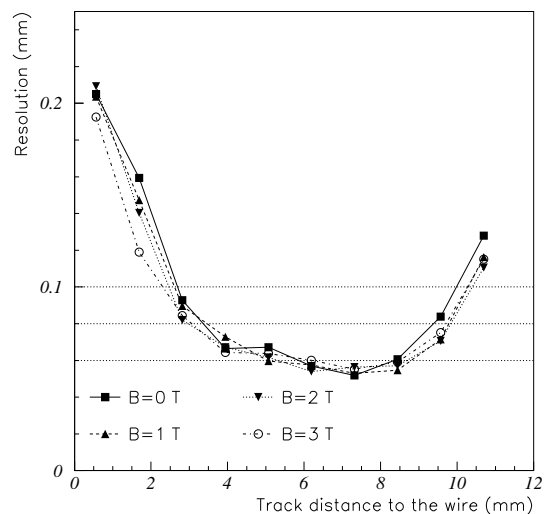
Chapter 2 describes how the Lorentz angle affects the resolution. In case the resolution is dominated by diffusion and the longitudinal and transverse diffusion are approximately equal, an improvement of the resolution can be expected for measurements in high magnetic fields (see appendix A for more details). The simulated resolution curves for different values of the magnetic field are shown in figure 6.46. The resolution curves are nearly identical due to the small Lorentz angle and the relatively high value of the transverse diffusion with respect to the longitudinal diffusion (see figure 4.2).

The drift of electrons in combined electric and magnetic fields can be well simulated. The results of the measured resolution curves for the same values of the magnetic field as in the simulation are shown in figure 6.47. No deterioration of the resolution can be observed.

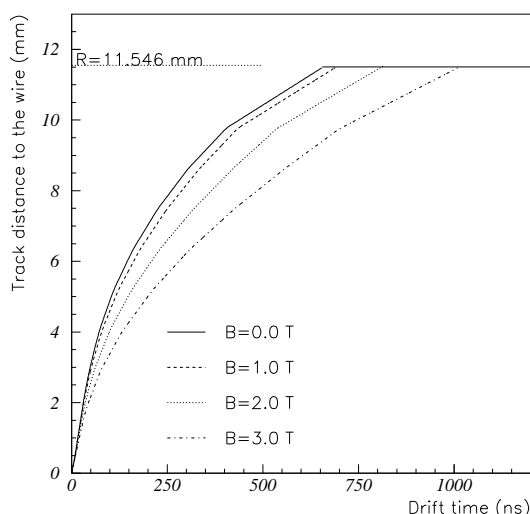
The simulations and measurements with the P3 chamber in strong magnetic fields are repeated for a drift gas with larger drift velocities and thus larger Lorentz angles. The gas mixture was Ar/CO<sub>2</sub>/C<sub>2</sub>H<sub>6</sub> 70/25/5 with a Lorentz angle of  $38^\circ$  ( $B = 3$  T) over most of the drift path and maximum Lorentz angle of  $50^\circ$  at  $r = 2.1$  mm. The simulated  $r(t)$  relations for the various values of the magnetic field are shown in figure 6.48. The experimentally determined curves for



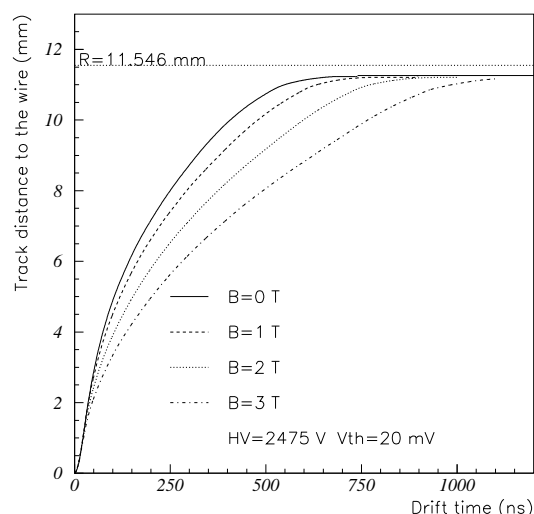
**Figure 6.46:** Simulated resolution of the P3 cell operated with Ar/CO<sub>2</sub> 50/50 for different magnetic field strengths. The simulated gain was  $1.5 \times 10^5$  and the discriminator threshold was set to 20 mV. The angle of incidence  $\theta$  was  $5^\circ$ .



**Figure 6.47:** Measured resolution of the P3 cell for the same settings as described in figure 6.46. The high voltage was set to 2950 V and the resolution was measured close to the end-comb ( $x=250$  cm).



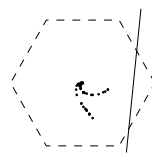
**Figure 6.48:** Simulated  $r(t)$  curves as in figure 6.44, the drift gas was Ar/CO<sub>2</sub>/C<sub>2</sub>H<sub>6</sub> 70/25/5.



**Figure 6.49:** Measured  $r(t)$  curves as in figure 6.45, the drift gas was Ar/CO<sub>2</sub>/C<sub>2</sub>H<sub>6</sub> 70/25/5 and the anode wires were put on 2475 V.

the same values of the  $B$  field are shown in figure 6.49. Note the increased shift of the  $r(t)$  for high field with respect to the measurements and computations shown for Ar/CO<sub>2</sub> 50/50.

The resolution of the P3 cell for Ar/CO<sub>2</sub>/C<sub>2</sub>H<sub>6</sub> 70/25/5 has been computed for different values of the  $B$  field. The results of the computations are shown in figure 6.50. A small deterioration of 10  $\mu$ m is observed going from zero field to full field. The resolution deteriorates because the



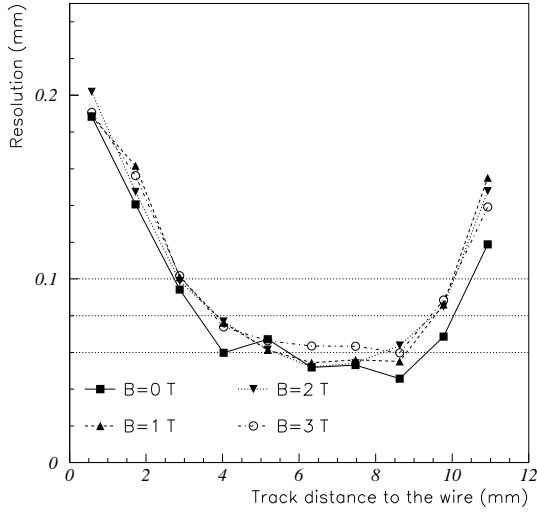


**Figure 6.50:** Simulated resolution as in figure 6.46, the drift gas was Ar/CO<sub>2</sub>/C<sub>2</sub>H<sub>6</sub> 70/25/5.

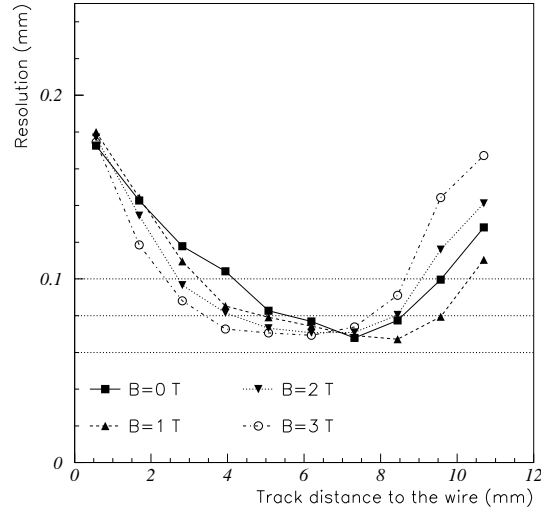


**Figure 6.51:** Measured resolution as in figure 6.47, the drift gas was Ar/CO<sub>2</sub>/C<sub>2</sub>H<sub>6</sub> 70/25/5 and the anode wires were put on 2475 V.

diffusion contribution is for non-zero Lorentz angles the vector sum of a longitudinal and transverse diffusion contribution. The amplitude of this vector sum is then reduced as described in appendix A. Because the transverse diffusion is much larger than the longitudinal diffusion, the overall result is a worsening of the measured spatial resolution.

The measured resolution for the same settings as the computed results in figure 6.50 are shown in figure 6.51. The measured results are not well described by the simulation. The measured resolution improves for short drift distances in case the magnetic field is increased. For large drift distances, however, the resolution deteriorates relatively more than predicted by the simulation.

One possible explanation might be the mis-interpretation of the MAGBOLTZ values for the transverse diffusion. The MAGBOLTZ longitudinal and transverse diffusion are used in the simulation as the random movement of the electron parallel and perpendicular to the *direction of motion* of the electron. Because the MAGBOLTZ programme is not documented nor supported, it could not be excluded that the computed diffusion parameters are given with respect to the *direction of the electric field*. In the last case, the computed resolution will improve with respect to the assumption used in the simulation. This is always true if the transverse diffusion is larger than the longitudinal diffusion and the electric field is approximately perpendicular to the isochrones.

The isochrones in figure 6.42 and 6.43 are pure circles close to the wire and approach a hexagonal shape in the outer regions of the cell. Two features of the isochrones are remarkable. Firstly, the isochrones show a  $2\pi/6$  periodicity with relatively straight sections and relatively strongly bend sections. Secondly, the orientation of the straight and bend sections of the isochrones depend on the value of the magnetic field. In case no magnetic field is applied (see figure 6.42, the tracks with angle of incidence  $\theta = 0^\circ$  will be parallel to the straight sections. For 3 T magnetic field, the tracks at approximately  $15^\circ$  will be parallel to the straight sections (see figure 6.43).

As we have seen in section 6.3.3, the resolution improves in case the isochrones are parallel to the muon track over a relatively long path. In this situation the primary ionisation clusters



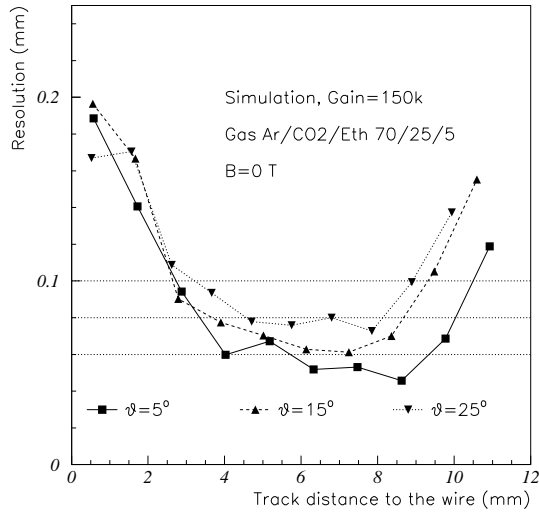


**Figure 6.52:** Simulated resolution of the P3 cell with Ar/CO<sub>2</sub> 70/25/5 for different angles  $\theta$  of the muon tracks.  $B = 0$  T.

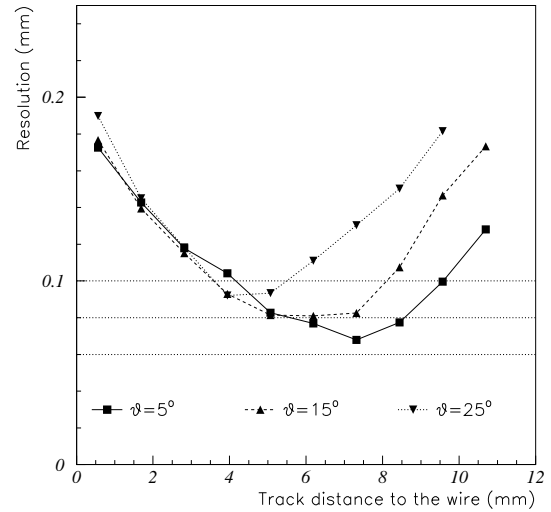


**Figure 6.53:** Measured resolution for the same situations as simulated in figure 6.52. The resolution at  $\theta = 25^\circ$  is more degraded than expected from the simulation.

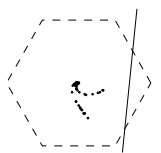
will be produced on the same isochrone. This will lead to a better timing of the drift time and thus an improved spatial resolution. One can see immediately that the isochrone being tangent to the tracks at  $\theta = 25^\circ$  (for  $B = 0$  T) are strongly bent and the primary ionisation density and transverse diffusion will deteriorate the resolution with respect to the case where the isochrones are hardly bent ( $\theta = 0^\circ$  for  $B = 0$  T).

Now we have explained why the resolution deteriorates in the P3 cell for large radii at  $\theta = 25^\circ$ . It can be expected that the resolution curves for tracks at different  $\theta$  will be different for the  $B = 3$  T case. In figure 6.52 the simulated resolutions are shown of the P3 cell with Ar/CO<sub>2</sub>/C<sub>2</sub>H<sub>6</sub> 70/25/5 for  $B = 0$  T. The same behaviour of the resolution is observed as in figure 6.29. The best performance is simulated for tracks with  $\theta = 5^\circ$  and the worst performance is computed for tracks with  $\theta = 25^\circ$ . The measured resolution for the same angles  $\theta$  as in the simulation are shown in figure 6.53. Those results are well comparable to the measured resolutions as function of  $\theta$  with Ar/CO<sub>2</sub> 50/50 drift gas (see figure 6.28).

The simulation and measurement of the resolution of the P3 cell at various angles  $\theta$  of the muon tracks has been repeated at  $B = 3$  T. The results of the simulations are shown in figure 6.54. Surprisingly, the resolution for  $\theta = 15^\circ$  is worse than the resolutions at  $\theta = 5^\circ$  and  $\theta = 25^\circ$ , but the differences are only marginal. The effect of the magnetic field on the  $\theta$  dependency of the measured resolution is much more pronounced. The measured resolutions for  $\theta = 5^\circ$ ,  $15^\circ$  and  $25^\circ$  are shown in figure 6.55. The resolution curves for tracks with  $\theta = 5^\circ$  and  $15^\circ$  have changed their relative positions with respect to the  $B = 0$  T case in figure 6.53.

The effect of a magnetic field on the  $r(t)$  and resolution curves was measured for the P1 chamber with Ar/CO<sub>2</sub> 50/50 drift gas. The measured  $r(t)$  curves are shown in figure 6.56. Measurements are done at  $B = 0$  T and  $B = 3$  T with the anode wires at 2200 V and an additional measurement is performed at  $B = 3$  T with the anode wires at 2300 V. The  $r(t)$  relations shift relatively as function of the magnetic field and changed drift field as expected.

The measured resolution curves are shown in figure 6.57. The resolution in case of moderate



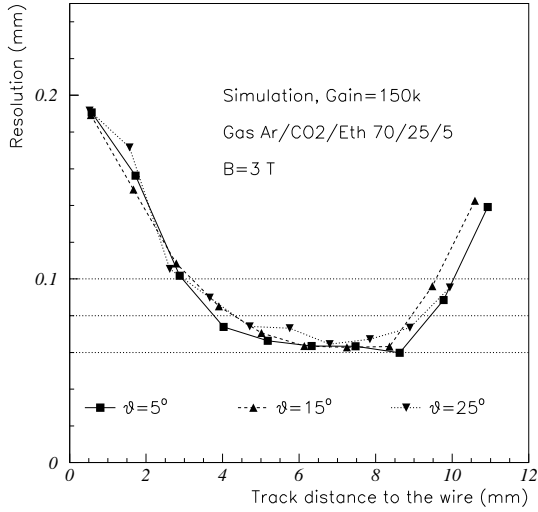


**Figure 6.54:** Simulation of the resolution of P3 for different values of  $\theta$  as in figure 6.52. The simulation is performed for  $B = 3$  T.

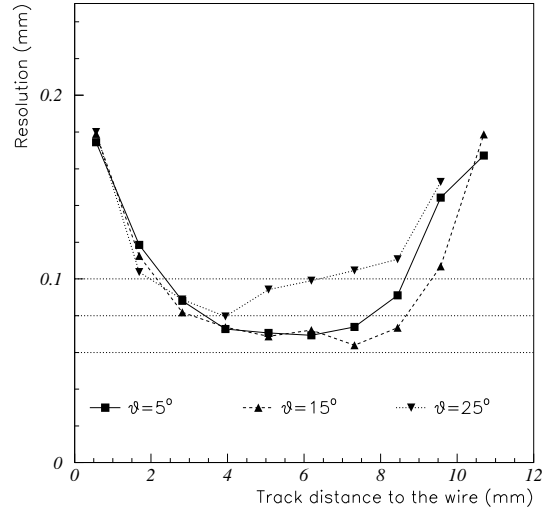


**Figure 6.55:** Measured resolution of P3 for different values of  $\theta$  as in figure 6.53. The measurement is done at  $B = 3$  T.

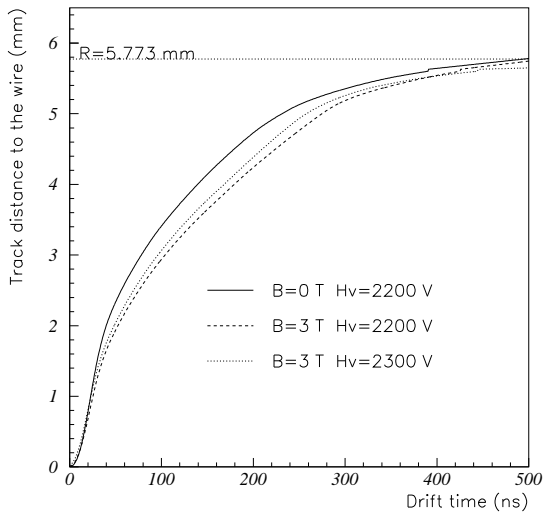


**Figure 6.56:** Measured  $r(t)$  of the P1 cell with Ar/CO<sub>2</sub> 50/50 drift gas for different combinations of the magnetic field and high voltage on the anode wires. The angle of incidence  $\theta$  of the muons was  $15^\circ$  and the threshold was set to 15 mV.

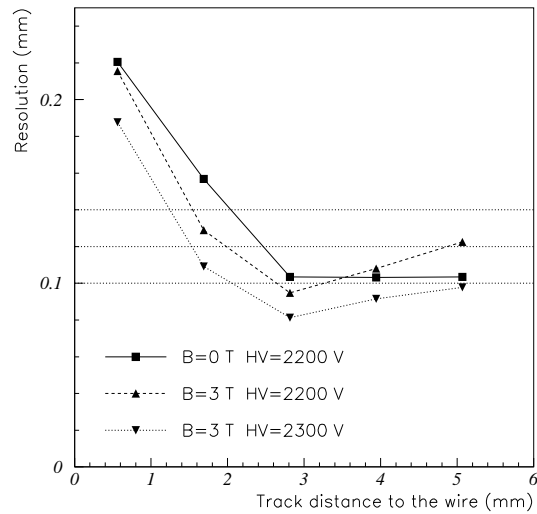


**Figure 6.57:** Measured resolution for the same settings as figure 6.56. See the text for the discussion.

high voltage (2200 V) and no magnetic field has already been shown in figure 6.17 when comparing the characteristics of several drift gases. In case  $B = 3$  T, the dashed curve is measured and the tendency in the resolution as function of the magnetic field is equal to the response of the P3 cell (see figure 6.51). The resolution close to the wire improves for increased magnetic fields and in the outer regions of the cell a deterioration of the resolution can be observed.

Finally, the high voltage, and thus the gain, was increased to 2300 V and the dotted resolution curve was measured. The resolution improved approximately  $15\text{ }\mu\text{m}$  over the whole range of the cell, indicating that the resolution was gain-limited during this series of experiments with the P1 chamber in the RD5 muon beam.

### 6.3.8 P3 versus P3A

The cathodes of the P3 chamber consisted of folded Mylar/copper strip foil, as used for the P2 chamber. It was not foreseen to read out the cathode strips and therefore all strips were grounded. The choice for the strip foil was taken on basis of the availability of the material and the simplicity to fold the material on the existing folding machine. In the P3A chamber, a copy of P3, the cathode material was replaced by plain aluminium foil. Only one cosmic ray run has been done with the P3A chamber. The chamber was operated at 2900 V and 15 mV discriminator threshold. The P3A chamber could not be operated at 3000 V (as P3) due to leakage currents on the high voltage distribution printed circuit boards. The P3 detector was not operated on 2900 V in cosmic rays, so the performance of P3A at 2900 V will be compared with P3 at 3000 V. The thresholds on the discriminator was 15 mV for both experiments.

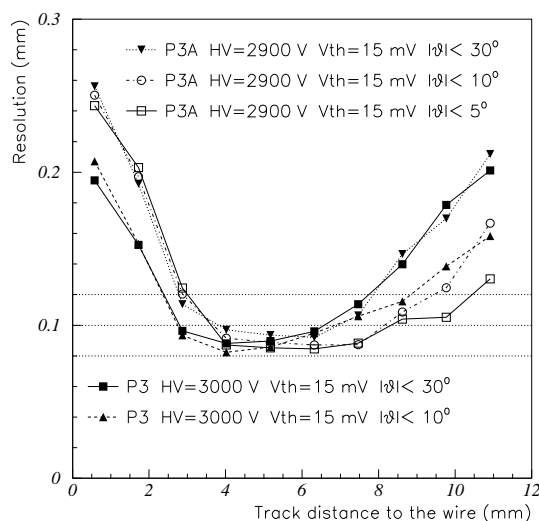


**Figure 6.58:** Measured resolution curves of the P3 and P3A detectors for different high voltages on the anode wires and  $\theta$  cuts on the angle of incidence of the cosmic muons. The drift gas was Ar/CO<sub>2</sub> 50/50 and the threshold setting on the discriminator was 15 mV.

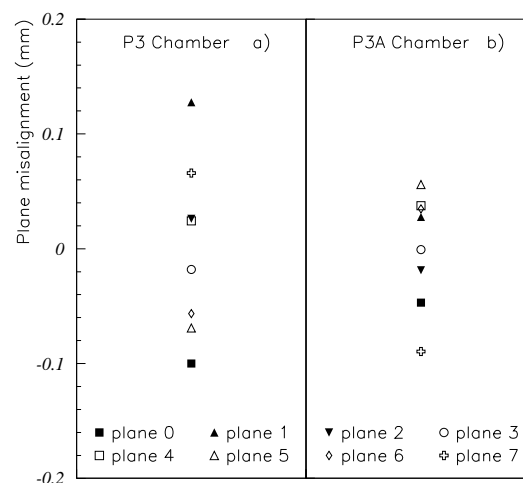
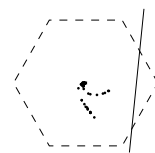


**Figure 6.59:** Fitted relative shift of the planes of the P3 (a) and P3A (b) detector in the  $z$  coordinate. The measurements are done close to the end-comb of the detectors ( $x=250\text{ cm}$ ) in cosmic ray experiments.

In figure 6.58 the measured resolution is shown for the P3 and P3A cosmic ray experiments and various cuts on the acceptance angle  $\theta$ . Both chambers were flushed with Ar/CO<sub>2</sub> 50/50. The P3 chamber performs better close to the wire as can be expected given the difference of 100 V in high voltage on the anode wires (this is approximately a factor two in gain). At the outer regions of the cell, the resolution of P3 and P3A are equal, depending for both chambers on the applied cut on  $\theta$  of the muon tracks.

Further, the relative positions of the monolayers in  $z$  are fitted from the data as described in



section 6.3.6. The relative shift of the planes are shown in figure 6.59 for both the P3 and P3A detector. The positioning of the layers of P3A is more precise than for P3. The relative positions of the planes of P3 should match the measured shift of the planes of the same detector in the RD5 testbeam. The measurement with cosmic rays was taken at the same position along the wires at  $x=250$  cm in the RD5 muon testbeam in figure 6.39 and 6.41.

## 6.4 Conclusions and outlook

Finally, some remarks can be made about the status of our understanding of the Honeycomb Strip Chamber:

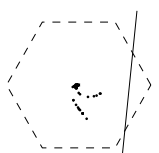
- Although the simulation of the HSC gives good insight in the main dependence of the various parameters on the performance of the HSC, not all measurements can be reproduced yet. Especially, the test with the P1 chamber in the 3 T EHS magnet suffered from pick-up noise. This resulted in a serious deterioration of the measured resolution with respect to the cosmic ray experiments at NIKHEF.
- Shielding of the detector and front-end electronics of HSCs is of large importance. Since the detection of the first electron arriving on the anode wire provides the best resolution, the HSC should be operated at the lowest signal threshold and highest gain possible. Only after the production of the P1 and P2 detectors, we did address the shielding and grounding strategy at the right moment: at the start of the design process.
- Due to problems with the P2 Mylar/copper foils (many interruptions in the strips), the simultaneous operation of both the wire and strip readout systems, without loss of precision, has not been proven yet.
- In case autocalibration is performed on data with many noise hits, the robust algorithm performs better. In ATLAS it will be simpler to clean the data sample from noise hits because a global track fit through three stations can be performed, while no reference points of the track were used during our prototype tests. The determinant of the 'autocalibration matrix', as described in chapter 5, will only provide information about the stability of the obtained  $r(t)$  in case the data sample is absolutely 'clean'. It can, nevertheless, be very useful to use the algorithm as described in chapter 5 on simulated data to verify if autocalibration will be possible for the given settings.
- In order to explain some of the differences between the simulations of the HSC and the measured performance more research is needed on the basic processes (like primary ionisation, attachment and gas gain mechanisms) in the drifttube. Those processes have to be studied in more detail, especially if one aims for a single wire resolution below  $100\text{ }\mu\text{m}$  combined with a low gas gain and fast response. Those studies are currently performed by the ATLAS muon community. The performance of the ATLAS muon detector is foreseen to be  $60\text{ }\mu\text{m}$  resolution,  $500\text{ ns}$  maximum drift time with a tube radius of  $15\text{ mm}$ . In order to achieve this performance, the drift gas will be pressurised to 3 bar.
- Considering the simulation of the HSC, several processes can be improved. Firstly, the spatial size of the cluster is not taken into account. Secondly,  $\delta$ -rays produced in the cathode and ionising the gas are not taken into account. Those processes are at too low energy scale to compute with GEANT. The  $\delta$ -rays produced in the cathode may be the explanation for the deteriorated resolution of the P3 detector at  $\theta = 25^\circ$  because of the small angle

between the sides of the cathode and the muons. Thirdly, the role of photons in the gas gain process has been neglected in all simulations up to now. In order to have a fast signal with large amplitude, the gas amplification process has to be as local (near the wire) as possible. One can easily imagine the effect of the photons escaping from the gas amplification area. Fourthly, the induced signals from the electrons 'drifting' towards the wire in the gas amplification process has been neglected. Recent simulations in the ATLAS detector physics group show that the signal on the wire is affected by these drifting electrons. The last point concerns the simulation of the electronic circuit. Attenuation and reflections of the signal on the wire are not taken into account, nor is the effect of the capacitance of the wire ( $\approx 10$  pF/m).

- The tests with the HSCs have shown that the performance is as good as commonly used drift tubes. The remaining discrepancies with simulations are not specific HSC related. Furthermore, no deterioration is observed in the performance of the HSC for magnetic fields up to 3 T. Since the HSC offers many advantages on construction topics, it may be concluded that the HSC has overcome its adolescence.

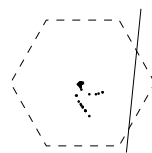
## References

- |  |  |
|--|--|
| <p>[1] M. Della Negra <i>et al.</i>, Status report of the RD5 experiment, CERN/DRDC/93-49, 5 January 1994.</p> <p>[2] R. Bergman, Thesis on the TRACAL detector in RD5, Title to be announced, University of Nijmegen, PhD Thesis, 1996, Nijmegen.</p> <p>[3] M. Aalste <i>et al.</i>, Measurement of hadron shower punchthrough in iron, <i>Z. Phys.</i> <b>C60</b> (1993) 1–</p> | <p>10. C. Albajar <i>et al.</i>, Measurement of momentum and angular distribution of punchthrough muons at the RD5 experiment, Submitted to <i>Z. Phys.</i> <b>C</b>.</p> <p>C. Albajar <i>et al.</i>, Measurement of hadron shower punchthrough in a magnetic field, Accepted for publication by <i>Z. Phys.</i> <b>C</b>, CERN-PPE/95-61.</p> <p>[4] LeCroy Model 2277 16-channel TDC.</p> |
|--|--|





# Appendices







# Appendix A

## The classical theory of drift of electrons in gases

### Contents

---

A.1	Equation of motion for a free electron with $\mathbf{E} \perp \mathbf{B}$	133
A.2	The macroscopic drift velocity	134
A.3	The Lorentz angle $\alpha_L$	135
A.4	Diffusion in the microscopic picture	136
A.5	Determination of $v_0$ by energy conservation	136
A.6	Druyvesteyn versus Maxwell model	138
A.6.1	Electron-velocity distribution	138
A.6.2	Electron-position distribution	139
A.6.3	Determination of $D_L^2$ and $D_T^2$	140

---

**T**he macroscopic gas quantities like the drift velocity, diffusion and Lorentz angle will be derived based on the equation of motion of a free electron in crossed  $\mathbf{E}$  and  $\mathbf{B}$  fields.

### A.1 Equation of motion for a free electron with $\mathbf{E} \perp \mathbf{B}$

In the ATLAS muon spectrometer, the wires will be parallel to the magnetic field lines. Therefore, we will study the case where the drift field  $\vec{E}$  is perpendicular to the magnetic field  $\vec{B}$ . The  $\mathbf{E}$ -field is considered to have its components in the (x,y) plane. The  $\mathbf{B}$ -field is directed along the z-axis. The resulting relations can be simply applied in a drift tube geometry with the z-axis along the wire. So:

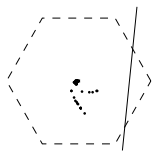
$$\vec{E} = (E_x, E_y, 0), \quad \vec{B} = (0, 0, B_z). \quad (\text{A.1})$$

The equation of motion between two successive collisions with gas molecules is:

$$m \frac{d\vec{v}}{dt} = e\vec{E} + e[\vec{v} \times \vec{B}]. \quad (\text{A.2})$$

Because we are considering the microscopic motion of the electron, the velocity  $v_0$  immediately after a collision is not equal to zero. From equation A.1 and A.2 we find the following set of equations:

$$\begin{aligned} \dot{v}_x &= \mathcal{E}_x + \omega v_y \\ \dot{v}_y &= \mathcal{E}_y - \omega v_x \\ \dot{v}_z &= 0, \end{aligned} \quad (\text{A.3})$$



with initial condition:

$$\vec{v}(t=0) = (v_x(0), v_y(0), 0), \quad (\text{A.4})$$

for which

$$\begin{aligned} \varepsilon_x &= \frac{e}{m} E_x \\ \varepsilon_y &= \frac{e}{m} E_y \\ \omega &= \frac{e}{m} B. \end{aligned} \quad (\text{A.5})$$

Solving this set of equations gives expressions for  $v_x(t)$  and  $v_y(t)$  with 3 constants A, B and C:

$$\begin{aligned} v_x(t) &= A \cos \omega t + B \sin \omega t + \frac{\varepsilon_y}{\omega} \\ v_y(t) &= -A \sin \omega t + B \cos \omega t + C. \end{aligned} \quad (\text{A.6})$$

By applying the initial conditions for  $t = 0$  we find for A, B and C:

$$\begin{aligned} A &= v_x(0) - \frac{\varepsilon_y}{\omega} \\ B &= v_y(0) + \frac{\varepsilon_x}{\omega} \\ C &= -\frac{\varepsilon_x}{\omega}. \end{aligned} \quad (\text{A.7})$$

By inserting the initial conditions  $x = x(0)$  and  $y = y(0)$  at  $t = 0$ , we find for the trajectory of the particle between two collisions:

$$\begin{aligned} x(t) &= x(0) + \frac{\varepsilon_x}{\omega^2}(1 - \cos \omega t) + \frac{\varepsilon_y}{\omega}t - \frac{\varepsilon_y}{\omega^2} \sin \omega t + \frac{v_x(0)}{\omega} \sin \omega t + \frac{v_y(0)}{\omega}(1 - \cos \omega t) \\ y(t) &= y(0) + \frac{\varepsilon_y}{\omega^2}(1 - \cos \omega t) - \frac{\varepsilon_x}{\omega}t + \frac{\varepsilon_x}{\omega^2} \sin \omega t + \frac{v_y(0)}{\omega} \sin \omega t - \frac{v_x(0)}{\omega}(1 - \cos \omega t). \end{aligned} \quad (\text{A.8})$$

This is an interesting result, because the position in space in the  $x$  and  $y$  direction is composed of two contributions. The first term in equation A.8 gives the actual position of the electron. The next three terms give the relation between position and time due to the E and B-field. The last two terms depend completely on the initial velocity of the electron immediately after the collision. We keep in mind that we assume the scattering to be non-directional. Because we are mostly interested in the velocity behaviour of the electrons we differentiate equation A.8 to get the velocity in  $x$  and  $y$  as function of time:

$$\begin{aligned} v_x(t) &= \frac{\varepsilon_x}{\omega}(\sin \omega t) + \frac{\varepsilon_y}{\omega}(1 - \cos \omega t) + v_x(0) \cos \omega t + v_y(0) \sin \omega t \\ v_y(t) &= \frac{\varepsilon_y}{\omega}(\sin \omega t) - \frac{\varepsilon_x}{\omega}(1 - \cos \omega t) + v_y(0) \cos \omega t - v_x(0) \sin \omega t. \end{aligned} \quad (\text{A.9})$$

## A.2 The macroscopic drift velocity

One can now derive the macroscopic quantities like the mean velocity in  $x$  and  $y$  and the Lorentz angle. The average velocities in  $x$  and  $y$  direction are defined by:

$$\begin{aligned} \langle v_x \rangle &= \int_0^\infty \frac{1}{\tau} e^{-\frac{t}{\tau}} v_x(t) dt \\ \langle v_y \rangle &= \int_0^\infty \frac{1}{\tau} e^{-\frac{t}{\tau}} v_y(t) dt, \end{aligned} \quad (\text{A.10})$$

with  $\tau$  the mean free drift time, given by:

$$\frac{1}{\tau} = N\sigma v_0, \quad (\text{A.11})$$

where  $N$  the gas-density,  $\sigma$  the scattering cross section and  $v_0$  the average random velocity of the electron. As can be seen in equation A.10, the macroscopic drift parameters are extracted from the solution of the equation of motion by taking a suitable weight function. Two approaches can be followed. The first is written down in equation A.10 and assumes a constant probability of a collision in time, where the mean free time is given by equation A.11. This approach will result in the Maxwell velocity distribution for the electron and will give results in terms of mean free drift time  $\tau$ . The second approach will assume that the mean free path  $l_0$  is a constant and will result in the Druyvesteyn distribution for the electron velocity [1]. The relation between  $l_0$  and  $\tau$  is given by:

$$l_0 = v_0 \tau = \frac{1}{N\sigma}. \quad (\text{A.12})$$

Since the averaging in the Druyvesteyn approach can only be done numerically, I will give all analytically derived results in the Maxwell assumption. In section A.6 the models will be compared by a Monte Carlo approach.

By averaging over  $t$ ,  $v_x(0)$  and  $v_y(0)$  we get the following equation for the macroscopic drift velocity  $u$  in terms of  $\tau$  and  $\omega$ :

$$\begin{aligned} u_x &= \langle v_x \rangle = \frac{\varepsilon_x \tau + \varepsilon_y \omega \tau^2}{1 + \omega^2 \tau^2} + \frac{\langle v_x(0) \rangle + \langle v_y(0) \rangle \omega \tau}{1 + \omega^2 \tau^2} \\ u_y &= \langle v_y \rangle = \frac{\varepsilon_y \tau - \varepsilon_x \omega \tau^2}{1 + \omega^2 \tau^2} + \frac{\langle v_y(0) \rangle - \langle v_x(0) \rangle \omega \tau}{1 + \omega^2 \tau^2}, \end{aligned} \quad (\text{A.13})$$

from which only the first terms remain because  $\langle v_x(0) \rangle = \langle v_y(0) \rangle = 0$ . For the macroscopic drift velocity in case of crossed E and B fields we find the result:

$$u^2 = \langle v_x \rangle^2 + \langle v_y \rangle^2 = \frac{\varepsilon^2 \tau^2}{1 + \omega^2 \tau^2}, \quad (\text{A.14})$$

with  $\varepsilon^2 = \varepsilon_x^2 + \varepsilon_y^2$ .

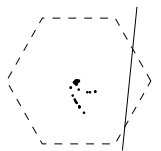
### A.3 The Lorentz angle $\alpha_L$

The Lorentz angle  $\alpha_L$  is defined as the angle between the drift direction of the electron and the electric field (drift direction for  $B=0$ ). So the Lorentz angle is  $0^\circ$  in case of no magnetic field and increases with increasing B-field. From equation A.13 we compute the components of the drift velocity perpendicular ( $u_\perp$ ) and parallel ( $u_\parallel$ ) to the electric field:

$$\begin{aligned} u_\parallel &= \frac{\varepsilon \tau}{1 + \omega^2 \tau^2} \\ u_\perp &= \frac{\varepsilon \omega \tau^2}{1 + \omega^2 \tau^2}, \\ u^2 &= \frac{\varepsilon^2 \tau^2}{1 + \omega^2 \tau^2}. \end{aligned} \quad (\text{A.15})$$

The Lorentz angle is defined by:

$$\tan \alpha_L = \frac{u_\perp}{u_\parallel} = \omega \tau. \quad (\text{A.16})$$



## A.4 Diffusion in the microscopic picture

In this section an expression will be derived for the width of an electron cloud, starting point-like and diffusing spatially after some time of drift. So, the result will be a Gaussian probability function with width  $\sigma_x$  for finding a single electron at a certain position in the cloud.

In order to calculate the diffusion coefficient  $D$  (in  $\sqrt{\text{cm}}$ ) we have to take the random velocity  $v_0$  and the macroscopic drift velocity  $u$  or  $u_{\parallel}$  into consideration. Let us first consider the spatial width of an electron cloud after  $N$  encounters with gas atoms. We can write for the width of the cloud:

$$\sigma_x^2 = rms^2 = \sum_{i=1}^N (r_i \cos \theta_i)^2, \quad (\text{A.17})$$

where  $\theta_i$  is the random scattering angle and  $r_i$  is the radial free path, being the radial displaced position after travelling time  $t$  over the trajectory of the electron:

$$r^2(t) \approx \frac{v_0^2}{\omega^2} (2 - 2 \cos \omega t). \quad (\text{A.18})$$

Converting the summation into integrals over  $\theta$  and  $t$ , using the probability function  $g(t)$  for averaging over  $t$  as in equation A.10:

$$g(t)dt = \frac{1}{\tau} e^{-\frac{t}{\tau}} dt, \quad (\text{A.19})$$

we find the following expression for the  $\sigma_x^2$ :

$$\sigma_x^2 = \frac{N}{2\pi\tau} \int_0^{2\pi} \cos^2 \theta d\theta \int_0^{\infty} r^2(t) e^{-\frac{t}{\tau}} dt = N v_0^2 \frac{\tau^2}{1 + \omega^2 \tau^2}. \quad (\text{A.20})$$

Here, the term  $1/(1 + \omega^2 \tau^2)$  is often referred to as the reduction in the transverse diffusion (with respect to the B-field) due to the Lorentz angle. We can calculate the number of collisions during drifting over a distance  $x_{\parallel}$  towards the wire. We will calculate the diffusion in terms of drift over  $x_{\parallel}$ , which is the projection of  $x$  on a field line, because this will be the unit to integrate over when considering a cluster of electrons drifting towards the wire. The distance of drift towards the wire is given by:

$$x_{\parallel} = N \tau u_{\parallel}, \quad (\text{A.21})$$

with  $u_{\parallel}$  given in equation A.15. Substituting this result in equation A.20, one obtains the following result for the diffusion in presence of a magnetic field:

$$\sigma_x^2 = D^2 x_{\parallel}, \quad D^2 = \frac{v_0^2}{\varepsilon}, \quad (\text{A.22})$$

with  $v_0^2$  given in equation A.29.

## A.5 Determination of $v_0$ by energy conservation

We have seen that the Lorentz angle, drift velocities and diffusion depend on an unknown velocity  $v_0$ . This velocity is the average velocity of the electron immediately after the collision with a gas atom. Its magnitude can be calculated by regarding the energy balance before and after

the collision. We start with the definition of the total kinetic energy  $H$  of the electron, which is composed of a term coming from the electric field  $H_E$  and a thermal term:

$$H = \frac{1}{2}mv^2 = H_E + kT, \quad (\text{A.23})$$

with  $kT$  the kinetic energy for two degrees of freedom and  $H_E$  the total energy gained from the electric field. We consider the total energy of the electron immediately after a collision  $H_0$ :

$$H_0 = \frac{1}{2}mv_0^2 = H_{E,0} + kT, \quad (\text{A.24})$$

with  $H_{E,0}$  the total energy out of the electric field immediately after a collision. Immediately after the collision the electron starts to accelerate in the electric field and will gain some energy while it travels along a field line:

$$\Delta H_E = eE\Delta x, \quad (\text{A.25})$$

where  $\Delta H_E$  is the gain of energy from the field during a distance  $\Delta x$  in the direction of the field. Since  $\langle \Delta x \rangle$  equals  $\tau u_{\parallel}$ , one can write:

$$\langle \Delta H_E \rangle = \frac{m\varepsilon^2\tau^2}{1 + \omega^2\tau^2}. \quad (\text{A.26})$$

Now the total energy of the electron just before the collision is known. We will call this energy  $H_1$ :

$$H_1 = H_{E,0} + \frac{m\varepsilon^2\tau^2}{1 + \omega^2\tau^2} + kT. \quad (\text{A.27})$$

I will assume that the energy transfer from the electron to the gas atom can be described by a partial energy loss  $\lambda$ . In case of  $\lambda = 0$  the energy loss is zero which means that no energy is transferred to the gas. In case of  $\lambda = 1$  all energy is transferred to the gas atom. For a collision one can write down the following energy balance:

$$kT + \left( H_{E,0} + \frac{m\varepsilon^2\tau^2}{1 + \omega^2\tau^2} \right) (1 - \lambda) = H_{E,0} + kT, \quad (\text{A.28})$$

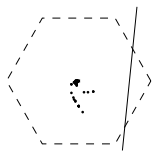
where  $kT$  is not reduced with a factor  $(1 - \lambda)$  because the electron receives exactly as much thermal energy from the gas atoms as it transfers to them in case of thermal equilibrium. By substitution of equation A.24 in equation A.28 one gets the following expression for  $v_0$  in terms of the reduced magnetic field  $\omega$ , the mean free time of drift  $\tau$ , the thermal energy  $kT$ , the reduced electric field  $\varepsilon$  and the partial energy loss  $\lambda$ :

$$v_0^2 = \left( \frac{1}{\lambda} - 1 \right) \frac{2\varepsilon^2\tau^2}{1 + \omega^2\tau^2} + \frac{2kT}{m}. \quad (\text{A.29})$$

In the following we will refer to the thermal limit as the situation where  $\lambda \rightarrow 1$  and  $v_0$  is dominated by  $kT$ . For so called "hot gases" the opposite is true,  $\lambda \rightarrow 0$  and the  $kT$  term is negligible. We can write for the equilibrium velocity  $v_0$  for both limits:

$$\text{Thermal limit : } \lambda \rightarrow 1 \quad v_0^2 = \frac{2kT}{m} \quad (\text{A.30})$$

$$\text{Hot gas : } \lambda \rightarrow 0 \quad v_0^2 = \frac{2}{\lambda} \frac{\varepsilon^2\tau^2}{1 + \omega^2\tau^2}. \quad (\text{A.31})$$



## A.6 Druyvesteyn versus Maxwell model

The models with a constant mean free path (Druyvesteyn) and constant mean free time (Maxwell) are studied by means of a Monte Carlo (MC) calculation. In this MC, 3000 electrons are tracked in a crossed  $E$  and  $B$  field during 100 ns. The velocity of the electron after each collision as well as the final position in the x-y plane are recorded. The E-field was fixed at 1000 V/cm and the B-field varied between 0.5 and 7.5 T. The model is kept as simple as possible, so an electron-velocity independent fractional energy loss  $\lambda = 10^{-3}$  was chosen. In the Maxwell assumption, the mean free drift time was chosen to be 1.0 ps and in the Druyvesteyn assumption, the mean free path was 1.0  $\mu\text{m}$ . In the following, the results will be discussed.

### A.6.1 Electron-velocity distribution

In figure A.1 and A.2 the velocity distributions are given for both the models for a large range of B-fields. Two remarkable facts appear. First: the Maxwell model has a much longer tail to high velocities. Secondly, the velocity distributions shift to lower values with increasing B-field. This means for the Maxwell model that the tail becomes shorter and the peak is more pronounced. From those distributions, one can conclude that the diffusion compression by the magnetic field

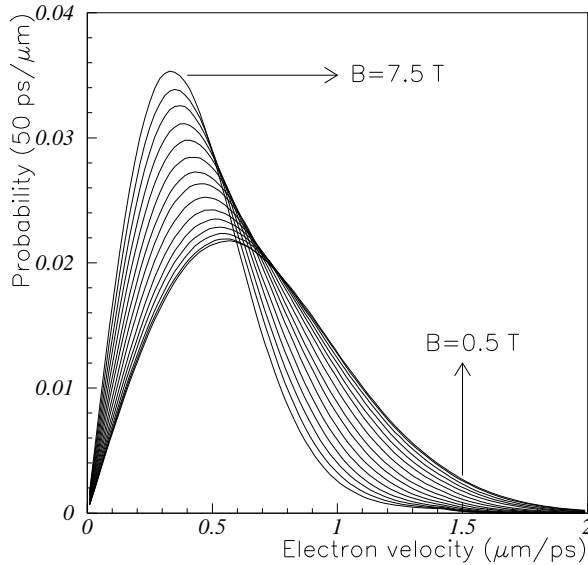


**Figure A.1:** Velocity distribution of a drifting electron in a perpendicular electric and magnetic field in the Maxwell approximation:  $\tau = \text{constant}$ . The Monte Carlo computation is done with  $E = 1000$  V/cm,  $\lambda = 10^{-3}$ ,  $\tau = 1$  ps and  $B$  ranging from 0.5 T, with 0.5 T steps, to 7.5 T.

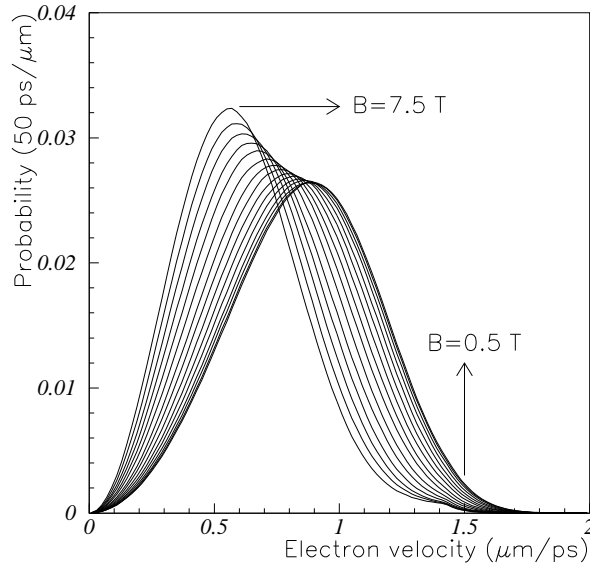


**Figure A.2:** Velocity distribution of a drifting electron as in figure A.1. The computation is performed in the Druyvesteyn approximation with the mean free path fixed at  $l=1.0$   $\mu\text{m}$ .

will be more pronounced in the Maxwell model than in the Druyvesteyn model. The numerical evidence for this difference will be found when we analyse the width of the cloud of 3000 electrons after 100 ns of drift.

## A.6.2 Electron-position distribution

In figure A.3 and A.4 the final positions of 3000 electrons are plotted after 100 ns of drift. The B-field is along the z-axis and the E-field along the x-axis, so all forces on the electrons will be in the x-y plane. For each of the two studied models, four final situations are depicted for  $B=0.5, 2.5, 5.0$  and  $7.5$  T. Also the trajectory of one individual electron is plotted. It is clear that for increasing B-field, the Lorentz angle increases. One can also observe that the size of the cloud decreases with increasing B field. From the size of the cloud parallel and transverse to the

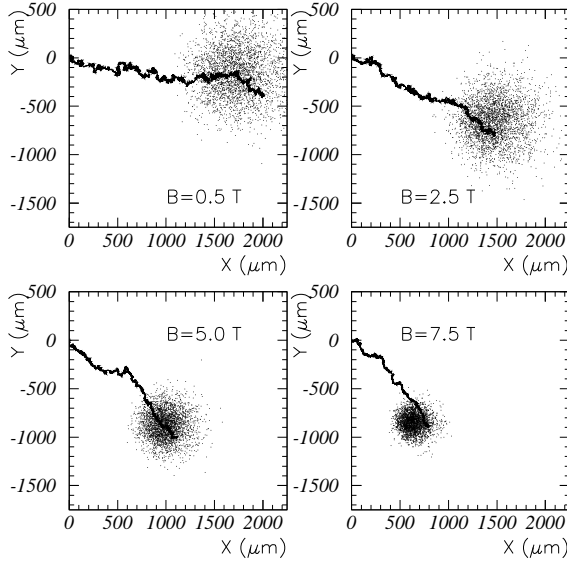


**Figure A.3:** Scatter plot of the position of 3000 electrons after 100 ns of drift, initially at rest in the origin. The Monte Carlo calculation is performed for different B-fields and the E-field of 1000 V/cm parallel to the x-axis. The mean free time  $\tau$  is assumed to be constant (Maxwell) and was 1.0 ps. Also the path of one electron is shown during its drift.

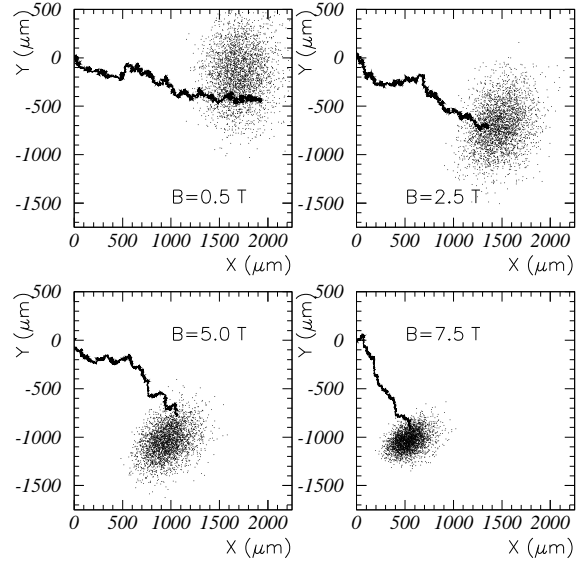
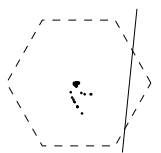


**Figure A.4:** Scatter plot of the final positions of 3000 electrons after 100 ns of drift as in figure A.3. The computation is performed in the Druyvesteyn approximation with the mean free path fixed at  $l=1.0 \mu\text{m}$ . Note the asymmetry in the width of the cloud parallel and perpendicular to the drift direction.

drift direction and the total travelled distance parallel to the E-field (x-direction), we can derive the diffusion constant  $D^2$  according to formula A.22. From figure A.4 we can see that here the cloud is not circularly symmetric in the Druyvesteyn approximation. For all B-fields the width of the cloud perpendicular to the drift direction is significantly larger than that parallel to the drift direction. This effect does not appear in the Maxwell model (figure A.3). We will introduce two diffusion constants:  $D_L^2$  and  $D_T^2$ :

$$\begin{aligned} D_L^2 &= \frac{\sigma_L^2}{x_{\parallel}}, \\ D_T^2 &= \frac{\sigma_T^2}{x_{\parallel}}, \end{aligned} \quad (\text{A.32})$$

where  $\sigma_L$  and  $\sigma_T$  the width of the cloud longitudinal and transverse to the drift direction after a drift of  $x_{\parallel}$  parallel to the E-field (x-axis).



### A.6.3 Determination of $D_L^2$ and $D_T^2$

In figure A.5 and A.6, the extracted diffusion constants are plotted for the Maxwell and Druyvesteyn approximations. Also the theoretical value of  $D^2$  is given for the Maxwell approximation using equations A.22 and A.29.

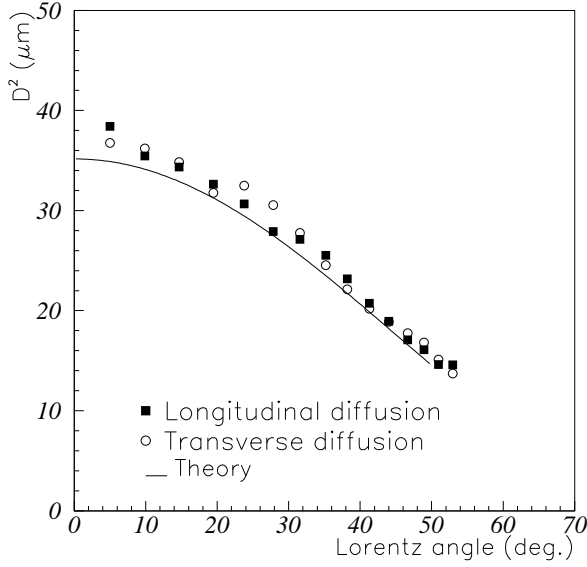


**Figure A.5:** The diffusion coefficients  $D_L^2$  and  $D_T^2$  versus the Lorentz angle  $\alpha_L$ . The coefficients are computed by a Monte Carlo approach (see figure A.3) and the result of the calculation is compared with the theoretical curve of the diffusion according to Maxwell.

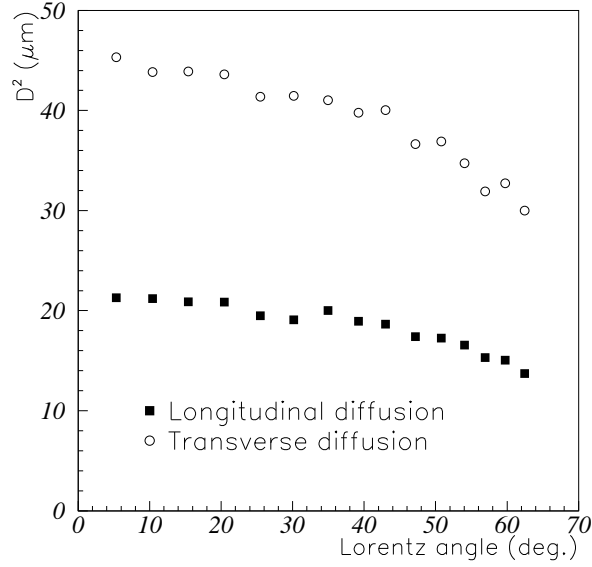


**Figure A.6:** Transverse and longitudinal diffusion computed with the Druyvesteyn model. The data is obtained with a Monte Carlo calculation and shows a less pronounced reduction of the diffusion coefficients for high  $B$ -fields as in the Maxwell model.

For the Maxwell model, the Monte Carlo data follows the theory very well and no asymmetries are observed for the longitudinal and transverse diffusion.

For the Druyvesteyn model, where no analytical expression exists for the diffusion, an asymmetry appears between the longitudinal and transverse components of the diffusion. The transverse diffusion exceeds the longitudinal diffusion for all  $B$ -fields. This behaviour can indeed be verified in figure A.4. The reduction of the diffusion due to the magnetic field is less pronounced in the Druyvesteyn model and becomes only significant for Lorentz angles above  $45^\circ$ .

The situation in a real gas will show a combination of the discussed models, where neither the mean free time  $\tau$ , nor the mean free path  $l$  will be constant for all electron velocities. Neither will the fractional energy loss  $\lambda$  be a constant for all electron velocities. The discussed models are meant to describe the processes involved during drift of an electron in gases and to obtain some insight in the magnitude of the involved parameters.

## References

- [1] W. Blum and L. Rolandi, Particle detection with drift chambers, Accelerator Physics, Springer-

Verlag, 1993, ISBN 3-540-56425-X.



# Appendix B

## Alignment with the CCD/RASNIK

*The text and figures of this appendix are extracted from the ATLAS muon note: "The CCD/RASNIK 3D alignment system, H. Groenstege et al. ".*

### Contents

<b>B.1 Principle</b>	<b>141</b>
<b>B.2 Practical realisation</b>	<b>141</b>
<b>B.3 Prototype Results</b>	<b>142</b>

### B.1 Principle

**T**he CCD/RASNIK principle is shown in figure B.1; it has three components: an illuminated<sup>a</sup> mask, a lens and a CCD with readout electronics. The lens projects a part of the mask onto the CCD. Commercial video electronics captures the CCD video frame and stores the digitized CCD response as a binary file. This file is used to determine the location of the lens center with respect to the optical axis as defined by the centers of the CCD and the mask.

Optimal performance requires a sharp image of the mask on the CCD. This imposes a constraint on the distance  $b$  between the lens and the CCD, the distance  $v$  between the lens and the mask and the focal length  $f$  of the lens:

$$\frac{1}{f} = \frac{1}{v} + \frac{1}{b} \quad (\text{B.1})$$

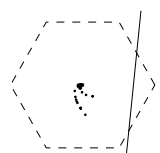
The accuracy of the alignment information is directly related to the mask pattern: the larger the number of 'features' i.e. black/white transitions the better the accuracy. A natural choice for the mask pattern is, therefore, a simple alternation of square black and white fields: a 'chess-board' as shown figure B.2a. Every 9<sup>th</sup> row and column of the chess board pattern contains encoded information to allow the unique identification of the part of the mask registered by the CCD. The size of the mask defines the maximum allowed mis-alignment. In principle arbitrary large masks can be employed; in practice commercially available precision masks (notably those used in the semiconductor industry) are limited to  $100 \times 100 \text{ mm}^2$ .

### B.2 Practical realisation

CCD/RASNIK is a genuine 3-dimensional relative position monitor:

---

<sup>a</sup>To operate the CCD/RASNIK system almost independent of external light conditions, an infrared lightsource is used together with an infrared filter mounted directly in front of the CCD.



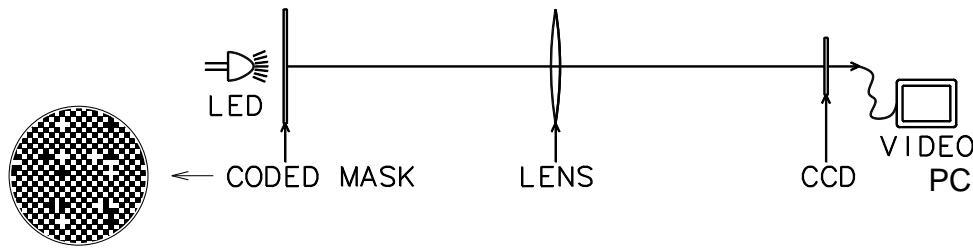


**Figure B.1:** Principle of the CCD/RASNIK system.

- In the plane perpendicular to the optical axis, the mis-alignment is determined from the part of the mask seen by the CCD. E.g. for a system with  $v = b = 2f$ , a displacement of the lens perpendicular to the optical axis of  $d \mu\text{m}$  is seen as a  $2 \times d \mu\text{m}$  shift of the mask pattern on the face of the CCD.
- Along the optical axis, the mis-alignment is determined from the scale factor i.e. the ratio of the periodicity (size of an individual black or white field) as measured by the CCD and the known periodicity of the mask. For example a longitudinal mis-alignment  $\varepsilon$  for the same system as above; i.e.  $v = 2f + \varepsilon$  and  $b = 2f - \varepsilon$ , yields for the scale factor,  $A$ :

$$A \equiv \frac{b}{v} = \frac{2f - \varepsilon}{2f + \varepsilon} \quad \Rightarrow \quad \varepsilon = \frac{1 - A}{1 + A} \times 2f \approx (1 - A) \times f \quad (\text{B.2})$$

The accuracy of the perpendicular and longitudinal alignment information depends in principle on the geometry i.e.  $v$ ,  $b$  and  $f$  of the system (sharpness and nominal scale factor), on the intrinsic precision of the mask and the CCD and on the image reconstruction. Mask and CCD production rely on the same, very precise  $\ll 1 \mu\text{m}$ , technology: (successive) photographic etching of silicon wafers. The other performance limitations are discussed and illustrated in the next section with results achieved on prototype systems with  $v = b = 2f$ .

### B.3 Prototype Results

The setup used for the pilot performance tests consists of: a Philips (VCM 3250/00/CCIR) CCD with  $512(h) \times 582(v)$  pixels each  $12.8(h) \times 8.4(v) \mu\text{m}^2$  large, a  $23 \times 23 \text{ mm}^2$  large illuminated mask (alternate  $170 \times 170 \mu\text{m}^2$  large black and white fields; global code information present on each 9<sup>th</sup> row and column as shown in figure B.2a) and a lens with a focal length of  $f = 60 \text{ mm}$  or  $f = 1355 \text{ mm}$ . These components (CCD, lens and mask) are mounted on a common optical rail via mechanisms which allow manual setting of the position of each component separately in three orthogonal directions over a 10 mm range with a  $1 \mu\text{m}$  precision. Only the first 512 horizontal rows of the CCD are read out and digitized by a personal computer using consumer video electronics (a Datatranslation DT 2859 video multiplexer, and a Datatranslation DT 2855/50 Hz frame grabber resulting in  $768 \times 512$  single bytes i.e. 393216 bytes of data for an image).

The offline image processing and position reconstruction proceeds along three steps:

1. Identify the ‘features’ i.e. the transitions between black and white squares. Standard computer science algorithms like differential filters are used for this, an example of the ‘raw’ and the filtered CCD output is shown as an insert in figure B.2b. Typically an individual transition is reconstructed with a  $5\text{--}10 \mu\text{m}$  precision. The total number of transitions identified in the present setup is between 10000 and 20000.

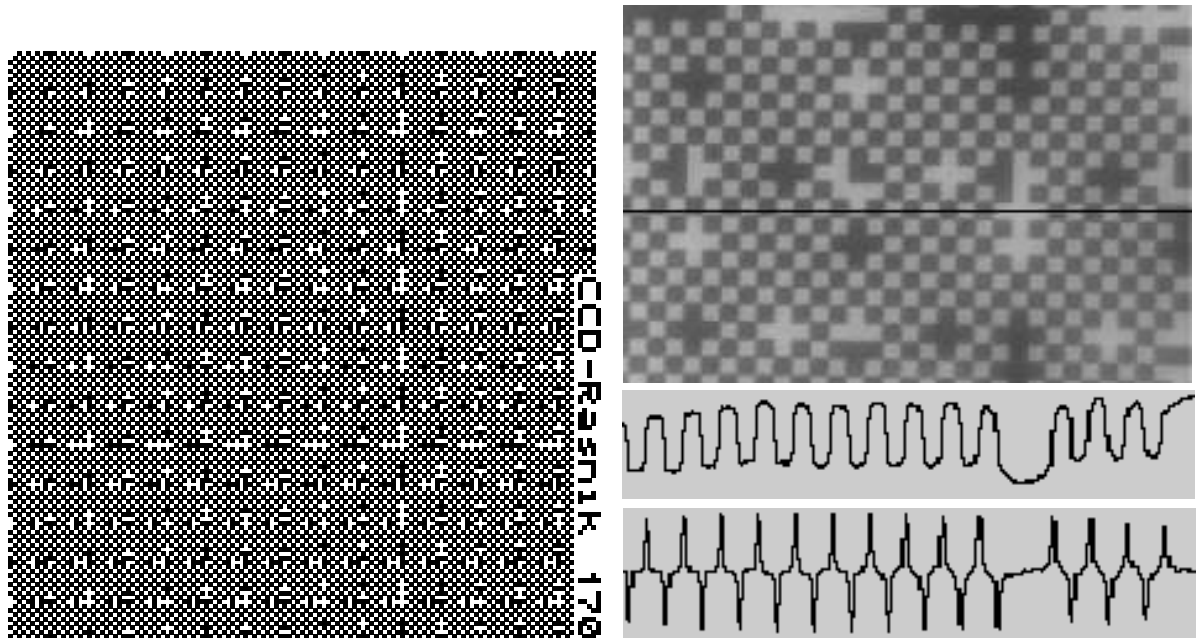
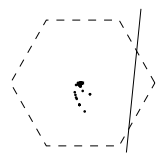


**Figure B.2:** (a) The mask. The irregularities on every 9<sup>th</sup> row and column are due to the encoded information. (b) Digitized CCD response (0 – 255) shown on a grey scale (0 = black and 255 = white). The inserts show, along a horizontal line, the digital output and the result of a differential filter, which clearly shows the black/white transition localizing power of such a filter.

2. Calculate for each selected black/white transition the minimal distance to an orthogonal grid of equidistant lines. Define a  $\chi^2$  as the sum of the squares of all these minimal distances and minimize this  $\chi^2$ . The five fit parameters are a common rotation angle, a periodicity and an offset in each of the two directions orthogonal to the optical axis. The periodicity divided by 170  $\mu\text{m}$  (size of the basic squares on the mask) is the scale factor needed, together with the focal length  $f$ , to obtain the mis-alignment along the optical axis.
3. Identify and decode the global code information. Together with the two offsets this yields the mis-alignment information in the plane perpendicular to the optical axis.

To evaluate the performance of the CCD/RASNIK alignment monitor in either the longitudinal or the transverse direction w.r.t. the optical axis, three methods are used. The simplest method is to collect multiple images at a fixed position. The r.m.s. of the distribution of the reconstructed positions gives the accuracy on the alignment information of a single image. An alternative method is to scan one of the components, mask, lens or CCD, in, say, the transverse direction and to perform a straight line fit on the set of input - and reconstructed positions. The residuals of this fit are used to calculate the accuracy on the alignment information of a single image. This method suffers from the 1  $\mu\text{m}$  setting accuracy of the position adjustment mechanism, but yields on top of the reconstruction precision also information on the linearity of the system. Finally the errors on the reconstructed positions obtained from the  $\chi^2$  fit can be used as a measure of the accuracy on the alignment information of a single image. For the  $f = 60$  mm system, the methods yield consistent results; an example of the scan method for the longitudinal coordinate is shown in figure B.3b. For the  $f = 1355$  mm system, the errors obtained from the  $\chi^2$  fit are substantially smaller than the results of the other two methods; this is probably due to air turbulence which leads to ‘jitter’ of the mask image on the CCD. If so, this jitter can probably be overcome by the averaging of multiple images since it is an artefact of the alignment monitor



and has nothing to do with the relative mask-lens-CCD positions. Indeed averaging of multiple successive images reduces the discrepancies between the alternative methods to evaluate the CCD/RASNIK accuracy.

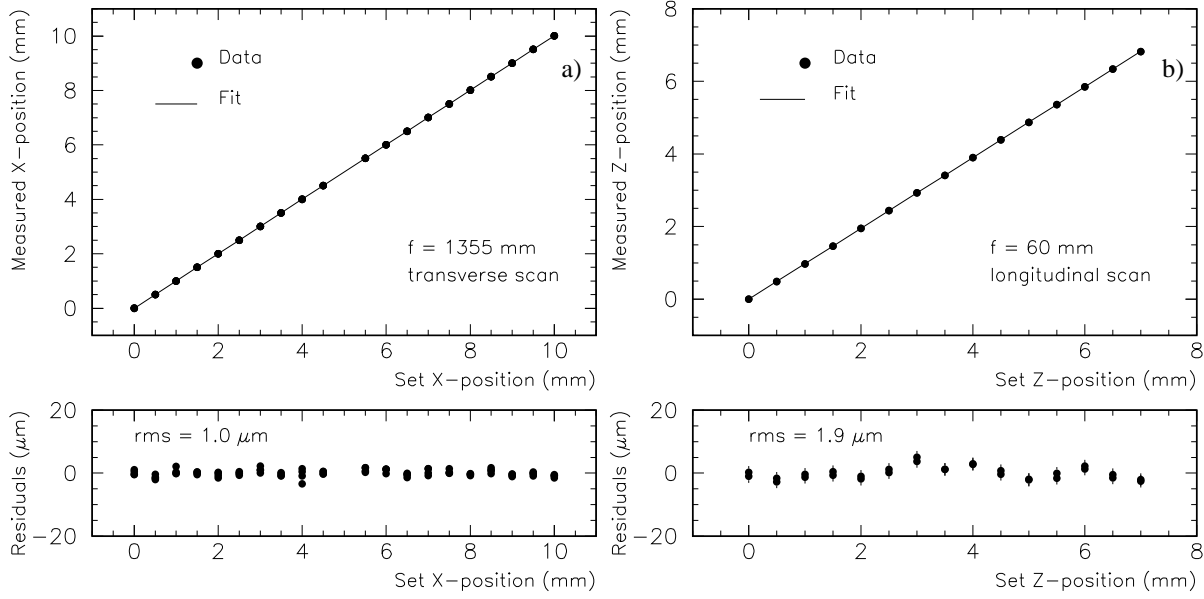


**Figure B.3:** (a) Example of a performance scan for a setup with  $f = 1355$  mm and  $v \approx b \approx 2710$  mm. The position of the mask was varied over 10 mm in the plane perpendicular to the optical axis. The r.m.s. of the residuals is only  $1.0 \mu\text{m}$  and the linearity of the system is evident. (b) Example of a performance scan for a setup with  $f = 60$  mm and  $v \approx b \approx 120$  mm. The position of the lens was varied over about 7 mm in the direction along the optical axis. The r.m.s. of the residuals is only  $1.9 \mu\text{m}$  and the linearity of the system is evident.

Focal Length $f$	Transverse Direction	Longitudinal Direction	
	one image	one image	four images
60 mm	$1.0 \mu\text{m}$	$1.9 \mu\text{m}$	—
1355 mm	$1.0 \mu\text{m}$	$40 \mu\text{m}$	$20 \mu\text{m}$

**Table B.1:** CCD/RASNIK performance, the columns headed ‘one image’ applies to the analysis of single images and the column headed ‘four images’ applies to the analysis of the average of four successive images. These performance figures are from the ‘scan’ method; they are limited by the  $1 \mu\text{m}$  setting accuracy of the moving mechanism.

The results are summarized in table B.1 for the two lenses investigated; for a system with an arbitrary lens we expect a longitudinal accuracy of about  $0.03 \times f \mu\text{m}$  ( $f$  in mm). From these studies we conclude that the CCD/RASNIK alignment monitor operates at or below the  $1 \mu\text{m}$  level in the plane transverse to the optical axis and at the  $0.03 \times f \mu\text{m}$  ( $f$  in mm) level in the direction along the optical axis.

# Appendix C

## The HGANA analysis programme

### Contents

---

C.1 Introduction . . . . .	145
C.2 Layout of the programme . . . . .	146
C.3 The wire data analysis . . . . .	146
C.4 The strip data analysis . . . . .	147
C.5 The datacards . . . . .	148

---

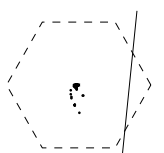
### C.1 Introduction

**T**he prototype performances as presented in chapter 6 are extracted from the raw data by the fortran77 programme HGANA. The first version of HGANA was written by H. van der Graaf in 1991 to analyse simulated data, generated with his first ad-hoc HSC simulation programme.

This initial version of HGANA was adopted by the author of this thesis to analyse the data from the first cosmic ray experiment with the P1 detector in 1992. Since then HGANA has developed into an allround HSC data analysis programme with fitting algorithms for both drift time and pulse height data.

The main features of HGANA are:

- High flexibility in data input formats. ASCII datafiles generated by the CAVIAR read-out computer during the cosmic test as well as ZEBRA and EPIO formatted files from beam experiments can be handled.
- Advanced pattern recognition algorithms to distinguish between noise hits and real hits in the wire and strip analysis.
- Implementation of various autocalibration algorithms. In case of many noise hits a more robust algorithm can be chosen. In case of clean signals, the faster algorithm as described in chapter 5 can be used.
- The geometry of the detector can be fitted from the measured muon tracks. The planes can be shifted relatively in  $x$  and  $z$  direction and the position of the wires can be fitted individually in  $z$  and  $y$ . The  $T_0$  can be fitted for each individual wire.
- The autocalibration, plane and wire fits and  $T_0$  determination is separated from the pattern recognition routines. This makes that HGANA runs fast.
- Two-dimensional event displays perpendicular to the wires as well as perpendicular to the strips.



## C.2 Layout of the programme

The programme runs several times over the data. During the first iteration a TDC spectrum is made from all measured drift times. This TDC spectrum is used to compute the so-called 'initial  $r(t)$ '. In the second and later iterations the tracks are fitted in the wire and strip coordinates and a database is filled with hit information for autocalibration and geometry fits. The (optional) fit of the wire and strip positions and autocalibration of  $r(t)$  is performed at the end of each iterations.

The weights of the hits in the trackfit is equal to the inverse resolution of the hit. In the first and second iteration those weights are set to the equivalent of 1 mm resolution in  $x$  and  $z$ . During all successive iterations the weights are calculated from the measured resolution in the iteration before. The weights for hits on the anode wires depend on the measured drift time, while for the strip read-out the weights (and thus the resolution) are assumed to be constant over the width of the strip. This procedure to compute the weights from the data has been tested on simulated data with known resolution and the agreement between the reconstructed resolution and input resolution in the simulation appeared to be very well (see chapter 5). The programme was stopped after typically 7 to 10 iterations when all results like  $r(t)$ , resolution and wire/strip positions had converged to constant values.

The structure of the main programme is:

<pre> program hgana  call readcards      Read datacards (see C.5) if (anawire) then   In case the wire analysis is ON   call iniwire      Initialise wire analysis endif if (anastrip) then  In case the strip analysis is ON   call readcal       Read strip calibration   call readped       Read ADC pedestals   call inistrip      Initialise strip analysis endif  10 if (anawire) then → NEXT ITERATION   call readzplanes   Read z per plane   call readzywires   Read (z,y) per wire   call readt0        Read To per wire   call readrt        Read r(t)   call readweight    Read weights   call resetwire     Reset wire variables endif if (anastrip) then </pre>	<pre>   call readxplanes   Read x per plane   call resetstrip    reset strip variables endif  do nrdatnow=1,nr_datfiles  Over all datafiles   call opendata          Open datafile   do neve=1,nevemax      Over all events     call clear            Reset variables     call readevent        Read data from file     if (anawire) call wire Fit wire data     if (anastrip) call strip Fit strip data   enddo   call closedata          Close datafile enddo  if (anawire) call outwire Autocal., geom. fit if (anastrip) call outstrip Geometry fit call dumpstat             Write run info.  iter=iter+1 if (iter.le.nrun) goto 10  Next iteration ? end </pre>
---	---

## C.3 The wire data analysis

The measured drift times of all hit wires are first corrected with the  $T_0$ s. The drift time of each hit is then converted to drift distance making use of the current  $r(t)$ . The hits can be represented by circles around the hit wires. The track will be the tangent to the constructed circles.

The circles of equal drift time and two reconstructed tracks are shown in figure C.1 for a event measured in one of the P2 chambers.

The pattern recognition routines have to find the most likely track(s). A track is per definition the tangent to three or more circles associated with the hits. The number of required hits can be varied. For tracks between  $-30^\circ$  and  $30^\circ$  the maximum number of hits is eight, but the average is about 6.8 due to the small gaps between two neighbouring cells. In order to compensate for inefficiencies the minimum number of required hits on the track was 4 during all analysis.

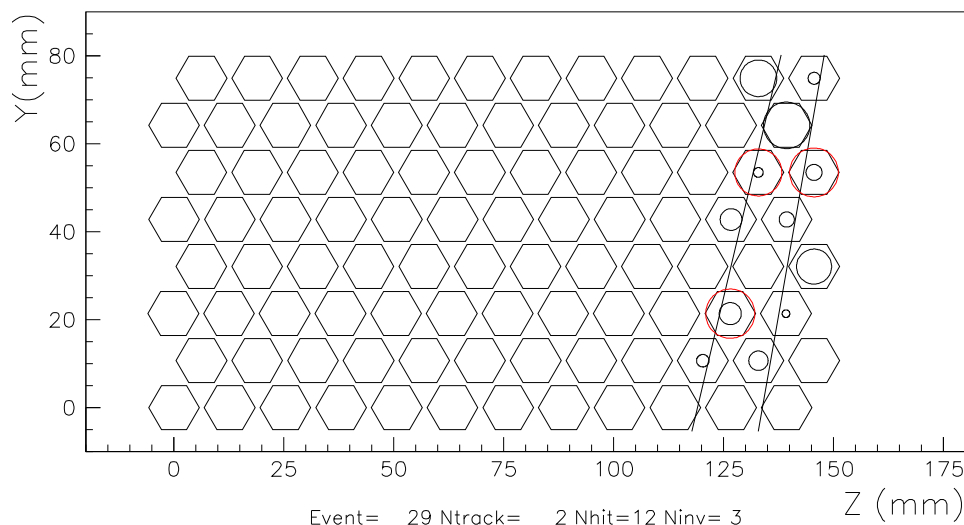


**Figure C.1:** Event display of wire read-out.

The search for tracks in a sample of hits is performed by running over all pairs of hits. For a pair of hits, one can define four possible so-called 'candidate tracks' (two ambiguities per hit). The distance from the candidate track to all remaining hit wires is compared with the measured drift distance. In case the measured drift distance matches the distance from the candidate track to the wire, this hit is added to the set of so-called 'candidate hits'. In case more than e.g. four candidate hits are found, a global track fit is made and the  $\chi^2$  of the fit is compared with a maximum tolerated value. During the whole analysis, the  $\chi^2$  should not exceed 5.0.

If not enough hits are found on a candidate track or the  $\chi^2$  exceeds the threshold, the next candidate track is tried. In case all four candidate tracks do not result in a successful fit of a track, a new pair of hits is tried with four new candidate tracks. The algorithm stops in case no more pair of hits can be made or in case all hits are assigned to tracks.

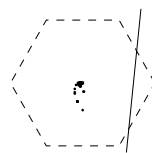
For autocalibration, only events are used with single tracks and (optionally) more hits can be required for this sub-dataset. The parameters of the hits of selected events for autocalibration are stored in a database and this database is used at the end of each iteration to perform autocalibration, plane and wire position fits and  $T_0$  fits.

## C.4 The strip data analysis

The pattern recognition on the pulse height data of the cathode strips is far simpler than the above discussed anode wire data pattern recognition. For all combinations of three adjacent strips, combinations are selected with a total charge that exceeds a threshold and where the charge on the 'left' and 'right' strips is less than the middle strip. For all those combinations of three adjacent strips, the position of the hit is computed from the pulse heights on the three strips (see equation 4.6).

Then a candidate track is defined from at least two planes with single hits. In all other planes the hit nearest to the candidate track are included in the global track fit. Then the track is accepted or rejected on the basis of a  $\chi^2$  criterium.

In figure C.2 the same event is displayed as in figure C.1, now the view is perpendicular to the strips. Only one track is visible in this view. This means that the other track has passed the chamber at a position where no strip front-end was mounted. The indicated charge  $Q_{\max}$  at the



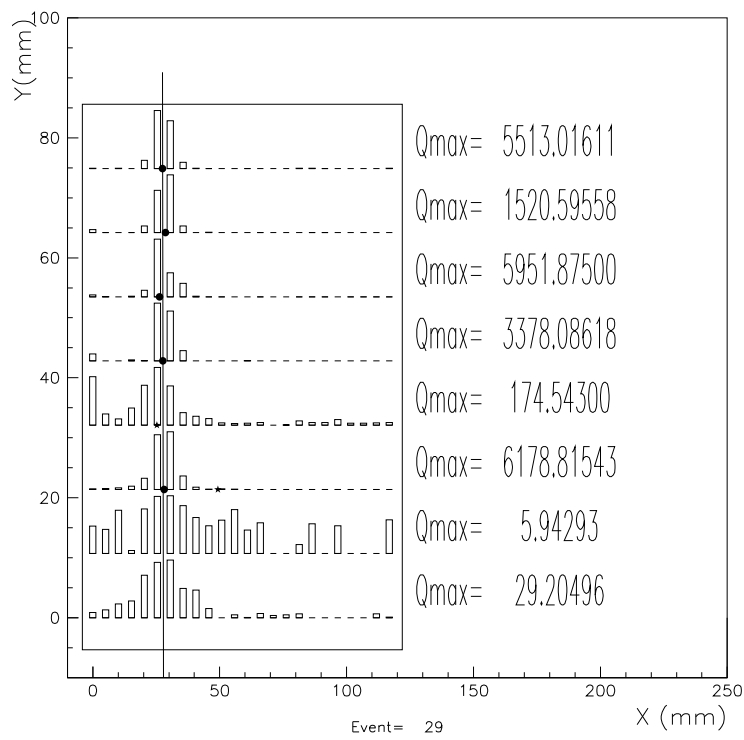


**Figure C.2:** Event display of strip read-out.

right side of each plane indicates the maximum measured charge on a strip in the plane.

## C.5 The datacards

HGANA starts by reading the data cards. These cards define the input files and the run parameters. An example of such a card is shown with comments on the function of the card.

```

C -----> DATA FILES <-----
NDAT 1                               Number of input data files
DATA 1='/stage/instr/p3a/190894.dat   ' Name of the data files(s)
ZPLN '/user/i94/rd5/geom/vzplane.190894 ' Input file with alignment errors in z-direction per plane
XVAL '                               ' x-coordinate per track, for correlation studies with wire read-out
TZER '/user/i94/rd5/t0/t0_p3A.190894 ' To per wire and global To for all wires
PEDE '                               ' Pedestal data for strip ADCs
CALI '                               ' Calibration coefficients for strip pre-amplifiers

C -----> RUN CONTROL <-----
FORM 'P3C3'                          HSC experiment, e.g. here the P3 1993 cosmics data is analysed
NFOR 0                               Data format switch within the HSC experiment
CHAM 1                               Number of the detector if data of more HSCs is in one data file
TRIG 0                               Iteration number of first run, it is possible to skip the initialisation iteration
REND 7                               Number of last iteration over the data
FRST 1                               First event number to analyse on data file
LAST 50000                           Last event number to analyse on data file
IBUG 0                               Number of debug events (verbose output)
FCTR 101                             Sets the amount of output during fits
GRPH OFF                             Switch for graphics production every event
SCRN OFF                             Switch for graphics production on display
SOUN ON                              Switch for sound effects
HLAS OFF                             Switch for histogram output after all iterations or last iteration

C -----> WIRE ANALYSIS <-----
WIRE ON                              Switch for wire analysis
WHIT 4                               Number of hits required on a track during pattern recognition
WHAC 4                               Number of hits required on a track for autocalibration
IVRT OFF                             Switch to indicate common start or stop mode

```

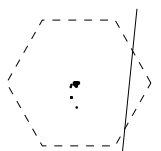






# Glossary and abbreviations

ADC	Analogue to Digital Converter, electronic unit to convert the pulse height into a digital number
ATLAS	General-purpose p-p detector, LHC experiment
CCD/RASNIK	Red Alignment System NIKhef based on CCD readout
CERN	European organisation for nuclear research
CHEOPS	CHarm Experiment with Omni-Purpose Setup at CERN
CHORUS	Neutrino oscillation experiment at CERN
CMS	The Compact Muon Solenoid, LHC experiment
ECL	Emitter Coupled Logic
EHS-magnet	Superconducting solenoid 3 T magnet, designed and constructed for the European Hybrid Spectrometer, currently used by the RD5 experiment
GARFIELD	Drift chamber simulation package
GEANT	Software package for detector simulation. The interaction between the high energetic particles and the detector material is simulated in detail
HERA-B	Experiment to study CP violation in the B system at the DESY
HGANA	Fortran77 programme to analyse HSC drift time and pulse height data
HSC	Honeycomb Strip Chamber
L3	One of the LEP experiments (LEP-3)
LEGO block	Mold-injected precision plastic block defining the wire positions
LEP	Large Electron Positron collider, $e^+e^-$ collider at CERN, currently upgraded to LEP200 with a centre of mass energy $\sqrt{s} = 200$ GeV
LHC	The Large Hadron Collider
LHC-B	Dedicated B-physics experiment at LHC
MAGBOLTZ	Fortran77 programme to compute the gas transport parameters for gas mixtures
Monolayer	Plane of parallel hexagonal tubes
MSGC	Micro Strip Gas Counter
Multilayer	Stack of monolayers
MX5	Charge sensitive pre-amplifier chip for 128 MSGC channels
NIM	Standard pulse in nuclear physics experiments, $V=0.6$ V, $Z=50$ $\Omega$
P1,P2,P3,P3A	HSC prototype 1,2,3 and aluminium P3
RD5	Research & Development experiment at CERN
$r(t)$	Relation between the most probable distance of the track from the anode wire and the measured drift time.
Sagitta	Maximum deviation of a bend track from a straight line which is defined by the two outer points on the track
Sirocco	Flash ADC for MSGC pulse height measurement
TDC	Time to Digit Converter, electronic unit which notes the moment of threshold crossing of the wire signal.
TRACAL	TRAcing CALorimeter: experimental set-up of iron absorbers and monolayer HSCs
Often used symbols	
$\Theta$	Polar angle in a collider experiment, defined with respect to the beamline
$\Phi$	Azimuthal angle in a collider experiment, defined with respect to the vertical
$\theta$	Angle of incidence in the HSC with respect to the normal to the chamber and in the plane perpendicular to the wires
$\phi$	As $\theta$ , but defined in the plane perpendicular to the strips

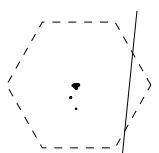




# Bibliography

## References Chapter 1

- [1] Proceedings of the Large Hadron Collider Workshop, Aachen, 4–9 October 1990, Vol I,II,III, CERN 90-10.
- [2] G. Brianti, The Large Hadron Collider in the LEP tunnel, LHC Working group, published in [1].
- [3] J. Feltesse, Experimentation at LEP/LHC, published in [1].
- [4] The ATLAS collaboration, ATLAS Technical Proposal, CERN/LHCC/94-43, LHCC/P2, 15 December 1994.
- [5] The LHC study group, The Large Hadron Collider, Conceptual design, CERN/AC/95-05 (LHC), 20 October 1995.
- [6] D. Denegri, Standard Model physics at the LHC (pp collisions), 27 November 1990, published in [1].
- [7] A. Sopczak, Status of Higgs Hunting at the Z Resonance and its Prospects at LEP2, CERN-PPE/94-73, 9 May 1994.
- [8] I.I. Bigi, V.A. Khoze, N.G. Uraltsev, and A.I. Sanda, The question of CP noninvariance as seen through the eyes of neutral Beauty, published in “CP Violation, Advanced series on directions in High Energy Physics-Vol 3, ed. C. Jarlskog, World Scientific, 1989”.
- [9] The LHC-B collaboration, LHC-B, A dedicated LHC Collider Beauty Experiment, for Precision Measurements of CP-Violation, Letter of intent, CERN/LHCC 95-5, LHCC/I 8, 25 August, 1995.
- [10] L. Montanet *et al.*, Physical Review **D50**, 1173 (1994) and 1995 off-year partial update for the 1996 edition, available on the PDG WWW pages (URL: <http://www-pdg.lbl.gov/>).
- [11] The CDF collaboration, Evidence for Top Quark Production in  $\bar{p}p$  Collisions at  $\sqrt{s} = 1.8$  TeV, FERMILAB-PUB-94/097-E, CDF/PUB/TOP/PUBLIC/2561.
- [12] Z. Kunszt, The Standard Model Higgs at LHC: Branching Ratios and Cross-Sections, published in [1].
- [13] S. Spira, A. Djouadi, D. Graudenz and P.M. Zerwas, Higgs boson production at the LHC, DESY 94-123, GPP-UdeM-TH-95-16, CERN-TH/95-30, hep-ph/9504378, February 1995.
- [14] I. Hinchliffe, The Higgs Boson, LBNL publication, published in [10].
- [15] C. Seez and T. Virdee, L. DiLella, R. Kleis, Z. Kunszt and W.J. Stirling, Photon decay modes of the intermediate mass Higgs, published in [1].
- [16] The CMS collaboration, CMS Technical Proposal, CERN/LHCC/94-38, LHCC/P1, 15 December 1994.
- [17] D. Froidevaux, Experimental review of the search for the Higgs boson, published in [1].
- [18] R. Hawkings, Intermediate mass  $H \rightarrow 4l$ : A particle level and isolation study, ATLAS Internal note, PHYS-NO-062, 5 January 1995.
- [19] M. Della Negra, D. Froidevaux, K. Jakobs, R. Kinnunen, R. Kleiss, A. Nisati and T. Sjöstrand, Search for  $H \rightarrow Z^*H^*$  leptons at LHC, published in [1].
- [20] T. Sjöstrand (CERN), High-energy physics event generation with PYTHIA 5.7 and JETSET 7.4., CERN-TH-7111-93, December 1993. Published in Comput. Phys. Commun. **82** (1994), 74–90.
- [21] B. van Eijk and R. Kleiss, On the calculation of the exact  $gg \rightarrow Zb\bar{b}$  cross section including Z decay and b quark mass effects, published in [1].
- [22] The ATLAS collaboration, Letter of Intent for a General-Purpose p-p Experiment at the Large Hadron Collider at CERN, CERN/LHCC/92-4, LHCC/I 2, 1 October 1992.
- [23] A. Nisati, Search for  $p-p \rightarrow H \rightarrow ZZ \rightarrow \mu^+\mu^-\mu^+\mu^-$  at the LHC, published in [1].
- [24] F. Cavanna, D. Denegri and T. Rodrigo, Top search at the LHC: Signal versus Background, published in [1].
- [25] S. Drell and T.M. Yan, Phys. Rev. Lett. **25** (1970) 316. G. Moreno *et al.*, Phys. Rev. **D43** (1991) 2815. P.L. McGaughy *et al.*, Phys. Rev. **D50** (1994) 3038. <http://www.rarf.riken.go.jp/~rarf/rhic/phys/DY/DY.html>.
- [26] A. Henriques and L. Poggioli, Detection of the  $Z'$  vector boson in the jet decay mode ( $Z' \rightarrow q\bar{q}$ )( $g \rightarrow jj$ ): Resolution and pile-up studies, ATLAS Internal note, PHYS-NO-010, 1 October 1992.
- [27] F. Del Aguila *et al.*, New vector bosons at LHC, published in [1].
- [28] G. Altarelli, B. Mele and M. Ruiz-Altaba, Searching for new heavy vector bosons in  $p\bar{p}$  colliders, Z. Phys. C **45**, (1989), 109–121.
- [29] M.C. Cousinou and C.P.P.M. Marseille, Search for a  $W'$  in the  $lv$  channel, ATLAS Internal note, PHYS-NO-059, 19 December 1994.
- [30] F. Pauss, Beyond the Standard Model in pp collisions, published in [1].
- [31] P. Camarri, V. Cvasinini and C. Wulz,  $Z'$  into leptons, published in [1].



## References Chapter 2

- [1] The ATLAS collaboration, ATLAS Technical Proposal, CERN/LHCC/94-43, LHCC/P2, 15 December 1994.
- [2] R.L. Gluckstern, Uncertainties in track momentum and direction, due to multiple scattering and measurement errors, Nucl. Instr. & Methods **24** (1963) 381-389.
- [3] H. van der Graaf *et al.*, The honeycomb strip chamber: the application in LHC/SSC experiments and the test results of a prototype, Nucl. Instr. & Methods **A307** (1991) 220.
- [4] C. Guyot and H. van der Graaf, ATLAS MUON NOTE, Alignment of the muon system. .

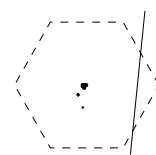
## References Chapter 3

- [1] H. van der Graaf *et al.*, The honeycomb strip chamber: the application in LHC/SSC experiments and the test results of a prototype, Nucl. Instr. & Methods **A307** (1991) 220.
- [2] G. Charpak, R. Bouclier, T. Bressani, J. Favier and Č. Zupančič, Nucl. Instr. & Methods, **62** (1968) 262.
- [3] T. Bressani, G. Charpak, D. Rahm and Č. Zupančič, Track localization by means of a drift chamber, Proc. Dubna Meeting *Filmless and streamer chambers*, April 1969.
- [4] W. Blum and L. Rolandi, Particle detection with drift chambers, Accelerator Physics, Springer-Verlag, 1993, ISBN 3-540-56425-X.
- [5] The ATLAS collaboration, ATLAS Technical Proposal, CERN/LHCC/94-43, LHCC/P2, 15 December 1994.
- [6] F. Bakker *et al.*, The construction and performance of single-layer honeycomb strip chambers in the TRACAL detector of RD5, Nucl. Instr. & Methods **A330** (1993) 40.
- [7] R. Bergman, Thesis on the TRACAL detector in RD5, Title to be announced, University of Nijmegen, PhD Thesis, 1996, Nijmegen.
- [8] P. Duinker *et al.*, Some methods and tools for testing and optimizing proportional wire chambers, Nucl. Instr. & Methods **A273** (1988) 814-819.
- [9] R. Bock *et al.*, Wire fixation for proportional and drift chambers using a Cu-Te alloy, Nucl. Instr. & Methods **A336** (1993) 128, I. Physikalisches Institut, Rheinisch-Westfälische Technische Hochschule, Aachen, Germany.
- [10] V.A. Chechin, L.P. Kotenko, G.I. Merson, V.C. Yermilova, The relativistic rise of the track density in bubble chambers, Nucl. Instr. & Methods, **98** (1972) 577-587.
- [11] J.D. Jackson, Classical Electrodynamics, John Wiley & sons, Second Edition, 1975, ISBN 0-471-43132-X.
- [12] W.W.M. Allison and J.H. Cobb, Relativistic charged particle identification by energy loss, Ann. Rev. Nucl. Sci. **30** (1980) 253.
- [13] U. Fano, Ann. Rev. Nucl. Sci, **13** (1963) 1.
- [14] J.H. Cobb, W.W.M. Allison and J.N. Bunch, The ionisation loss of relativistic charged particles in thin gas samples and its use for particle identification; Theoretical predictions, Nucl. Instr. & Methods, **133** (1976) 315-323.
- [15] L. Landau, J. Phys. (USSR) **8** (1944) 201.
- [16] F. Harris *et al.*, Nucl. Instr. & Methods, **107** (1973) 413.
- [17] J.H. Cobb, D. Phil. thesis (Univ. of Oxford, 1975). Available from Rutherford as HEP/T/55.
- [18] O. Blunck and S. Leisegang, Z. Physik **128** (1950) 500.
- [19] K.A. Ispirian, A.T. Margarian and A.M. Zverev, A monte-carlo method for calculation of the distribution of ionization losses, Nucl. Instr. & Methods **117** (1974) 125-129.
- [20] V.C. Ermilova, L.P. Kotenko and G.I. Merzon, Fluctuations and the most probable value of relativistic charged particle energy loss in thin gas layers, Nucl. Instr. & Methods, **145** (1977) 555-563.
- [21] F. Lapique and F. Piuz, Simulation of the measurement by primary cluster counting of the energy lost by a relativistic ionizing particle in argon, Nucl. Instr. & Methods, **175** (1980) 297-318.
- [22] Hansjörg Fischle, Joachim Heintze and Bernard Schmidt, Experimental determination of ionization cluster size distributions in counting gases, Nucl. Instr. & Methods, **A301** (1991) 202-214.
- [23] E.J. Kobetich and R. Katz, Energy deposition by electron beams and delta rays, Phys. Rev. **170** (1968) 391.
- [24] F. Sauli, Principles of operating of MultiWire Proportional and Drift Chambers, CERN 77-09, 1977.
- [25] V. Palladino and B. Sadoulet, Application of classical theory of electrons in gases to drift proportional chambers, Nucl. Instr. & Methods **128** (1975) 323-335.
- [26] E.B. Wagner, F.J. Davies and G.S. Hurst, Time-of-flight investigations of electron transport in some atomic and molecular gases, J. Chem. Phys. **47** (1967) 3138.
- [27] M. Huk, P. Igo-Kemenes and A. Wagner, Electron attachment to oxygen, water and methanol, in

- various drift chamber gas mixtures, Nucl. Instr. & Methods **A267** (1988) 107–119.
- [28] S. Biagi, MAGBOLTZ source code, CERN, obtained by private communication, Biagi@cernvm.cern.ch for information.
- [29] L.C. Pitchford, S.V. O’Neil and J.R. Rumble Jr., Extended Boltzmann analysis of electron swarm experiments, Phys. Rev. A **23-1** (1981) 294–304.
- [30] S.F. Biagi, Accurate solution of the Boltzmann transport equation, Nucl. Instr. & Methods **A273** (1988) 533–535.
- [31] S.F. Biagi, A multiterm Boltzmann analysis of drift velocity, diffusion, gain and magnetic-field effects in argon-methane-water-vapour mixtures, Nucl. Instr. & Methods **A283** (1989) 716–722.
- [32] K.F. Ness, Multi-term solution of the Boltzmann equation for electron swarms in crossed electric and magnetic fields, J. Phys. D: Appl. Phys. **27** (1994) 1848–1861.
- [33] G. Battistoni *et al.*, Influence of gas mixture and cathode material on limited streamer operation, Nucl. Instr. & Methods **217** (1983) 433–439.
- [34] W. Diethorn, A methane proportional counter system for natural radiocarbon measurements, US-AEC report (1956) NY06628, Also doctoral dissertation, Carnegie Inst. of technology (1956).
- [35] J.C. Armitage, S.P. Beingessner, R.K. Carnegie, E.F. Ritchie and J. Waterhouse, A study of the effect of methane and carbon dioxide concentration on gas amplification in argon based gas mixtures, Nucl. Instr. & Methods **A271** (1988) 588–596.
- [36] J. Grog, E. Schenuit and H. Spitzer, Computer simulation of the electron avalanche in cylindrically symmetric electric fields, Nucl. Instr. & Methods **A283** (1989) 730–734.
- [37] M. Matoba, T. Hirose, T. Sakae, H. Kametani, H. Ijiri and T. Shintake, Three dimensional Monte Carlo simulation of the electron avalanche around an anode wire of a proportional counter, IEEE Transactions on Nuclear Science NS-32 **1** (1985) 541–544.
- [38] R. Bellazzini and M.A. Spezziga, Electric field, avalanche growth and signal development in Micro-Strip Gas Chamber and Micro-Gap Chamber, INFN internal note INFN PI/AE 94/02, INFN-Pisa and University of Pisa, June 1994, Paper submitted for publication in La Rivista del Nuovo Cimento.
- [39] S.C. Curran, A.L. Cockroft and J. Angus, Phil. Mag. **40** (1949) 929.
- [40] J. Byrne, Proc. Roy. Soc. Edinburgh **A66** (1962) 33.
- [41] A. Lansiaart and J.P. Morucci, J. Phys. Radium **23** (1962) 102A, suppl. no 6.
- [42] G.D. Alkhazov, Statistics of electron avalanches and ultimate resolution of proportional counters, Nucl. Instr. & Methods **89** (1970) 155–165.
- [43] H. van der Graaf, Signal development and processing in Multi Wire Proportional Chambers, University of Technology, PhD Thesis, 19 June 1986, Delft.
- [44] S. Ahlen, A. Marin and B. Zhou, Basic information relating to Use of PDT’s: specification for wire/wall a-concentricity, PDT/BU Memo no. 2, February 1992, SSC-note.

## References Chapter 4

- [1] S. Biagi, MAGBOLTZ source code, CERN, obtained by private communication, Biagi@cernvm.cern.ch for information.
- [2] Rob Veenhof, GARFIELD, a drift-chamber simulation program, User’s guide, CERN, Version 5.05, 3 November, 1994.
- [3] H. van der Graaf *et al.*, The honeycomb strip chamber: the application in LHC/SSC experiments and the test results of a prototype, Nucl. Instr. & Methods **A307** (1991) 220.
- [4] H. van der Graaf, Signal development and processing in Multi Wire Proportional Chambers, University of Technology, PhD Thesis, 19 June 1986, Delft.
- [5] Hansjörg Fischle, Joachim Heintze and Bernard Schmidt, Experimental determination of ionization cluster size distributions in counting gases, Nucl. Instr. & Methods, **A301** (1991) 202–214.
- [6] E. Gatti, A. Longoni, H. Okuno and P. Semenza, Optimum geometry for strip cathodes or grids in MWPC for avalanche localization along the anode wires, Nucl. Instr. & Methods **163** (1979) 83–92.
- [7] F. Piuze, R. Roosen and J. Timmermans, Evaluation of systematic errors in the avalanche localization along the wire with cathode strips read-out MWPC, Nucl. Instr. & Methods **196** (1982) 451–462.
- [8] J. Chiba *et al.*, Study of position resolution for cathode readout MWPC with measurement of induced charge distribution, Nucl. Instr. & Methods **206** (1983) 451–463.
- [9] H. van der Graaf and J.P. Wagenaar, A calculation in three dimensions of the induced charge on the electrodes of an MWPC, Nucl. Instr. & Methods **217** (1983) 330–334.
- [10] J.S. Gordon and E. Mathieson, Cathode charge distributions in multiwire chambers; I. Measurement and theory, Nucl. Instr. & Methods **227** (1984)



267–276.

- [11] J.R. Thompson, J.S. Gordon and E. Mathieson, Cathode charge distributions in multiwire cham-

bers; B. Distribution in anode wire direction, Nucl. Instr. & Methods **A234** (1985) 505–511.

## References Chapter 5

- |   |   |
|---|---|
| <p>[1] G. Viehhauser, Detector Physics of the ATLAS MDT muon precision chambers, University of Vienna, PhD Thesis, 1996, Vienna, CERN.</p> <p>[2] A.P. Colijn, Cosmic ray and beam tests with the Honeycomb Strip Chamber, Master thesis, University of Utrecht, The Netherlands, November 21, 1994.</p> <p>[3] P.R. Rewiersma, Internal Documentation EA, NH 19-6523, NIKHEF-H, Amsterdam, 1986.</p> | <p>[4] P.R. Rewiersma, Internal Documentation EA, NH 19-6121, NIKHEF-H, Amsterdam, 1986.</p> <p>[5] LeCroy Model 4208 8-channel wide range real time TDC, User's manual, Geneva, 1982.</p> <p>[6] J. Schmitz, The Microstrip Gas Counter and its application in the ATLAS inner tracker, University of Amsterdam, PhD Thesis, 14 October 1994, Amsterdam.</p> |
|---|---|

## References Chapter 6

- |   |  |
|---|--|
| <p>[1] M. Della Negra <i>et al.</i>, Status report of the RD5 experiment, CERN/DRDC/93-49, 5 January 1994.</p> <p>[2] R. Bergman, Thesis on the TRACAL detector in RD5, Title to be announced, University of Nijmegen, PhD Thesis, 1996, Nijmegen.</p> <p>[3] M. Aalste <i>et al.</i>, Measurement of hadron shower punchthrough in iron, Z. Phys. <b>C60</b> (1993) 1–</p> | <p>10. C. Albajar <i>et al.</i>, Measurement of momentum and angular distribution of punchthrough muons at the RD5 experiment, Submitted to Z. Phys. <b>C</b>.</p> <p>C. Albajar <i>et al.</i>, Measurement of hadron shower punchthrough in a magnetic field, Accepted for publication by Z. Phys. <b>C</b>, CERN-PPE/95-61.</p> <p>[4] LeCroy Model 2277 16-channel TDC.</p> |
|---|--|



# Summary

**T**his thesis describes the construction and performance of the Honeycomb Strip Chamber (HSC). The HSC offers several advantages with respect to classical drift chambers and drift tubes. The main features of the HSC are:

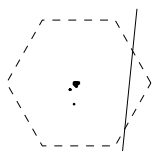
- The detector offers the possibility of simultaneous readout of two orthogonal coordinates with approximately the same precision.
- The HSC technology is optimised for mass production. This means that the design is modular (monolayers) and automatisation of most of the production steps is possible (folding and welding machines).
- The technology is flexible. The cell diameter can easily be changed from a few millimetres to at least 20 mm by changing the parameters in the computer programme of the folding machine. The number of monolayers per station can be chosen freely to the demands of the experiment.
- The honeycomb structure gives the detector stiffness and makes it self supporting. This makes the technology a very transparent one in terms of radiation length which is important to prevent multiple scattering of high energetic muons.
- The dimensions of the detector are defined by high precision templates. Those templates constrain for example the overall tolerance on the wire positions to 20  $\mu\text{m}$  rms. Reproduction of the high precision assembly of the detector is thus guaranteed.

The above summarised qualities of the HSC focus mainly on topics related to the production of the detector. In this thesis the performance of several prototypes have been studied as well in experiments as with computer simulations. The hexagonal shape and the segmentation in strips of the cathode might offer drawbacks in the performance. Special attention has to be given to the determination of the relation between drift time and drift distance. This is done in chapter 5. The detector has to be operational in strong magnetic fields. This is verified by measurements and simulations in chapter 6.

Chapter 1 introduces the Large Hadron Collider and the physics potential of this machine. Special attention is given to physics processes which have their signature in the muon system of the LHC experiments, like  $H \rightarrow ZZ^{(*)} \rightarrow \mu^+\mu^-\mu^+\mu^-$  and  $Z' \rightarrow \mu^+\mu^-$ . For the last two decays where at least one muon pair is on the Z-shell it is desirable for background reduction to measure the invariant mass of a  $\mu^+\mu^-$  pair with a precision in the order of 1%.

In chapter 2 the physics requirements on the muon system are translated to the layout of the ATLAS muon spectrometer. The use of the anode wire readout for the bending coordinate is justified in case of HSC technology as precision muon detector in the ATLAS barrel. An estimation is made of the total particle fluxes in the different muon stations of ATLAS.

In chapter 3 the main processes involved in operating the HSC as a drift tube are discussed. This discussion includes the process of primary ionisation, diffusion in magnetic fields, attachment and gas gain properties. Remarkable is the discovery that the diffusion contribution to the spatial resolution is *not* quadratically proportional to the path length in inhomogeneous electric fields. In some cases this effect results in a decrease in the spatial uncertainty for longer drift paths in drift tubes with a  $1/r$  dependence of the electric field. In this chapter, also the construction of the various HSCs is described.



In chapter 4 the computer simulation package is described to compute the characteristics of the drift tube and front end electronics. The input in the programs are the processes described in chapter 3 and the output is essentially the distance-time relation, spatial resolution and efficiency of the defined detector setup.

The ATLAS muon detectors will be operated in strong (up to 1 T) inhomogeneous magnetic fields. The distance-time  $r(t)$  relation is strongly coupled to the strength and direction of the magnetic field via the Lorentz angle. This results in variations of  $r(t)$  from detector to detector and in some cases even within one detector. The ATLAS drift tube muon chambers rely heavily on the in situ calibration (autocalibration) of the  $r(t)$  relation from the muon data itself. In chapter 5 an algorithm is suggested to perform autocalibration on a dataset with redundant track position information. The algorithm shows that the required redundancy is not always available, even if a track is defined by more hits than the number of degrees of freedom to describe the track. The suggested algorithm writes the correlation between the corrections on the  $r(t)$  in a matrix equation. The determinant of this matrix is a direct measure of the uniqueness of the resulting  $r(t)$ . The algorithm is also faster than conventional algorithms. Finally the principle of autocalibration is demonstrated in a reference experiment with four MSGC counters which define the  $r(t)$  independently from the autocalibration method. The agreement between both methods is excellent.

In chapter 6 the main prototype test results are summarised and comparisons with simulations as described in chapter 4 are made. The tests are performed in cosmic ray experiments at NIKHEF as well in the muon testbeam of the RD5 experiment at CERN. Two HSCs have been tested at the RD5 experiment in a 3 T magnetic field.

The performance of the HSC as a drift tube is well understood and can well be simulated for tracks crossing the cell over a large range of its radius. For tracks crossing the cell in the outer regions, however, simulations predict a better resolution than is realised in experiments.

The single wire resolution is a strong function of the drift gas (and thus the maximum drift time), gas gain and the value of the applied threshold on the signal. In the P1 detector with inner tube radius of 5 mm, an average resolution has been measured of 105  $\mu\text{m}$  with Ar/CO<sub>2</sub> 80/20 drift gas ( $T_{\text{max}} = 250$  ns) and  $2 \times 10^5$  gas gain. With Ar/CO<sub>2</sub> 50/50 as drift gas, 80  $\mu\text{m}$  resolution has been measured.

The HSC prototypes with 10 mm cell inner radius (P3, P3A) show a deteriorated resolution in the outer regions of the cell, due to its hexagonal shape. This effect is also seen in the simulations (although less pronounced). For the HSC with small (5mm inner radius) cells, no deterioration is expected and measured due to the hexagonal shape. A small (15%) effect in the resolution close to the cathode is measured due to the segmentation of this cathode in strips.

Two HSC prototypes have been operated in 3 T magnetic fields. The increase in the drift time of the electrons due to the Lorentz force can well be simulated. The changed relation between the track distance to the wire and the measured drift time  $r(t)$  can well be reconstructed by autocalibration and averaged over the drift-volume. No degradation of the resolution has been observed.

Tests with a large prototype (P3) have shown that the relative positions of the monolayers of a HSC detector can be measured with muon tracks.

Finally, I like to mention here that the HSC technology is used for the construction of  $3 \times 3 \text{ m}^2$  CHORUS muon stations. For these chambers, no strip readout is applied and the cathodes are produced from POCALON foil, a conductive plastic. Furthermore, the HSC technology will be used for the HERA-B tracking detector and is a candidate for the LHC-B and CHEOPS tracking detectors.

# Samenvatting

**I**n dit proefschrift wordt de constructie en werking van de Honingraat Strip Kamer (HSC) beschreven. De HSC is een nieuw type muon detector en biedt vele voordelen ten opzichte van bestaande driftkamers. Enkele hiervan zijn:

- De HSC heeft de mogelijkheid om de coördinaten van een passerend deeltje in twee loodrecht op elkaar staande richtingen te bepalen met een hoge nauwkeurigheid in beide richtingen.
- De HSC is geschikt voor massaproductie van de kamer. Dit betekent dat het ontwerp modulair is (mono-lagen) en dat de meeste productiestappen geautomatiseerd kunnen worden (vouw- en lasmachines).
- De HSC is niet gebonden aan standaard maten. De geometrie kan voor iedere toepassing geoptimaliseerd worden.
- De honingraat structuur van de kathodes geeft de detector mechanische stijfheid en voorkomt de noodzaak van zware draagstructuren. Dit maakt de HSC met name geschikt voor toepassingen waar de hoeveelheid materiaal in het experiment kritisch is.
- De vorm van de mono-lagen wordt gedefinieerd door een mal. De mal zorgt ervoor, dat de relatief slappe (dunne) folies hun vorm behouden tijdens assemblage van de kamer en dat de anode draden met de vereiste nauwkeurigheid van  $20\text{ }\mu\text{m rms}$  worden gepositioneerd.

In dit proefschrift wordt ingegaan op het gedrag van de HSC in experimenten met een testbundel en in computersimulaties.

Er is een uitgebreide studie verricht naar de bepaling van de relatie tussen de gemeten drifttijd  $t$  en bijbehorende driftafstand  $r$ .

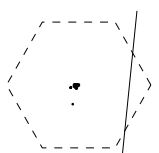
De HSC is ontwikkeld voor een toepassing die werking van de technologie in sterke magneetvelden vereist (de ATLAS muon kamers). Hiervoor zijn experimenten en berekeningen gedaan om het karakteristieke gedrag van de HSC in sterke magneetvelden te bepalen.

In hoofdstuk 1 wordt de *Large Hadron Collider* geïntroduceerd. Enige fysische processen die zich duidelijk manifesteren in het detectie-systeem voor muonen (muonsysteem) van de LHC experimenten worden besproken.

In hoofdstuk 2 worden de specificaties van het ATLAS muonsysteem en de bijbehorende muondetectietechnologie afgeleid van de verschijningsvorm van interessante gebeurtenissen in ATLAS. Er wordt ingegaan op de vraag, hoe de HSC technologie optimaal benut kan worden als precisiedetector in het ATLAS muonsysteem.

In hoofdstuk 3 worden de fysische processen in de HSC als gevolg van het passeren van een geladen deeltje besproken. Door het sterke inhomogene karakter van het elektrisch veld in de HSC-buis, is de diffusiebijdrage in de plaatsresolutie niet langer evenredig met de wortel van de driftafstand. In dit hoofdstuk wordt tevens de constructie van diverse HSC proefmodellen beschreven.

In hoofdstuk 4 wordt de simulatie beschreven die gebruikt is om de eigenschappen van de driftbuis en de detector-electronica te berekenen. De in hoofdstuk 3 beschreven processen zijn als invoergegevens gebruikt en in de simulatie worden alle belangrijke detector parameters berekend, zoals de maximale drifttijd, plaatsresolutie en efficiëntie.



Aangezien de relatie tussen de afstand van het spoor tot de draad en gemeten drifttijd ( $r(t)$ ) sterk afhangt van het magnetisch veld in de driftbuis is het belangrijk om deze afhankelijkheid goed te berekenen of te kunnen meten. In hoofdstuk 5 wordt een methode afgeleid om deze  $r(t)$  relatie uit de gemeten drifttijden zelf af te leiden (autocalibratie). Dit is mogelijk doordat een recht spoor met twee vrijheidsgraden wordt beschreven en met meer dan twee punten wordt gemeten. Het voorgestelde algoritme om  $r(t)$  uit de data te reconstrueren is sneller dan conventionele algoritmes en heeft de mogelijkheid om de eenduidigheid van het resultaat te bepalen. Tevens wordt de werking van autocalibratie bewezen in een referentie experiment, waarin  $r(t)$  zowel door autocalibratie als door externe onafhankelijke spoordetectoren is verkregen.

In hoofdstuk 6 worden de testresultaten van proefmodellen gepresenteerd. De gemeten resultaten zijn vergeleken met de uitkomsten van simulaties zoals beschreven in hoofdstuk 4. De HSC proefmodellen P1, P2 en P3 zijn zowel in Amsterdam met kosmische stralen als op CERN met een muonbundel getest.

De werking van de HSC als een driftbuis is goed begrepen en met de simulaties worden de metingen met betrekking tot de meeste situaties voorspeld. Voor sporen die het buitenste deel van de buis passeren, geeft de simulatie echter een betere resolutie aan, dan momenteel wordt gemeten.

De plaatsresolutie van de HSC driftbuis is sterk afhankelijk van het gebruikte driftgas, de gasversterking en de drempelwaarde waarop het signaal op de anode wordt gedetecteerd. Met de P1 detector is een gemiddeld oplossend vermogen gerealiseerd van  $105\ \mu\text{m}$  met Ar/CO<sub>2</sub> 80/20 driftgas ( $T_{\text{max}} = 250\ \text{ns}$ ) en  $2 \times 10^5$  gasversterking. Met Ar/CO<sub>2</sub> 50/50 is een gemiddeld oplossend vermogen van  $80\ \mu\text{m}$  gemeten.

De HSC proefmodellen met een buisdiameter van 20 mm (P3, P3A) vertonen een verminderde nauwkeurigheid voor sporen op relatief grote afstand van de draad ten gevolge van de hexagonale vorm van de buis. Dit effect wordt door de simulaties ook voorspeld, zij het in mindere mate. Voor de HSCs met 10 mm buisdiameter is deze verslechtering in de buitenste regio's van de buis minder significant. In de P2 detector is gemeten, dat de resolutie langs de draad (voor sporen dicht bij de kathode) variaties vertoont van 15% ten gevolge van de segmentatie van de kathode in strippen.

Twee HSCs zijn getest in magnetische velden tot 3 T, parallel aan de anodedraad. De toename van de drifttijd van de elektronen ten gevolge van de Lorentzkracht is in overeenstemming met de simulatie. De veranderde  $r(t)$  relatie is met succes bepaald door autocalibratie en de gemiddelde plaatsresolutie van de detector werd niet negatief beïnvloed door de aanwezigheid van een sterk (homogeen) magneetveld.

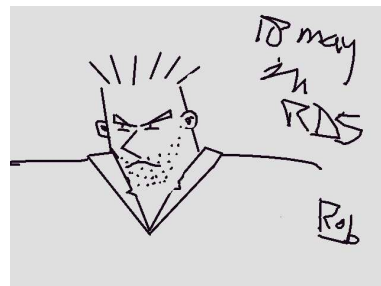
Uit experimenten met de P3 detector is ook gebleken, dat de relatieve positie van de monolagen kan worden bepaald met behulp van muon sporen.

Tenslotte wil ik er op wijzen dat de HSC technologie gebruikt wordt voor de constructie van  $3 \times 3\ \text{m}^2$  CHORUS muonstations. Deze detectoren hebben geen strip uitlezing nodig en de kathodedefolies zijn derhalve gemaakt van POCALON, een geleidend plastic. Verder wordt de HSC technologie toegepast in de HERA-B detector en is de HSC kandidaat voor toepassing in de LHC-B en CHEOPS experimenten.

# Acknowledgements

**T**his page is devoted to all people who contributed somehow to this work. Since I will almost certainly forget some persons I like to ask forgiveness to those people and, yes, thank you too !

First, there is my partner during all test beams in RD5 who worked with me with the same enthusiasm and everlasting energy on all those exciting test beams: 'The Yellow Bird, Malloot' Rob Bergman. Rob, thanks a lot and good luck finishing your part. Together with Rob I felt 'at home' in the RD5 experiment. I can not mention everybody, but Gyorgy Bencze, Claudia E. Wulz, Fritz Szoncsó, Chris Seez, Grzegorz Wrochna, David Peach, Pascal Petiot, Gerhard Waurick and Ernst Radermacher offered all the facilities a detector physicist could wish. It only cost me some bottles of Heineken. I have experienced the work at RD5 with Jim Shank, Vinny Polychronakos, Pierluigi Zotto, Lino Casoli, David Chrisman, Anna Di Ciaccio, Thomas Moers, Leandro Nisati, Hans Reithler, Hans Tuchscherer, Rui Ribeiro, Marco Verzocchi and of course Jan van Eldik as very encouraging. I hope it was meant this way.



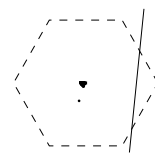
Jumping from RD5 to ATLAS, I like to thank my always hard working equivalent Georg Viehhauser and Werner Riegler for the fruitful discussions. A special thanks to Rob Veenhof who implemented the hexagon in his drift chamber simulation programme GARFIELD and who was a never ending source of tips and hints on all drift chamber topics. I thank Steve Biagi for all MAGBOLTZ related E-mail contacts. Further, I like to thank Walter Blum and Chris Fabjan for their contribution to the discussions in the ATLAS muon working group.

In general I like to thank the NIKHEF-L3 community at CERN for the resources I could use, like computer accounts and both the Nikkies. Special thanks to Gerjan Bobbink who borrowed me half the L3 experiment. During all testbeams I was supported by a group of electronics specialists. Special thanks to Frank Bakker, Sandro Sman, Thei Wijnen, Cees Brouwer, Adriaan König, Henk Groenstege, Marinko Gospic and even Wim Gotink.

At NIKHEF I like to thank Gras van Apeldoorn, Fred Udo and Fred Hartjes for their experienced input and Gras especially for all the work in the lab. Harry van der Graaf and I started this ATLAS HSC project, but I really appreciated the discussions with Graziano Massaro and Frank Linde. Frank, good luck with the tubes! Also thanks to Kors Bos who introduced me in the world of GEANT, Frans Crijns and Carel Pols for their simulation efforts. The design and production of the HSCs has been impossible without the effort of Joop Buskens, Henk Schuylenburg, Gerard Evers and their groups. Special thanks to Paul Rewiersma who was the source of inputs for the front-end simulation programme. Thanks to Willem van Leeuwen and Rene Wilhelm for their support on computer related problems.

NIKHEF did not only bring me science, but also friendship. I can devote pages to anecdotes about my colleagues. 'Draaideur' Els, Jurriaan and Saskia, Jan, 'Big Business' Erwin, Ivar, 'Bull shit' Jiri, Frenk, Monty and Valerie, 'Godmejjâar' Marcel and Esther you are all very special.

For reading and correcting my thesis I like to thank Harry, Bob van Eijk and Cees Daum. Thanks to Martin Woudstra for reading the manuscript. I wish him a good time in the ATLAS muon community. But, as always, the responsibility for the contents is all mine. Thanks to Auke



Pieter Colijn. I have to give him all the credits for the reference experiment with the P1 and MSGCs.

A very important contribution to this work came from my sister and her husband: Marloes and Wil who welcomed me even to their home when I was homeless for a while. Thanks. Annet Menheere, Bert de Vries, Frans Vos, my brother Twan and my parents contributed to this work in an unexplainable way.

Finally I like to ask forgiveness to my dearest friend, girlfriend and partner for all the lonesome evenings and week-ends. Monique, you know how it is to live with a physicist. Thanks and good luck. The last line of this acknowledgement is to Boul, our chinchilla. Bon appetit on this thesis.

# Curriculum vitae

**T**he author of this thesis was born on the 14th of July 1967 in Rosmalen, a small village in the south of the Netherlands, laying between 's Hertogenbosch and the river 'la Meuse'. After two years of elementary school, he was advised by his teacher to start again at the first grade. The boy knew better (of course) and persisted to continue his scientific training in the third grade. From that moment it was clear to everybody that he was stubborn enough to become a physicist.

After elementary school he continued his career at the 'Jeroen Bosch' High school where he passed his HAVO exam in 1984 and Atheneum exam in 1986.

Without any doubt (from his side, the more from his teachers again), he started in 1986 at the University of Technology Eindhoven with his physics studies. During those studies he was active as a sportsman and member of the board of the athletics sports club of the University. During his periods of practical training he first worked for three months on high  $T_c$  superconductors at the University of Eindhoven. Then he moved for six months to Orsay (20 km south of Paris), to work on the injection beam line of the AGOR cyclotron. This cyclotron was during his presence in 1990 under construction in Orsay and is momentarily in use at the KVI at Groningen (the Netherlands). After his return from Orsay, he started his exam research in the group 'Nuclear physics techniques' of prof. dr. M.J.A. de Voigt under supervision of dr. L.J. van IJzendoorn at his home University at Eindhoven. His degree thesis was on the detection of small dose of light nuclei on heavy nuclei carriers by scattering high energetic (25 MeV)  $\alpha$ -particles on the sample of interest.

He started in December 1991 at the Dutch institute for nuclear and high energy physics NIKHEF, Amsterdam with his PhD research. He worked four years in the ATLAS/instrumentation group on the Honeycomb Strip Chamber. This work resulted in this thesis.

